Broadband vibration control using nonlinearly interfaced piezoelectric elements

Linjuan Yan

▶ To cite this version:

Linjuan Yan. Broadband vibration control using nonlinearly interfaced piezoelectric elements. Other. INSA de Lyon, 2013. English. NNT : 2013ISAL0107 . tel-00961224

HAL Id: tel-00961224

https://theses.hal.science/tel-00961224

Submitted on 19 Mar 2014

N° d'ordre 2013-ISAL-0107 Année 2013

Thèse

Contrôle de vibrations large bande à l'aide d'éléments piézoélectriques utilisant une technique non-linéaire

-

Broadband vibration control using nonlinearly interfaced piezoelectric elements

Présentée devant
L'Institut National des Sciences Appliquées de Lyon

Pour obtenir
Le grade de docteur

École doctorale : Electronique, Electrotechnique et Automatique
Spécialité : Energie et Système

Par
Linjuan YAN
Soutenue le 04 Octobre 2013 devant la Commission d'examen

Jury MM.

Directeur	D.	GUYOMAR	Professeur à l'INSA de Lyon
Co-directeur	M.	LALLART	Maître de conférences à l'INSA de Lyon
Rapporteurs	M.	COLLET	Directeur de Recherche à FEMTO-ST
	J.-F.	DEU	Professeur au CNAM
Président	J.	POUGET	Professeur à l'Université Pierre et Marie Curie
Examinateur	M.	ICHCHOU	Professeur à l'Ecole Centrale de Lyon

Laboratoire de recherche : Laboratoire de Génie Electrique et Ferroélectricité (LGEF) de l'INSA de Lyon

INSA Direction de la Recherche - Ecoles Doctorales – Quinquennal 2011-2015

SIGLE	ECOLE DOCTORALE	NOM ET COORDONNEES DU RESPONSABLE
CHIMIE	**CHIMIE DE LYON** **http://www.edchimie-lyon.fr** Sec :Renée EL MELHEM Bat Blaise Pascal 3^{e} etage Insa : R. GOURDON	M. Jean Marc LANCELIN Université de Lyon – Collège Doctoral Bât ESCPE 43 bd du 11 novembre 1918 69622 VILLEURBANNE Cedex Tél : 04.72.43 13 95 directeur@edchimie-lyon.fr
E.E.A.	**ELECTRONIQUE, ELECTROTECHNIQUE, AUTOMATIQUE** **http://edeea.ec-lyon.fr** Secrétariat : M.C. HAVGOUDOUKIAN eea@ec-lyon.fr	M. Gérard SCORLETTI Ecole Centrale de Lyon 36 avenue Guy de Collongue 69134 ECULLY Tél : 04.72.18 60.97 Fax : 04 78 43 37 17 Gerard.scorletti@ec-lyon.fr
E2M2	**EVOLUTION, ECOSYSTEME, MICROBIOLOGIE, MODELISATION** **http://e2m2.universite-lyon.fr** Insa : H. CHARLES	Mme Gudrun BORNETTE CNRS UMR 5023 LEHNA Université Claude Bernard Lyon 1 Bât Forel 43 bd du 11 novembre 1918 69622 VILLEURBANNE Cédex Tél : 06.07.53.89.13 e2m2@ univ-lyon1.fr
EDISS	**INTERDISCIPLINAIRE SCIENCES-SANTE** **http://www.ediss-lyon.fr** Sec : Insa : M. LAGARDE	Mme Emmanuelle CANET-SOULAS INSERM U1060, CarMeN lab, Univ. Lyon 1 Bâtiment IMBL 11 avenue Jean Capelle INSA de Lyon 696621 Villeurbanne Tél : 04.72.68.49.09 Fax :04 72 68 49 16 Emmanuelle.canet@univ-lyon1.fr
INFOMATHS	**INFORMATIQUE ET MATHEMATIQUES** **http://infomaths.univ-lyon1.fr** Sec :Renée EL MELHEM Bat Blaise Pascal 3^{e} etage infomaths@univ-lyon1.fr	Mme Sylvie CALABRETTO LIRIS – INSA de Lyon Bat Blaise Pascal 7 avenue Jean Capelle 69622 VILLEURBANNE Cedex Tél : 04.72. 43. 80. 46 Fax 04 72 43 16 87 Sylvie.calabretto@insa-lyon.fr
Matériaux	**MATERIAUX DE LYON** **http://ed34.universite-lyon.fr** Secrétariat : M. LABOUNE PM : 71.70 –Fax : 87.12 Bat. Saint Exupéry Ed.materiaux@insa-lyon.fr	M. Jean-Yves BUFFIERE INSA de Lyon MATEIS Bâtiment Saint Exupéry 7 avenue Jean Capelle 69621 VILLEURBANNE Cedex Tél : 04.72.43 83 18 Fax 04 72 43 85 28 Jean-yves.buffiere@insa-lyon.fr
MEGA	**MECANIQUE, ENERGETIQUE, GENIE CIVIL, ACOUSTIQUE** **http://mega.universite-lyon.fr** Secrétariat : M. LABOUNE PM : 71.70 –Fax : 87.12 Bat. Saint Exupéry mega@insa-lyon.fr	M. Philippe BOISSE INSA de Lyon Laboratoire LAMCOS Bâtiment Jacquard 25 bis avenue Jean Capelle 69621 VILLEURBANNE Cedex Tél :04.72 .43.71.70 Fax : 04 72 43 72 37 Philippe.boisse@insa-lyon.fr
ScSo	**ScSo*** **http://recherche.univ-lyon2.fr/scso/** Sec : Viviane POLSINELLI Brigitte DUBOIS Insa : J.Y. TOUSSAINT	M. OBADIA Lionel Université Lyon 2 86 rue Pasteur 69365 LYON Cedex 07 Tél : 04.78.77.23.86 Fax : 04.37.28.04.48 Lionel.Obadia@univ-lyon2.fr

*ScSo : Histoire, Géographie, Aménagement, Urbanisme, Archéologie, Science politique, Sociologie, Anthropologie

Acknowledgements

This work has been done in the laboratory of “Génie Electrique et Ferroélectricité (LGEF)” of INSA-Lyon under the guidance of Prof. Daniel GUYOMAR and Dr. Mickaël LALLART. It would not have been finished on time without the support of many people. Thus, I would like to express my sincere gratitude to them for their help in these years.

First and foremost, I would like to extend my deepest appreciation to Prof. GUYOMAR for giving me an opportunity to pursue my Doctor degree in LGEF and offered me the freedom for my academic research on such an interesting and interdisciplinary subject.

Additionally, I would like to extend my endless gratitude to my co-supervisor Mickaël LALLART for his academic guidance and continuous encouragement. His inspirational guidance, patience and careful explanation were extremely valuable for achieving the progress theoretically and experimentally.

Secondly, I would like thank all the members of my Ph.D. jury for evaluating my work and for attending my defence. I would like extend my special and sincere appreciation to Prof. Manuel COLLET and Prof. Jean-François DEÜ for reviewing this manuscript and for their effort and time commitment. I am grateful to them for their valuable remarks and suggestions. I would like to thank Prof. Mohamed ICHCHOU and Prof. Joël POUGET for examining this present work. I also extend my sincere gratefulness to Prof. Joël POUGET for chairing the committee.

I would like to acknowledge the support of Prof. Einar HALVORSEN for his precious help in the noise generation. I do owe my unfeigned thanks to my supervisor in my master stage, Prof. Zhichun YANG, for always sharing his experience with me over these years. I also wish to express my sincere gratitude to Prof. Jiankang LU and Prof. Wei ZHANG for their help and encouragement. Besides, I would like thank all the colleagues in LGEF.

Finally, I would like thank China Scholarship Council (CSC) for the financial support.

On a personal note, I owe special thanks to my parents for their continuous support, understanding and endless love. I do appreciate that my boyfriend is always there and provides me his encouragement, support and love. I would also like to thank all my friends.

Table of Contents / Table des Matières

List of Figures / Listes des Illustrations

Partie française

English part

List of Table / Liste des Tableaux

Partie française

English part

Notation and abbreviation

Notation

Greek characters

Symbol	*Signification*
α	Force factor
β	Proportional damping coefficient
β_{sum}	Threshold parameter for sum switch
$\beta_{differnece}$	Threshold parameter for difference switch
γ	Inversion coefficient
δ	Phase difference
ε	Electrical permittivity
ε_0	Vacuum permittivity
η	Logarithmic decay
θ	Bending slope
κ	Global coupling coefficient
λ	Eigenvalues
υ	Poisson's ratio
ρ	density
σ	Direction of polarization of piezoelectric insert
ζ	Damping ratio
ω	Angular frequency
Ω	Ratio of external frequency to resonant frequency of host structure

Alphabetic characters

Symbol	Signification
c	Damping
d_{31}	Piezoelectric charge coefficient
d	Variables vector of each node
f	Frequency
k	Stiffness
k_b	Complex wavenumber

l	Length of each element
m	Mass
n	Number of elements
r	Ratio
s	Mechanical compliance tensor of piezoelectric element
t	Thickness
t_i	Inversion time
w	Width
x_c	Neutral axis
C	Damping matrix
C_0	Clamped capacitance of piezoelectric patch
D	Electric displacement
D_{thres}	Displacement threshold
E	Electrical field intensity
F	External force in time domain
$\tilde{F}$	External force in frequency domain
H	Crenel funtion
H_{er}	Hermitian shape function
K	Stiffness matrix
L	Length
L_{in}	Inductance
M	Mass matrix
N	Calculated points in a given time window
$Ncell$	Number of cells
$\tilde{P}$	External force and moment vector in frequency domain
Q	Electric charge
R	Resistance
S	Strain
T	Stress
T_{es}	Given time window
V_p	Piezovoltage
X	Displacement response in time domain
$\tilde{X}$	Displacement response in frequency domain
Y	Young's modulus

Subscripts

$classical$	Classical SSDI approach
$enhanced$	Enhanced SSDI strategy based on spatial filtering
b	Substrate beam
d	Difference
e	Experiments
m	Mass
p	Piezoelectric patch
s	Simulation
S	Sum
ω	Angular frequency
ζ	Damping ratio

Superscripts

E	Constant electric field
T	Constant stress
e	Element
N_{cell}	The $N_{\mathrm{cell}}^{\mathrm{th}}$ periodic cell

Abbreviation

Symbol	Signification
SSD	Synchronized switching damping
SSDI	Synchronized switching damping on inductor
TMD	Tuned mass damper
TDOF	Two-degree-of-freedom

Résumé Français

Résumé

Afin de limiter les contraintes dans les matériaux pour accroître leur durée de vie et améliorer la sécurité des structures (par exemple dans les transports), ainsi que d'améliorer le confort des utilisateurs, le contrôle de vibrations mécaniques et leur amortissement a fait l'objet d'abondantes recherches scientifiques depuis de nombreuses décennies. De plus, la prolifération récente des matériaux dits « intelligents » couplant plusieurs disciplines de la physique telles que la mécanique et l'électricité a permis l'élaboration de techniques de contrôle de vibration fiables, robustes et performantes tout en étant très intégrables, permettant ainsi de disposer de méthodes totalement adaptées aux systèmes embarqués ou aux structures où les contraintes d'encombrement sont relativement restrictives. Notamment, il a récemment été proposé l'utilisation de techniques non linéaires basées sur une commutation synchronisée d'éléments piézoélectriques sur une impédance afin d'améliorer la conversion d'énergie mécanique sous forme électrique et ainsi de disposer de systèmes de contrôle de vibrations très performants et intégrables.

Néanmoins, du fait du principe de cette commutation synchronisée avec la déformation, le contrôle de vibrations large bande, très présentes dans les environnements réels, conduit à une dégradation des performances de ces techniques. L'objectif des travaux rapportés dans cette thèse consiste à proposer et à étudier théoriquement et expérimentalement des approches dérivées de ces techniques mais totalement adaptées au large bande.

Ainsi, après une introduction relatant l'état de l'art en termes de contrôle vibratoire, la première technique exposée dans cette thèse propose d'utiliser un filtrage spatial permettant de séparer les modes de vibration pour ensuite connecter de manière appropriée des éléments piézoélectriques afin de pouvoir simultanément contrôler plusieurs modes de vibration en flexion.

La deuxième méthode pour disposer de systèmes de contrôle de vibrations efficaces se base sur la combinaison d'amortisseurs à masse accordée avec l'approche non-linéaire afin d'améliorer le pouvoir d'amortissement par un contrôle supplémentaire des transferts énergétiques via le couplage électromécanique, conduisant à une méthode efficace, robuste et pouvant être installée facilement.

La troisième et dernière approche consiste à utiliser les propriétés remarquables des structures périodiques en les couplant avec l'approche non-linéaire, cette dernière permettant une augmentation de l'amortissement et un élargissement significatif des bandes fréquentielles réduisant significativement l'amplitude de l'onde.

Enfin, une conclusion générale exposera les principaux résultats obtenus et proposera des pistes d'évolution des concepts exposés.

Chapitre FR-1. Etat de l'art

FR-1.1. Motivations

Les vibrations sont parmi les effets physiques les plus communs dans notre existence, et sont le plus souvent bénéfiques (parole, musique, avertissement, nettoyage…). Néanmoins, certaines sources de vibration sont indésirables et peuvent conduire à un inconfort (par exemple à cause de nuisances sonores dues à des travaux ou une route fréquentée, ou encore les vibrations des sièges des transports) ou à une fatigue voire un endommagement fatal des structures (l'un des exemples les plus marquants est celui du pont de Tacoma Narrows qui entra en résonance sous l'action des rafales de vents - Figure FR-1.1).

Figure FR-1.1. Effondrement du pont de Tacoma Narrows du fait des vibrations induites par les rafales de vent [1].

Par conséquent, de nombreuses recherches ont été menées afin de se prémunir de ces vibrations indésirables. De nombreuses approches et méthodes ont été développées dans ce sens, comme par exemple éviter les phénomènes de résonance, contrer la force d'excitation, apporter un amortissement adéquat, utiliser un absorbeur etc… Ce chapitre propose ainsi d'exposer les approches classiques pour limiter les vibrations d'un système, en s'attachant tout d'abord à l'aspect matériau, pour ensuite aborder les différentes techniques qu'il est possible de leur associer.

FR-1.2. Matériaux et dispositifs pour le contrôle vibratoire

L'une des approches les plus communes pour limiter les vibrations d'une structure consiste à accroître les pertes afin de dissiper l'énergie mécanique.

FR-1.2.1. Matériaux viscoélastiques

La façon la plus simple de dissiper l'énergie mécanique sous forme de chaleur consiste à ajouter à la structure une couche mécanique supplémentaire présentant un facteur de perte élevé. Pour ce faire, les matériaux viscoélastiques sont particulièrement adaptés. Ces matériaux peuvent soit être implémentés directement de manière non contrainte (dans ce cas la dissipation se fait directement par la déformation) soit de manière contrainte en « sandwich » (où la dissipation est réalisée par le cisaillement), ainsi qu'illustré en Figure FR-1.2. Ces techniques peuvent par ailleurs être combinées avec des approches de conversion d'énergie (par exemple piézoélectrique) afin d'améliorer les capacités d'amortissement, les matériaux viscoélastiques purs étant relativement inefficaces en basse fréquence et/ou haute température.

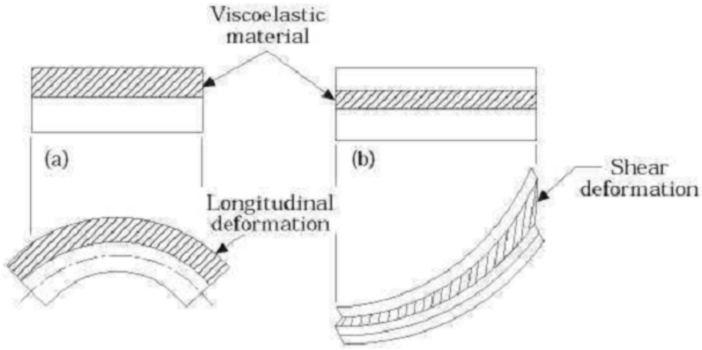

Figure FR-1.2. Configurations basiques des matériaux viscoélastiques : (a) non contraint et (b) contraint [7].

FR-1.2.2. Systèmes d'amortissement particulaires

Une autre manière de dissiper l'énergie mécanique sous forme de chaleur consiste à utiliser les chocs qui peuvent intervenir entre des particules. L'énergie dissipée lors des impacts réduit ainsi l'énergie mécanique dans la structure conduisant donc à un effet d'amortissement. Différentes études ont montré l'effet de la taille des particules, de la friction entre ces dernières, et de la nature des matériaux les composant. La manière dont est implémentée cette technique (par exemple par piston ou cavité - Figure FR-1.3) influe également sur les performances du système. Bien que ces systèmes soit adaptatifs et de taille relativement modeste, les problèmes de vieillissement et d'érosion dus aux chocs entre les particules limitent l'étendu de cette approche.

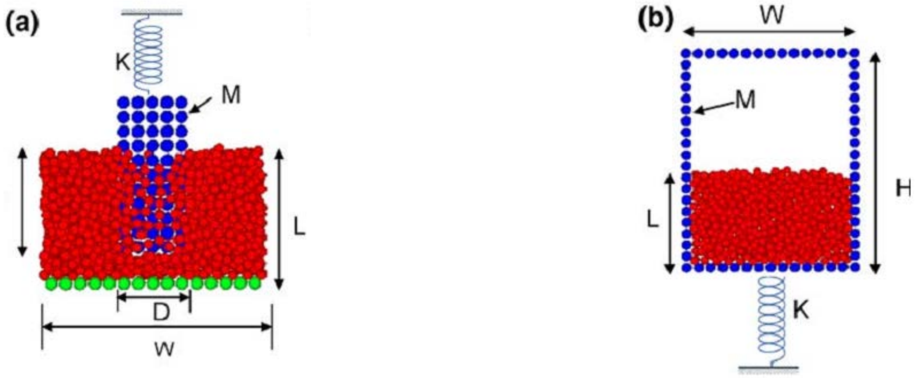

(a) Piston (b) Encapsulé

Figure FR-1.3. Exemples d'amortisseurs particulaires [22]

FR-1.2.3. Systèmes dynamiques accordés

Les systèmes dynamiques accordés se basent sur une structure résonante supplémentaire pour assurer la fonction d'amortissement. Contrairement aux matériaux viscoélastiques et aux systèmes particulaires, les dispositifs accordés sont très dépendants de la structure hôte sur laquelle ils sont implémentés, du fait de la nécessité d'accorder correctement les paramètres dynamiques tels que la masse dynamique et le coefficient d'amortissement. D'un point de vue général, les systèmes accordés peuvent être subdivisés en deux catégories : les absorbeurs accordés (*Tuned Vibration Absorbers* – TVA) et les amortisseurs à masse accordée (*Tuned Mass Dampers* – TMD), les premiers générant une force de réaction égale en amplitude mais opposée en sens alors que les second se basent sur un transfert de l'énergie mécanique de la structure hôte vers l'amortisseur dans le but de la dissiper (ce système étant particulièrement efficace à la résonance). Ainsi, du fait de la nécessité d'accordage, les TMDs ne sont vraiment efficaces qu'autour d'une fréquence bien définie, bien que des systèmes de contrôle large bande basés par exemple sur l'association de plusieurs dispositifs aient été proposés dans la littérature. Enfin, les dispositifs accordés peuvent être combinés avec des matériaux intelligents (par exemple des fluides magnétorhéologiques) afin de pouvoir faire varier certains paramètres pour accroître les capacités d'amortissement et/ou les capacités de contrôle large bande.

FR-1.2.4. Systèmes d'amortissement "intelligents"

Avec le développement des matériaux dits « intelligents » capables de lier les différents domaines de la physique (Figure FR-1.4), les possibilités de contrôler les vibrations se sont grandement élargies. Les différents matériaux couplant le domaine mécanique avec d'autres domaines incluent typiquement les fluides magnéto- et électro-rhéologiques, les matériaux magnétostrictifs et électrostrictifs, les alliages à mémoire de forme, les matériaux électromagnétiques et piézoélectriques.

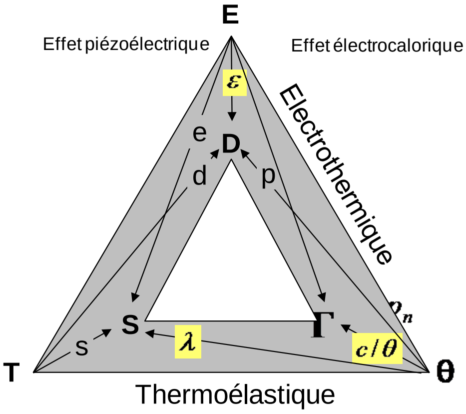

Figure FR-1.4. Couplages multiphysiques

Les fluides magnéto- et électro-rhéologiques sont des systèmes capables de changer rapidement et significativement leurs propriétés mécaniques lorsqu'ils sont respectivement soumis à un champ magnétique ou électrique, en passant d'une phase liquide à une phase visqueuse par orientation des molécules les composant. Ceci se traduit typiquement par un changement de la viscosité ou de la rigidité du système, qui peut dès lors être utilisé pour le contrôle de vibrations, voire combiné avec d'autres matériaux (viscoélastiques par exemple).

Les alliages à mémoire de forme (AMF ou SMA : *Shape Memory Alloy*), qui ont connu un essor sans précédent ces dernières années, font également partie des dispositifs de plus en plus utilisés pour le contrôle de vibrations. Exploitant l'effet de mémoire de forme et de superélasticité, ces matériaux capables de retrouver leur forme d'origine même après l'application de déformations extrêmes basent leurs propriétés uniques sur des changements de phase intrinsèque qui créent ainsi un comportement hystérétique traduisant les capacités de dissipation pour le contrôle de vibrations.

Les matériaux magnétostrictifs et électrostrictifs sont également une classe importante de matériaux capables d'être efficacement utilisés dans l'optique du contrôle vibratoire. Ces matériaux, présentant un couplage magnétomécanique et électromécanique très important, peuvent ainsi efficacement réduire l'énergie mécanique dans la structure en convertissant cette dernière sous une autre forme. De plus, la possibilité de les obtenir sous forme de films polymères les rend particulièrement bien adaptés au contrôle de vibrations de structures flexibles. Néanmoins, ces systèmes requièrent une activation pour pouvoir efficacement convertir l'énergie, nécessitant l'application de champs magnétiques ou électriques relativement élevés.

Les systèmes magnétiques (bobine en mouvement dans un champ magnétique) ou piézoélectriques sont quant à eux naturellement actifs et sont naturellement polarisé, ne nécessitant pas d'activation. En particulier pour les dispositifs intégrés, les matériaux piézoélectriques sont parmi les matériaux les plus utilisés pour le contrôle de vibration, grâce à leur intégrabilité, forte densité de puissance et possibilité de contrôle basse fréquence. Ces matériaux possèdent la capacité unique de se déformer lorsqu'un champ électrique est appliqué (effet inverse) et de générer un champ électrique lorsqu'ils sont contraints (effet direct). Ainsi, leur application au contrôle de vibration est parfaitement adaptée, les différentes approches possibles étant décrites en détail dans le paragraphe suivant.

FR-1.3. Méthodes de contrôle de vibrations électromécaniques par effet piézoélectrique

Le paragraphe précédent s'est attaché à exposer les différents matériaux et couplages qui peuvent être utilisés pour le contrôle vibratoire. Dans la continuité de ce chapitre, il est proposé ici d'exposer les lois de contrôle pour les systèmes d'amortissement à base de matériaux piézoélectriques.

FR-1.3.1. Techniques électromécaniques passives

Les éléments piézoélectriques convertissant l'énergie mécanique sous forme électrique, la façon la plus simple de les utiliser dans le cadre du contrôle vibratoire consiste à dissiper cette énergie. Ainsi, la connexion d'une résistance aux bornes du matériau actif est la manière la plus directe pour réduire l'énergie mécanique dans la structure en dissipant celle-ci une fois convertie sous forme électrique. De plus, afin de maximiser les capacités de conversion d'énergie, l'utilisation d'une inductance (en série ou en parallèle avec la résistance) peut être envisagée, bien que la valeur typique de l'inductance optimale soit souvent prohibitive à basse fréquence (plusieurs dizaines ou centaines d'Henry). Les éléments piézoélectriques peuvent par ailleurs être mis en réseau, comme dans le cas de structures périodiques par exemple, afin de disposer d'un système plus efficace. Enfin, plutôt que de dissiper l'énergie, il peut également être envisagé d'éviter la résonance en connectant l'élément piézoélectrique à une capacité, permettant ainsi de contrôler la fréquence de résonance dans une plage plus ou moins limitée selon le coefficient de couplage électromécanique global de la structure.

D'un point de vue général, les techniques passives sont simples à implémenter, ne nécessitent pas d'énergie extérieure, mais offrent des performances limitées pour des valeurs de composants réalistes et sont très sensibles aux variations environnementales et ne peuvent réaliser de contrôle large bande qu'au prix de structures relativement complexes.

FR-1.3.2. Techniques électromécaniques actives

Afin de palier le problème de performances limitées et de contrôle large bande délicat, les techniques actives proposent l'utilisation d'une chaîne de traitement complète, incluant capteurs, contrôleur, calculateur, amplificateur et actionneurs (Figure FR-1.5), ces derniers ayant pour but de contrer la vibration. De nombreuses méthodes actives sont disponibles, de la plus simple (contrôle proportionnel, PI…) aux plus complexes comme les algorithmes H_∞ ou l'utilisation d'observateurs (ces derniers étant par ailleurs limités par une très grande sensibilité à l'identification des paramètres de la structure), mais toute approche peut soit être vue comme rebouclée (*feedback*) ou par anticipation (*feed forward*), ainsi qu'illustré en Figure FR-1.6.

Bien que les techniques de contrôle actives permettent une réduction importante et robuste des vibrations ainsi qu'un contrôle large bande, la nécessité de traitements complexes ainsi que l'utilisation d'amplificateurs nécessitant une alimentation extérieure conséquente limitent leur application dans le cas de structures de faibles dimensions et/ou de systèmes embarqués.

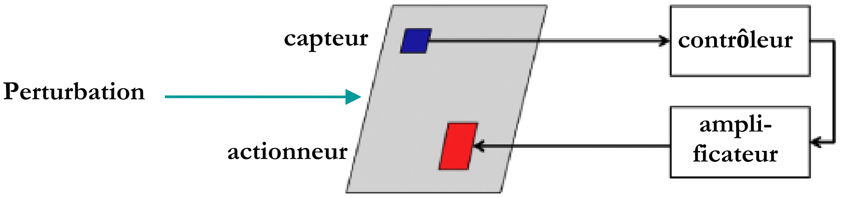

Figure FR-1.5. Système de contrôle actif typique.

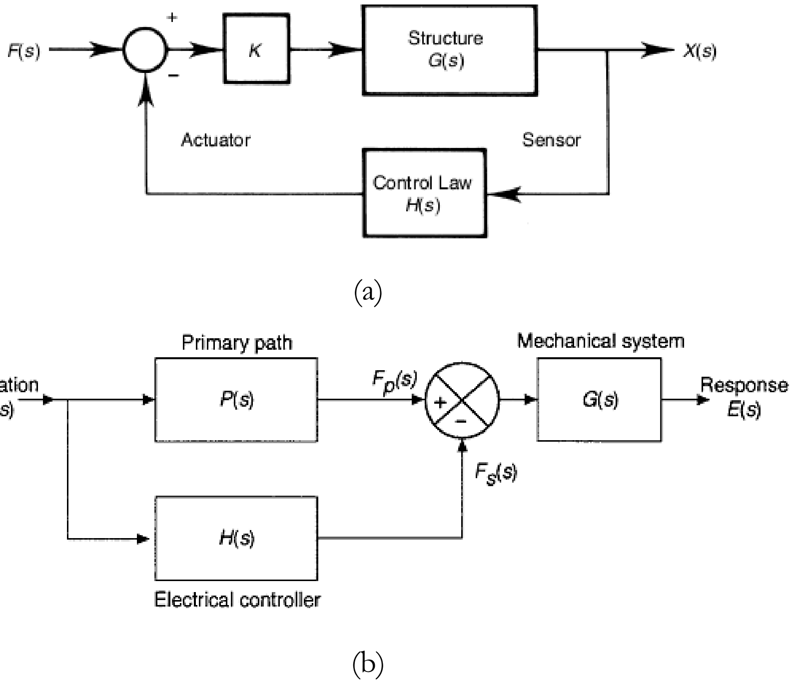

(b)

Figure FR-1.6. Type de contrôle actif : (a) rebouclé [95] ; (b) par anticipation [96].

FR-1.3.3. Techniques électromécaniques semi-passives et semi-actives

Afin de combiner les avantages des systèmes passifs (simplicité et efficacité énergétique) et des systèmes actifs (robustesse et performances) sans souffrir de leurs inconvénients respectifs, l'utilisation de techniques semi-passives et semi-actives a été proposée. On différenciera ces deux dénominations selon qu'aucune énergie extérieure n'est nécessaire dans la partie de puissance (mais possiblement - et très faiblement - dans la partie de commande – techniques semi-passives) ou qu'une petite quantité d'énergie extérieure y soit fournie (techniques semi-actives).

Les techniques semi-passives et semi-actives sont généralement basées sur un élément non-linéaire (typiquement un commutateur), qui change les conditions aux limites électriques de l'insert piézoélectrique (commutation sur des capacités, sur un court-circuit etc…) afin de changer son comportement mécanique équivalent. En particulier, on mentionnera les techniques dites « SSD » (*Synchronized Switch Damping* - Figure FR-1.7) qui consistent à commuter pendant un temps très bref (bien plus court que la période de vibration) l'élément piézoélectrique sur un court-circuit ou une inductance (conduisant à une inversion imparfaite de la tension dans ce dernier cas), conduisant ainsi à une augmentation de l'énergie convertie sous forme électrique (elle-même étant subdivisée en énergie électrostatique disponible sur l'élément piézoélectrique et en énergie dissipée dans l'étage de commutation) créant ainsi un effet mécanique de frottement sec amortissant par là-même les vibrations. Ces techniques peuvent même être auto-alimentées [116-117], c'est-à-dire que l'énergie nécessaire pour la commande du commutateur est directement prélevée sur l'élément piézoélectrique, permettant de disposer d'une technique fermée sur le plan énergétique. Afin d'améliorer les performances, une source de tension extérieures peut être incluse dans la branche de commutation, mais dès lors la technique devient semi-active et ne peut plus être auto-alimentée.

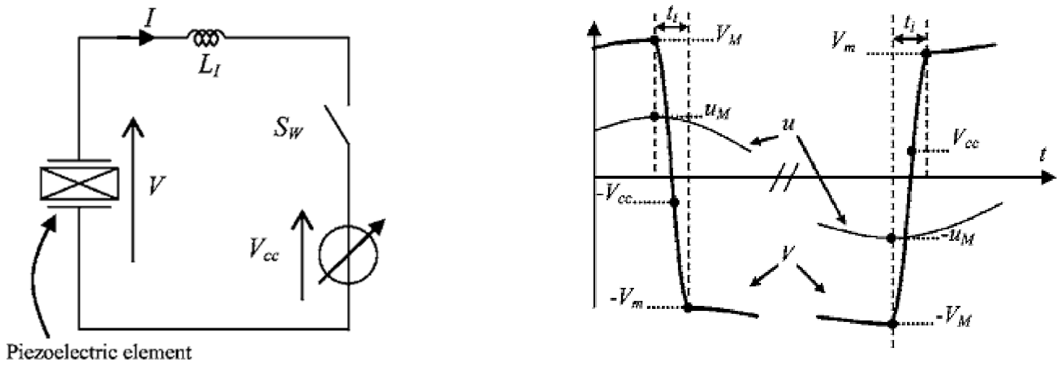

(a) (b)

Figure FR-1.7. Techniques SSD (a) schéma et (b) forme d'ondes typique de déplacement et tension [126]

En sus de la dissipation d'énergie, des techniques semi-passives de contrôle de raideur permettent également d'effectuer le contrôle de vibrations en s'assurant que l'excitation est hors bande passante.

D'un point de vue général, la Figure FR-1.8 présente les différentes méthodes de contrôle passives (appelées ici linéaires) et semi-passives (appelées ici non-linéaires), organisées selon leur nature.

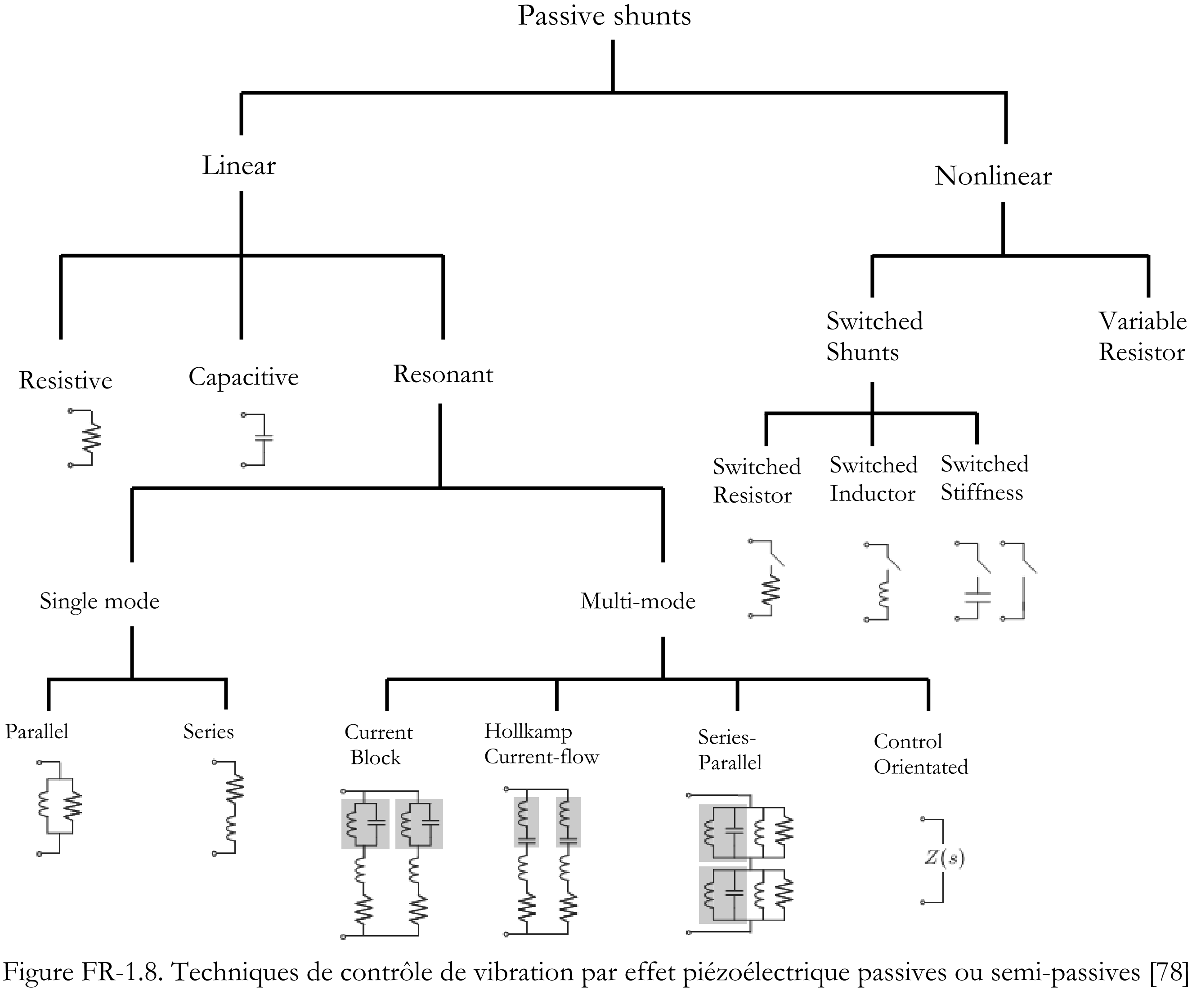

Figure FR-1.8. Techniques de contrôle de vibration par effet piézoélectrique passives ou semi-passives [78].

FR-1.3.4. Techniques électromécaniques hybrides

Enfin, la combinaison de technique semi-actives, réduisant grandement l'énergie nécessaire pour piloter l'actionneur tout en conservant les performances autour des fréquences où l'élément est le mieux couplé, avec des approches actives, permettant de profiter d'un contrôle plus large bande ainsi que de compenser les couplages faibles autour de certains modes, a été proposée, conduisant à un compromis intéressant en termes de performance, d'intégrabilité et de consommation énergétique. Un exemple d'un tel contrôle est présenté en Figure FR-1.9, qui combine la partie de traitement par observateur des techniques actives avec une approche non-linéaire de type SSD.

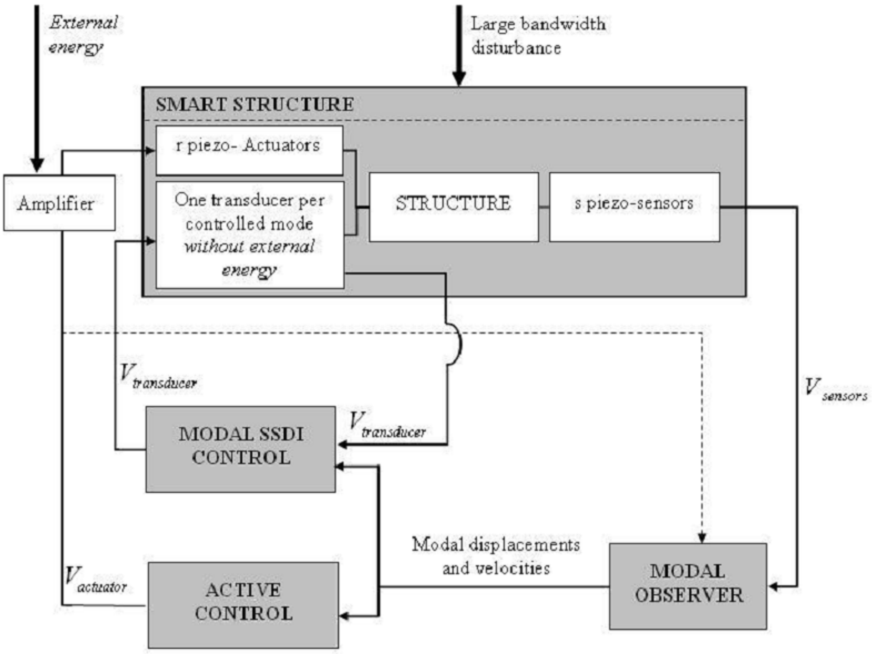

Figure FR-1.9. Stratégie de contrôle hybride [133].

FR-1.4. Conclusion

Ce Chapitre s'est attelé à la description des principaux matériaux et techniques pour le contrôle de vibrations de structures. Il est ainsi apparu qu'en termes de dispositifs intégrés, l'utilisation d'éléments piézoélectriques couplés à des approches semi-passives non-linéaires permet la conception de systèmes de faibles dimensions, tout en étant fiables et performants. Par la suite, il sera présenté de nouvelles techniques utilisant ces méthodes et matériaux et étendant les possibilités du contrôle vibratoire semi-passif exploitant l'effet piézoélectrique.

Chapitre FR-2. Amortissement par commutation synchronisée basé sur un filtrage spatial

FR-2.1 Introduction et principes

Les travaux précédents ont montré que les techniques SSD voient leurs performances dégradées dans le cas d'une excitation large bande ([134]), car elles se concentrent par nature sur la plus haute fréquence détectable. Afin de limiter cette dégradation, il a été proposé de ne commuter que sur des extrema globaux sélectionnés à partir d'un seuil (la commutation n'étant autorisée que si le signal de référence – tension ou déplacement – est supérieur au seuil), ce dernier pouvant être calculé par exemple à partir de considérations probabilistes ou statistiques ([117,134-139]). Néanmoins, quasiment toutes les méthodes de contrôle large bande SSD se basent sur l'historique du signal, via l'utilisation de filtres dans le domaine temporel. Ce Chapitre a pour but d'introduire une nouvelle approche pour un tel contrôle, en se basant non plus sur l'aspect temporel, mais sur un filtrage spatial permettant de sélectionner efficacement les modes d'intérêt.

Le principe de la méthode exposée dans ce Chapitre consiste à effectuer une combinaison linéaire, peu gourmande en calcul, de la tension de sortie d'un réseau d'éléments piézoélectriques pour ensuite interconnecter ceux-ci de manière adaptée afin de contrôler le(s) mode(s) sélectionné(s) (Figure FR-2.1). Afin d'illustrer ce concept, une structure de type poutre encastrée-encastrée et munie de quatre inserts piézoélectriques (à chacun des emplacements proches des encastrements, au-dessus et au-dessous de la poutre) sera utilisée tout au long de ce chapitre. A partir de la Figure FR-2.2, il peut être observé qu'une connexion particulière selon que le mode considéré soit pair ou impair permet de cibler ceux-ci sans influencer les autres. Ainsi, la connexion d'un patch avec un autre situé à l'autre bout et de l'autre coté de la structure permet un échange de charges pour les modes impairs tout en étant transparent pour les modes pairs, alors que la connexion d'un patch avec un autre situé à l'autre bout mais du même coté de la structure permet un échange de charges pour les modes pairs tout en étant transparent pour les modes impairs (Figure FR-2.3). Ainsi la première connexion est active pour les modes impairs et la seconde pour les modes pairs. Dans le cas du SSDI, une analyse similaire est menée pour la connexion des éléments électroactifs. Néanmoins, une différence importante réside dans le choix de l'instant de commutation. En effet, pour le contrôle des modes impairs l'instant de commutation est choisi lorsque la somme des tensions des deux patches situés de part et d'autre de la poutre mais du même côté atteint un extremum, alors que la différence de ces tensions est considérée dans le cas du contrôle des modes pairs (Figure FR-2.4).

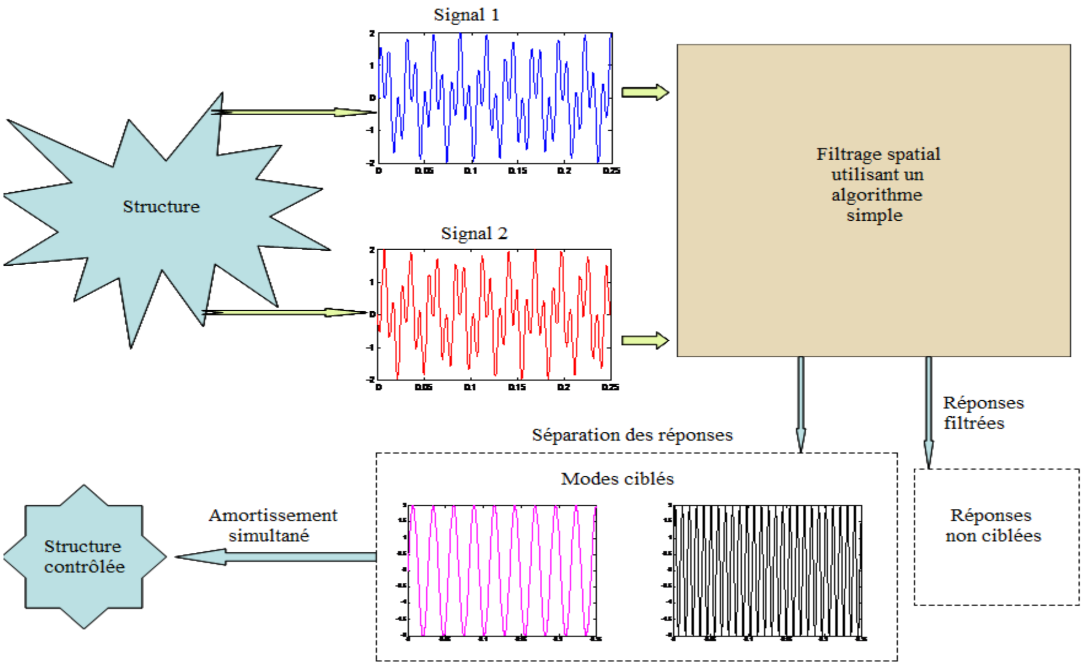

Figure FR-2.1. Concept du SSDI basé sur un filtrage spatial

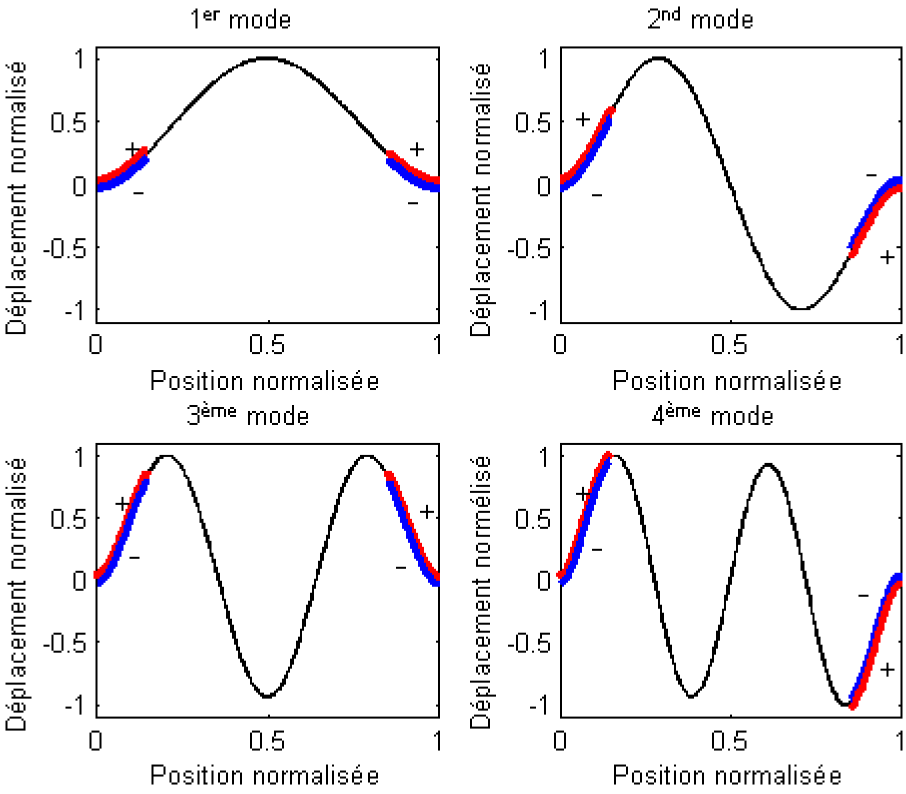

Figure FR-2.2. Quatre premiers modes de vibrations d'une poutre encastrée-encastrée et représentation des éléments piézoélectriques (en trait gras).

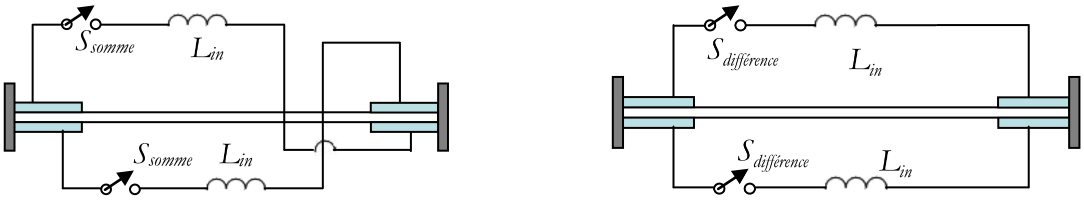

Figure FR-2.3. Connexion pour (a) les modes impairs : (b) les modes pairs.

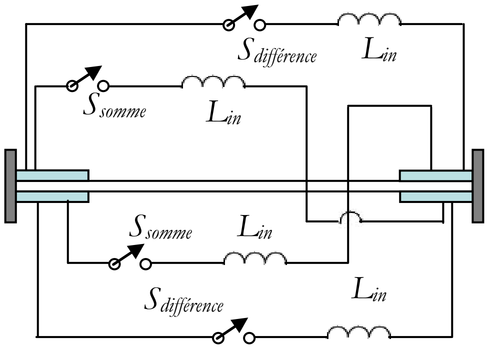

Figure FR-2.4. Application de la technique de filtrage spatial au SSDI.

FR2.2. Modélisation

Ce paragraphe présente la modélisation par éléments finis de la structure utilisée dans ce Chapitre comme exemple d'illustration. En faisant les hypothèses suivantes :

1. La structure mécanique suit les hypothèses d'Euler-Bernoulli
2. La déformation est plane
3. Le champ électrique est constant dans l'élément piézoélectrique
4. L'élément piézoélectrique est isotrope transverse

il est possible d'exprimer la relation entre le vecteur $\{d\}$ de déplacement et pente et celui $\{F\}$ de force et moment selon :

$$\begin{cases} [M]\{\ddot{d}\}+[C]\{\dot{d}\}+[K]\{d\}-[B_1]\{V_p\}=\{F(t)\} \\ \{Q\}=[B_2]\{d\}+[B_3]\{V_p\} \end{cases} \qquad \text{(FR-2. 1)}$$

où les matrices $[M]$, $[C]$, $[K]$ sont les matrices de masse dynamique, coefficient d'amortissement structurel et raideur en court-circuit obtenues à partir de l'assemblage des matrices de chaque élément, ces dernières étant obtenues en considérant comme fonctions de base la famille des splines cubiques d'Hermite. $[B_1]$ et $[B_2]$ sont les matrices assemblées traduisant respectivement les couplages piézoélectriques inverse et direct et $[B_3]$ est la matrice traduisant l'effet diélectrique au sein du matériau, obtenue de manière similaire aux précédentes.

Lorsque l'élément piézoélectrique est en circuit ouvert, la tension V_{pi} aux bornes de l'élément piézoélectrique i s'exprime en fonction de la pente de la déflection θ par :

$$\dot{V}_{pi} = -\frac{t_p^{\,2}\left(\sigma d_{31}\right)_i}{L_{pi}\left[\varepsilon_{33}^T\left(s_{11}^E+s_{12}^E\right)-2d_{31}^{\,2}\right]}\dot{\theta}\Big|_{x_{i0}}^{x_{i0}+L_{pi}} \qquad \text{(FR-2. 2)}$$

avec t_p, L_{pi} et x_{i0} l'épaisseur, la longueur et la position de l'insert, s^E le tenseur des compliances à champ électrique constant, ε^T le tenseur des permittivités à contrainte constante, d le tenseur traduisant l'effet piézoélectrique et σ le sens de la polarisation du matériau ($\sigma=\pm 1$).

Dans le cas où l'élément est connecté à une inductance L_{in} présentant des pertes modélisées par une résistance R (SSDI classique), l'expression de la tension est donnée par :

$$\ddot{V}_{pi} = \frac{1}{L_{in}C_{oi}}V_{pi} - \frac{R}{L_{in}}\dot{V}_{pi} \text{ avec } C_{0i} = \frac{wL_{pi}\left[\varepsilon_{33}^T\left(s_{11}^E+s_{12}^E\right)-2d_{31}^{\,2}\right]}{t_p\left(s_{11}^E+s_{12}^E\right)} \qquad \text{(FR-2. 3)}$$

De la même manière, pour la technique basée sur le filtrage spatial, cette expression devient :

$$\begin{Bmatrix}\ddot{V}_{pi}\\ \ddot{V}_{pj}\end{Bmatrix} = \frac{1}{L_{in}C_0}\begin{bmatrix}-1 & -1\\ -1 & -1\end{bmatrix}\begin{Bmatrix}V_{pi}\\ V_{pj}\end{Bmatrix} - \frac{R}{L_{in}}\begin{Bmatrix}\dot{V}_{pi}\\ \dot{V}_{pj}\end{Bmatrix} \qquad \text{(FR-2. 4)}$$

pour la connexion se focalisant sur les modes impairs et

$$\begin{Bmatrix}\ddot{V}_{pi}\\ \ddot{V}_{pj}\end{Bmatrix} = \frac{1}{L_{in}C_0}\begin{bmatrix}-1 & 1\\ 1 & -1\end{bmatrix}\begin{Bmatrix}V_{pi}\\ V_{pj}\end{Bmatrix} - \frac{R}{L_{in}}\begin{Bmatrix}\dot{V}_{pi}\\ \dot{V}_{pj}\end{Bmatrix} \qquad \text{(FR-2. 5)}$$

pour la connexion se focalisant sur les modes pairs. On pourra noter que le coefficient d'inversion de la technique de filtrage spatial est légèrement supérieur que dans le cas du SSDI pur, du fait de la connexion de deux patches entre eux.

FR2.3. Résultats de simulation et expérimentaux

Cette partie propose de valider le concept de filtrage spatial pour le contrôle SSDI large bande ainsi que la modélisation par éléments finis présentée dans le paragraphe précédent par des mesures expérimentales se focalisant sur les deux premiers modes de la structure. Dans le cas de la modélisation par éléments finis, un script Matlab a été spécialement développé. Concernant l'expérimentation, un système dSpace a été utilisé pour effectuer la somme/différence des tensions et contrôler les commutateurs, selon l'algorithme présenté en Figure FR-2.5.

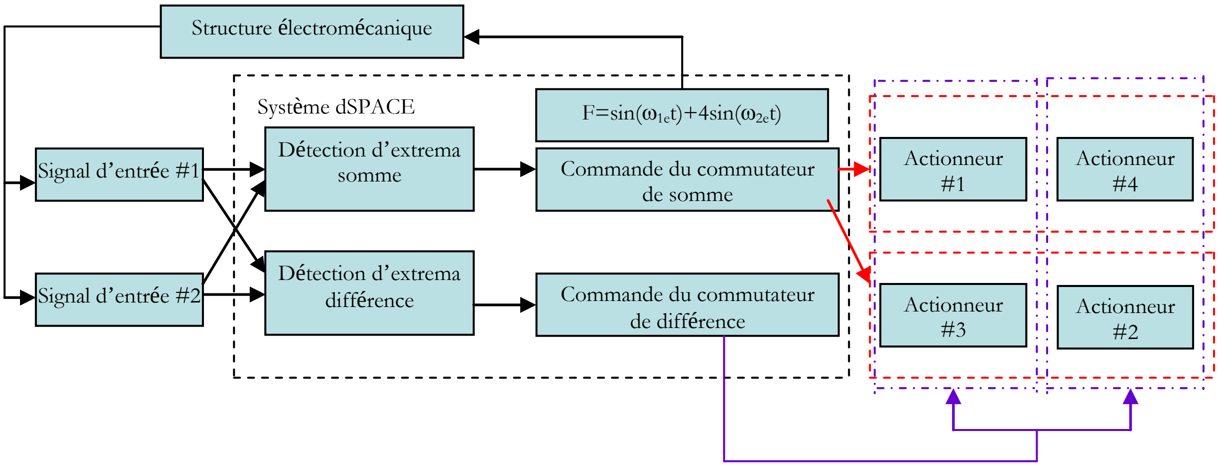

Figure FR-2.5. Implémentation expérimentale de la technique de filtrage spatial.

Le Tableau FR-2.1 résume les différentes atténuations obtenues avec la simulation ou constatées expérimentalement dans le cas d'excitations monochromatiques à la première et seconde résonance, ainsi que les résultats dans un cas bimodal (où la valeur efficace du déplacement est utilisée pour calculer l'atténuation). Le déplacement est pris à environ un tiers de la poutre à partir de l'encastrement.

Les résultats obtenus en simulation et durant l'expérience montrent une très bonne concordance, validant la modélisation. Il peut être remarqué que, du fait de la connexion particulière des patches dans le cas de la technique utilisant le filtrage spatial, une légère amélioration de l'amortissement est constatée dans les cas monochromatiques. Néanmoins, le point le plus important de ces résultats réside dans l'excitation bimodale, qui montre un effondrement des performances de la technique SSDI classique, qui se concentre sur la plus haute fréquence détectable (le second mode dans ce cas), qui est en général moins bien couplé. Grâce au concept de filtrage spatial, les performances de l'approche proposée dans ce chapitre demeurent quasiment inchangées, car les modes peuvent être efficacement séparés pour être traités simultanément.

Tableau FR-2.1. Atténuations simulées et expérimentales pour différentes excitations

		$F=\sin\left(\omega_{1s}t\right)$	$F=\sin\left(\omega_{2s}t\right)$	$F=\sin\left(\omega_{1s}t\right)+4\sin\left(\omega_{2s}t\right)$
SSDI classique	Simu	-19.91 *dB*	-19.36 *dB*	-12.6 *dB*
	Exp	-17.19 *dB*	-15.89 *dB*	-10.28 *dB*
SSDI avec filtrage spatial	Simu	-21.13 *dB*	-19.81 *dB*	-20.43 *dB*
	Exp	-18.24 *dB*	-18.65 *dB*	-17.63 *dB)*

Ces résultats sont encore plus probants dans le cas d'une excitation large bande par un bruit blanc filtré (Figure FR-2.6), où la technique SSDI conduit à un amortissement très limité, surtout pour le premier mode alors que l'approche par filtrage spatial conserve un pouvoir d'amortissement élevé. On pourra même noter une atténuation du troisième mode qui n'apparaît pas dans le cas du SSDI ; ce mode étant hors de la plage d'excitation du bruit blanc pouvant apparaître du fait de non-linéarités de l'excitation via un électro-aimant. Bien que ce dernier point semble surprenant (le filtrage spatial étant ici concentré sur une séparation des modes pairs et impairs, le mode 3 devrait limiter les capacités d'atténuation autour de la première résonance), ceci peut être attribué au fait que, la technique de filtrage spatial permettant une meilleure décomposition des modes, le mode 3 peut être efficacement atténué de telle manière qu'il ne soit plus aisément détectable, ce qui permet de se concentrer sur le premier mode.

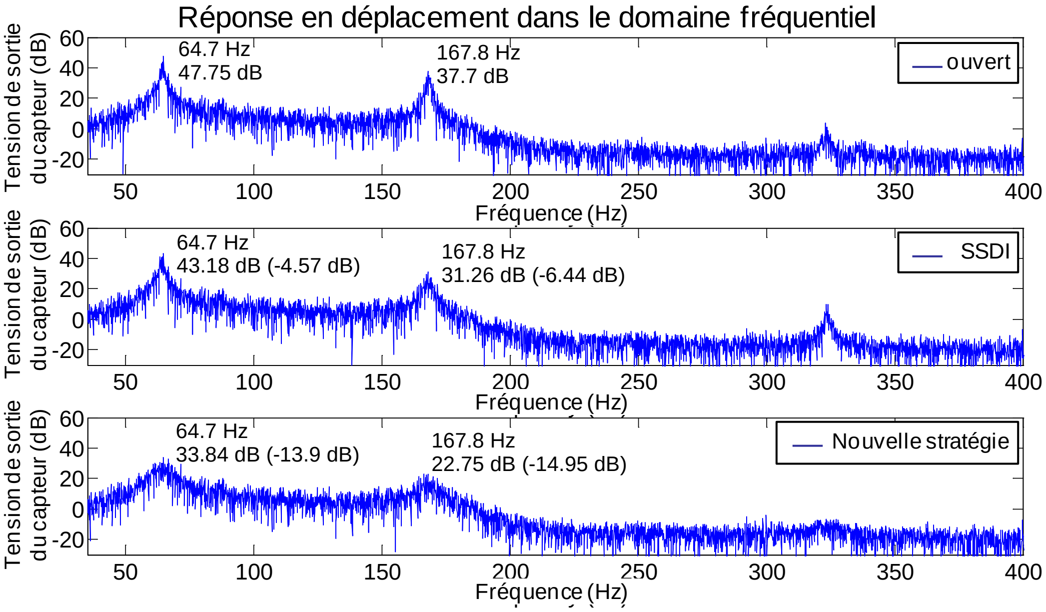

Figure FR-2.6. Résultats expérimentaux dans le cas d'une excitation en bruit blanc filtré (10-210 Hz).

FR2.4. Combinaison avec les techniques de filtrage temporel

Il a été démontré que la technique de filtrage spatial s'avère particulièrement efficace pour le contrôle semi-passif basé sur la technique non-linéaire SSDI dans le cas large bande, du fait de sa capacité à séparer les modes pour un meilleur contrôle. Ce paragraphe propose de plus amples discussions sur les possibilités de combinaison avec l'approche par filtrage temporel afin de profiter d'un système compact, robuste et efficace pour le contrôle multimodal.

L'approche de filtrage temporel combinée avec le principe de filtrage spatial retenue ici se base pour la définition du seuil sur la moyenne de N amplitudes de déplacement (en valeur absolue) observée sur une fenêtre de temps définie, et pondéré par un coefficient fixé par l'utilisateur. Afin de prendre en compte les spécificités de la technique de filtrage spatial, un seuil est défini pour chaque combinaison linéaire (dans notre cas, somme et différence) des tensions de sortie de capteurs piézoélectriques donnant les déplacements à chaque extrémité de la poutre. De même, il est possible de fixer un coefficient utilisateur différent pour la somme et la différence, mais les résultats présentés ici n'étant qu'exploratoire, ces deux coefficients (nommés β_{somme} et $\beta_{différence}$) sont choisis égaux.

Les résultats de simulation obtenus dans le cas d'une excitation en bruit blanc filtré couvrant les quatre premiers modes de flexion ainsi qu'une excitation impulsionnelle sont résumés dans le Tableau FR-2.2, où l'atténuation a été calculée à partir de la valeur efficace du déplacement en un point donné (environ le tiers de la poutre à partir de l'encastrement) sur la fenêtre de temps considérée, et illustrés par la Figure FR-2.7 dans le cas impulsionnel. Outre le fait que l'approche par filtrage spatial permet un meilleur amortissement que dans le cas SSDI standard, ces résultats démontrent l'avantage de combiner l'approche par filtrage spatial avec le principe de filtrage temporel, permettant d'étendre les capacités offertes par le découplage de mode du filtrage spatial. Ceci est encore plus remarquable lorsque l'on décompose les atténuations obtenues pour chacun des trois premiers modes (Tableau FR-2.3), qui montre une excellente adaptabilité de l'approche combinée pour le contrôle multimodal, la technique de filtrage spatial palliant partiellement la limite de contrôlabilité de l'approche par filtrage spatial. On pourra néanmoins noter une dépendance au coefficient du seuil (Figure FR-2.8), mais les performances restent cependant toujours supérieures aux deux autres techniques envisagées.

Tableau FR-2.2. Atténuations obtenues à partir de la valeur efficace du déplacement au point considéré en considérant un bruit blanc filtré ou une impulsion.

	SSDI classique	SSDI avec filtrage spatial	SSDI avec filtrage spatial et temporel
Bruit blanc filtré (10 -610 Hz)	-3.15 dB	-4.16 dB	-7.31 dB
Impulsion	-2.02 dB	-2.94 dB	-5.99 dB

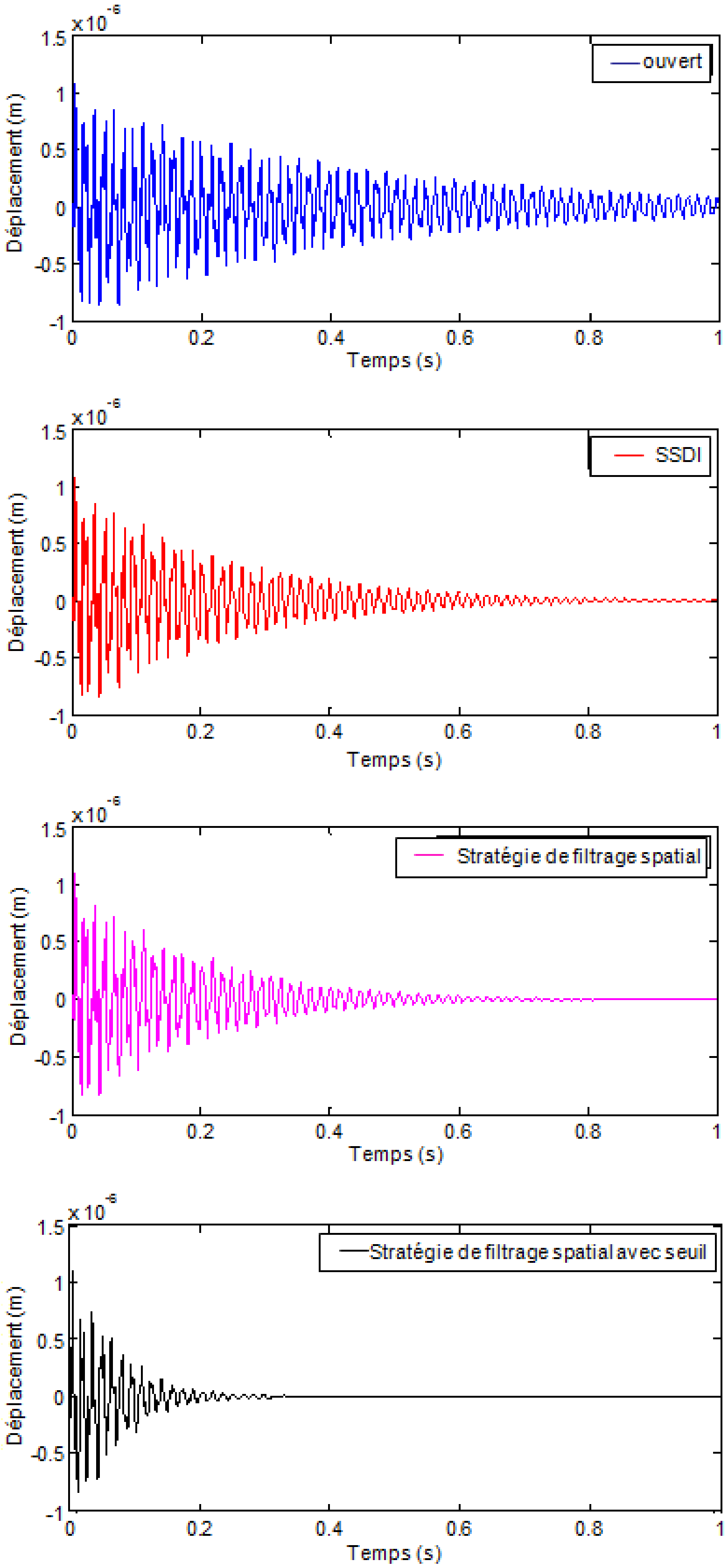

Figure FR-2.7. Résultats temporels de simulation dans le cas du système sans contrôle, du SSDI classique, de l'approche par filtrage spatial et de la combinaison du filtrage spatial avec le filtrage temporel dans le cas d'une excitation impulsionnelle.

Tableau FR-2.3. Atténuations obtenues pour chaque mode pour une excitation impulsionnelle.

	Premier mode	Second mode	Troisième mode
SSDI classique	-4.3 *dB*	-8.90 *dB*	-7.6 *dB*
SSDI avec filtrage spatial	-8.28 *dB*	-12.34 *dB*	-4.28 *dB*
SSDI avec filtrage spatial et temporel	-24.50 *dB*	-28.55 *dB*	-9.87 *dB*

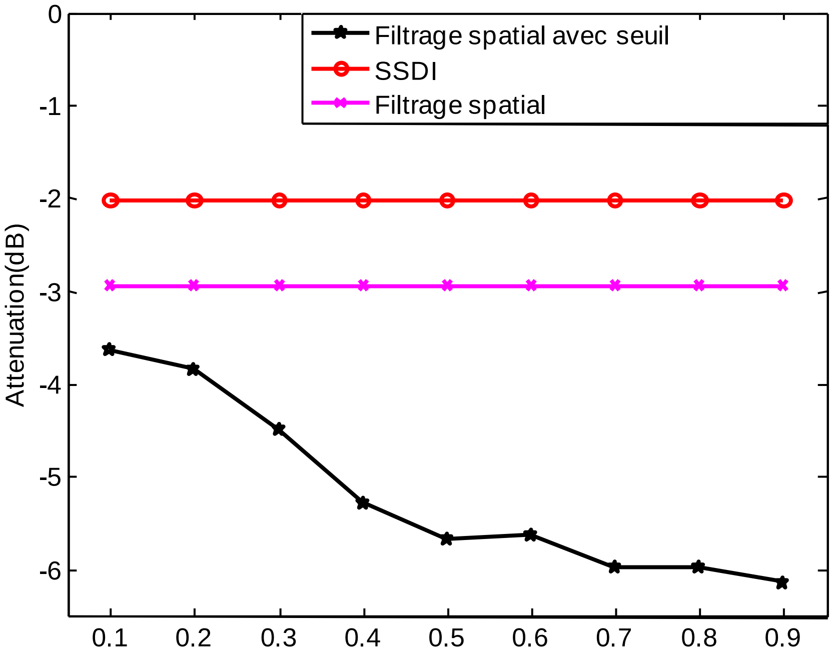

Figure FR-2.8. Résultats de simulation de l'atténuation en fonction du coefficient de seuil dans le cas d'une excitation impulsionnelle.

FR2.5. Conclusion

Ce chapitre a exposé le principe d'une technique de contrôle utilisant un réseau d'actionneur et la combinaison linéaire de leurs tensions de sortie afin de déterminer les instants optimaux de commutation (les connexions étant différentes selon la combinaison linéaire qui présente un extremum), conduisant ainsi au concept de filtrage spatial. Grâce à cette approche, il est possible de décomposer efficacement les modes de vibration qui peuvent dès lors être contrôlés séparément mais simultanément (contrairement à l'approche temporelle qui prend en compte tous les modes). Une modélisation par éléments finis ainsi que des mesures expérimentales ont confirmé l'excellente capacité de cette approche à effectuer un contrôle multimodal efficace tout en étant relativement simple et peu consommatrice d'énergie (aucune énergie extérieure n'étant nécessaire dans la branche de puissance). Bien que ce Chapitre se soit basé sur l'exemple d'une poutre encastrée-encastrée et se soit focalisé sur le contrôle des deux premiers modes de vibrations, les principes de la techniques de filtrage spatial font qu'elle peut être appliquée à tout type de structure et un nombre plus important de modes. Par ailleurs, dans ce dernier cas, il a été démontré que la combinaison de l'approche par filtrage spatial et des techniques de filtrage temporel basées sur un seuil de non-commutation permet d'augmenter artificiellement la contrôlabilité du système, permettant d'avoir à disposition un système de contrôle de vibration large bande efficace, compact et très peu consommateur d'énergie.

Chapitre FR-3. Amortisseurs à Masse Accordée avec interface non-linéaire de commutation

FR-3.1 Introduction

Ce Chapitre expose la combinaison d'un amortisseur à masse accordée (TMD : *Tuned Mass Damper*) avec la technique non-linéaire de commutation synchronisée sur inductance SSDI (*Synchronized Switch Damping on Inductor*), cette dernière ayant jusqu'alors été employée uniquement dans le cas d'éléments piézoélectriques directement collés sur une structure hôte. Une telle technique permet ainsi de combiner les avantages des dispositifs à masse accordée, en termes de performances et de facilité d'implémentation avec ceux du SSDI (efficacité et simplicité). Il sera ainsi mis en avant et discuté théoriquement (par un modèle à constantes localisées ainsi qu'un modèle à éléments finis) et expérimentalement les performances de cette combinaison par rapport aux TMDs classiques, ainsi que par rapport à la technique SSDI classique (c'est-à-dire par couplage direct avec la structure hôte).

FR-3.2 Modèle à constantes localisées à deux degrés de liberté

Cette partie propose dans un premier temps une analyse simple basée sur un système à deux degrés de liberté formé de deux systèmes masse-ressort-amortisseur dont l'un inclut possiblement un couplage électromécanique par effet piézoélectrique. On distinguera les cas d'un TMD purement mécanique, où aucune conversion d'énergie n'est présente au niveau de l'amortisseur, des cas électromécaniques où le TMD inclut un élément piézoélectrique, et dans ce dernier cas on fera la différence entre le système passif (où l'élément actif est simplement connecté à une charge résistive – une charge inductive étant difficilement réalisable d'un point de vue pratique) et le système non-linéaire semi-passif incluant l'étage de commutation SSDI (Figure FR-3.1). u et F sont le déplacement et la force appliquée à la structure hôte. Les paramètres m, c, k, α et C_0 représentent la masse dynamique, le coefficient d'amortissement structurel, la raideur (en court-circuit dans le cas d'un système électromécanique), le facteur de force et la capacité bloquée du système. Les indices *1* et *2* réfèrent respectivement à la structure hôte et au TMD.

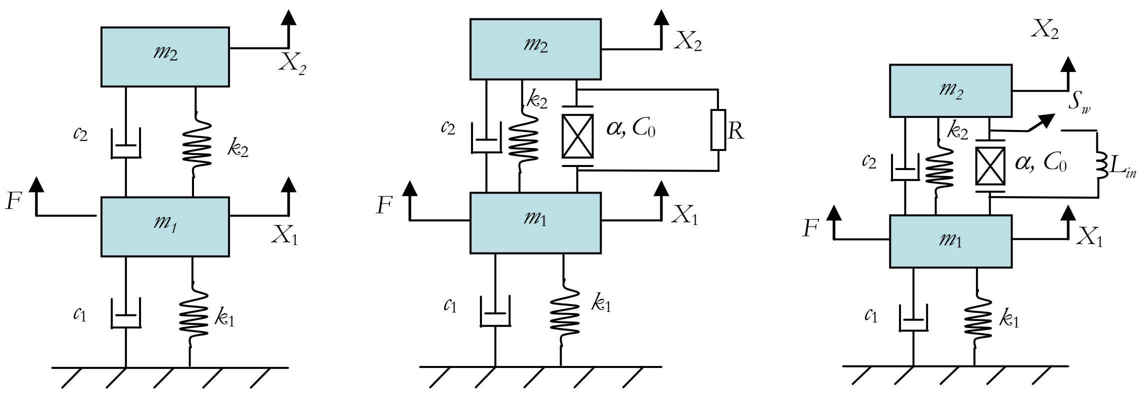

(a) (b) (c)

Figure FR-3.1. Amortisseurs à masse accordée étudiés : (a) purement mécanique ; (b) électromécanique passif ; (c) électromécanique semi-passif.

FR-3.2.1 Analyse théorique

A partir du bilan des forces s'exerçant sur chacun des sous-systèmes et en appliquant le principe fondamental de la dynamique, il est possible d'exprimer les relations mécaniques régissant les structures dans le domaine fréquentiel selon :

$$\left(-\omega^2 m_1 + j\omega c_1 + k_1\right)\tilde{X}_1 = \tilde{F}_1 \tag{FR-3.1}$$

dans le cas de la structure hôte seule (c'est-à-dire sans TMD),

$$\left\{-\omega^2\begin{bmatrix} m_1 & 0 \\ 0 & m_2 \end{bmatrix} + j\omega\begin{bmatrix} c_1+c_2 & -c_2 \\ -c_2 & c_2 \end{bmatrix} + \begin{bmatrix} k_1+k_2 & -k_2 \\ -k_2 & k_2 \end{bmatrix}\right\}\begin{Bmatrix} \tilde{X}_1 \\ \tilde{X}_2 \end{Bmatrix} = \begin{Bmatrix} \tilde{F}_1 \\ 0 \end{Bmatrix} \tag{FR-3.2}$$

pour le système incluant un TMD purement mécanique

$$\begin{bmatrix} m_1 & 0 \\ 0 & m_2 \end{bmatrix}\begin{Bmatrix} \ddot{X}_1 \\ \ddot{X}_2 \end{Bmatrix} + \begin{bmatrix} c_1+c_2 & -c_2 \\ -c_2 & c_2 \end{bmatrix}\begin{Bmatrix} \dot{X}_1 \\ \dot{X}_2 \end{Bmatrix} + \begin{bmatrix} k_1+k_2 & -k_2 \\ -k_2 & k_2 \end{bmatrix}\begin{Bmatrix} X_1 \\ X_2 \end{Bmatrix} + \begin{bmatrix} -\alpha \\ \alpha \end{bmatrix} V = \begin{Bmatrix} F_1 \\ 0 \end{Bmatrix} \tag{FR-3.3}$$

dans le cas d'un TMD électromécanique, avec V la tension aux bornes de l'élément piézoélectrique et ω la pulsation. Dans ce dernier cas, le courant délivré par l'élément piézoélectrique s'exprime également par :

$$I = \alpha\left(\dot{X}_2 - \dot{X}_1\right) - C_0\dot{V} \tag{FR-3.4}$$

Dans le cas d'une charge purement résistive et adaptée en fonction de la fréquence pour le TMD électromécanique passif, la relation tension-courant obtenue conduit à l'expression de l'équation mécanique suivante :

$$\left\{-\omega^2\begin{bmatrix} m_1 & 0 \\ 0 & m_2 \end{bmatrix} + j\omega\begin{bmatrix} c_1+c_2 & -c_2 \\ -c_2 & c_2 \end{bmatrix} + \begin{bmatrix} k_1+k_2 & -k_2 \\ -k_2 & k_2 \end{bmatrix} + \frac{(1+j)\alpha^2}{2C_0}\begin{bmatrix} 1 & -1 \\ -1 & 1 \end{bmatrix}\right\}\begin{Bmatrix} \tilde{X}_1 \\ \tilde{X}_2 \end{Bmatrix} = \begin{Bmatrix} \tilde{F}_1 \\ 0 \end{Bmatrix} \tag{FR-3.5}$$

Pour le système de commutation non-linéaire de type SSDI, il peut être montré que ce traitement induit une composante constante par morceau en phase avec la vitesse, dont l'expression fréquentielle en faisant l'approximation du premier harmonique conduit à l'expression de la tension :

$$\tilde{V} \approx \left(\frac{\alpha}{C_0} + j\frac{4}{\pi}\frac{1+\gamma}{1-\gamma}\frac{\alpha}{C_0} \right) \begin{bmatrix} -1 & 1 \end{bmatrix} \begin{bmatrix} \tilde{X}_1 \\ \tilde{X}_2 \end{bmatrix} \qquad \text{(FR-3.6)}$$

avec γ le coefficient d'inversion compris entre *0* et *1*. L'équation du mouvement devient ainsi dans ce cas :

$$\left\{ -\omega^2 \begin{bmatrix} m_1 & 0 \\ 0 & m_2 \end{bmatrix} + j\omega \begin{bmatrix} c_1 + c_2 + \frac{4}{\pi}\frac{1+\gamma}{1-\gamma}\frac{\alpha^2}{C_0\omega} & -c_2 - \frac{4}{\pi}\frac{1+\gamma}{1-\gamma}\frac{\alpha^2}{C_0\omega} \\ -c_2 - \frac{4}{\pi}\frac{1+\gamma}{1-\gamma}\frac{\alpha^2}{C_0\omega} & c_2 + \frac{4}{\pi}\frac{1+\gamma}{1-\gamma}\frac{\alpha^2}{C_0\omega} \end{bmatrix} + \begin{bmatrix} k_1 + k_2 + \frac{\alpha^2}{C_0} & -k_2 - \frac{\alpha^2}{C_0} \\ -k_2 - \frac{\alpha^2}{C_0} & k_2 + \frac{\alpha^2}{C_0} \end{bmatrix} \right\} \begin{Bmatrix} \tilde{X}_1 \\ \tilde{X}_2 \end{Bmatrix} = \begin{Bmatrix} \tilde{F}_1 \\ 0 \end{Bmatrix} \qquad \text{(FR-3.7)}$$

A partir des équations dynamiques, il peut ainsi être possible d'exprimer le déplacement normalisé de la structure hôte utilisant les paramètres adimensionnels de fréquence normalisée Ω, rapport de fréquence de résonance r_Ω, rapport de masse r_m, rapport de coefficient d'amortissement r_ζ et coefficient de couplage électromécanique global κ :

$$\left(\frac{k_1 \tilde{X}_1}{\tilde{F}_1} \right) = \frac{1}{\left(-\Omega^2 + j\Omega 2\zeta_1 + 1 \right)} \qquad \text{(FR-3.8)}$$

$$\left(\frac{\tilde{X}_1}{F_1} \right)_{pur} = \frac{1}{k_1 \left[\left(-\Omega^2 + j\Omega 2\zeta_1 + 1 \right) + \frac{-\Omega^2 r_m r_\omega \left(j\Omega 2 r_\zeta \zeta_1 + r_\omega \right)}{\left(-\Omega^2 + j\Omega 2 r_\zeta \zeta_1 r_\omega + r_\omega{}^2 \right)} \right]} \qquad \text{(FR-3.9)}$$

$$\left(\frac{\tilde{X}_1}{\tilde{F}_1} \right)_{res\_optimal} = \frac{1}{k_1 \left[-\Omega^2 + j\Omega 2\zeta_1 + 1 + \frac{-\Omega^2 r_m r_\omega \left(j\Omega 2 r_\zeta \zeta_1 + r_\omega + \frac{(1+j)}{2}\frac{\kappa^2}{\left(1-\kappa^2\right)} r_\omega \right)}{\left[-\Omega^2 + j\Omega 2 r_\zeta \zeta_1 r_\omega + r_\omega{}^2 + \frac{(1+j)}{2}\frac{\kappa^2}{\left(1-\kappa^2\right)} r_\omega{}^2 \right]} \right]} \qquad \text{(FR-3.10)}$$

$$\left(\frac{\tilde{X}_1}{\tilde{F}_1} \right)_{semi-passif} = \frac{1}{k_1 \left[\left(-\Omega^2 + j\Omega 2\zeta_1 + 1 \right) + \frac{-\Omega^2 r_m r_\omega \left[j\Omega 2 r_\zeta \zeta_1 + r_\omega + \frac{\kappa^2}{\left(1-\kappa^2\right)} r_\omega \left(1 + j\frac{4}{\pi}\frac{1+\gamma}{1-\gamma} \right) \right]}{\left[-\Omega^2 + j\Omega 2 r_\zeta \zeta_1 r_\omega + r_\omega{}^2 + \frac{\kappa^2 r_\omega{}^2}{\left(1-\kappa^2\right)} \left(1 + j\frac{4}{\pi}\frac{1+\gamma}{1-\gamma} \right) \right]} \right]} \qquad \text{(FR-3.11)}$$

respectivement pour la structure hôte seule, le TMD purement mécanique, le TMD électromécanique passif et TMD électromécanique semi-actif.

FR-3.2.2 Discussion

A partir des expressions adimensionnelles du déplacement de la structure hôte dans chacun des cas considérés, cette partie propose de comparer théoriquement les performances obtenues pour les systèmes envisagés dans ce Chapitre.

a) Cas accordé

On se propose ici d'évaluer les performances des différentes configurations dans le cas où le TMD est bien accordé à la structure hôte (rapport de fréquence r_Ω unitaire). Deux valeurs de coefficient d'amortissement, respectivement 0,002 et 0,02, seront considérées pour la structure hôte. Les Figure FR-3.2, Figure FR-3.3 et Figure FR-3.4 présentent les différentes atténuations obtenues (définies comme le rapport entre le déplacement avec contrôle sur celui sans contrôle – une valeur négative relatant donc un amortissement et une valeur positive une amplification) dans les cas respectifs de TMDs purement mécanique, électromécanique passif et électromécanique semi-passif.

On remarque, dans tous les cas, qu'au-delà d'un certain rapport de masse moins dépendant du facteur d'amortissement de la structure hôte que du rapport d'amortissement, les performances se retrouvent dégradées, le système pouvant même passer d'un comportement amortisseur à un comportement amplificateur. Ce comportement dépend également du couplage dans le cas électromécanique ainsi que du coefficient d'inversion (ce dernier étant lié à l'augmentation artificielle du couplage dans le cas de la technique SSDI) pour le système semi-passif. Ce dernier point est un résultat des plus intéressants, car il met en avant une différence fondamentale entre l'approche SSDI par couplage direct et par utilisation de TMD ; l'atténuation dans le premier cas étant une fonction monotone du coefficient d'inversion (plus ce dernier est grand, plus l'amortissement est important), alors que dans le cas du TMD un facteur d'inversion optimal apparaît au-delà duquel les performances diminuent.

En termes de performances, on remarque que, grâce au degré de liberté supplémentaire offert par la conversion électromécanique (en plus de la conversion mécano-mécanique de base), les capacités d'amortissement des TMDs électroactifs sont augmentées. La technique de commutation SSDI permettant de plus une augmentation artificielle du couplage, ses performances dépassent largement les autres structures envisagées, surtout pour des coefficients de couplages modestes. On notera également, que du fait du processus de conversion d'énergie supplémentaire, la dépendance de la masse optimale avec le rapport d'amortissement est fortement réduite, facilitant ainsi la conception de ces systèmes, notamment lors de dérives du facteur de qualité mécanique.

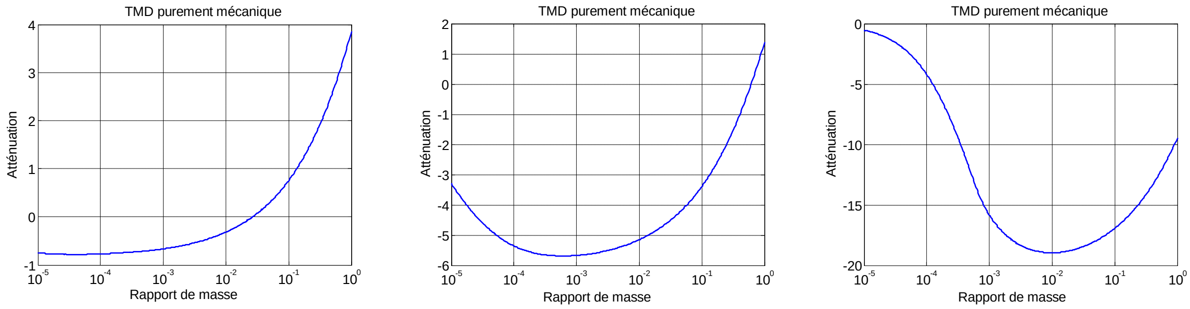

(a) $r_\zeta = 0.1$ (b) $r_\zeta = 1$ (c) $r_\zeta = 10$

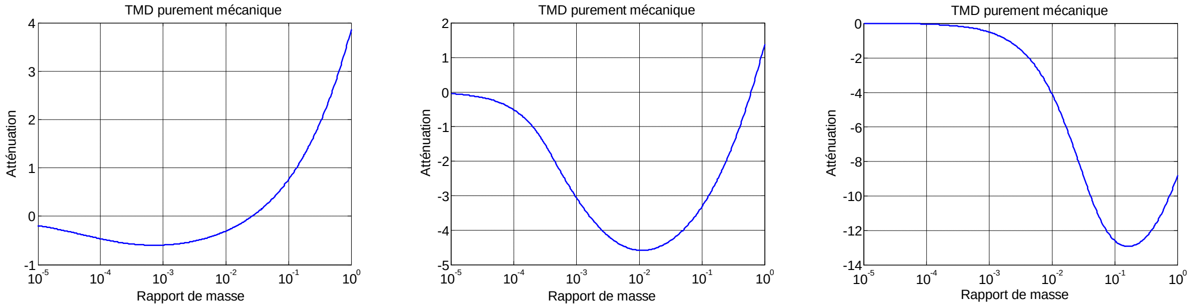

(a) $r_\zeta = 0.1$ (b) $r_\zeta = 1$ (c) $r_\zeta = 10$

Figure FR-3.2. Atténuations obtenues pour le TMD purement mécanique pour (a-c) ζ_l=0,002 ; (d-f) ζ_l=0,02 et plusieurs valeurs de rapports d'amortissement.

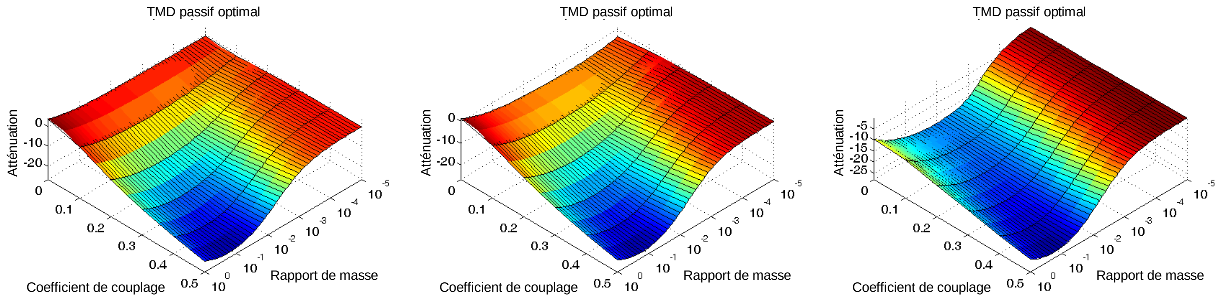

(a) $r_\zeta = 0,1$ (b) $r_\zeta = 1$ (c) $r_\zeta = 10$

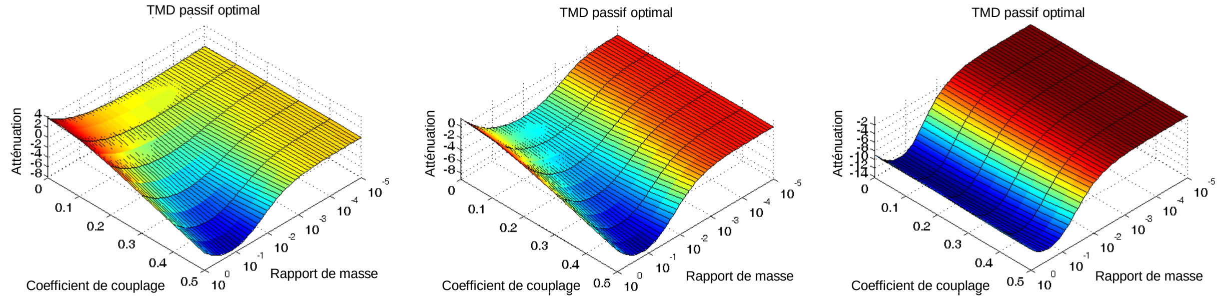

(a) $r_\zeta = 0,1$ (b) $r_\zeta = 1$ (c) $r_\zeta = 10$

Figure FR-3.3. Atténuations obtenues pour le TMD électromécanique passif pour (a-c) ζ_l=0,002 ; (d-f) ζ_l=0,02, et plusieurs valeurs de rapports d'amortissement.

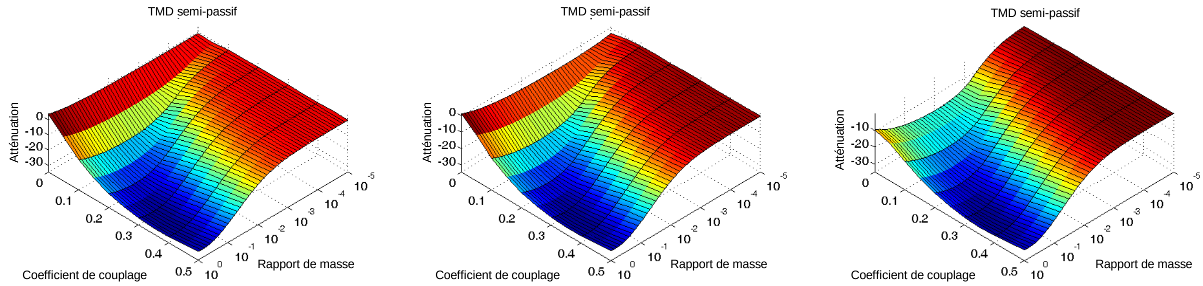

(a) r_ζ=0,1 et γ=0,6 (b) r_ζ=1 et γ=0.6 (c) r_ζ=10 et γ=0.6

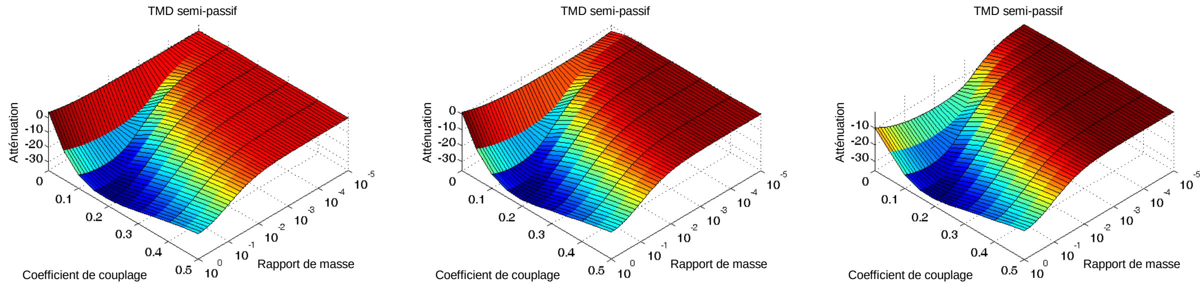

(d) r_ζ=0,1 et γ=0,9 (e) r_ζ=1 et γ=0,9 (f) r_ζ=10 et γ=0,9

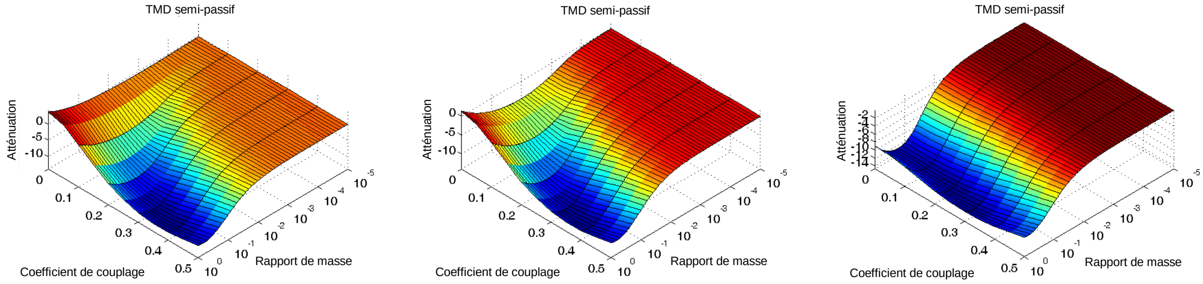

(g) r_ζ=0,1 et γ=0,6 (h) r_ζ=1 et γ=0,6 (i) r_ζ=10 et γ=0,6

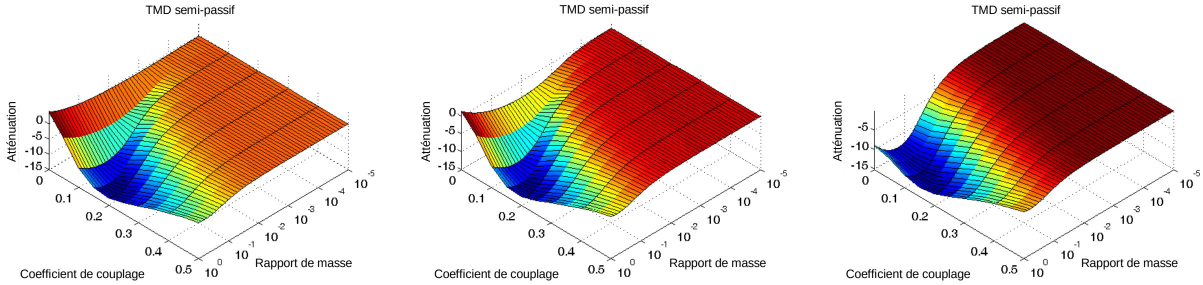

(j) r_ζ=0,1 et γ=0,9 (k) r_ζ=1 et γ=0,9 (l) r_ζ=10 et γ=0,9

Figure FR-3.4. Atténuations obtenues pour le TMD électromécanique semi-passif pour (a-f) ζ_1=0,002 ; (g-l) ζ_1=0,02, et plusieurs valeurs de rapports d'amortissement et de coefficients d'inversion.

b) Cas désaccordé

D'un point de vue des systèmes implémentés dans un environnement réaliste, assurer l'exact accord de fréquence de résonance peut s'avérer très délicat dans la conception du système, voire impossible lorsque l'on considère les possibles dérives dues au vieillissement ou au changement des conditions environnementales. L'étude d'un désaccordage des fréquences de résonance de +/- 20% montre que les performances d'amortissement sont significativement réduites pour un TMD ayant une fréquence de résonnance plus élevée que la structure hôte mais quasiment inchangées (voire légèrement meilleures) pour un rapport de *0,8*. Cependant, dans ce cas, la masse optimale correspondant à l'amortissement maximal est significativement impactée, changeant de manière inverse au désaccordage. Il apparaît de plus que la dégradation des performances dans le cas désaccordé est plus sensible à un rapport de masse plus élevé que le rapport optimal. Ainsi, il est possible d'en conclure qu'il vaut mieux légèrement sous-dimensionner le système afin de se prémunir d'une chute trop importante des capacités d'amortissement. De plus, dans le cas électromécanique et notamment le cas SSDI, la conversion d'énergie supplémentaire ainsi que le contrôle de l'amélioration de la conversion (via les coefficients de couplage et d'inversion) offrent des degrés de liberté supplémentaires permettant de compenser l'effet d'un désaccordage.

FR-3.3 Validation expérimentale et comparaison avec la théorie

Cette partie propose de valider le concept de TMD électromécanique semi-passif non-linéaire ainsi que de discuter de ses performances et de les comparer aux analyses théoriques (modèle à deux degrés de liberté) et de simulation (méthode par éléments finis, mené de manière similaire au Chapitre précédent).

La structure envisagée est présentée en Figure FR-3.5, et consiste en une structure hôte de type poutre encastrée-libre (bien que tout autre structure puisse être envisagée dans la réalité) à laquelle une poutre de même type mais de dimensions plus faibles est attachée à l'extrémité libre et agit comme TMD.

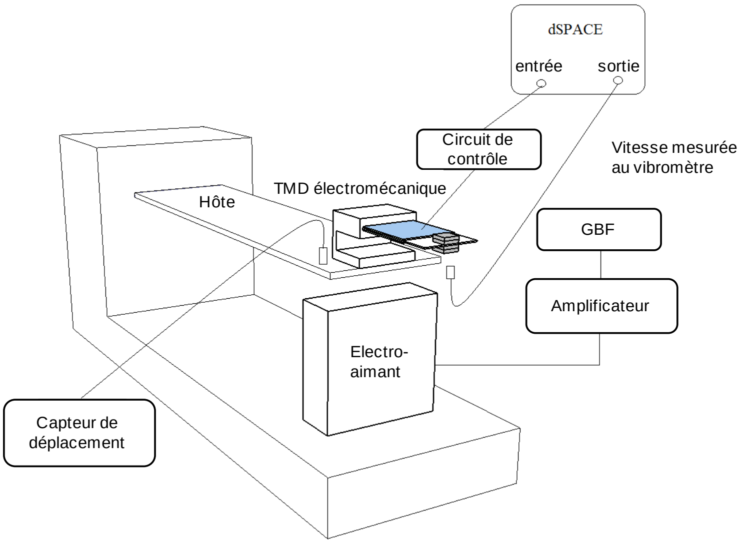

Figure FR-3.5. Schéma du dispositif expérimental.

Les résultats expérimentaux, théoriques et de simulation par éléments finis sont présentés dans la Figure FR-3.6 (les résultats théoriques et de simulation ayant été respectivement obtenus après une identification préliminaire des paramètres du modèle et à partir des caractéristiques des matériaux utilisés) et les différents amortissements obtenus résumés dans le Tableau FR-3.1. On constate ainsi un très bon accord entre théorie, simulation et pratique, ce qui confirme l'excellente capacité du système électromécanique couplé à l'interface de traitement non-linéaire SSDI pour amortir les vibrations de la structure hôte de manière efficace, le tout en utilisant un faible volume d'élément piézoélectrique (dans le cas d'un couplage direct avec la structure hôte à volume d'élément actif constant, le très faible coefficient de couplage conduirait à des performances très limitées). On pourra néanmoins remarquer que, dans le cas du TMD électromécanique semi-passif, l'approche par constantes localisées ne permet par d'inclure les effets de réinjection d'harmoniques dus à la commutation (du fait de l'hypothèse du premier harmonique), ce qui conduit à de légères différences entre les réponses fréquentielles relevées expérimentalement et les prédictions théoriques (cette disparité n'apparaissant pas entre les courbes expérimentales et obtenues par l'analyse par éléments finis, cette dernière ne faisant aucune simplification sur le comportement de la technique non-linéaire).

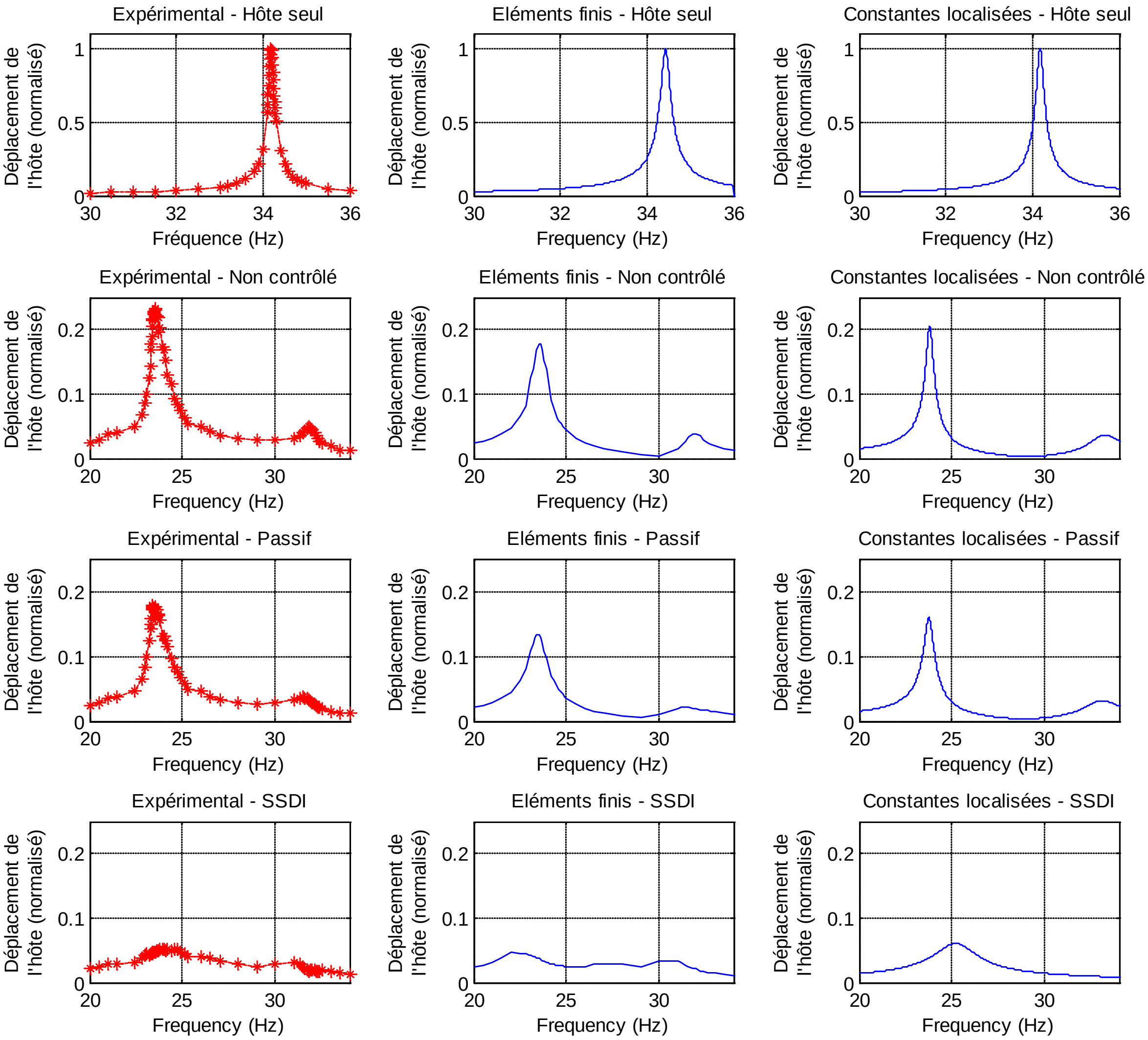

Figure FR-3.6. Résultats expérimentaux et comparaison avec les prédictions théoriques et de simulation.

Tableau FR-3.1. Amortissements obtenus expérimentalement, théoriquement et par simulation (à partir des valeurs maximales de déplacements dans la plage de fréquence considérée)

	TMD purement mécanique	TMD électromécanique passif optimal	TMD électromécanique semi-passif non-linéaire
Expérimental	-12.65 *dB*	-15.01 *dB*	-25.60 *dB*
Constantes localisées	-13.76 *dB*	-16.02 *dB*	-24.18 *dB*
Eléments finis	-14.98 *dB*	-17.48 *dB*	-26.55 *dB*

FR-3.4 Conclusion

Ce Chapitre a proposé l'utilisation des systèmes d'amortissement à masse accordée, permettant des performances très intéressantes tout en étant adaptables avec les techniques de contrôle non-linéaires SSDI, offrant ainsi des capacités remarquables en termes d'amélioration de la conversion électroactive conduisant à une bien meilleure extraction de l'énergie électrique. Ainsi, il a été démontré théoriquement, par simulation et par l'expérience qu'un TMD avec un couplage piézoélectrique combiné à l'interface SSDI présente des capacités d'amortissement des vibrations tout à fait uniques et adaptables, dépassant celles des TMDs purement mécaniques et ceux électromécaniques passifs. Ces propriétés remarquables s'expliquent par la possibilité de contrôler séparément le couplage mécanique entre la structure hôte et le TMD, le couplage électromécanique au sein du TMD, et l'amélioration de ce dernier via l'inversion de tension opérée par l'approche SSDI. Par ailleurs, il convient de noter d'importantes différences entre l'approche SSDI classique par couplage directe et l'approche SSDI via un TMD ; dans ce dernier cas l'amortissement n'étant pas une fonction monotone du coefficient d'inversion.

Ce Chapitre a également discuté des enjeux en termes d'implémentation réaliste des systèmes. En particulier, il a été montré que l'approche SSDI permet une réduction significative du volume d'inserts électroactifs nécessaire par rapport au cas directement couplé, conduisant à un système compact, moins coûteux et très efficace. L'effet d'un désaccordage des fréquences de résonance entre la structure hôte et le TMD a également été envisagé, auquel cas il a été montré que, pour une variation de -20 % de la fréquence de résonance du TMD, les performances sont peu impactées voire légèrement améliorées (alors qu'une fréquence de résonance du TMD 20% plus importante que celle de l'hôte entraîne une forte diminution des capacités d'amortissement) mais le rapport de masse optimal est significativement changé ; une dérive négative permettant par ailleurs moins de contraintes de dimensionnement du fait de la présence d'un « palier » autour de la masse optimale.

Chapitre FR-4. Amortissement d'ondes mécaniques à partir de structures périodiques électroactives incluant une interface non-linéaire

FR-4.1 Introduction

Dérivées de la photonique, les structures périodiques possèdent des propriétés uniques permettant de disposer de bandes fréquentielles où l'onde est bloquée. Ainsi, de manière différente des Chapitres précédents où l'atténuation des vibrations est obtenue par l'augmentation des pertes de la structure d'un point de vue mécanique, ce Chapitre propose d'appliquer le concept de structures périodiques couplées à la technique non-linéaire SSDI afin de disposer d'un dispositif permettant de bloquer la propagation d'une onde et donc de réduire les vibrations mécaniques. Un certain nombre de travaux sur les structures périodiques mécaniques utilisées pour l'amortissement ont été menés par la passé, avec un possible couplage à des éléments électroactifs afin de pouvoir contrôler et/ou accroître les capacités de blocage de l'onde (Figure FR-4.1). Ces capacités d'amortissement se traduisent généralement par l'étude des valeurs propres de la matrice de transfert reliant une cellule unitaire à une autre, la partie logarithmique imaginaire donnant la décroissance logarithmique de l'onde lorsque cette dernière traverse la cellule (Figure FR-4.2). On pourra également noter qu'une légère apériodicité de la structure peut également accroître la largeur des zones fréquentielles de coupure.

Ce Chapitre propose ainsi l'étude de telles structures, lorsque celles-ci incluent un ou plusieurs élément(s) piézoélectrique(s) interfacé(s) avec la technique de traitement non-linéaire SSDI.

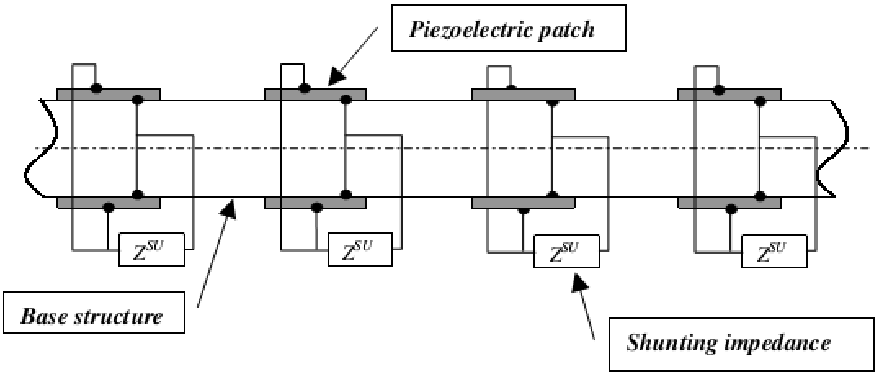

Figure FR-4.1. Structure périodique électromécanique utilisant des éléments piézoélectriques shuntés **[156]**.

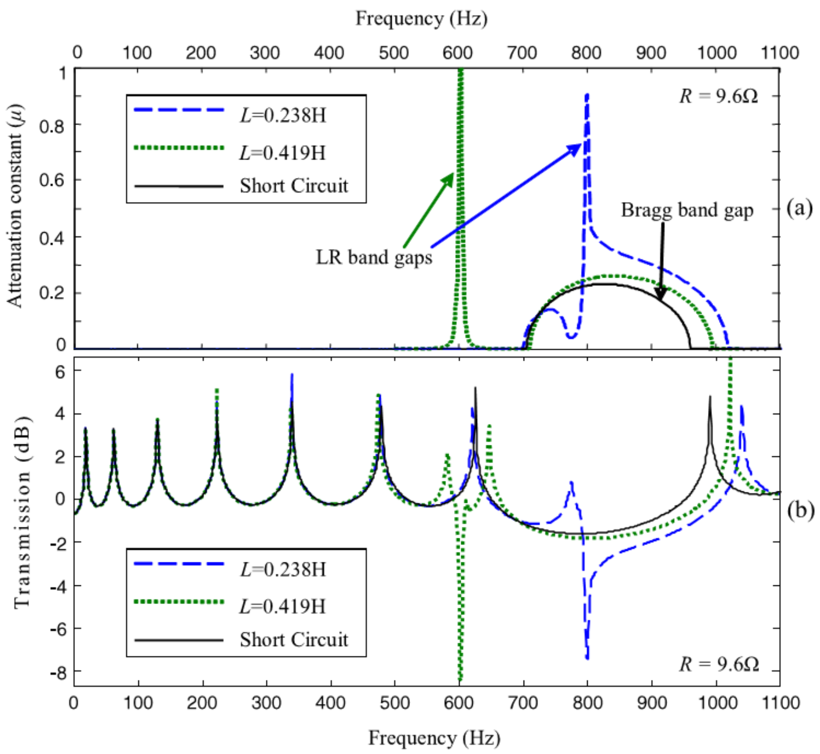

Figure FR-4.2. Exemple de constantes d'atténuation et de transmission obtenues pour une structure composée de cellules incluant des shunts résonants ([163]).

FR-4.2 Analyse théorique

Cette partie propose l'étude semi-analytique d'une structure périodique, représentée de manière schématique en Figure FR-4.3, composée de *N* cellules unitaires chacune équipée d'inserts piézoélectriques qui peuvent être interfacés de manière différente : circuit ouvert (dans ce cas, le comportement est similaire à un cas purement mécanique), shunt résistif et interface SSDI. Le principe de l'analyse se base sur l'étude des valeurs propres de la matrice de transfert entre chaque cellule, celle-ci étant obtenue par une modélisation par éléments finis d'une cellule unitaire.

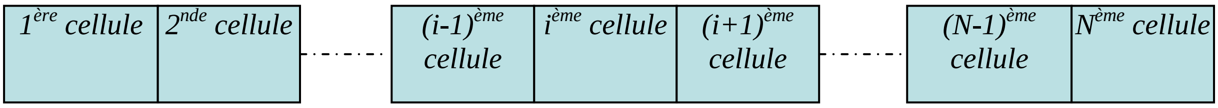

Figure FR-4.3. Structure périodique.

FR-4.2.1 Analyse par éléments finis pour une cellule unitaire

La première étape de la modélisation consiste à isoler une cellule unitaire et de la décomposer en *n* éléments, comme indiqué en Figure FR-4.4. Dans ce cas, l'application de la méthode des éléments finis de manière similaire aux Chapitres précédents à ces *n* éléments conduit à la relation matricielle suivante :

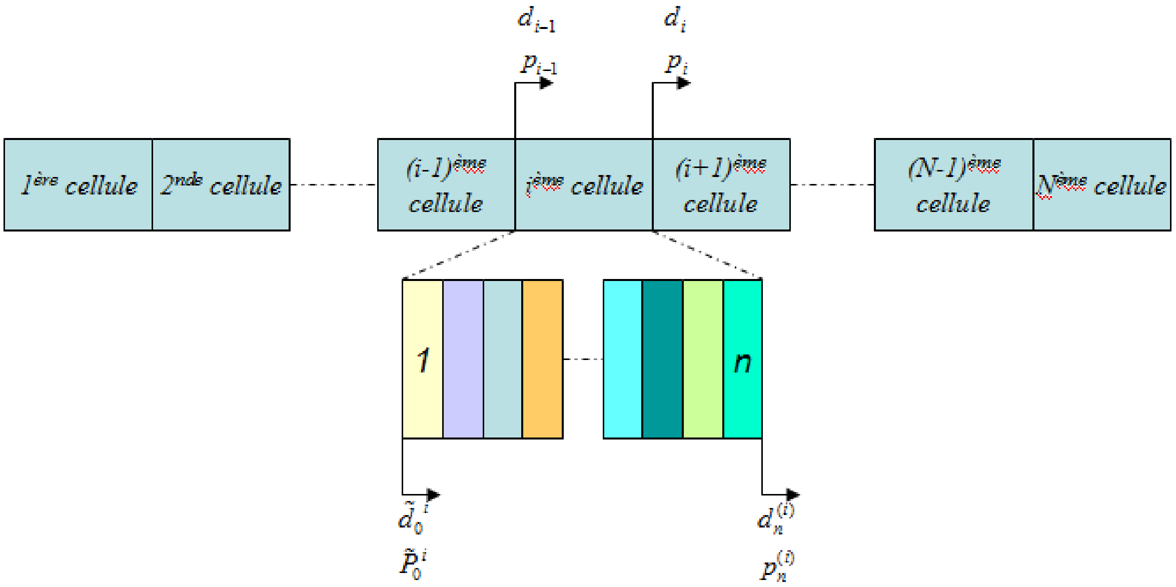

Figure FR-4.4. Schéma d'une cellule unitaire.

$$[A]\begin{Bmatrix} \tilde{d}_0^{\,i} \\ \vdots \\ \tilde{d}_j^{\,i} \\ \vdots \\ \tilde{d}_n^{\,i} \end{Bmatrix} - [B_1]\begin{Bmatrix} \tilde{V}_1^{\,i} \\ \vdots \\ \tilde{V}_{j_p}^{\,i} \\ \vdots \\ \tilde{V}_{np}^{\,i} \end{Bmatrix} = \begin{Bmatrix} \tilde{P}_0^{\,i} \\ \vdots \\ \tilde{P}_j^{\,i} \\ \vdots \\ \tilde{P}_n^{\,i} \end{Bmatrix} \qquad \text{(FR-4.1)}$$

où les vecteurs $\tilde{d}$ et $\tilde{P}$ sont respectivement les vecteurs de déplacement et pente et de force et moment et $\tilde{V}_{j_p}$ la tension du $j_p^{\grave{e}me}$ élément piézoélectrique. L'exposant i représente la cellule i étudiée et l'indice j le $j^{\grave{e}me}$ élément de cette cellule.

Dans le cas d'un court-circuit, la tension est nulle et l'équation du mouvement se simplifie sous la forme suivante :

$$[A]\begin{Bmatrix} \tilde{d}_0^{\,i} \\ \vdots \\ \tilde{d}_j^{\,i} \\ \vdots \\ \tilde{d}_n^{\,i} \end{Bmatrix} = \begin{Bmatrix} \tilde{P}_0^{\,i} \\ \vdots \\ \tilde{P}_j^{\,i} \\ \vdots \\ \tilde{P}_n^{\,i} \end{Bmatrix} \text{ ou } [A_{cc}]\begin{Bmatrix} \tilde{d}_0^{\,i} \\ \vdots \\ \tilde{d}_j^{\,i} \\ \vdots \\ \tilde{d}_n^{\,i} \end{Bmatrix} = \begin{Bmatrix} \tilde{P}_0^{\,i} \\ \vdots \\ \tilde{P}_j^{\,i} \\ \vdots \\ \tilde{P}_n^{\,i} \end{Bmatrix} \qquad \text{(FR-4.2)}$$

En circuit ouvert et en reprenant les résultats obtenus dans les chapitres précédents, il est possible d'exprimer directement les différentes tensions en fonction du vecteur de déplacement et pente, ce qui conduit à l'équation du mouvement dans ce cas :

$$\left\{[A]-[B_1][B_4]\right\}\begin{Bmatrix}\tilde{d}_0^{\,i}\\ \vdots\\ \tilde{d}_j^{\,i}\\ \vdots\\ \tilde{d}_n^{\,i}\end{Bmatrix}=\begin{Bmatrix}\tilde{P}_0^{\,i}\\ \vdots\\ \tilde{P}_j^{\,i}\\ \vdots\\ \tilde{P}_n^{\,i}\end{Bmatrix} \text{ ou } [A_{co}]\begin{Bmatrix}\tilde{d}_0^{\,i}\\ \vdots\\ \tilde{d}_j^{\,i}\\ \vdots\\ \tilde{d}_n^{\,i}\end{Bmatrix}=\begin{Bmatrix}\tilde{P}_0^{\,i}\\ \vdots\\ \tilde{P}_j^{\,i}\\ \vdots\\ \tilde{P}_n^{\,i}\end{Bmatrix} \tag{FR-4.3}$$

qui ne fait apparaître que des termes mécaniques équivalents.

Dans le cas où un élément purement résistif *R* est directement connecté à chaque élément actif, la tension à leurs bornes s'exprime par :

$$\left\{\tilde{V}^i\right\}=\left([I]-Rj\omega[B_3]\right)^{-1}\cdot j\omega R[B_2]\left\{\tilde{d}^i\right\}=[B_5]\left\{\tilde{d}^i\right\} \tag{FR-4.4}$$

et l'équation du mouvement devient :

$$\left\{[A]-[B_1][B_5]\right\}\begin{Bmatrix}\tilde{d}_0^{\,i}\\ \vdots\\ \tilde{d}_j^{\,i}\\ \vdots\\ \tilde{d}_n^{\,i}\end{Bmatrix}=\begin{Bmatrix}\tilde{P}_0^{\,i}\\ \vdots\\ \tilde{P}_j^{\,i}\\ \vdots\\ \tilde{P}_n^{\,i}\end{Bmatrix} \text{ ou } [A_R]\begin{Bmatrix}\tilde{d}_0^{\,i}\\ \vdots\\ \tilde{d}_j^{\,i}\\ \vdots\\ \tilde{d}_n^{\,i}\end{Bmatrix}=\begin{Bmatrix}\tilde{P}_0^{\,i}\\ \vdots\\ \tilde{P}_j^{\,i}\\ \vdots\\ \tilde{P}_n^{\,i}\end{Bmatrix} \tag{FR-4.5}$$

$$\text{avec } [B_5]_{opt}=\frac{-j[B_3]^{-1}[B_2]}{(1+j)}$$

Enfin, lorsque l'on considère que chaque élément piézoélectrique est interfacé avec l'étage SSDI (ce dernier fonctionnant indépendamment pour chaque insert), il est possible, en considérant une excitation monochromatique, d'appliquer l'approximation du premier harmonique sur la tension de sortie des éléments électroactifs (de manière similaire au Chapitre précédent), ce qui conduit aux expressions respectives de la tension et de l'équation du mouvement :

$$\left[V^i\right]=[B_4]\left([I]+\frac{4j}{\pi}diag\left(\frac{1+\gamma_{j_p}}{1-\gamma_{j_p}}\right)\right)\left\{d^i\right\}=[B_6]\left\{d^i\right\} \tag{FR-4.6}$$

$$\left\{[A]-[B_1][B_6]\right\}\begin{Bmatrix}\tilde{d}_0^{\,i}\\ \vdots\\ \tilde{d}_j^{\,i}\\ \vdots\\ \tilde{d}_n^{\,i}\end{Bmatrix}=\begin{Bmatrix}\tilde{P}_0^{\,i}\\ \vdots\\ \tilde{P}_j^{\,i}\\ \vdots\\ \tilde{P}_n^{\,i}\end{Bmatrix} \text{ ou } [A_{ssdi}]\begin{Bmatrix}\tilde{d}_0^{\,i}\\ \vdots\\ \tilde{d}_j^{\,i}\\ \vdots\\ \tilde{d}_n^{\,i}\end{Bmatrix}=\begin{Bmatrix}\tilde{P}_0^{\,i}\\ \vdots\\ \tilde{P}_j^{\,i}\\ \vdots\\ \tilde{P}_n^{\,i}\end{Bmatrix} \tag{FR-4.7}$$

FR-4.2.2 Matrice de transfert entre les cellules

Maintenant que l'équation du mouvement pour chaque cas considéré est établie, il est possible de modéliser le système à un niveau supérieur (celui d'une cellule unitaire) par l'obtention de sa matrice de transfert. En notant de manière générale les matrices A_{cc}, A_{co}, A_R et A_{ssdi} obtenues précédemment une forme générale $A_{condition}$ décomposée selon ses sous-matrices extrêmes et internes :

$$A_{condition} = \begin{bmatrix} a_{00} & a_{0j} & a_{0n} \\ a_{j0} & a_{jj} & a_{jn} \\ a_{n0} & a_{nj} & a_{nn} \end{bmatrix} \tag{FR-4.8}$$

il est possible de réarranger l'équation du mouvement sous la forme :

$$\begin{bmatrix} a_{00} & a_{0n} & a_{0j} \\ a_{n0} & a_{nn} & a_{nj} \\ a_{j0} & a_{jn} & a_{jj} \end{bmatrix} \begin{Bmatrix} \tilde{d}_0^{\,i} \\ \tilde{d}_n^{\,i} \\ \tilde{d}_j^{\,i} \end{Bmatrix} = \begin{Bmatrix} \tilde{P}_0^{\,i} \\ \tilde{P}_n^{\,i} \\ \tilde{P}_j^{\,i} \end{Bmatrix} \tag{FR-4.9}$$

ce qui permet, en considérant qu'aucune force externe n'est appliquée ailleurs que sur les bords de la cellule, d'appliquer la réduction de Guyan pour avoir l'équation de mouvement réduite :

$$\begin{bmatrix} a_{00} - a_{0j} a_{jj}^{-1} a_{j0} & a_{0n} - a_{0j} a_{jj}^{-1} a_{jn} \\ a_{n0} - a_{nj} a_{jj}^{-1} a_{j0} & a_{nn} - a_{nj} a_{jj}^{-1} a_{jn} \end{bmatrix} \begin{Bmatrix} \tilde{d}_0^{\,i} \\ \tilde{d}_n^{\,i} \end{Bmatrix} = \begin{bmatrix} \alpha_{11} & \alpha_{12} \\ \alpha_{21} & \alpha_{22} \end{bmatrix} \begin{Bmatrix} \tilde{d}_0^{\,i} \\ \tilde{d}_n^{\,i} \end{Bmatrix} = \begin{Bmatrix} \tilde{P}_0^{\,i} \\ \tilde{P}_n^{\,i} \end{Bmatrix} \tag{FR-4.10}$$

qui conduit à la matrice de transfert T :

$$[T] = \begin{bmatrix} -\alpha_{12}^{-1}\alpha_{11} & \alpha_{12}^{-1} \\ -\alpha_{21} + \alpha_{22}\alpha_{12}^{-1}\alpha_{11} & -\alpha_{22}\alpha_{12}^{-1} \end{bmatrix} = \begin{bmatrix} t_{11} & t_{12} \\ t_{21} & t_{22} \end{bmatrix} \tag{FR-4.11}$$

L'analyse des valeurs propres λ_i de cette matrice conduit à la définition de quatre valeurs, chacune correspondant à un type d'onde (propagative ou évanescente) dans l'une ou l'autre direction. De plus, la réécriture sous forme exponentielle :

$$\lambda_i = e^{\eta + j\delta}, i \in [1,2,3,4] \tag{FR-4.12}$$

permet de faire apparaître la constante de propagation complexe $\eta + j\delta$ dont la partie imaginaire correspond au déphasage lors de la traversée de la cellule ainsi que la décroissance logarithmique η ; cette dernière traduisant l'atténuation.

FR-4.3 Comparaison théorique et validation expérimentale

Cette partie propose de mettre en application l'approche par matrice de transfert exposée précédemment dans des cas concrets de structure ainsi que de discuter des performances comparées des structures périodiques purement mécaniques, électroactives passives et électroactives semi-passives non-linéaires. L'analyse se base sur la structure expérimentale exposée dans la partie suivante, sans la prise en compte des pertes mécaniques afin de mettre en avant les spécificités de chaque configuration périodique envisagée.

FR-4.3.1 Capacités d'amortissement

Les résultats en termes de parties imaginaire et réelle de la constante de propagation (la partie réelle relatant l'atténuation) sont présentés dans la Figure FR-4.5. Ces résultats démontrent les capacités de la structure envisagée à présenter des zones fréquentielles où l'onde est significativement atténuée. L'utilisation du couplage électromécanique avec la technique passive consistant en l'ajout d'une résistance ne change pas significativement les capacités d'atténuation dans les zones de coupures. Néanmoins, hors de ces zones et grâce au couplage électromécanique, il apparaît une atténuation qui n'est pas présente dans le cas équivalent purement mécanique (court-circuit et circuit ouvert). Les résultats dans le cas du SSDI sont encore plus significatifs. En effet, non seulement cette technique permet d'augmenter significativement les capacités d'atténuation dans les zones de coupure, mais surtout étend ces zones dans les zones normalement passantes, conduisant à des performances remarquables en termes d'amortissement, qui peuvent être attribuées non seulement aux capacités de la technique non-linéaire à augmenter artificiellement le couplage électromécanique, mais également à la capacité du SSDI de s'adapter au changement de fréquence grâce au principe de détection d'extrema. On pourra également noter que le SSDI diminue très légèrement la partie réelle de la constante de propagation dans le cas de l'onde évanescente, mais cette dernière reste très largement supérieure à celle de l'onde de propagation.

La Figure FR-4.5 montre également un léger changement de la partie imaginaire de la constante de propagation de l'onde de propagation dans le cas du SSDI dans les bandes de coupure qui n'est plus un plateau. Ce phénomène apparaît également dans le cas de l'onde évanescente (de même pour le cas électromécanique passif), ce qui dénote une possible conversion d'onde.

Les performances en termes d'atténuation reflétées par la valeur de la partie réelle de la constante de propagation en fonction du coefficient d'inversion sont représentées en Figure FR-4.1. Cette figure montre que l'augmentation du coefficient d'inversion, qui accroît l'amélioration du couplage, permet d'obtenir des capacités d'amortissement de plus en plus importantes tout en élargissant les bandes de coupure, conduisant donc à un système de plus en plus efficace pour la réduction des vibrations.

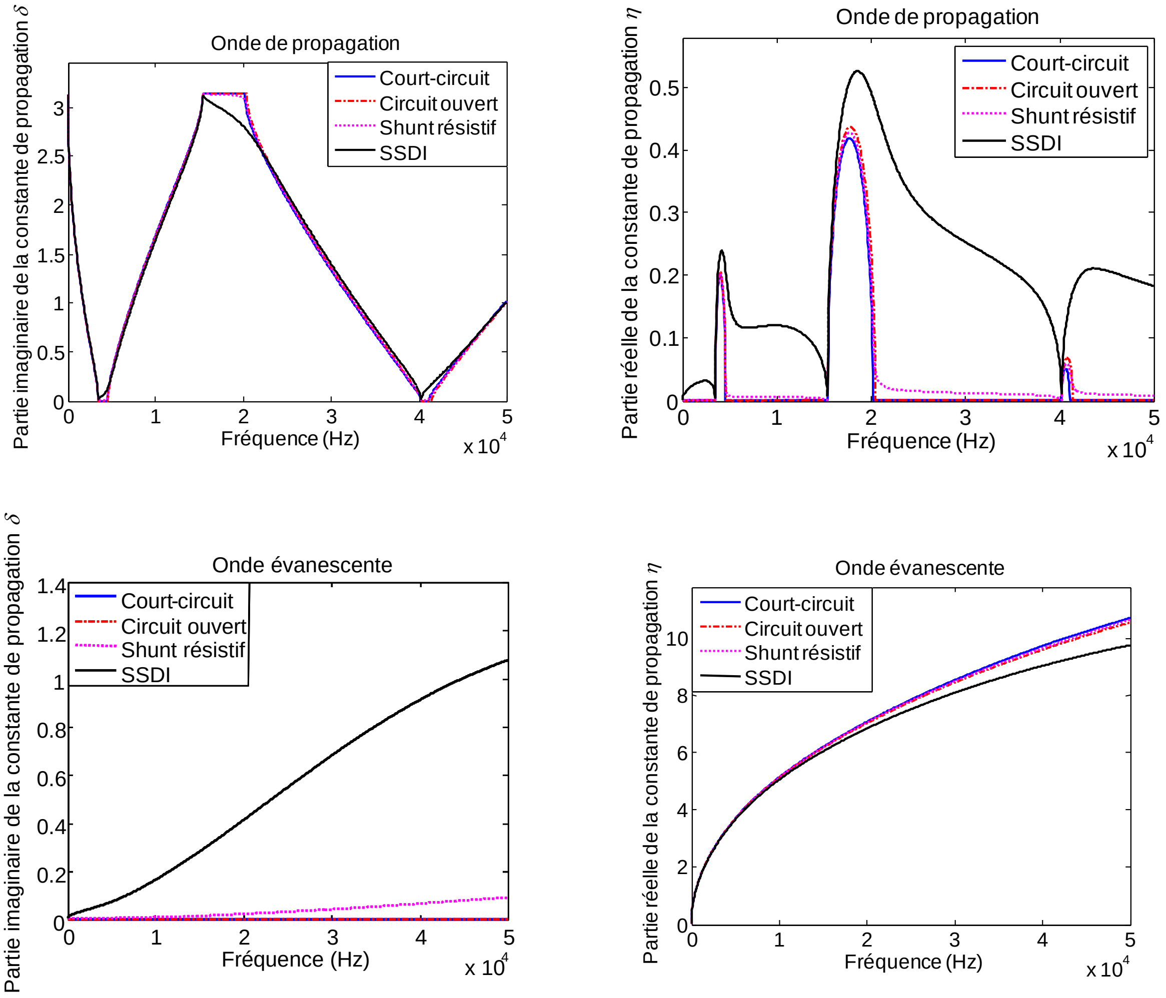

Figure FR-4.5. Résultats de simulation des constantes de propagation (sans pertes mécaniques).

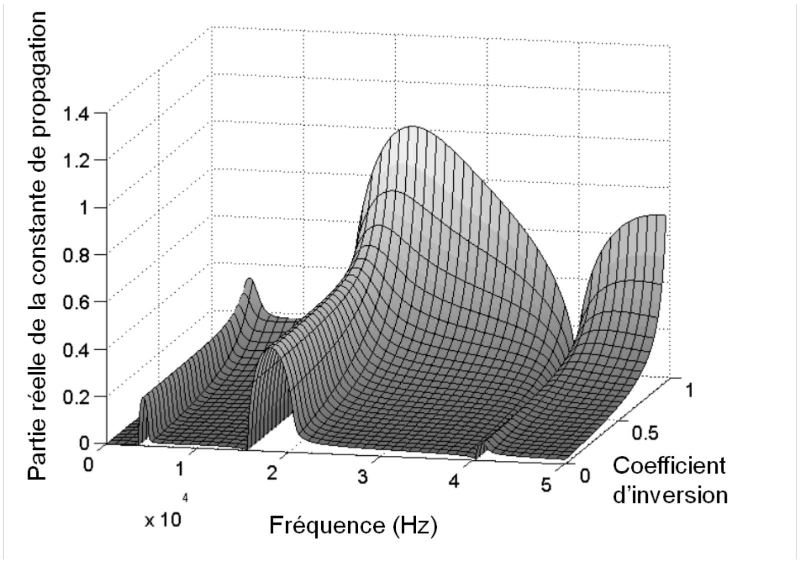

Figure FR-4.6. Partie réelle de la constante de propagation de l'onde propagative en fonction du coefficient d'inversion.

FR-4.3.2 Réponse sous différentes conditions aux limites

La modélisation par matrice de transfert permet d'exprimer la réponse en chaque point de liaison *i* entre cellules selon la forme :

$$\begin{Bmatrix} \tilde{d}_i \\ \tilde{P}_i \end{Bmatrix} = [T]^i \begin{Bmatrix} \tilde{d}_0 \\ \tilde{P}_0 \end{Bmatrix} + [T]^{(i-N)} \begin{Bmatrix} 0 \\ \tilde{P}_e \end{Bmatrix} \tag{FR-4.13}$$

où $\tilde{P}_0$ et $\tilde{d}_0$ correspondent respectivement aux vecteur force et moment et vecteur déplacement et pente à l'extrémité gauche de la structure, et $\tilde{P}_e$ est l'excitation extérieure appliquée au point *N*. En considérant que la structure est composée de N_{cell} cellules, la réponse en bout de poutre est donnée par :

$$\begin{Bmatrix} \tilde{d}_{N_{cell}} \\ \tilde{P}_{N_{cell}} \end{Bmatrix} = [T]^{N_{cell}} \begin{Bmatrix} \tilde{d}_0 \\ \tilde{P}_0 \end{Bmatrix} + [T]^{(N_{cell}-N)} \begin{Bmatrix} 0 \\ \tilde{P}_e \end{Bmatrix} \tag{FR-4.14}$$

Par la suite, il est possible d'appliquer les conditions aux limites selon les différents cas de figure pour pouvoir obtenir $\tilde{d}_{N_{el}}$, $\tilde{P}_{N_{el}}$, $\tilde{d}_0$ et $\tilde{P}_0$ ce qui permet d'avoir accès à la réponse en chaque point du système par l'utilisation de l'équation (FR-4.13). A titre d'exemple, le Tableau FR-4.1 présente les cas de poutres encastrée-libre et encastrée-encastrée.

Tableau FR-4.1 Expression des inconnues dans le cas d'une poutre encastrée-libre ou encastrée-encastrée

	Conditions aux limites	**Expression des inconnues**
Encastrée-libre	$\tilde{d}_0 = 0$ $\tilde{P}_{N_{cell}} = 0$	$\tilde{P}_0 = -\left(t_{21}^{\{N_{cell}-N\}} t_{12}^{\{N\}} + t_{22}^{\{N_{cell}-N\}} t_{22}^{\{N\}}\right)^{-1} \left(t_{22}^{\{N_{cell}-N\}}\right) \tilde{P}_e$ $\tilde{d}_{N_{cell}} = \Big\{-\left(t_{11}^{\{N_{cell}-N\}} t_{12}^{\{N\}} + t_{12}^{\{N_{cell}-N\}} t_{22}^{\{N\}}\right)$ $\times \left(t_{21}^{\{N_{cell}-N\}} t_{12}^{\{N\}} + t_{22}^{\{N_{cell}-N\}} t_{22}^{\{N\}}\right)^{-1} \left(t_{22}^{\{N_{cell}-N\}}\right) + t_{12}^{\{N_{cell}-N\}} \Big\} \tilde{P}_e$
Encastrée-encastrée	$\tilde{d}_0 = 0$ $\tilde{d}_{N_{cell}} = 0$	$\tilde{P}_0 = -\left(t_{12}^{\{N_{cell}\}}\right)^{-1} t_{12}^{\{N_{cell}-N\}} \tilde{P}_e$ $\tilde{P}_{N_{cell}} = \left[-t_{22}^{\{N_{cell}\}} \left(t_{12}^{\{N_{cell}\}}\right)^{-1} t_{12}^{\{N_{cell}-N\}} + t_{22}^{\{N_{cell}-N\}}\right] \tilde{P}_e$

FR-4.3.3 Validation expérimentale

Cette partie propose de valider les concepts précédemment présentés dans le cas d'une poutre encastrée-encastrée composée de 4 cellules d'une longueur de 20 mm chacune et incluant un élément piézoélectrique de 10 mm de longueur en leur milieu (Figure FR-4.7). L'excitation est appliquée au quart de la poutre et le déplacement relevé aux trois quarts. Dans la modélisation, l'amortissement est considéré suivre une loi de Rayleigh comme dans les Chapitre précédents.

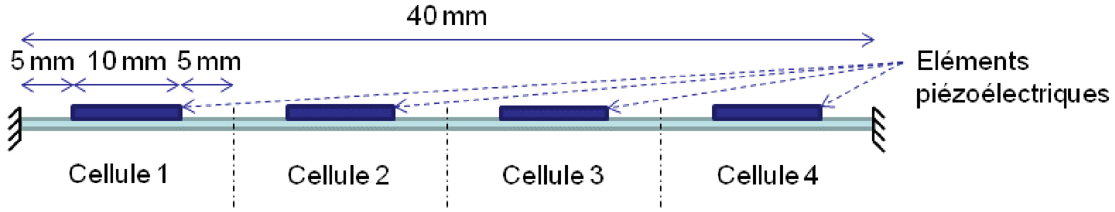

Figure FR-4.7. Schéma de la structure expérimentale.

Les résultats expérimentaux et théoriques illustrés en Figure FR-4.8 montrent une relative bonne concordance entre théorie et expérience, bien que certaines différences apparaissent, probablement du fait d'une force non ponctuelle et non exactement appliquée entre deux cellules, ainsi qu'une légère apériodicité. Néanmoins, on remarque dans tous les cas un bien meilleur amortissement offert par l'utilisation de la technique SSDI.

FR-4.4 Discussion et extensions

Cette Section propose d'aller plus en avant dans l'utilisation des structures périodiques en exposant des possibilités d'amélioration ainsi que des considérations pratiques. Tout d'abord, ainsi que mentionné dans les Chapitres précédents, l'auto-alimentation de la technique SSDI est tout à fait envisageable en utilisant les architectures exposées dans les références [116] et [117]. Egalement, comme certaines études disponibles dans la littérature l'ont montré, une apériodicité, par exemple sur le facteur d'inversion, pourrait être bénéfique au système afin de disposer d'un contrôle encore plus large bande.

Néanmoins, l'une des pistes les plus intéressantes à développer dans l'optique de réseaux d'actionneurs pour le contrôle de vibrations distribué consiste à considérer l'interconnexion électrique des différents inserts électroactifs (plutôt que des opérations indépendantes), comme illustré dans la Figure FR-4.9. A partir de l'expression du circuit obtenu sous la forme d'une source unique (avec son impédance interne) en utilisant le théorème de Norton, il est alors possible d'exprimer sous l'hypothèse du premier harmonique l'impédance linéarisée équivalente Z présentée par le dispositif de commutation :

$$Z = \frac{\pi(1-\gamma)}{2\omega(1+\gamma)C_0} + \frac{2j}{\omega C_0} \qquad \text{(FR-4.15)}$$

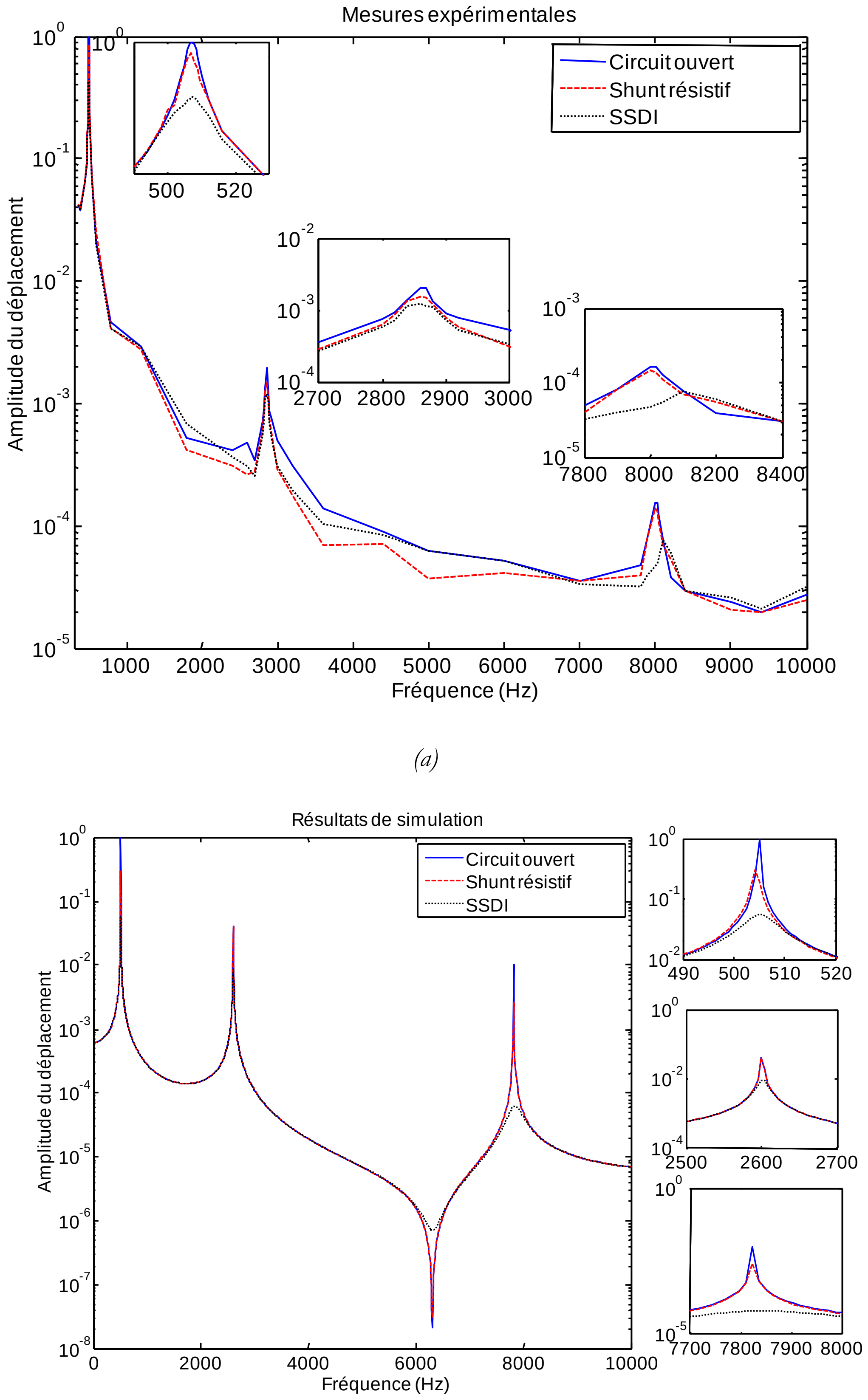

(a)

(b)

Figure FR-4.8. Résultats (a) expérimentaux et (b) théoriques.

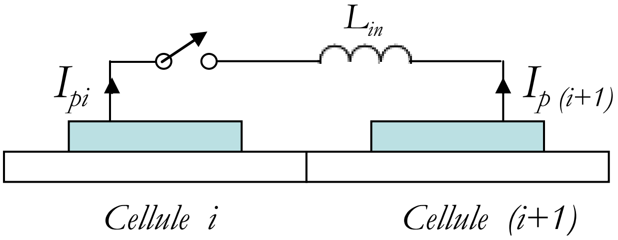

Figure FR-4.9. Structure périodique avec interconnexion électrique.

pour laquelle il est intéressant de noter que la partie imaginaire correspond parfaitement à l'impédance adaptée de l'élément piézoélectrique (le facteur *2* provenant de l'interconnexion des deux patches) ; seul le terme résistif impacte les performances.

Dès lors, il est possible d'utiliser cette expression dans la relation de transfert entre les grandeurs d'entrée (cette fois-ci incluant également des grandeurs électriques) et celles de sortie dans le cas où la charge est une impédance *R* :

$$\begin{Bmatrix} \{\tilde{P}^i\} \\ \tilde{V}_{i+1} \\ \tilde{I}_{i+1} \end{Bmatrix} = \begin{bmatrix} [A] & -[B_1] & R[B_1] \\ 0 & 1 & -R \\ j\omega[B_2] & j\omega[B_3] & 1-j\omega R[B_3] \end{bmatrix} \begin{Bmatrix} \{\tilde{d}^i\} \\ \tilde{V}_i \\ \tilde{I}_i \end{Bmatrix} \tag{FR-4.16}$$

La Figure FR-4.10 présente le facteur d'amortissement logarithmique obtenu dans le cas interconnecté via une simple résistance ou par le dispositif de commutation, en utilisant les paramètres issus de l'identification de la structure expérimentale précédemment présentée. Il apparaît clairement que la technique non-linéaire permet une augmentation des capacités d'atténuation en haute fréquence. En basse fréquence néanmoins, du fait de la longueur d'onde relativement grande par rapport à la périodicité de la structure, cette augmentation est grandement amoindrie.

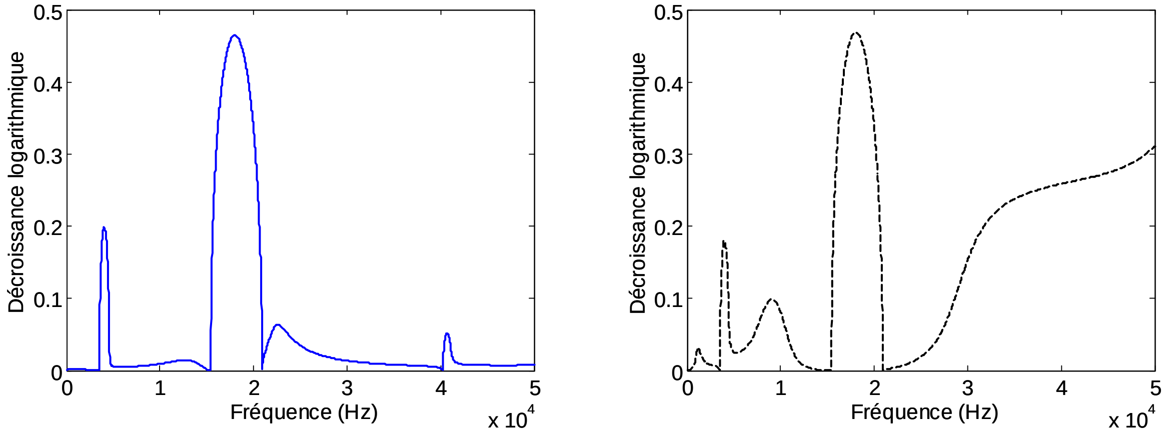

(a) Cas purement résistif (b) Cas commuté SSDI

Figure FR-4.10. Facteur d’amortissement de l’onde de propagation dans le cas d’éléments interconnectés.

FR-4.5 Conclusion

Ce Chapitre a exposé une nouvelle approche pour l’amortissement large bande de structures mécaniques en utilisant une architecture périodique couplée à la technique de traitement non-linéaire SSDI. L’approche utilisée, consistant en une méthode semi-analytique utilisant une analyse par éléments finis au niveau de la cellule unitaire permettant d’avoir accès à la matrice de transfert qui peut être utilisée pour obtenir la réponse globale du système, a montré une excellente capacité d’amortissement de la technique proposée. L’analyse des constantes de propagation a ainsi montré que la technique SSDI peut non seulement accroître le pouvoir d’amortissement dans les zones de coupure, mais également d’étendre ces dernière à des plages de fréquence normalement passantes dans les autres cas considérés (structure purement mécanique et amortissement électromécanique passif), ce qui est non seulement expliqué par les capacités de la technique non-linéaire à améliorer artificiellement le couplage électromécanique, mais également par la possibilité de s’adapter à chaque fréquence du fait du principe de détection d’extrema. L’application expérimentale à une structure de type poutre encastrée-encastrée a confirmé l’analyse menée, démontrant les capacités d’amortissement supérieures et l’adaptabilité de la technique non-linéaire appliquée aux structures périodiques.

Chapitre FR-5. Conclusion générale et perspectives

Les travaux de cette thèse se sont attelés au développement de nouvelles techniques de contrôle vibratoire basées sur un traitement non-linéaire de la tension de sortie d'éléments piézoélectriques. Egalement, la combinaison de cette approche avec d'autres méthodes de contrôle vibratoire a été étudiée afin de disposer d'un système de limitation des vibrations au sein des structures performant et compact. Cette thèse a également été empreinte d'une forte volonté de réalisme, s'efforçant de valider toutes les démarches de modélisation théorique et de simulation par des mesures expérimentales, et en intégrant au mieux la nature complexe des signaux large bande d'environnements réels, ainsi que la faisabilité (notamment au sens énergétique) des stratégies envisagées.

Ainsi, après un état de l'art des différentes méthodes d'amortissement, le second Chapitre s'est intéressé à l'amélioration des capacités d'amortissement de la technique non-linéaire SSDI dans le cas d'une excitation large bande. En effet, l'approche SSDI classique se concentre par nature sur la plus haute fréquence détectable au détriment des premiers modes, qui sont généralement les plus énergétiques. La technique proposée dans ce Chapitre se base sur un filtrage spatial des réponses des éléments piézoélectriques, permettant une séparation des modes visés conduisant, par une mise en réseau adéquate des éléments actifs, d'amortir simultanément plusieurs modes. Afin de réduire la complexité du système et accroître artificiellement l'observabilité du système, la combinaison de ce filtrage spatial avec une méthode basée sur l'historique du signal et précédemment étudiée dans la littérature a montré des capacités d'amortissement tout à fait remarquables sous des conditions d'excitation large bande.

Le troisième Chapitre s'est intéressé à la combinaison de la technique non-linéaire SSDI avec des amortisseurs à masse accordée (TMD), permettant de disposer d'amortisseurs modulables dont les performances sont également remarquables et qui peuvent s'adapter à leur environnement. En effet, comparé aux TMDs purement mécaniques, le couplage électromécanique supplémentaire (en plus du couplage mécano-mécanique entre la structure hôte et l'amortisseur) permet un meilleur contrôle des transferts énergétiques au sein du système et donc des performances d'amortissement. Parmi les autres résultats remarquables de cette étude et du fait des différents transferts énergétiques, il a été montré que l'amélioration de la conversion d'énergie mécanique sous forme électrique peut conduire à une détérioration des performances (le couplage électromécanique influençant le couplage mécano-mécanique).

Enfin, le quatrième et dernier Chapitre s'est intéressé à l'utilisation de structures périodiques, présentant des propriétés remarquables en termes de propagation, avec les techniques non-linéaires. Les performances obtenues dépassent de manière exceptionnelle celles des structures périodiques classiques ou électromécaniques passives, permettant non seulement une augmentation de l'amortissement dans les zones de coupure grâce à l'augmentation artificielle du couplage électromécanique offerte par le SSDI, mais également un élargissement des plus importants de ces zones de coupure du fait de la nature adaptative de l'approche non-linéaire, conduisant à une possibilité de limiter les vibrations sur une large gamme de fréquence.

Les travaux exposés dans cette thèse se voulant d'une nature novatrice avec une validation du concept de base, d'autres axes de recherches peuvent en découler. Les études ultérieures pourront porter, selon la technique envisagée, sur :

- Pour la technique de filtrage spatiale : la validation expérimentale de la technique hybride combinant filtrage temporel et spatial pourrait déboucher sur de nouvelles idées de combinaison afin de disposer de méthodes encore plus efficace. De même, une généralisation du principe de filtrage spatial à tout type de structure et avec un nombre non prédéfini d'actionneurs/capteurs travaillant en réseau pourrait conduire à l'élaboration d'algorithme de contrôle performant, robuste et peu consommateur.
- Pour les amortisseurs à masse accordée : la mise en réseau de plusieurs TMDs et leur interconnexion en vue d'une amélioration de l'amortissement et/ou l'extension à des signaux large bande pourraient être envisagées (un exemple consistant en l'utilisation de la technique de filtrage spatial). En particulier, le contrôle en temps réel des flux énergétiques (mécaniques mais aussi électriques) semble être une piste très prometteuse. Egalement, une étude approfondie sur la compréhension des différents échanges énergétiques directs et inverses permettrait d'évaluer l'impact des différents paramètres du système (citons par exemple le cas du facteur d'inversion).
- Pour les structures périodiques : bien qu'ébauchées dans ce manuscrit, les approches de mise en réseau électrique ouvre un champ d'applications et de recherches très important. Notamment, par une interconnexion non-linéaire appropriée utilisant le concept de commutation synchronisée avec un algorithme adapté, les performances du système pourraient être encore plus spectaculaires. De même, les effets de l'introduction d'une certaines apériodicité (notamment d'un point de vue électrique) en vue d'un contrôle encore plus large bande est une piste à sérieusement creuser.

En conclusion, les travaux présentés ici ont, par la proposition de nouvelles approches de contrôle vibratoire, pu ouvrir de nouvelles perspectives réalistes afin de disposer de systèmes performants dans un environnement réel.

English Part

Abstract

In order to protect structures, extend their lifespan and decrease the incomfort resulting from undesired vibrations, plenty of works have been reported for reducing the vibration. Along with the development of smart materials such as piezoelectric materials which are extensively used for vibration control and noise reduction due to their unique features (high integrability, compactness, light weight and high bandwidth), the control system can be designed in a more compact and simple form. Additionally, due to the conversion between mechanical energy and electrical energy, the vibration can be effectively attenuated by electromechanical approaches.

Synchronized Switch Damping on Inductor (SSDI) technique attracted lot of attentions as an effective semi-passive technique which can artificially increase the converted energy by nonlinear voltage inversion process, thus allowing a superior control performance compared to passive technique with low power requirement and simple control algorithm.

Based on this semi-passive control technique, the objectives of the work reported in the manuscript are threefold. The first aim is improving the multimodal/broadband control performance of SSDI technique in multimodal/ broadband vibration. An enhanced strategy based on spatial filtering according to the mode shapes of the vibrating structure is proposed. In order to separate the uninterested modes and effectively damp the targeted modes, sum switch and different switch respectively based on the sum of the piezovoltages of two anti-symmetrically bonded patches and the voltage difference of the two symmetrically bonded piezoelectric elements are introduced. Since the vibration modes can be spatially filtered by these connections, the multimodal vibrations can be damped significantly and simultaneously as the sum and difference switches are employed, with an increase of total inversion coefficient.

Then, electromechanical TMD (tuned mass damper) featuring piezoelectric materials combined with the semi-passive nonlinear technique SSDI is presented. Using this electromechanical semi-passive nonlinear TMD, the mechanical energy is not only transferred between host structure and TMD device but also converted as electrical energy stored in the piezoelectric patches and/or dissipated in the connected circuit, which allows excellent damping performance for limiting the vibration of host structure.

The last investigated method consists in electromechanical periodic structures featuring the nonlinear switching interface are investigated. Such a structure can effectively attenuate the elastic waves and damp the vibration in a wider frequency band since it has the capability of filtering propagative waves within stop bands attributed to the structural periodicity and the superior damping ability which is attributed to the nonlinear voltage inversion process that increases the voltage amplitude and decreases the phase between voltage and speed.

Finally, a conclusion proposes a summary of the main results obtained in this thesis, as well as new extensions and ways of the proposed techniques.

Chapter 1. Background and Literatures Review

Vibration is a common physical phenomenon which can be easily found in universe. Though some vibrations can enrich people's life, harmful vibrations may induce fatal disaster or incomfort. To prevent these troubles happening, plenty of researchers concentrate on vibration control. This chapter reviews the state of the art of the structural control. Various damping materials, devices and control techniques involved in vibration control are outlined. As effective and extensive semi passive/active treatments, the development of Synchronized Switch Damping (SSD) techniques is introduced in detail.

1.1. Necessity of damping

It appears that people started to seek out the rules and laws of sound/vibration since the first musical instruments were created, though at that time they did not reach a scientific level [1]. With the understanding of physical phenomena and development of theories, vibration is extensively used. Vibration therapy is one of the utilized profitably in consumer and industrial applications, which uses mechanical vibrations to supposedly prevent, treat and promote recovery from a variety of physical ailments through a variety of massage tools and/or specialized equipment [2]. Vibration is also put to work in washing machine, electric toothbrushes, dentist's drills and clocks. Moreover, it can be used in pile driving, vibratory testing of materials, vibratory finishing processes (Figure 1.1) and electronic circuits to filter out the unwanted frequencies [1].

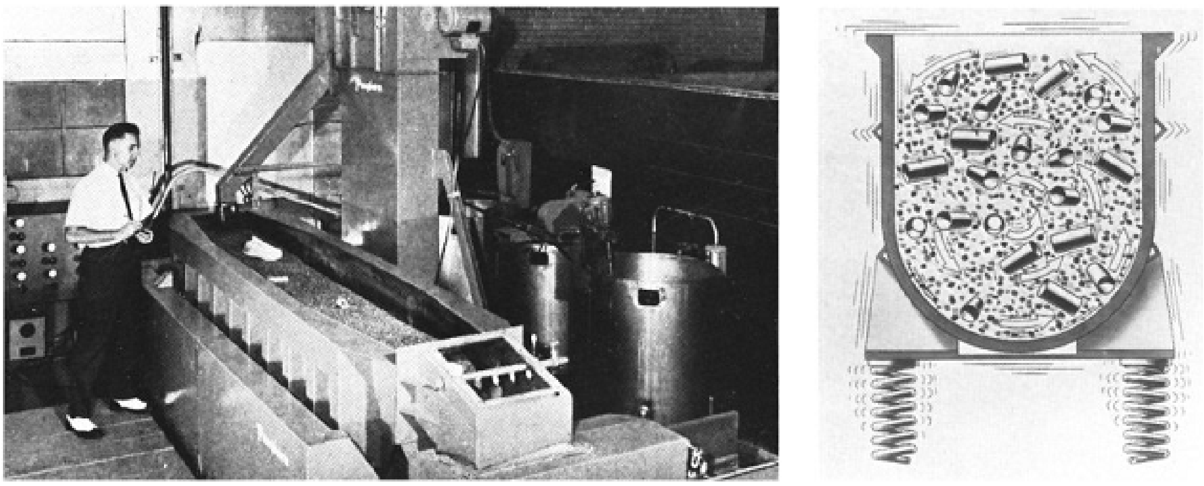

Figure 1.1.Vibratory finishing process [1].

However, the undesirable and harmful vibrations can lead to some adverse and detrimental effects. Human body exposed to some vibration environments may cause discomfort, adversely affect performance, aggravate pre-existing back injuries and present a health and safety risk [3] [4] [5]. In engineering domain, vibrations may cause excessive wear of bearings and gears, loosening of fasteners, structural and mechanical failures, frequent and costly maintenance of machines, electronic malfunctions and noise. Devastating effects and system failures (Figure 1.2) will bring about by resonance which occurs whenever the natural frequency of vibration of a machine or structure coincides with the frequency of external excitation.

Figure 1.2. Tacoma Narrows bridge collapse under wind-induced vibration [1].

Consequently, plenty of scholars focus on vibration control to prevent the problems induced by the undesirable vibration. Numerous research and investigations have been reported in the past decades. Generally, there are several methods for vibration control such as avoiding resonance, balancing/controlling the external forces, providing adequate damping, utilizing vibration isolator or vibration absorber and so on. In the following part, the vibration control methods are reviewed in two main aspects: damping materials and/or devices and electromechanical control techniques utilized piezoelectric devices.

1.2. Damping materials and devices

As one of the effective vibration control principles, increasing damping means improving the energy dissipation ability of a vibrating system or structure, which has led to a large number of damping materials and devices reported for vibration suppression. Some investigations of the more common damping materials and devices are introduced in this section.

1.2.1. Viscoelastic damping system

Damping materials have been used as treatments to improve damping performance for a few decades. The most common damping materials are viscoelastic materials which possess both elastic and viscous properties and dissipate system energy by deformation. For elastic materials, the stored energy during loading is recovered when the load is removed, which refers to in phase stress-strain relationship (Figure 1.3a). Contrary to elastic materials, for viscous materials, there is no recovered energy which lost as 'pure damping' after removing the load and the phase angle between stress and strain is exactly $\pi/2$ radians (Figure 1.3b). Since the viscoelastic materials falls between elastic and viscous behaviours, only part of the stored energy can be recovered after the load removal and the other part is dissipated in the form of the thermal energy. Thus, for viscoelastic materials, the phase shift between stress and strain is always less than $\pi/2$ radians (Figure 1.3c). Additionally, larger phase angle shift is more effective for damping the unwanted vibration when the viscoelastic treatment is implemented [6].

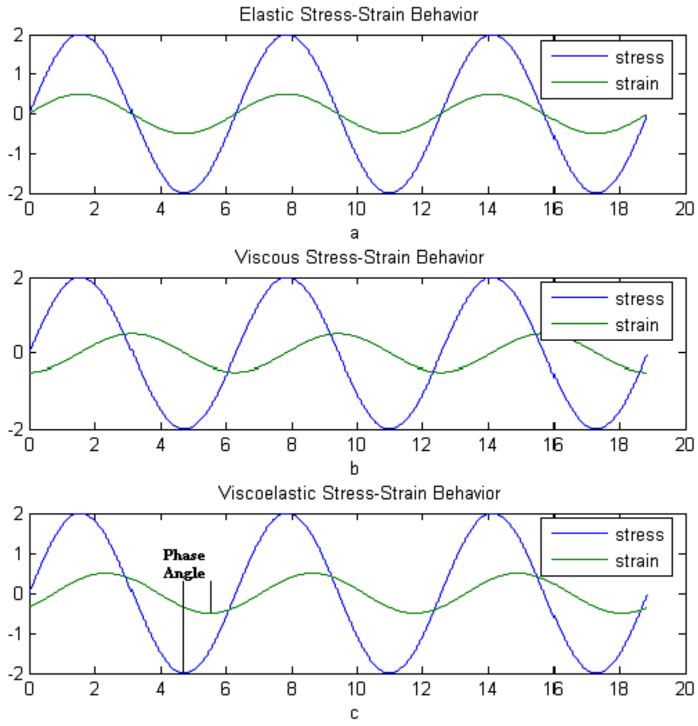

Figure 1.3. a) elastic stress-strain behaviour; b) viscous stress-strain behaviour; c) viscoelastic stress-strain behaviour [6]

Generally, there are two basic configurations for viscoelastic damping implementation as shown in Figure 1.4. The vibratory energy is dissipated due to direct strains in the case of unconstrained viscoelastic materials and predominantly by shear strains in the constrained viscoelastic materials [7].

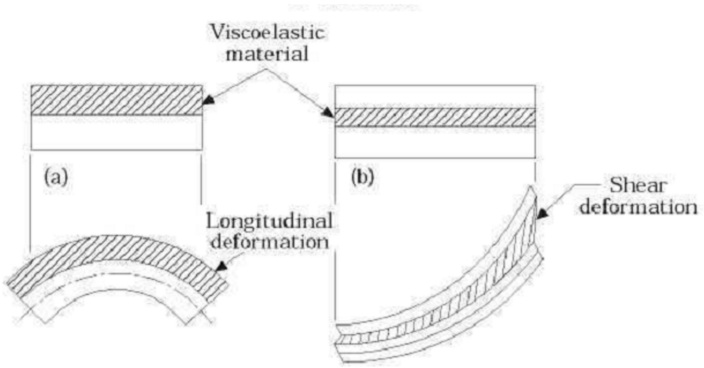

Figure 1.4. Basic configurations for viscoelastic damping: (a) unconstrained and (b) constrained treatment [7].

Ghoneim [8] combined the constrained layer damping with shunted piezoelectric to investigate the dynamic characteristics of cantilever beam. The effects of storage modulus ratios, material loss factors, thickness ratios and the axial location of the proposed electromechanical surface damping (EMSD) element were considered with finite element algorithm. The effectiveness of the EMSD technique for controlling the first two resonances of the cantilever beam has been demonstrated.

Due to the material, packaging, weight and cost constraints in practical applications, partial layer damping treatments were developed. Sometimes, it can be as effective as a complete treatment if the correct implemented areas are targeted. Kung and Singh [9] presented a method for analyzing the harmonic responses of sandwich beams which is either fully or partially covered with multiple constrained layer viscoelastic patches. The effects of patch boundary conditions, patch cutouts and locations and mismatched patch combination were analytically and experimentally studied.

Hu and Huang [10] derived a generally analytical method for a three-layer sandwich structure with viscoelastic core to obtain the flexural response and bandwidth damping analysis, which can be applied to the structure with constrained layer damping (CLD) as well. From the investigation of core thickness, authors concluded that before reaching a certain core thickness value, increasing the core thickness or viscoelastic materials thickness yield better damping effects, whereas further increasing gives worse damping if it exceeds that value. It is therefore expected that there is optimal combination of core layer and viscoelastic material thickness as the provided total thickness is constrained.

Since it has been proved that higher damping ratios could be obtained through the use of multi-damping for vibrating plate at the expense of adding considerable weight, the viscoelastic layer damping treatment is limited for many applications where the weight is critical design parameter, especially for low frequencies. To overcome this disadvantage, Park and Baz [11] investigated the damping performance of active constrained layer damping (ACLD) treatments (Figure 1.5) for controlling the first two bending modes of plates using proportional and derivative control laws. The ACLD is achieved by either replacing or augmenting the constrained layer with an active element, usually a piezoceramic layer. Theoretical investigation based on finite element model was experimentally validated at various operating temperatures. The obtained results indicated that the ACLD treatment is a more effective mean for damping structural vibrations particularly over wide temperature and frequency ranges compared with conventional passive constrained layer damping (PCLD) since it combines the attractive attributes of both the passive and active controls to produce lower amplitudes of vibration. It is also observed that increasing the control gain has resulted in improved attenuation characteristics of ACLD treatment. The ACLD damping method was then extended for nonlinear vibration control of a simply supported beam by Ray and Baz [12]. Since the viscoelastic layer was constrained by a piezoelectric constraining layer, the shear of the viscoelastic layer can be enhanced when the piezoelectric layer operate actively, which resulted in improved damping characteristics. From the numerical comparison with PCLD based on von Kármán type large deformations, the ACLD treatment enhances the damping and has been proved as an effective method for nonlinear vibrations control as well.

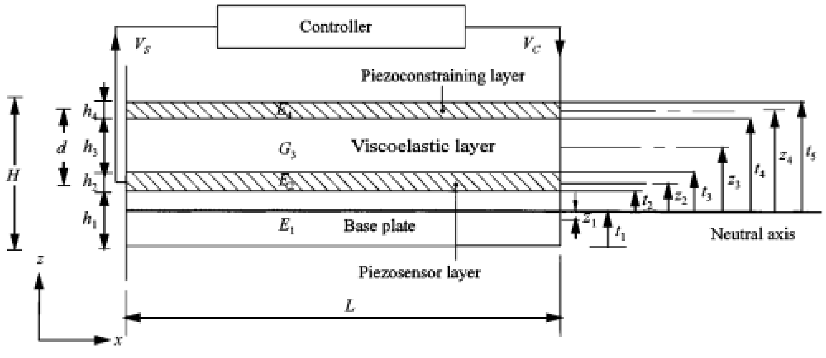

Figure 1.5. Schematic drawing of the plate/ACLD system. [11]

Chantalakhana and Stanway [13] concerned with a clamped-clamped aluminium plate to control both the bending and torsional vibrations. A model-based approach for control design was involved to minimize the amount of control hardware required whilst avoiding spill-over problems which are liable to degrade the control performance. Passive constrained damping layer was also investigated for comparison. It was found that only higher modes benefit significantly from the introduction of passive constrained damping layer. Moreover, the numerical and experimental results showed that with the active control, the first two modes were attenuated without incurring problems due to spill over.

Moreover, the damping effects of fiber-reinforced composite materials, ply angle of compliant layers, location of viscoelastic layers were discussed by Zhang and Chen [14] with finite element method. From their research, it has been proved that the damping performance of the fiber-reinforced composite materials is concerned with the fiber orientation and mode shapes. The flexural modulus of the compliant layers is reduced with increasing of ply angle, the rate of shearing and energy dissipation in the damping layer. Furthermore, separated placement of damping layers in the vicinity of mid-plane of the beam will be beneficial to improve the damping characteristics.

Substantial researches showed that viscoelastic damping can be used for vibration and noise control, especially for higher frequency and moderate temperatures (below 500° F). However, for lower frequency modes, it usually requires additional control scheme or the technologies associated with smart materials to enhance the damping effectiveness. Besides, at low and high temperatures, their performance is poor. Generally, the characteristics of viscoelastic materials are dependent on several factors such as dynamic excitation, temperature and strain rate. Moreover, these damping materials also exhibit nonlinear dynamics over some range of the aforementioned dependencies and gradually lose their effectiveness with time, thus requiring periodic inspection and replacement.

1.2.2. Particles damping system

Impact dampers [15] with advantages of ruggedness, reliability and insensitiveness to extreme temperatures, are simple and efficient passive devices used to reduce the vibration of attached primary system by the exchange of momentum and dissipated energy during the impact between solid particle and system. However, during the impact, the high-level accelerations and the significant contact forces can cause material deterioration and high noise levels. Additionally, the performance of single-mass impact damper may become sensitive to the coefficient of restitution, level and frequency of the excitation, as well as the container dimension, which result the potentially more efficient particles damping systems proposed in the mid 1980s. As a derivative device, the solid particle in the container of an impact damper is usually replaced by metal or ceramic particles or powers of smaller size (~0.05-5mm in diameter). Metal particles of high density such as lead or tungsten steel (Figure 1.6) are the most common materials for better damping performance [16]. Different from the viscoelastic materials which dissipate the stored elastic energy, particle damping treatments suppress the vibration by collision, friction and shear damping which involves the potential of energy absorption and dissipation through momentum exchange between moving particles and vibrating walls, friction, impact restitution and shear deformations.

(a) lead particles (b) tungsten carbide particles

Figure 1.6. metal particles as damping materials [16]

The behaviours of a particle damper under harmonic excitation were investigated by Papalou and Masri [17]. The effects of various system parameters including particle size, container dimensions, intensity and frequency of excitation were studied using SDOF model. It is found that compared with single particle damper, considerable improvements are gained with respect to reduction of interface material deterioration, high noise levels and sensitivity of the particle damper effectiveness to the size of the container and to the amplitude of the excitation.

Fowler *et al.* [18] developed an analytical method based on particle dynamics method which has then been incorporated into a comprehensive particle damper design methodology. Since the effectiveness of particle dampers is based on relatively large number of system parameters whose effects may be confounded, for instance the particle size and number, coefficient of friction, external excitation etc, analytical sensitivity studies were performed on a cantilever aluminium beam with various particle dampers attached to the beam tip. The results indicated that the coefficient of friction has a differing effect on single and multiple particle dampers at least in the studied cavity configuration and excitation case. For the single dampers, increasing the coefficient of friction tends to increase the damping; while for the particle dampers, increasing the coefficient of friction appears to have little damping effect, even a slight adverse effect. In addition, for single particle dampers, orienting the dampers such that gravity is in the direction of the vibratory motion tends to reduce the damping; the orientation of gravity appears to have much less effect on multiple particles dampers. Moreover, increasing the mass tends to increase damping. Conversely, decreasing the mass tends to reduce damping. The authors also pointed that at times, both single and multiple particle dampers may cause random, somewhat chaotic behaviour of the damped system.

Xu *et al.* [19] presented a numerical model which can capture the dominant mechanisms of particle damping, including energy dissipation by impact and friction during inter-particle and particle-wall collisions and by shear action due to strain gradient in the longitudinally packed particles. The nonlinear properties of particle damping and the relative effectiveness of these damping mechanisms in terms of a host of parameters such as particle size, packing density, frequency and amplitude of excitation can be characterized by this experimentally validated model. From the numerical and experimental investigation of a free-free beam of a constant cross-section with longitudinal particle holes, some specific observations were pointed out. The particular particle dampers are better suited for higher frequency range. Although it is nonlinear, energy dissipation is achieved within a broadband range. Moreover, the shear friction is determined to be the major contributing mechanism, especially at a high volumetric packing ratio near or at 100%. The authors [20] also pointed that since the beam is drilled, some torsion mode is excited under random excitation and longitudinal particle dampers has no effect for suppression the torsional vibration in their study. The particle damping treatment has also been extended to plate. The experimental results obtained from plate case confirmed that the damping performance of the particles is remarkably high especially in a high frequency range, while for lower resonance frequencies, the damping effect is not as high as usual. Furthermore, different arrangement of filling patterns has different damping performance.

Partical impact damping with different materials, particle sizes, clearances and the number of particles implemented on a cantilever beam were measured by Marhadi and Kinra [21]. Lead spheres, steel spheres, glass spheres, tungsten carbide pellets, lead dust, steel dust and sand were used for investigation. In their work, the relative motion between the particles is neglected and the static deflection due to gravity is no longer a constant. It is also assumed that the particles are in contact with the enclosure at velocity peaks. Within the confines of tested materials, it may be concluded that for a small number of particles, the materials affects the particle damping, whereas the effect of material seems to disappear as the number of particles increases. Corresponding experimental results indicated that a more advanced model of particle impact damper must include the size and the number of particles as additional independent parameter.

The roles of friction and inelastic collisions, as well as the wall effects during transient vibration of piston-based thrust dampers and box-based vibration dampers (Figure 1.7) were investigated by Bai *et al.* [22] with simulation. The comparison indicated that higher friction coefficient does not always result in better damping performance. It is sensitive to the friction coefficient under certain conditions such as box geometry, vibration frequency, excitation amplitude, material properties. Moreover, it has been found that the overall particle damping performance depends on both energy transfer and energy dissipation capacity. Since the two processes are not correlated, either one can become the limiting step. Depending on which one is the limiting step, the damping performance may or may not be sensitive to the friction coefficient. Therefore, although the wall is not very important for energy dissipation, it plays an essential role in energy transfer.

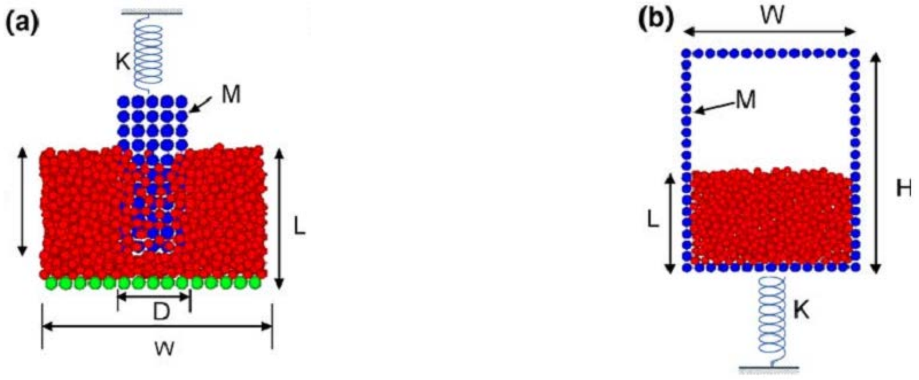

(a) piston-type damper (b) box-type damper

Figure 1.7. Two types of particle dampers [22]

Lu *et al.* [23] presented the concept of 'effective momentum exchange (EME)' to quantify the influence on the performance of particle dampers. Effects of a large number of system parameters were also evaluated using discrete element method. It is shown that a higher EME results in a better reduction. From their study, it is concluded that for the same size mass ratio, particle impact damping is insensitive to the type and size of particles, while for small size of the container, responses of the particle damper with a large number of particles are higher than that with small number of particles. Increasing the mass ratio of particles can reduce the response of the primary system, but the reduction is not directly proportional to the increase in mass ratio. Furthermore, the level of excitation plays a very important role. As the level of excitation increases, the efficiency of the damper increases. However, when the excitation is high enough to mobilize all the particles, the response amplitude becomes independent of the intensity of the excitation. Moreover, the effectiveness of the damper increases as the primary system damping decreases.

Particle damping becomes an attractive vibration control treatment due to its conceptual simplicity, potential effectiveness over broad frequency range, degradation insensitivity and low cost. It also has high resistance to temperature and corrosion, which can be used in harsh environments or semiconductor industry [24]. Nevertheless, it depends on several system parameters, which leads to difficulties for numerical prediction and optimization.

1.2.3. Tuned dynamic devices

Tuned dynamic devices are damping systems which utilize a secondary structure attached to a vibrating system to achieve mechanical to mechanical energy conversion or transformation. The difference from the aforementioned particle dampers is that the dynamic characteristics of secondary mass relate closely to that of the primary structure. By tuning the mass ratio, frequency ratio and damping ratio, a certain amount of damping can be produced. Generally, the tuned dynamic devices can be divided into two categories: tuned vibration absorber (TVA) and tuned mass damper (TMD). The former device producing an equal and opposite reaction force at its base and ideally bring its attachment point to the rest position is particularly appropriate when the vibration/noise issue occurs for single frequency, or across a very narrow frequency range. The latter device is always designed for suppressing the vibration of the host structure over a relatively wide frequency bandwidth by increasing the damping loss of the system. These devices have been widely investigated for suppressing the vibrations or seismic responses of structures since it was first proposed by Frahm [25]. In order to improve the performance of vibration absorber and/or damper, a flurry of optimization studies have been reported.

Marano *et al.* [26] proposed a robust optimal design criterion for a single TMD device, which is different as the conventional approach based on implicit assumption that all parameters involved are deterministically known. Not only mechanical parameters but also the input spectral contents were considered to be affected by uncertainty in their study. The covariance displacement of the protected main system subjected to stochastic dynamic loads was adopted as deterministic objective function and its mean and standard deviations were minimized. Robustness was investigated and compared with a conventional approach, which showed that the proposed robust approach induced a significant improvement in performance stability. Furthermore, the robust based design optimization problems for tuned mass dampers in fuzzy environments were also formulated and resolved by this research group [27]. The protected systems subjected to random vibrations were analyzed to extend the applicability of the proposed methodology to general dynamic loads. Fuzzy variables were included both in structure system and dynamic loads to take into account also epistemic uncertainties. In their recent work [28], a more complete approach was proposed and the parameters such as TMD stiffness, damping and mass ratio were optimized. Two different optimizations criteria which minimize the main system displacement or the inertial acceleration were investigated by a single degree of freedom model subjected to a coloured stationary white noise. Narrow, medium and broad band spectral contents were used. Results showed that considering the mass ratio as design variable are more efficient compared with those obtained without it. Besides, acceleration criterion presents optimal mass ratio greater than any practical application, while the displacement criterion presents some interesting ranges of application without a too great mass ratio.

Zuo and Nayfeh [29] proposed a minimax method which is used to maximize the minimal damping in a prescribed frequency range for general viscous or hysteretic multi-degree of freedom (MDOF) tuned mass systems. The efficiency of this method and the damping potential of MDOF tuned mass dampers were discussed by illustrative examples. Comparison with the H_2 and H_∞ approaches showed that the minimax algorithm generally yields more damping than the other two methods. Moreover, experimental results on a free-free beam showed that a MDOF TMD can be designed to provide higher damping in the first three flexural modes than that attained by multiple SDOF TMDs at the same location and of the same total mass. Furthermore, the authors [30] proposed that more than one mode of vibration of an absorber body relative to a primary system be tuned to suppress single-mode vibration of a primary system. The responses to random and harmonic excitations were also minimized by H_∞ and H_2 optimization. They pointed that a two-DOF absorber can attain better performance than the optimal SDOF absorber. Additionally, with properly chosen connection locations, the two-DOF absorber achieves better vibration suppression than two separate absorbers of optimized mass distribution.

Krenk and Høgsberg [31] concerned with the TMD under stationary wide-band stochastic case. They obtained simple approximate but accurate expressions for the response variance of a structure with initial damping in terms of both mass and damping ratios. It was demonstrated that while the exact optimal frequency tuning under random load is different from the classical tuning for harmonic load, the influence of this difference on the resulting response variance will be negligible in most cases if the applied damping is optimized. It was also pointed that the applied damping can be optimized in terms of the mass ratio alone, without influence from the structural damping.

Hoang *et al.* [32] optimized a TMD for SDOF structure under seismic loads. They found that with large mass ratio, performance of an optimal TMD is not too sensitive to uncertainty in its parameters and is recognized to be robust with respect to the deviation in the structural properties. Generally, optimal TMD has lower tuning frequency and high damping ratio with increasing mass ratio. The characteristic ground frequency has strong influence on the optimal tuning frequency than the optimal damping ratio of TMD.

Bekdas and Nigdeli [33] used a revised metaheurestic optimization method named harmony search to optimize the parameters of TMDs including mass, stiffness and damping. From the comparisons with several other documented methods by Matlab program, it was shown that the new approach was more effective and more feasible due to smaller TMD parameters.

A closed-form optimum design formula of vibration absorbers for linear damped systems subjected to random loads was provided by Tigli [34]. Minimizing the variance of the displacement, velocity and acceleration of the main mass were considered. Author pointed that for specific applications where all of the response parameters are desired to be minimized simultaneously. The design based on velocity criterion provides the best overall performance with the least complexity in the design equations.

From numerous researches, it has been shown that TMDs can achieve good performance in vibration control. However, it is very sensitive to tuning frequency ratio, even when it optimally designed. To overcome this disadvantage, multiple TMDs were proposed and investigated. The dynamic characteristics and effectiveness of multiple mass dampers (MMDs) with distributed natural frequencies, under random loading were reported by Kareem and Kline [35]. The parameters such as frequency range of MMDs, damping ratio of individual dampers and the number of dampers were optimized. It was found that a MMD with an optimal frequency range are more effective than a single TMD for a wide range of damping. The frequency range of MMDs is the most important parameter as it influences their robustness and effectiveness. The damping ratio and total number of dampers play a secondary role in the design of MMDs. Moreover, MMDs offer the advantages of portability and ease of installation since the size of an individual damper is reduced.

Zuo and Nayfeh [36] formulated the stiffness and damping of each TMD optimization as a decentralized H_2 control problem and proposed an efficient numerical algorithm. The effects of the mass distribution, number of dampers, total mass ratio, and uncertainties in system parameters were studied. The numerical results showed that larger mass ratios lead to smaller RMS responses. In addition, increasing the number of TMDs yields obviously better robustness to uncertainties in the natural frequency and damping of the primary system, though the benefits diminish as their number becomes very large. Decentralized H_2 and H_∞ control methods were also adopted to optimize the parameters of spring stiffness and damping coefficients for random and harmonic vibration of a new series multiple TMDs system by Zuo [37]. It was found that the series multiple TMDs are more effective and robust than the classical TMD, parallel multiple TMDs and multi-DOF TMDs. Unlike the parallel multiple TMDs, the optimal mass distributions among absorbers in series TMDs are far from the case of equal masses. Moreover, the series TMDs are also less sensitive to the parameter variance of the primary system than other TMDs.

The effectiveness and robustness of double tuned mass dampers (DTMD) for reducing the vibration under ground acceleration has been investigated by Li and Zhu [38]. The minimization of the minimum values of the maximum dynamic magnification factors (DMF) of the DTMD were used as optimization criterion for parameters selection. The comparison with TMD and MTMD systems showed that DTMD is an advanced control device since it performs significantly better than the TMD and MTMD in the robustness to the natural frequency tuning.

Except the investigations under harmonic or ground excitation, the multiple TMD system has also been used for damping the vibration induced by moving loads [39]. Compared with the single TMD system, the multiple TMDs have advantages of a wider effective frequency band and less sensitivity to tuning frequency, whereas it can not be retuned in real time, thus allowing the development of adaptive TMD systems.

Bonello *et al.* [40] [41] proposed an adaptive tuned vibration absorber (ATVA) with variable stiffness (Figure 1.8), which has the capability of retuning itself in response to a time-varying excitation frequency and can effectively control the vibration over a wide range of frequencies. In this absorber, the stiffness is varied by adjusting the curvature of piezoelectric actuated parallel curved beams. This design principle was illustrated using elementary analysis that neglected nonlinearities and the effect of the inertia of the beams. Theoretical and experimental results demonstrated the efficiency of this ATVA design in vibration control, particularly with respect to its agility in tracking rapidly varying forcing frequencies.

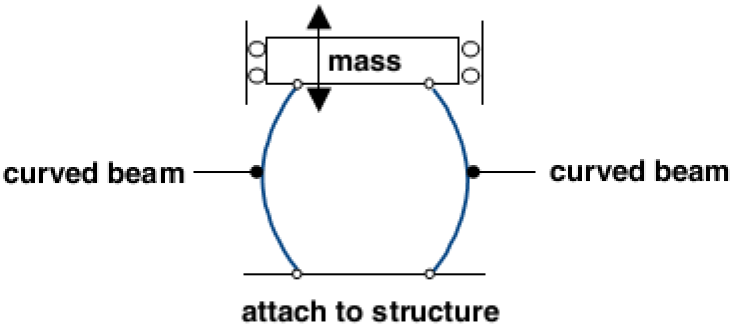

Figure 1.8. Vibration absorber with a stiffness element formed from parallel curved beams [41].

Another adaptive tuned mass damper whose stiffness and damping can be tuning in a real-time consisted of a tuned mass, a tuned passive spring and a magnetorheological (MR) damper as shown in Figure 1.9 has been presented by Weber *et al.* [42]. For this adaptive TMD, the friction-viscous damping and stiffness are controlled by the MR damper which is connected in parallel to the stiffness of passive TMD spring. Simulation results demonstrated that at the nominal frequency the adaptive TMD provides same reduction of steady state vibration amplitudes in target structure as passive TMD. However, at different frequencies, the adaptive TMD outperforms the passive TMD.

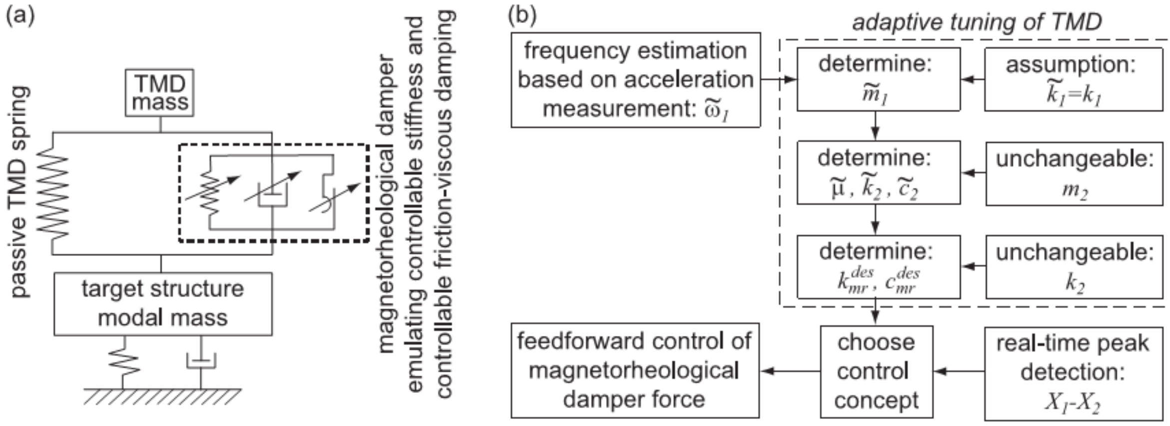

Figure 1.9. (a) An adaptive TMD with a controlled MR damper (b) flow chart [42].

In addition to previous introduced designs and optimizations of TMD systems, the superior effective performance and adaptiveness can also be achieved by alternative approaches such as combining the dynamic vibration devices with active or semi-active control techniques.

Hrovat *et al.* [43] proposed a semi-active TMD. Numerical simulations indicted that the semi-active TMD can achieve significant improvements with respect to conventional passive TMDs. Furthermore, they also found that the control performance is comparable to active system, while being less complex and requiring low energy.

Cunefare *et al.* [44] proposed a state switched absorber which has the ability to adaptively modify its resonance frequency instantaneously such as changing its stiffness by implementing piezoelectric elements and, thus can obtain vibration reduction over broader frequency range. The simulations were presented by a single state switch absorber model for base excitation with two harmonic spectral components. The results clearly indicated that SSA has the potential for performance gains compared with classical tuned vibration dampers and the relative performance will be a function of the mass ratio, forcing frequency spacing and amplitude, level of damping, etc.

Davis and Lesieutre [45] described a piezoelectric based vibration absorber which can tune its resonance frequency by using a ‘ladder’ external capacitive shunt circuit. It is pointed that the number of discrete capacitance values used in a specific application depends on the overall size of the frequency tuning range, the intrinsic damping of the absorber and the acceptable deviation from minimum response. Analyses and experimental results showed that 10 *dB* average improvements in vibration reduction across the tuning range compared with a pure passive absorber tuned to the centre frequency, with additional benefit extending beyond the tuning range.

The dynamic behaviours of multi story building equipped with a new semi-active TMD and active TMD (ATMD) suffered from E1 Centro and Kobe earthquakes respectively were compared numerically by Owji *et al.* [46]. This new semi-active TMDs called "SADA—TMD" which is a TMD with semi-active damper actuator. From the simulated responses, it was clear that the power required by SADA-TMD is significantly lower than those of ATMD. Furthermore, it has a great ability to subside structural displacement.

Jalili and Knowles IV [47] proposed an active resonator absorber (ARA) which consisted of a passive absorber and a PZT actuator. For applying active operation, the compensator parameters were designed and implemented through adjusting the external electrical voltage applied to PZT. The effectiveness and stability were demonstrated through numerical simulations and experimental results. An auto-tuning procedure was used to enable total vibration suppression even when the system parameters vary over time.

The dynamic analyses and parameters optimizations of both passive and active piezoelectric dynamic vibration absorbers were numerically and experimentally studied by Kim *et al.* [48]. Optimizations of passive absorbers implemented RL parallel shunt circuit and the active absorber implemented by feeding back the acceleration of the structure through a second-order low pass filter were investigated.

A hybrid vibration absorber (HVA) was proposed by Tso *et al.* [49] for suppressing stationary random vibration in flexible structures. This HVA has a rotational spring in form of a small thin beam with a lumped mass fixed at the free end of the beam. Piezoelectric elements were used as actuator and feedback sensor. Damping performances were simulated on a beam. The results showed a superior performance on global suppression of broadband vibration in comparison to other published designs of passive and hybrid vibration absorbers.

Tuned dynamic device is extensively utilized and investigated in civil/industrial sections due to its attractive control performance and simplicity. It can also be designed and optimized for damping nonlinear vibrations [50] [51] [52] and combined with smart materials such as magneto-rheological/piezoelectric materials to improve the adaptiveness and control performance in broadband vibration. Except the previously introduced dynamic devices, other variations or derivatives such as tuned liquid column damper [53] and tuned sloshing water damper [54] have been presented as alternative approaches for reducing winds induced vibration and seismic vibration under earthquakes.

1.2.4. Intelligent/smart damping systems

Along with the development of intelligent/smart materials, intelligent/smart systems have attracted lots of attentions since these systems possess artificial intelligence features. Generally, the smart materials including electrorheological (ER) fluids, magnetorheological (MR) fluids, magnetostrictive materials, electrostrictive materials, shape memory alloys (SMA), piezoelectric materials etc. act in a unique way which couple at least two of the given fields as shown in Figure 1.10 to provide the required functionality: mechanical, electrical, magnetic, thermal, chemical and optical [56]. Because of the coupling properties of these materials, they can sense and respond to the environmental conditions in useful manners, which allow extensive implementation in vibration control systems.

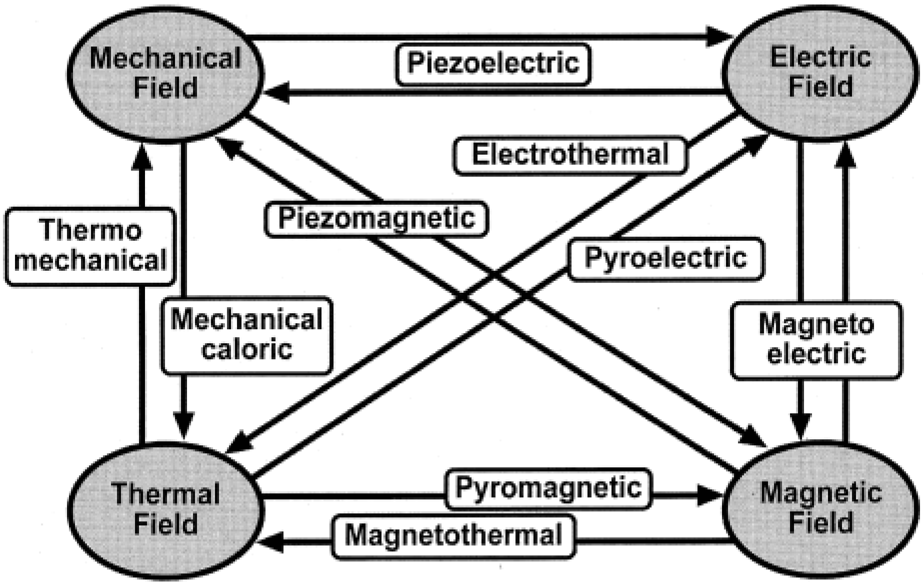

Figure 1.10. Coupling between mechanical, thermal, electric and magnetic fields in smart materials and structures [55].

ER fluids and MR fluids are smart materials with controllable rheological properties, which have capability of undergoing a rapid and dramatic change in their rheological properties in the presence of an external field. They are classified as electrorheological (ER) or magnetorheological (MR) fluids according to the applied electric or magnetic fields and made by mixing fine particles into a liquid with low viscosity. When an electric field or a magnetic field is applied, the particles can instantly respond by transforming from liquid to chain-like structures which results in enhancement of apparent viscosity and allows increasing the strength of the material within a few milliseconds. When the electric or the magnetic field strength reaches a certain value, the suspension will be solidified and has high yield stress; conversely, the suspension can be liquefied once more by the removal of the applied field. These features provide simple, quiet, rapid-response interfaces between electronic controls and mechanical systems. Usually, there are two approaches to use ER/MR fluids for vibration control: replacing conventional viscoelastic materials by the ER/MR fluids for structures with small size and thickness or utilizing the ER/MR mounts/dampers for relatively large or complicated structures.

Phani and Venkatraman [57] experimentally investigated the behaviour of a sandwich beam with ER fluid acting as the core material. Since the ER property is influenced by environmental temperature, humidity, particle size, shape, concentrations of the fluids and additives, these influences and their effect on ER activity and overall stability of the colloidal suspension were taken into consideration. It was proved that ER fluids hold significant potential for improving damping properties of structural elements. Moreover, the improvements in damping properties further depend upon the amplitude of excitation and the particle concentration. They pointed that higher concentration of particles leads to the formation of stronger chain network and hence increased damping. However, an upper limit exists which is governed by the stability considerations of the colloidal suspension.

Kumar and Ganesan [58] studied the damping behaviours of a hollow sandwich box column with a viscoelastic/electrorheological/magnetorheological fluid core layer with the clamped-free boundary condition. Effects of the core thickness, electric voltage and magnetic field were investigated. The damping performances of a clamped-free composite sandwich box column containing viscoelastic layer (VEL) or ER fluid core with constraining layer using finite element based on modal strain energy method were also compared by Ramkumar and Ganesan [59]. According to the analytical results, it can be observed that as the applied electric field increases, the natural frequency of the sandwich box column increases. Additionally, the modal loss factor of the composite sandwich column plays an important role on the stability of the damped structures. Hence, ER materials can be used to improve the stability of various mechanical devices.

Rajamohan *et al.* [60] compared the suppression performances of full-state and limited state flexible mode shape (FMS)-based controllers for free and forced vibration of a cantilever beam fully and partially treated with the MR fluid (Figure 1.11). The deflection responses of the beam using FMS based control method evaluated under an impulse and a white-noise force confirmed the effectiveness of the FMS-based limited state controller. It is also observed that the partially-treated beam with MR-fluid concentration near the free end yields vibration responses comparable to the fully treated beam.

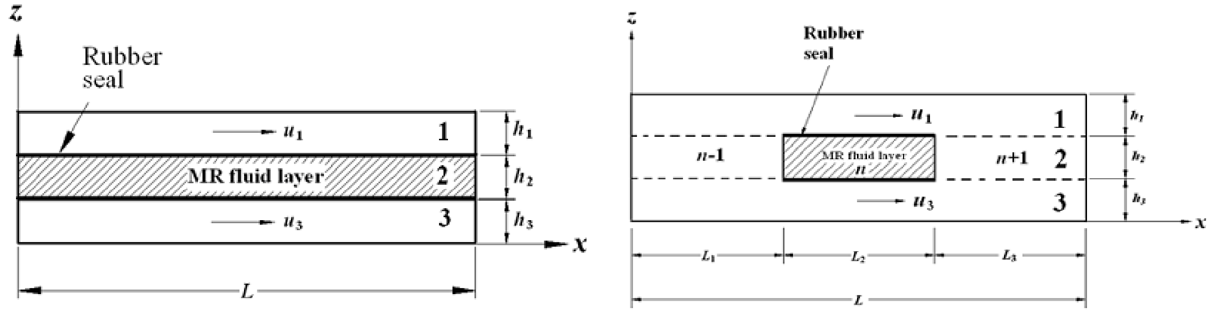

(a) (b)

Figure 1.11. (a) Fully treated MR sandwich beam. (b) Partially treated MR sandwich beam [60]

The ER mounts/dampers/absorbers used for vibration control can be classified as flow mode, shear mode and squeeze mode types. For the flow mode, it is assumed that two electrodes are fixed, and vibration control is achieved by controlling the flow motion between the electrodes. In shear mode, it is usually assumed that one of the electrodes is free to translate or rotate relative to the other and hence vibration control is achieved by controlling the shear force between them. For the squeeze mode, the electrode gap is varied and the ER fluid is squeezed by a normal force [61]. Hong *et al.* [61] designed a squeeze-mode electro-rheological (ER) mount for controlling the high-frequency (up to 80Hz) responses of frame structure. Experimental results showed that the displacement and acceleration can be reduced substantially by activating the ER mounts using the optimal controller. In this study, authors also pointed out that the MR fluid mounts can be designed using a similar scheme. Since the yield stress of MR fluid is higher than that of the ER fluid, MR mounts can be devised smaller.

Lim *et al.* [62] concerned with the design and application of an ER fluid damper synthesized with a semiactive artificial intelligent (AI) feedback controller which is usable at any constant speed with no negative effects for controlling the vibration of rotor systems. The computed and experimental results coincide well in the trends and showed excellent robustness and control performance in practice.

As mentioned in the last section, the parameters of dynamic absorbers are constant, which leads to tight frequency range of efficiency. Particularly, semi-active devices with smart fluids offer excellent potential for achieving control of vibration over a broad frequency range with only minimal external power. The controllable change of state with some desirable features, such as high strength, good stability, broad operational temperature range, and fast response time, gives rise to vibration control applications. In order to reduce the torsional rotor vibrations with variable speeds, an electrorheological dynamic torsional absorber, called smart ER dynamic absorber has been designed and experimentally observed by Sun and Thomas [63]. Experimental results and simulation results based on a nonlinear empirical model showed that the ER dynamic absorber exhibits very good performance in torsional rotor vibration control.

Even though both MR and ER fluids typically exhibit similar viscosity in their non-activated state, the MR fluids exhibit a much greater increase in viscosity when activated and need relatively low power compared with the ER fluids. Lai and Liao [64] investigated the vibration characteristics of the MR suspension system with perturbation by employing a sliding mode controller. The performances of the suspension system under bump input and random input cases were evaluated through computer simulation.

Yao *et al.* [65] presented a MR damper for semi-active control of vehicle suspension systems. The vibration responses of the suspension system over random road excitation were compared numerically and experimentally with passive suspension. Corresponding results showed that the MR damper has a very broad changeable damping force range under magnetic field and the damping coefficient increases with the electric current, but decreases with excitation amplitude. Moreover, the MR damper will become saturated as the applied electric current reaches a certain value. It also pointed that the semi-active control strategy is superior to both the passive control and the constant control strategies.

Rashid *et al.* [66] reported the design and the manufacture of a new MR damper based on an electromagnetic coil and described the optimization criteria. Laboratory tests and numerical simulations of this study clearly showed that the damping coefficient could be increased up to three times when the exciting current inside the coils is around 1 A, which indicated that the MR damper can operate over a wide range and is adequate for vibration control.

In order to attenuate unwanted vibration of the flexible structure system, Choi *et al.* [67] proposed a semi-active MR mount associated with the linear quadratic Gaussian (LQG) controller which consists of linear quadratic regulator (LQR) and Kalman-Bucy filter (KBF). Experimental implementation and control performances were evaluated, which confirmed that the semi-active MR mount can be effectively utilized to the vibration control of various structural systems.

Shape memory alloys (SMAs) are a class of novel smart materials that possess unique properties, including shape memory effect, superelasticity effect, extraordinary fatigue resistance, and high corrosion resistance and damping characteristics, which make them perfect candidates for applications in seismic resistant design and retrofit of structures. They have unique capability to restore their original shape after being deformed excessively to a strain. This feature lies in the ability of the SMA to transform from the parent phase (austenite), which is microstructurally symmetric to the less symmetric martensitic phase and revert back either by heating or by simply removing the load which caused the phase transformation. Based on the manufacturing process and chemical composition, a SMA could be categorized as either austenite which is also known as martensite or superelastic. As shown in Figure 1.12, the stress-strain behaviour of superelastic SMAs could be divided into linear austenite, phase transformation and linear martensite. It can be found from the figure that superelastic SMAs possess several characteristics that make them ideal for seismic applications including hysteretic damping, recentering capability (i.e. ability of the material to return to its undeformed configuration upon unloading), ability to undergo strain hardening at large strain levels (>6% strain), and the formation of stress plateau during phase transformation which controls the forces transmitted to the structure [68].

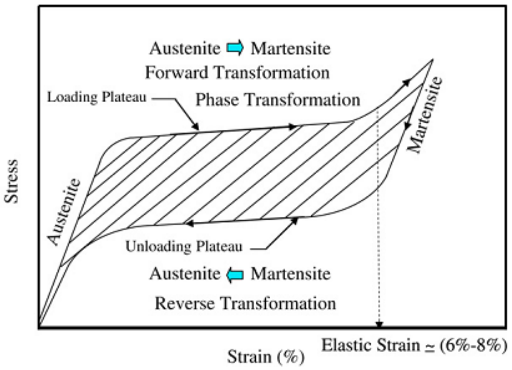

Figure 1.12. Typical stress-strain relationship of superelastic SMAs [68].

Sharabash and Andrawes [68] investigated the performance of a new passive seismic control device for cable-stayed bridges. The effectiveness of the shape memory alloy dampers in controlling the deck displacement and limiting the shear and bending moment demands on the bridge towers was assessed. In addition, the effect of variability in the SMAs hysteretic shape on their effectiveness as dampers for cable-stayed bridges was also addressed in their work. They concluded that SMA dampers are able to reduce the maximum bridge displacement, towers base shear, and tower base moment of the reference bridge. Increasing the number of the SMA dampers would improve the overall bridge performance with an extent that depends on the distribution of the dampers between pier and tower connections. Sensitivity study showed that on average, the variation of the SMAs strain hardening during phase transformation and hysteretic width affects the maximum deck displacement response. The variation in the SMAs strain hardening has a minor effect on the tower base shear and bending moment. However, the SMAs hysteretic width has more pronounced effect on the tower base shear and moment in the range of 10%~12%.

Zuo *et al.* [69] designed a SMA damper which is used to control the vibration of a practical cable under white noise excitations on the basis of Hamilton principle and linear quadratic regulator (LQR) active control algorithm. Numerical comparison showed that the optimum SMA damper achieved same control effectiveness as the LQR active control method.

Qian *et al.* [70] presented two case studies of structural seismic vibration control using SMAs. Experimental investigation showed that SMAs can improve the mechanical properties of concrete members. Moreover, a hybrid SMAs friction device (HSMAFD) which consists of pre-tensioned superelastic SMA wires and friction devices presented for structural dissipation has been proved as an effective method in reducing horizontal response of structures subjected to strong seismic excitation.

Significant advantages of SMA wires in comparison to other type of actuators are the relatively low voltage to generate a displacement, larger recovery force generated per unit volume by phase transformation, small size, high output excitation actuation for vibration control, its large displacement, the complete recovery deformation, high stiffness and electrical heating, which leads to extensive use as actuators in vibration control systems. Suzuki and Kagawa [71] demonstrated the feasibility of using shape memory alloys (SMAs) as actuators to control the bending and torsional modes of a flexible cantilever beam. In their work, two SMA actuators were arranged parallel to each other and inclined with respect to the beam, with each SMA controlled in a push-pull manner by restricting the control voltage during only the contraction process of the SMA. In their study, authors focused on three issues in designing a control system. Firstly, the system should control the vibrations to as high a frequency as possible. Secondly, the system should simultaneously control the bending and torsional modes using a minimum set of SMA actuators. Thirdly, the SMA should not be heated to exceed the modelled deformation. Corresponding results indicated that the controller significantly dampens both the bending and torsional modes. The calculated and experimental results agree reasonably well, verifying the effectiveness of the developed control system.

Dhanalakshmi *et al.* [72] developed an experimental platform which can analyze and control the vibration of a SMA actuated and piezoelectric sensed flexible beam. On/off controller, proportional plus integral (PI) controller and proportional (P) controller have been designed and implemented. Experimental results showed that the closed loop response obtained with these control schemes exhibit substantial reduction in the amplitude of flexural vibration at its first mode resonance.

Zhang *et al.* [73] designed a general scheme for SMA intelligent structures. Different physical quantities as a feedback signal were investigated in their study. Numerical analyses using ANSYS showed that using strain as a feedback signal is more suitable in a small amplitude vibration control.

An indirect intelligent sliding mode controller (IISMC) which manipulates applied voltage in order to alter SMA tendon temperature to track reference bending angles was introduced by Hannen *et al.* [74]. A hysteretic recurrent neural network (HRNN) which can map temperature (instead of voltage or current) to bending angle, ensuring rate independence and precise mapping when reference trajectories are unknown was presented in their study. Experimental validation of the developed controller was conducted on the flexible beam, which proved the control strategy provides robustness to model uncertainties and parameter variations.

Majewska *et al.* [75] used magnetic shape memory actuators which are ferromagnetic materials exhibiting large changes in their shape and size under an applied magnetic field for controlling, altering and tuning the forced vibration of a rotor. Experimental results confirmed the capability of magnetic shape memory actuators for vibration reduction and vibration control in the case of rotor systems.

Another type of smart materials named piezoelectric materials have capability to couple the electrical field and mechanical field, whose properties can be illustrated by Figure 1.13. When mechanical compression or tension is applied on a piezoelectric element, a voltage is generated (Figure 1.13 (b) and (c)), which is known as direct piezoelectric effect and the voltage value is linearly proportional, up to a specific stress depending on the material properties. Conversely, if a voltage is applied to a piezoelectric element, its shape deforms as longer and finer (Figure 1.13 (d)) or shorter and broader (Figure 1.13 (e)) according to the directions of polarity and applied voltage, which is known as inverse piezoelectric effect. Due to these properties, piezoelectric materials are extensively used as sensors, actuators or self-sensing actuators. Additionally, the high integrability, compactness, light weight and high bandwidth make piezoelectric materials well suited to be used and implemented in vibration control systems.

Piezoelectric shunt damping techniques have become a widespread branch for vibration suppression in intelligent systems since it first proposed by Forward in 1979 [76]. By implementing these approaches, structural mechanical energy can be converted into electrical energy or dissipating by shunt circuit which is connected cross the piezoelectric element. Lesieutre [77] primarily categorized the shunt circuits as four basic kinds: resistive, inductive, capacitive and switched circuits based on their different dynamic behaviours. Along with the development of piezoelectric damping techniques, other more detailed classification is depicted in Figure 1.14 [78]. More comprehensive developments of the piezoelectric based approaches will be reviewed in next section.

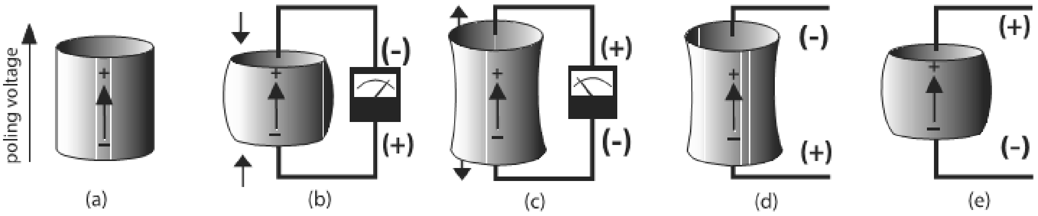

Figure 1.13. Reaction of a poled piezoelectric element to applied stimuli [78].

Apart from the previous illustrated materials, other intelligent materials are also popularly used for vibration reduction. Duan and Or [79] developed a novel self-sensing tunable vibration absorber (SSTVA) which consists of a piezoelectric ceramic-magnetostrictive composite sensoriactuator suspended in a mounting frame by two flexible beams connected to the axial ends of the sensoriactuator. Corresponding results have demonstrated great promise for deploying the SSTVA for active absorption of vibrations in vibrating structures.

A giant magnetostrictive actuator was put forward for the application of effective suppressing vibration by Zhang *et al.* [80]. A minimum variance self-tuning regulator (MVSTR) was incorporated into the design of a controller. The exerted vibration disturbances with either varying amplitude, frequency or both were controlled by employing adaptive control law. Simulation results with in LABVIEW and experimental control test results proved that the giant magnetostrictive actuator with the minimum variance self-tuning control law can perform effective control to low-frequency and micro-lever vibration.

As known that traditional magnetostrictive actuators is limited to high frequencies, to bypass this disadvantage Braghin *et al.* [81] designed an innovative low-frequency magnetostrictive inertial actuator for low frequency vibration control. Design parameters of the supporting structures, i.e. its lengths, widths, radii, points of connection to the inertial mass and to the magnetostrictive bar were optimized for implementing into active control systems.

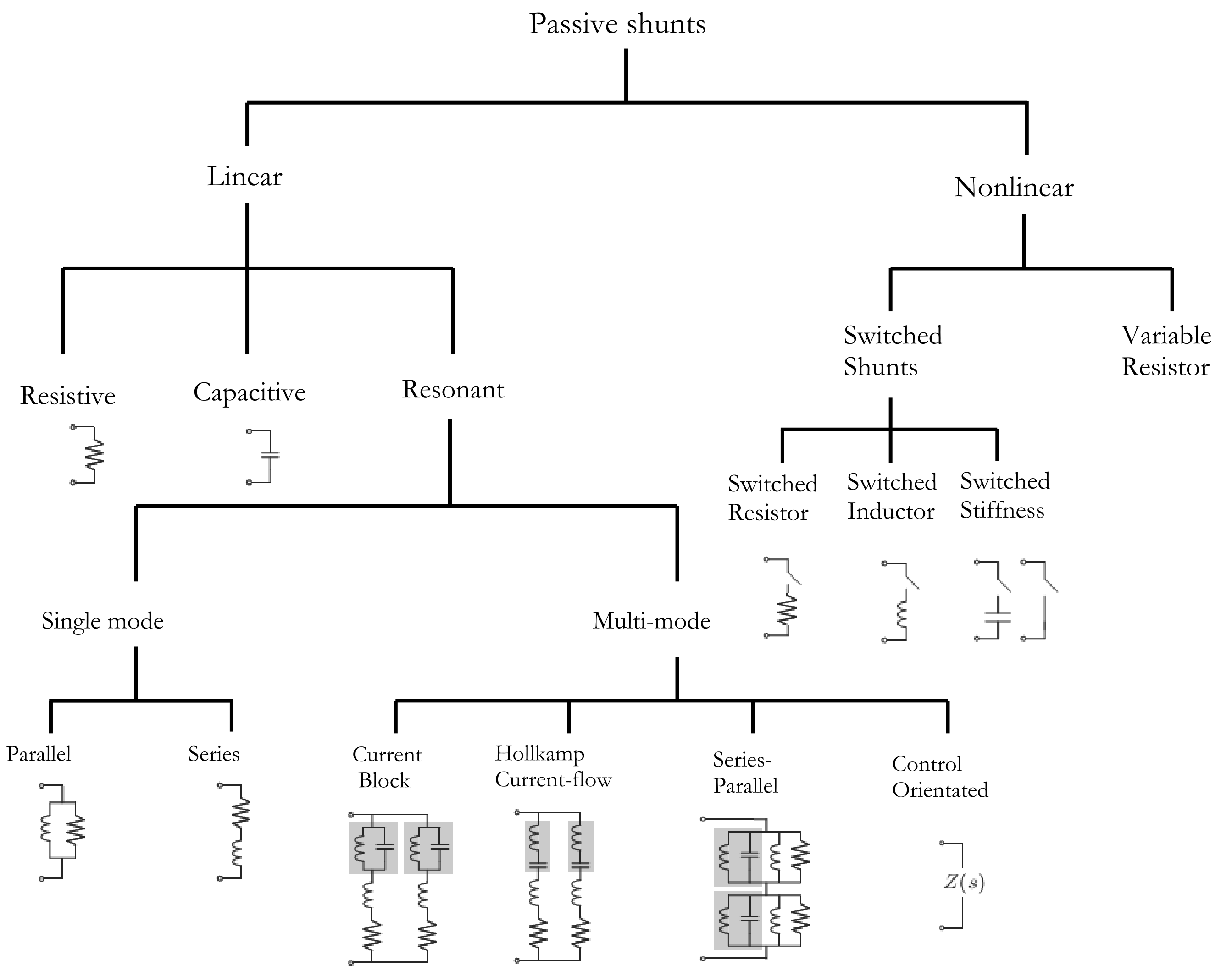

Figure 1.14. Passive piezoelectric shunt damping techniques. [78]

The magnetostrictive materials have the unique characteristics of high magneto-mechanical coupling property, large thrust ability and high driving stability. However, they as one of solid-state smart materials have strong nonlinear properties such as hysteresis, quadric frequency effect and saturation on magnetostriction, which significant influence on modeling accuracy and adaptation of control laws for magnetostrictive actuators. Moreover, thermal effect inherently existing in magnetostrictive mechanisms plays considerable side effect for high precision vibration control [80].

Ausanio *et al.* [82] reported a new elastomagnetic attenuator for adaptive-passive vibration control. This attenuator is based on an elastomeric core clasped between two strong permanent magnets, arranged with the opposite poles "face-to-face" in order to exert large, reciprocal attractive forces. Experimental investigation results of transverse oscillation and longitudinal oscillation showed that the elastomagnetic attenuators are particularly useful in limiting the effects of transverse vibrations propagating from the supported to the basis structure and longitudinal vibrations transmitted from the basis to the supported structure.

Kasarda *et al.* [83] proposed a novel active control solution with active magnetic damper. Test cases demonstrated that a between-bearing active magnetic damper can be very effective in reducing subsynchronous rotor vibrations through the addition of damping and stiffness, while the optimum location for subsynchronous vibration reduction may not be the best choice for overall vibration performance.

In this section, the dominating damping materials and damping devices are briefly introduced. Intelligent control systems integrated with different smart materials are summarized. Unique and major traits of the damping materials and devices are discussed. In following section, main piezoelectric based control techniques will be reviewed.

1.3. Electromechanical vibration control methods with piezoelectric materials

1.3.1. Electromechanical passive techniques

The piezoelectric effect was first discovered in 1880 by Pierre and Jacques Curie, who demonstrated that when certain crystalline materials were stressed, an electric charge was produced on the material surface. It was subsequently demonstrated that the converse effect was true. The unique features due to the asymmetry in the crystalline structure resulting from the displacement of ionic changes make them extensive used in industrial engineering domain. Significant development and progress of the applications of piezoelectric materials are achieved, such as the biomedical ultrasound generation and detection, vibration control, etc. Generally, electromechanical passive damping is referred to as piezoelectric shunt damping where the electric circuits act as mediums for energy dissipation. Hagood and Flotow [84] preliminarily investigated the possibility of dissipating mechanical energy by using piezoelectric materials shunted with passive electrical circuits. Two shunting circuits, namely resistive shunting (case of a resistor alone) and resonance shunting (constituted of a resistor and an inductor) were discussed numerically and experimentally with a cantilever beam. They found that for resistive shunting case which dissipates the energy through Joule heating, the materials properties exhibit frequency dependence similar to viscoelastic materials but with higher temperature stability. Moreover, the magnitude of loss factor is determined by the electromechanical coupling coefficient of the piezoelectric. For the resonance shunting case, the electrical resonance can be optimally tuned to the structural resonance so as to minimize the maximum of response, which is analogous to a mechanical vibration absorber and the inductance is equivalent to an electrical mass. Comparisons showed that this shunted circuit has large effects on the controlled mode while the resistor shunting has larger bandwidth. However, large inductor was necessary for low frequency vibration control with small inherent capacitance of piezoelectric.

To deal with this disadvantage, virtual grounded and floating inductors are required to implement the inductor elements. However, such virtual implementations are generally large in size, difficult to tune and are sensitive to the component variations. Moreover, they also require an external power source and a large number of costly high voltage components. Another method named synthetic admittance consisting of a voltage controlled current source and signal filter, contains very few high voltage components but still requires an external power supply. To bypass these drawbacks, Fleming *et al.* [85] suggested placing an additional capacitance across the terminals of the PZT to drastically reduce the required shunt inductance. A piezoelectric multimode shunt damping structure, namely series-parallel impedance structure (Figure 1.15), is introduced and experimentally verified. Although smaller inductances are used in this method, control effectiveness is decreased since additional capacitance is used, allows the decrease of coupling.

Hollkamp [86] extended the resonance shunting circuits for suppressing multiple modes with a single piezoelectric element. Additional electric components are added to the shunt circuit to obtain more electrical resonances as shown in Figure 1.16. Experimental demonstration of a two-mode device applied to a cantilever beam validated the multimode reduction while tuning one electric resonance will detune the rest of the circuit.

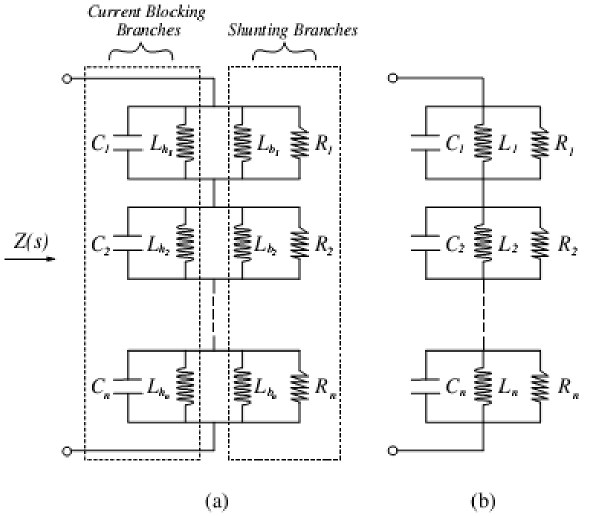

Figure 1.15. The series- parallel impedance structure (a) and simplified circuit (b) [85].

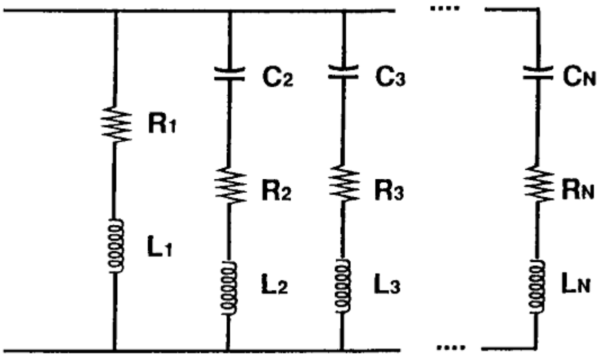

Figure 1.16. Resonance shunt network for the multimode piezoelectric damper. [86]

Wu [87] reported a blocking circuit in series with several parallel resistor-inductor shunt circuits for multiple modes control (Figure 1.17 (a)). Each shunt circuit with the addition of the blocking circuit is functional for its own mode, yet blocks or causes open circuit for all other frequency modes, thus there is no interference between them. To reduce the number of anti-resonant circuits, a modified shunt circuit is illustrated (Figure 1.17 (b)) and proved simpler to operate and more cost effective. Although this method can prevent interference among the various branches in the shunt circuit and was proved as an easier and more reliable method for fine-tuning and damping, if the piezoelectric transducer is located at a node or near low strain region of the interested modes, no damping performance will be achieved.

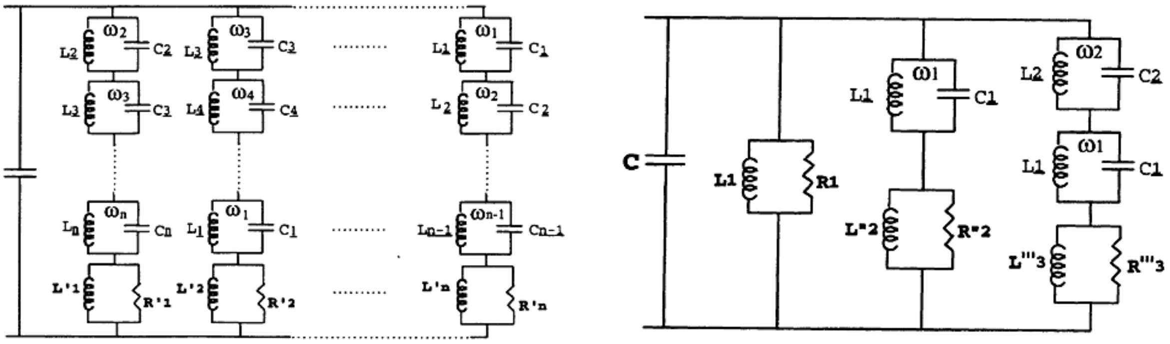

(a) (b)

Figure 1.17. (a) Generalized multiple-mode shunt circuit (b) Modified shunt circuit for shunt damping three modes at ω_1, ω_2 and ω_3. [87]

A similar circuit named as “current flowing” shunt which is simple and guaranteed to be stable was presented by Behrens *et al.* [88]. Instead of preventing the current from flowing at a specific frequency, the latter is allowed flowing, which is achieved by using a series of capacitor-inductor circuits as shown in Figure 1.18. Same as Wu’s “current-block” shunt circuit, the branch can introduce damping at particular frequency ω_i while not disturbing the other branches that are approximately open circuits (i.e. the impedance is very large at ω_i).

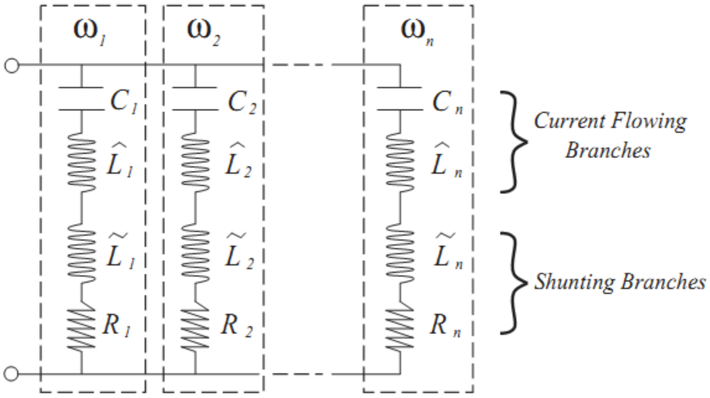

Figure 1.18. ‘Current flowing’ multiple mode shunt circuit. [88]

Moheimani *et al.* [89] presented a systematic way of designing the shunt impedance for multi-mode shunt damping and experimentally studied with laminated beam and plate. They suggested that the piezoelectric shunt damping problem can be viewed as a feedback control problem in which the controller is inside an inner feedback loop.

An alternative electromechanical passive damping method through distributed piezoelectric transducers was presented by Dell’Isola *et al.* [90]. The distributed piezoelectric elements can be interconnected by either by RL impedances or R impedances as in Figure 1.19. Experimental study proved that this concept of distributed control can reduce tuning inductances without affecting damping performance. Furthermore, the optimal damping performance depends exclusively on the dimensionless piezoelectric coupling parameter between corresponding electrical and mechanical modes.

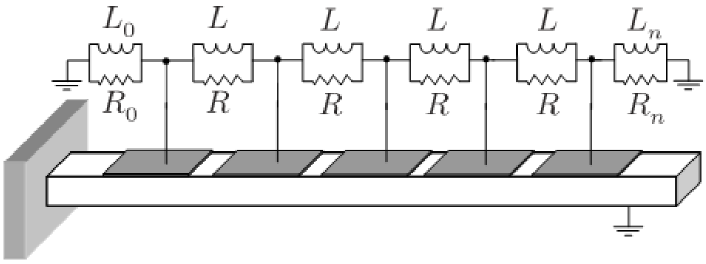

Figure 1.19. Sketch of a piezoelectromechanical beam with RL impedances [90].

Numerical and experimental investigations with a simply supported plate by Alessandroni *et al.* [91] proved that the use of an electric network which interconnects the uniformly distributed piezoelectric elements with passive electrical circuits can assure a multi-resonant and broadband electromechanical coupling. Andreaus *et al.* [92] further confirmed this conclusion and optimized the passive controller. Trindade and Maio [93] discussed the performance of multimodal passive vibration control of a sandwich beam using shear piezoelectric materials which are embedded in a sandwich beam core and connected to independent resistive shunt circuits. Optimal configurations were evaluated by parametric analysis based on the modal strain energy method. Average damping factors up to 1.5% were achieved using three shunted piezoelectric patches for damping the third, fourth and fifth modes of the sandwich beam.

It is well known that the piezoelectric based passive control methods are extremely simple compared with active methods. They are light, low cost, dispensing the use of any external feeding and stable. Although the multimodal control performance can be guaranteed with the implementation of appropriate control circuits, it is not always efficient and suffers from a degraded damping effect under environmental variations such as temperature. Moreover, it is extremely sensitive to any slight shift of the resonance frequency. Furthermore, for lower frequency vibration control, the unrealistic inductance may lead to larger size of control circuit or require external power.

1.3.2. Electromechanical active techniques

Active vibration control is a vast research area that incorporates interdisciplinary technologies. A typical active vibration control system (Figure 1.20) is an integration of mechanical and electronic components in synergistic combination with computer/microprocessor control. The major components of any active vibration control system include the mechanical structure influenced by disturbance (creating unwanted vibration), sensors (to perceive the vibration), controllers (to intelligently make use of the signals from the sensors and to generate the appropriate control signals), and actuators (which counteract the influence of the disturbance on the structure) [94].

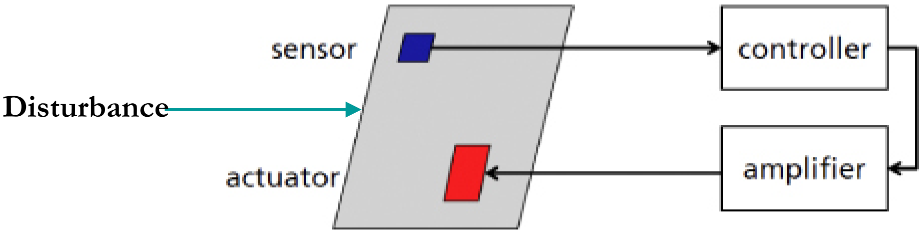

Figure 1.20. Typical active control system.

Generally, the algorithms utilized in active control can be classified as two main categories: feedback (Figure 1.21) and feedforward (Figure 1.22) control. The former consists of measuring the output or response of the structure and using that measurement to determine the force to apply to the structure to obtain a desired response. The latter approach provides an improved response by producing a second input to the system that effectively cancels the disturbance to the system [95]. The advantages and disadvantages were summarized by Alkhatib et al. [94], which is listed in Table 1.1. In this section, the researches concerning with the piezoelectric based (used as sensors, actuators or featured into the controllers) active control systems are briefly introduced.

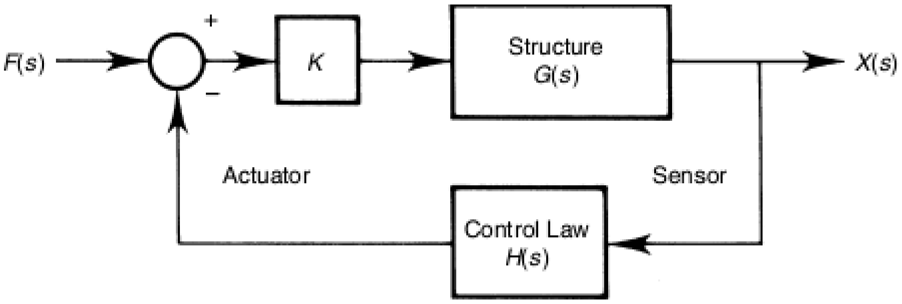

Figure 1.21. Feedback control system [95].

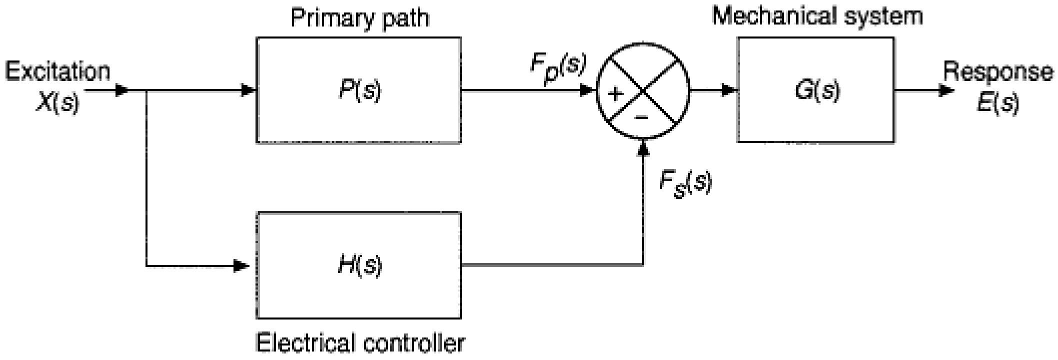

Figure 1.22. Equivalent block diagram of a feedforward control system [96].

Hubbard [97] disclosed an apparatus which uses a piezoelectric film to control or dampen vibrations in a mechanical system. This film can be directly applied to the protected system or fabricated as an intermediate layer. To dampen the vibration, proper amplitude and phase of voltage need to be fed across piezoelectric film in order to induce corresponding strain. Lester and Lefebvre [98] demonstrated their investigation with piezoelectric actuators which are not only effective for controlling the vibration but also efficient for controlling the interior noise of circular cylinders.

Typically, the electrical dynamics of piezoelectric materials are ignored when it is used as an actuator. Similarly, the structural dynamical effects produced by piezoelectric materials are also ignored when it used as a sensor. However, the dynamics of piezoelectric elements sometimes play an important role. For instance, the current drain could be influenced by the capacitance of the piezoelectric, thus corresponding current saturation of voltage amplifiers and electrode lead resistance may add critical phase lag to a control loop which will degrade the control performance of the whole system. To address the coupling dynamics between piezoelectric actuator and mechanical system, Hagood *et al.* [99] analysed the coupling effects using state space models. Direct voltage driven electrodes, direct charge driven electrodes and an indirect drive case were discussed. From the theoretical and experimental results, it can be found that the dynamics coupling can be used to add damping to structural modes or change the observability or controllability of the structure modes. It also demonstrated the usefulness of the actuator models in allowing the designer to modify plant dynamics in a predictable and beneficial way.

Lee *et al.* [100] used distributed sensors and actuators to control a one-dimensional cantilever plate. Since the sensor signal is proportional to the modal coordinate time derivative, the sensitivity and stability to resonance frequency variation can be minimized with velocity feedback control employment.

Table 1.1. Advantages and disadvantage of two main active algorithms [94]

Type of control	Advantage	Disadvantage
feedback		
Active damping	·Simple to implement and requires fewer computation ·Does not require accurate model of the plant ·Guaranteed stability when actuator and sensors are collocated	·Effective only near resonance
Model Based (LQG, H_∞)	·Global method ·Requires accurate model of the plant ·Attenuates all disturbance within the control bandwidth	·Limited bandwidth ·Requires low delay for wide bandwidth ·Spill over
feed forward		
Adaptive filtering of reference (x-filtered LMS)	·No model is necessary ·Robust to inaccuracies in plant estimate and no change in plant transfer functions ·More effective for narrowband disturbance	·Reference/error signal is required ·Local method and many amplify vibration somewhere else ·Large amount of real-time computations

Moreover, Balamurugan and Narayanan [101] discussed the control effectiveness of plates and shells with distributed piezoelectric elements, based on direct proportional feedback, constant-gain negative velocity feedback, Lyapunov feedback and LQR optimal control laws. It has been observed that velocity feedbacks like constant gain negative velocity feedback and Lyapunov feedback are more effective compared to displacement feedback like direct proportional feedback. However, LQR control methods are even more effective with lesser peak voltages.

Four illustrative cases of adaptive laminated structures were discussed by Moita *et al.* [102]. Static control of a cantilever laminated plate, forced response with active feedback control of a simply supported plate, forced response with active feedback control of a simple supported beam and forced response with active feedback control of a cantilever beam under sinusoidal loading were simulated by finite element model based on Kirchhoff classical laminated theory. It was concluded that the used negative velocity feedback control algorithm is effective for an active damping control of vibration response.

The combined effects of passive and active vibration control of a laminated plate with piezoelectric sensors/actuators were investigated by Hwang *et al.* [103]. In their study, the dynamic properties of the vibrating structure can be varied with the layer angles by passive treatment. The piezoelectric based electromechanical active control was achieved using negative velocity feedback. From the numerical simulation, they pointed that the two control methods would affect each other. Thus, to improve the damping capacities of the control system, one should improve the passive and active control simultaneously.

Trindade *et al.* [104] demonstrated the active control performance of damped sandwich beams with piezoelectric laminated surface layers and viscoelastic core. Parametric analyses indicated that linear quadratic regulator (LQR) controllers improve the selected modal damping. Although the derivative feedback controllers are less effective than LQR, their well-known spillover destabilizing effects can be attenuated by the increase of stability margins provided by the viscoelastic damping.

As it is known that piezoelectric element not only can connect to a passive shunt circuit for suppressing the undesired vibration but also can integrate into active controllers. To discuss the damping performance in the case where the piezoelectric materials are used as passive modal devices and active elements simultaneously, Agnes [105] developed a simple modal model and experimentally verified on a simple cantilever beam. It is indicated that piezoelectric devices combining active and passive techniques can significantly reduce the broadband structural response.

Leleu *et al.* [106] developed an energy based approach to obtain the optimal locations of piezoelectric actuators and sensors on a flexible structure, which is independent on the control law. It was noted that for complex systems, a numerical model is necessary for locating the optimal positioning of actuators and sensors.

Vibration control issue of the functionally graded material (FGM) plates was presented by He *et al.* [107]. A constant velocity feedback control was implemented in their work. Dynamic response showed that the vibration amplitude of the FGM plate can be attenuated at very high rate for appropriate gain values, which demonstrated the effectiveness for control the FGM plates.

Devoting to feedback control where one is particularly concerned with systems in which the excitation of the structure cannot be directly observed, Vasques and Rodrigues [108] compared and presented the classical control strategies (constant amplitude and constant gain velocity feedback (CAVF and CGVF)) and optimal control strategies (linear quadratic regulator (LQR) and linear quadratic Gaussian (LQG) controller) concerning the active control of a cantilever aluminium beam with an asymmetric piezoelectric sensor/actuator pair mounted closed to the clamped edge. Investigation results showed that for an initial displacement field the CAVF and LQG with the first mode weighted are the most interesting solutions. However, for a white noise disturbance, the CAVF only manages to reduce the mode under control and the others are destabilized. The LQG with all modes weighted presents a better control in bandwidth with a lower control voltage. Moreover, the perfect collocation of actuator/sensor pair will guarantee the stability of classical techniques. Furthermore, it was also pointed out that all the states must be measured when generating the control with LQR. For LQG controller, observation and control spillover problems related with the reduced or unobserved model dynamics may compromise stability.

As known that the locations of sensors and actuators have significant influence on the performance of the control system as well as the controlled response in active vibration control, the optimal placement of collocated piezoelectric actuator-sensor pairs on flexible beams was considered by Kumar and Narayanan [109]. It was found that the optimal location of actuator-sensor pairs is in the regions of high modal strain energies. Moreover, the control effectiveness offered by direct proportional feedback is insignificant when compared with the constant gain negative velocity feedback, which is due to the fact that the velocity feedback changes the system damping while the displacement feedback changes the natural frequencies. It was also further confirmed that the LQR optimal control offers an effective control with less peak actuator voltages compared to negative velocity feedback.

Moheimani [110] reviewed the recent work concerned with the problem of active vibration control using collocated piezoelectric actuators and sensors, self-sensing approaches and compared the performance of shunt damping system with that of active controlled systems.

Due to the unique dynamic characteristics of piezoelectric materials, the electromechanical active control systems with piezoelectric elements have been proven extremely efficient. Additionally, thanks to the ease of implementation of piezoelectric materials, these active control methods can be easily linked to dynamic vibration devices such as absorbers and dampers as well [47] [48]. It also can achieve multimodal control and robustness on a wide frequency band compared with the electromechanical passive techniques. However, since these methods require a complex signal processing with actuators, sensors, control units and heavy amplifiers as well as high power requirements to handle energy exchanges, it is bulky and not easy for integration with a large number of components, especially for weight limited applications such as aircrafts. Furthermore, the limitations as instabilities and spill over will degrade the control performance in some specific applications.

1.3.3. Electromechanical semi-passive and semi-active techniques

To tackle the disadvantages and drawbacks of electromechanical passive and active techniques and maintain the simplicity, ease of implementation, compactness, low power requirements, superior control performance and robustness, semi-passive/semi-active techniques have been proposed.

A semi-active control concept which retains the benefits of active system yet not pays the power and complexity penalties was presented Hrovat *et al.* [43]. From their comparative study, it has been proven that semi-active performance can be very similar (even slightly superior) to active control performance.

Clark [111] presented a semi-active control law to switch the electrical shunt circuit of a piezoelectric actuator between open circuit (high stiffness) and short or resistive circuit (low stiffness) states for energy dissipation. Simulation showed that the variation in stiffness allowed by piezoelectric materials can be used for vibration control applications. His subsequent research [112] showed that the state switch technique works better when the low-stiffness state is resistive shunts instead of a pure short-circuit. Furthermore, it has been pointed that the state switched approach provides better performance and is less sensitive to system parameters changes.

Cunefare *et al.* [44] reported a state-switchable dynamical system named state-switched absorber (SSA) which has the capability to instantaneously change its dynamic property such as stiffness. A piezoelectric material is used as one element of a series spring (Figure 1.23), whose stiffness is a function of the output impedance between the open- and short- circuit condition. To avoid mechanical transients, this spring must be switched when the strain in the stiffness element is zero, namely the relative displacement across the spring is null. Simulation results in their study clearly indicated that this semi-active has the potential for vibration control.

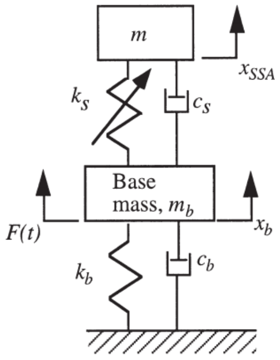

Figure 1.23. SSA attached to base system [44].

Another tunable vibration absorber using piezoelectric ceramic elements as part of device stiffness was demonstrated by Davis and Lesieutre [45]. The effective stiffness is adjusted electrically using an external passive capacitive shunt circuit to tune the resonance frequency between its short and open circuit resonance frequencies (Figure 1.24). The “ladder” circuit of discrete capacitors wired in parallel is shown in Figure 1.25. The effect of placing capacitors in parallel is a net capacitance equal to the sum of the individual capacitances. The number of the discrete capacitance values depends on the overall size of the frequency tuning range, the intrinsic damping of the absorber and the acceptable deviation from minimum response. Experimental comparison to pure passive absorber confirmed the improvements of this technique in vibration reduction. Furthermore, authors pointed that this semi-active method is a less complex yet effective method for stiffness change with low-power consumption.

In addition, a continuous switching semi-passive method named Synchronize Switch Damping on Short circuit (SSDS) approach which does not rely on any tuned electric load was first proposed by Richard *et al.* [113]. In this method, piezoelectric device is simply continuously switched from open circuit to short circuit synchronously to the mechanical strain (Figure 1.26). Since the switching process occurs on the extremum value of the displacement/piezovoltage, it leads to a distorted and shifted resulting piezovoltage in time domain from the deflection of flexible structure, which can be regarded more or less as an image of velocity and thus creates a damping quite similar to a dry friction. Experimental investigations with a cantilever beam excited under harmonic and pulse excitations showed that the SSDS approach is an inherently wide band nonlinear technique which can work at any frequency without need for large inductor and only very low power is required for driving the static switch and for the control circuit supplies which allows usage of batteries for a long time period and can be self-powered. Since the switching time is almost instantaneous compared with that in state switching technique, the SSD technique is referred to as "pulse switching" in some literature.

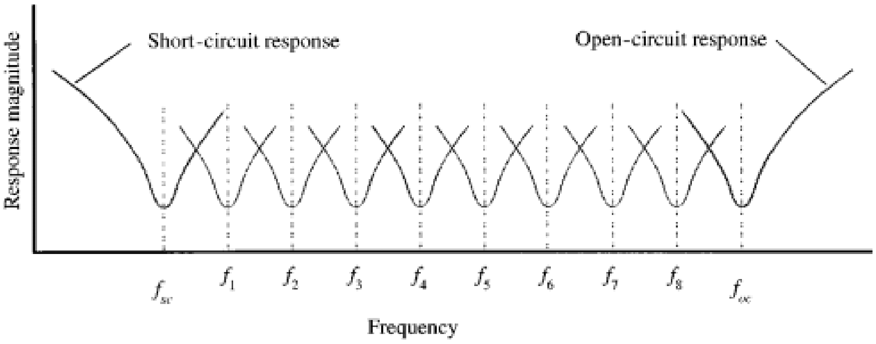

Figure 1.24. Frequency band shunt discretization [45]

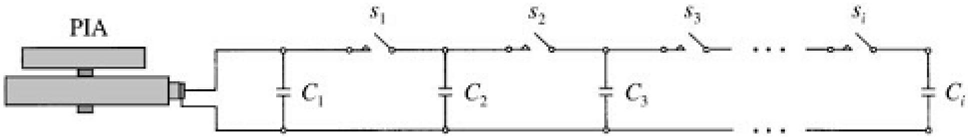

Figure 1.25. conceptual "ladder" capacitive shunt circuit [45]

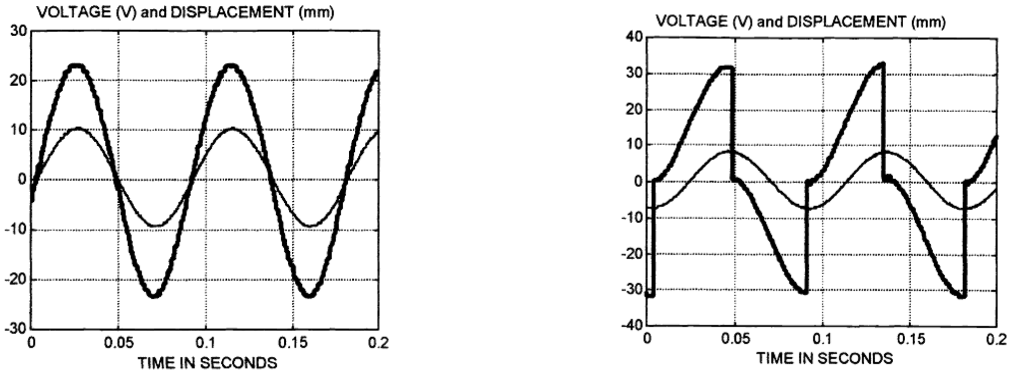

(a) (b)

Figure 1.26. The piezovoltage (in Volts, thick line) and the deflection of beam (in mm, thin line) are plotted as a function of time. (a) Open circuit case and (b) the proposed switching configuration. [113]

After that, based on the main principle of SSDS technique, Richard *et al.* [114] proposed another enhanced semi-passive technique named Synchronized Switch Damping on Inductor (SSDI).

Instead of connecting the piezoelectric elements to a short circuit, the converted electrical energy is transferred to an inductor when the displacement extremum of the vibrating structure is detected. At that moment, the static switch is closed, and the capacitance of the piezoelectric elements and the inductor shape an electrical oscillator. This oscillation is stopped after half a period which is very quick compared with the vibration motion, until the piezovoltage reversed. Since the energy relationship of an electromechanical system in a vibration period can be given as

$$\begin{gathered}\frac{1}{2}M\left[\dot{u}^2\right]_{t_1}^{t_1+\tau}+C\int_{t_1}^{t_1+\tau}\dot{u}^2dt+\frac{1}{2}K_E\left[\dot{u}^2\right]_{t_1}^{t_1+\tau}=\int_{t_1}^{t_1+\tau}F\dot{u}dt-\alpha\int_{t_1}^{t_1+\tau}V\dot{u}dt\\ \alpha\int_{t_1}^{t_1+\tau}V\dot{u}dt=\frac{1}{2}C_0\left[V^2\right]_{t_1}^{t_1+\tau}+\int_{t_1}^{t_1+\tau}VIdt\end{gathered}\tag{1.1}$$

it demonstrates that the increase of converted energy can be achieved by increasing the voltage or reduce the phase shift between voltage and velocity. As shown in Figure 1.27, by implementing this technique, the voltage amplitude is optimized and is 90 degrees out of phase with the structural motion, which artificially increases the damping mechanism. Harmonic and transient experimental comparison showed that SSDI approach outperforms SSDS while preserving the simplicity, low energy requirement, realistic inductance implementation and inherently wide band feature.

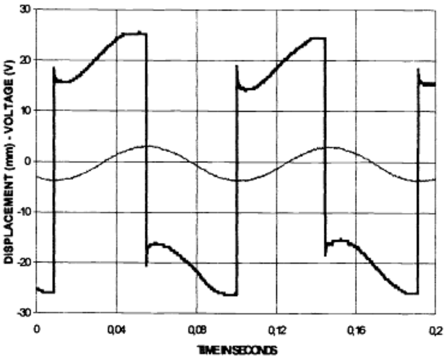

Figure 1.27. The piezovoltage (in Volts, thick line) and the deflection of beam (in mm, thin line) as a function of time for SSDI configuration. [114]

Quantification analysis of the added damping and the optimization of the electric circuit parameters were investigated by Ducarne *et al.* [115]. The case study of free and forced responses showed that the piezoelectric coupling factor is the only parameter to optimize and has to be maximized in order to maximize the added damping. Thanks to the low power requirement feature, it can be designed with self-powering capability by the implementation with self-powered SSDI [116] (Figure 1.28) or the self-powered adaptive SSDI (Figure 1.29) control blocks [117]. In the virtue of the self-powering capability, it allows SSDI as a flexible technique avoiding external energy requirements and bulky wirings.

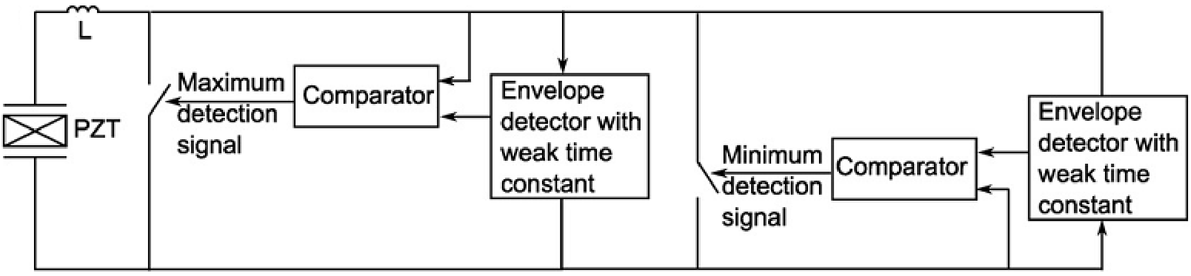

Figure 1.28. Original self-powered SSDI control block diagram designed by C. Richard. [117]

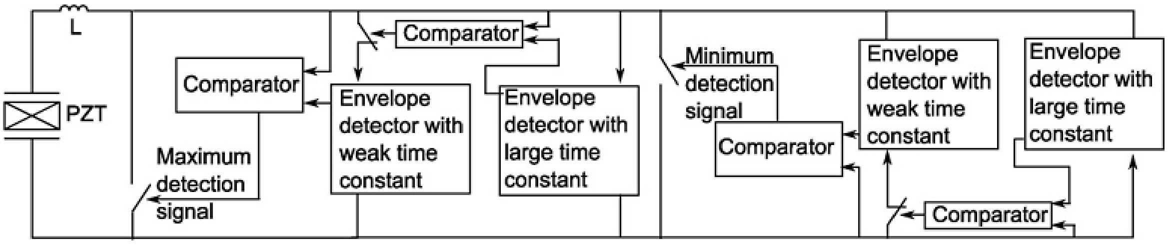

Figure 1.29. Self-powered adaptive SSDI control block diagram. [117]

Corr and Clark [118] described the energy dissipation of pulse switching (namely synchronized switch damping techniques) and compared with that of traditional passive resonant shunt technique and state switching. The direct velocity feedback (DVFB), state switching and pulse switching control were also qualitatively compared in their work. They found that the pulse switching is analogous to the DVFB control technique and the only difference is the applied voltage varies over the half cycle in the latter method and is maintaind as constant in the former technique. Moreover, the state switching and pulse switching are fundamentally same technique, while the pulse switching generally outperforms the state switching. In their subsequent work [119], the low-frequency damping of piezoelectric switching techniques were numerically and experimentally compared with a clamped-clamped beam. Since the state switching only dissipates mechanical energy over two quarters of the vibration cycle whereas the pulse switching and resonant shunt techniques dissipate mechanical energy for approximately the entire vibration cycle, simulation and experimental results confirmed the superior damping performances of pulse switching and resonant shunt technique. Moreover, the pulse switching technique has been proved easier to tune and is insensitive to the system changes by its self-tuning principle. Although the inductor in the control circuit of pulse switching technique can be chosen as any value because no specific frequency needs to be tuned, researchers pointed that upper and lower bounds of inductance should be set to optimize pulse switching performances. Usually, the electrical natural frequency is at least ten times higher than those of the mechanical modes of interest to ensure the generated charge remains approximately constant during switching process and no more than fifty times faster than the mechanical interested mode in order to avoid "chatter" phenomenon. In the succeeding research [120], a novel semi-active energy rate multi-modal vibration control technique was proposed based on the pulse switching resistor/inductor shunt. To remove energy from the mechanical system for multiple modes, the shunt switch for the piezoceramic actuator is determined to shut when the product of the applied charge and the sum of the voltage rates for the control modes is less than zero. A simple numerical and experimental test under random disturbance indicated that with a single piezoceramic actuator and the switched RL shunt circuit, the multiple modes can be effectively selected and controlled simultaneously. However, as the number of control modes increase, the performance of the control technique at any one mode is slightly diminished. This may set an upper bound to the number of control modes for a single actuator.

On the basis of storing the electrical energy in a piezoelectric transducer and then reusing this energy to suppress vibration of structures instead of dissipating, Makihara *et al.* [121] presented an advanced semi active energy-recycling method which can be categorized as nonlinear bang-bang control to suppress multiple modes of beam structure with multiple transducers. Numerical investigation showed that this energy-recycling method surpassed the conventional semi-active and optimally tuned passive methods under sinusoidal and random forces, as well in transient vibrations. Further investigations for controlling the vibration of typical continuous structure such as beam and typical tension-stabilized structure such as membrane with the energy-recycling semi-active techniques were also presented by this research group [122]. The performances with different switching circuits (Figure 1.30) were compared, which further confirmed the effectiveness of the energy recycling semi-active method against several vibrations. Moreover, it was also indicated that the semi-active approach can be used for controlling the vibration in real system. After this, Makihara *et al.* further devised a self-sensing vibration suppression method [123] which can avoid estimation blackout during closed-circuit status and lessen harmful influences from residual modes. Numerical and experimental study revealed that this self-sensing system can reduced the vibration in cooperation with state-switching and synchronized switch techniques. Moreover, the robustness against model error of this method was experimentally proven with an intentional frequency shift. Furthermore, it has been confirmed that one self-sensing controller can simultaneously handle multiple piezoelectric actuators, and can suppress multiple-mode vibration in a multiple degree of freedoms structure.

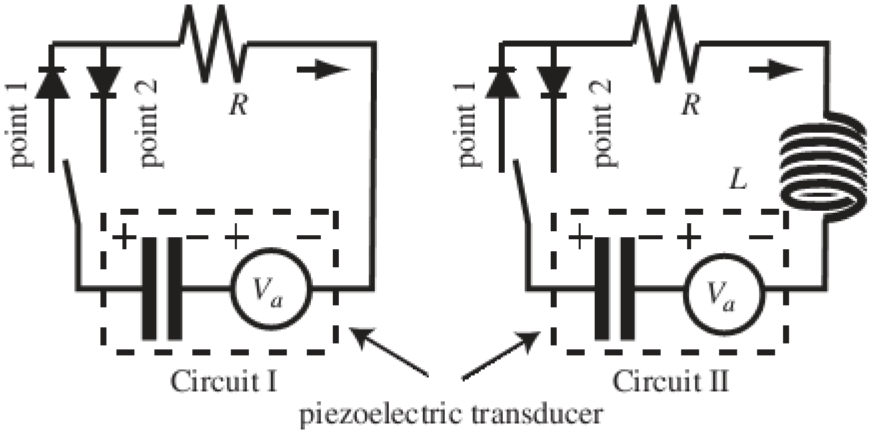

Figure 1.30. R-switching and LR-switching circuits for semi-active vibration suppression. [122]

In the study of Petit *et al.* [124], it was shown that the damping ability of SSDS and SSDI techniques is strongly correlated with the electromechanical coupling coefficient. To compensate this draw back, Lefeuvre *et al.* [125] presented a semi-active method named Synchronized Switch Damping on Voltage sources (SSDV) in order to artificially reinforce the electromechanical coupling by increasing the piezovoltage. As shown in Figure 1.31, the piezoelectric element is switched on a positive or negative voltage source across the LR shunt circuit. The additional constant voltage sources are used for increasing the inversed voltage amplitude in order to enhance the damping effect. Theoretical and experimental results showed that adding the voltage sources in the switching circuit can significantly increase the dissipated energy.

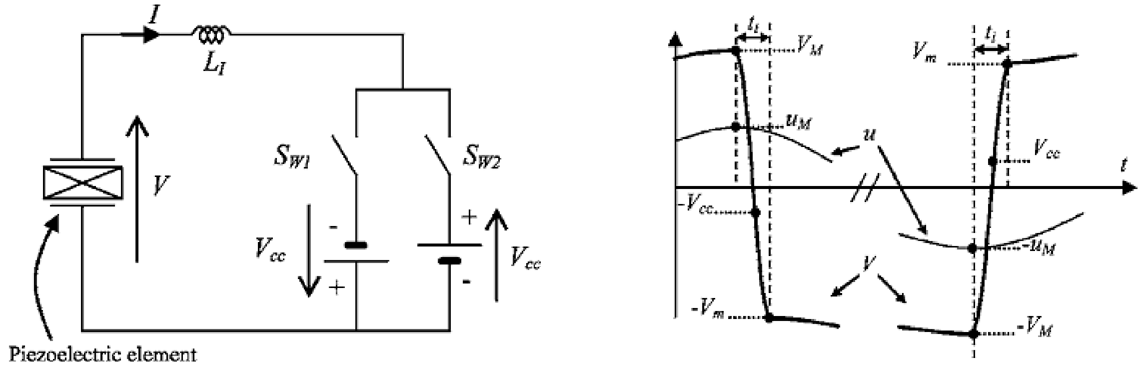

(a) (b)

Figure 1.31. (a) SSDV electric circuit and (b) displacement *u* and voltage *V* waveforms[126]

Although the usage of continuous voltage source in SSDV technique can increase the piezovoltage during inversion process allowing a superior damping effectiveness, its constant absolute value may lead to stability problem. Especially when the vibration level is low, implementing this technique may excite the structure instead of limiting the vibration. To ensure the stability, Badel *et al.* [126] presented an enhancement of SSDV technique using an adaptive continuous voltage source (Figure 1.32) for fitting the mechanical braking force resulting from the SSDV process to the vibration level. The value of the adaptive continuous voltage source V_{cc} can be obtained by

$$\begin{aligned} V_{cc} &= -\beta \frac{\alpha}{C_0} u_M \quad \text{on maximum strain} \\ V_{cc} &= \beta \frac{\alpha}{C_0} u_M \quad \text{on minimum strain} \end{aligned} \tag{1.2}$$

where C_0 is the blocked capacitance of piezoelectric elements and α is the force factor. u_M defines the amplitude of displacement. The proportional coefficient β is set by the user.

Experimental measurements obtained from cantilever beam indicated that the enhanced SSDV technique is inherently stable because the voltage source level is continuously adapted, whereas instabilities may be observed because of perturbations due to noise or harmonics are important compared to excited mode. Meanwhile, the experiments conducted on a smart board under white noise excitation showed that the enhanced SSDV technique can simultaneously control the different lower frequency modes of a composite plate.

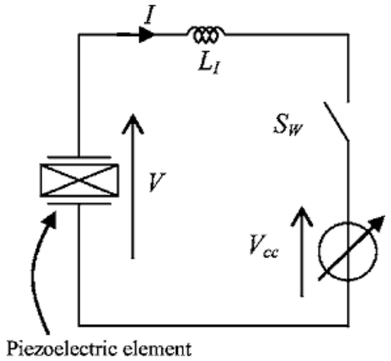

Figure 1.32. Enhanced SSDV electrical circuit. [126]

Lallart *et al.* [127], focusing on CICO stability (Converging Input, Converging Output) and robustness, discussed the stability of original SSDV and enhanced SSDV techniques using first harmonic method. Although it showed by theoretical study that the SSDV technique has infinite sensibility and is stable even if under the perfect switch condition, technological study using a differentiation technique showed that the SSDV is always unstable with a relationship between the oscillatory frequency and the differentiation delay. From this stability analysis, it was confirmed that controlling the voltage level with the amplitude of the piezovoltage/displacement as used in enhanced SSDV method can ensure the stability and preserve a significant damping performance.

Although the enhanced SSDV can improve the stability compared with original SSDV approach, optimal control performance is not always obtained since it depends on the experimental conditions to some extent. The optimal voltage source and optimal voltage coefficient need to be chosen according to several factors such as the amplitude of vibration, properties of switch or level of noise signal in measurement. Concerning with achieving optimal damping effectiveness, adaptive SSDV approach, in which the voltage coefficient is adjusted adaptively based on the sensitivity of the vibration amplitude with respect to voltage coefficient β, was proposed by Ji *et al.* [128]. An improved switching algorithm, which prevents the switch from over frequently switching actions, was also presented. Comparison on a cantilever composite beam showed that the adaptive SSDV exhibited the same damping performance as the optimal voltage source and optimal voltage coefficient were used with original SSDV and enhanced SSDV techniques, respectively. It also has been proved that the control performance can be optimized automatically with the adaptive SSDV method.

In the virtue of distinguishing features of SSD techniques such as simplicity, self-adaptiveness with frequency variation, ease of implementation, they can be combined with self-powered control block to achieve self-powering capability, or incorporated with self-sensing controller to eliminate extra sensors and simplify the control system. Moreover, the SSD techniques can also be extended for multimodal control by combing other techniques such as threshold detection [117][134][135][136][137], which will be discussed in detail in Chapter 2. Furthermore, the principles of SSD techniques can be extended using the dual actuator (i.e. electromagnetic transducer) and/or the dual electrical controlled parameter (i.e. current) (Figure 1.33). The advantages and drawbacks of each method in practical implementation were discussed by Lallart *et al.* [129]. Simulation and experimental results showed that the damping effect is equivalent whatever the technique used for similar electromechanical characteristics. Furthermore, though the dual electrical parameter is a weaker harmonic reinjection, the continuity of the controlled electrical parameter is not ensured, thus needing an external energy supply between two switch instants which prevents self-powering abilities.

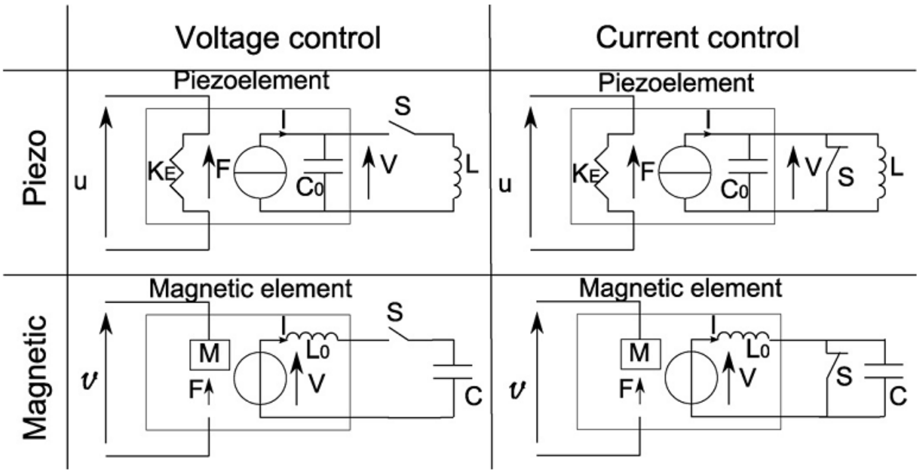

Figure 1.33. Control schematics. [129]

A similar semi-active called synchronized switch stiffness control (SSSC) which relies on connecting the piezoelectric element to the electrical network when the displacement (or equivalently the strain) crosses a zero value (Figure 1.34) was proposed by Guyomar *et al.* [130]. Theoretical and experimental measurements conducted on a cantilever beam under monochromatic excitation showed that it is an effective manner for controlling the stiffness. Different from Davis and Lesieutre's work, this nonlinear processing allows a control of the stiffness out of the open and short circuit limits.

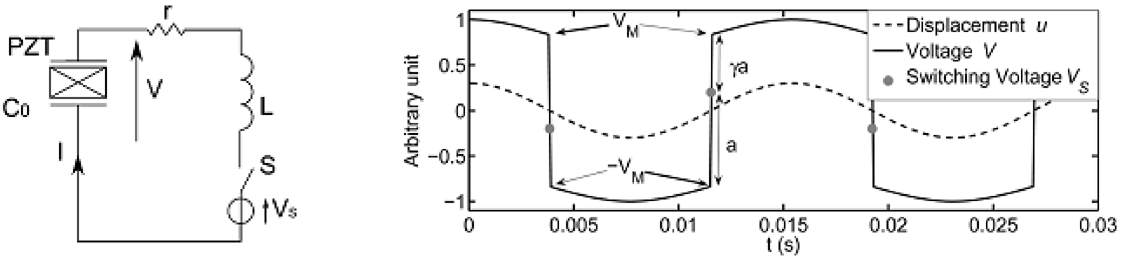

(a) (b)

Figure 1.34. (a) SSSC schematic and (b) SSSC control waveforms. [130]

A novel self-adaptive semi-active technique named blind switch damping (BSD) which consists in connecting the piezoelectric element on an electrical network at a relatively high frequency for a very short time and independently to the structure motion, thus providing a fully adaptive and broadband way for damping was proposed by Lallart *et al.* [131]. With this technique, the piezoelectric insert can be either switched on a short circuit (BSDS) or on a voltage source (Figure 1.35) which can be proportional to the displacement magnitude (BSDVp) or proportional to the instantaneous piezovoltage (BSDVa). From the waveforms given in Figure 1.36, it can be found that such a treatment shapes a voltage whose envelope is in phase with speed, thus creating a viscous friction effect that leads to vibration damping. Comparison to the SSD techniques showed that in terms of damping the BSD technique is less effective; however, it allows a control of re-injected harmonics by changing the number of switches per period *n*. Moreover, since the pseudo-frequency of the electrical network has to be much higher than that in SSD approaches, it leads to a dramatic reduction of the required inductance thus allowing a better integration of the system. Experimental study on a cantilever beam showed that in the case of the BSDVp, the choice of the value of *n* depends on the stability, whereas in the case of BSDS or BSDVa, this is justified by the trade-off between damping and speed reconstruction. Furthermore, it also confirmed that this control law is independent from the structural characteristics, thus offering a good robustness facing environmental drifts.

(a) (b)

Figure 1.35. (a) BSDS basic circuit and (b) BSDV basic circuit[131]

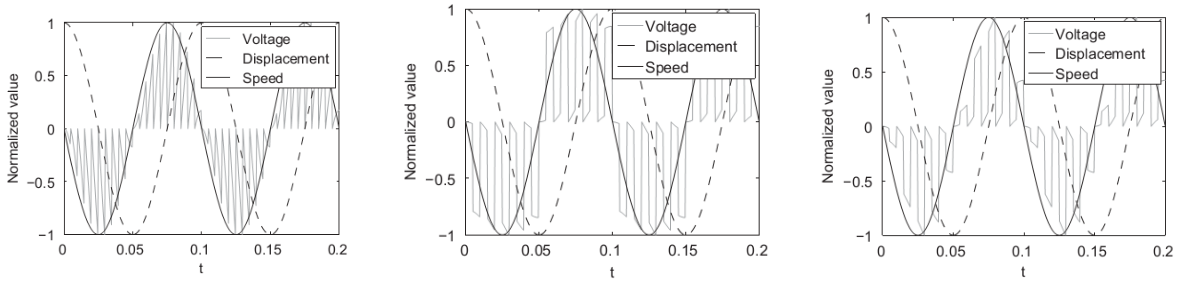

(a) (b) (c)

Figure 1.36. Control waveforms (a) BSDS, (b) BSDVp and (c) BSDVa. [131]

1.3.4. Electromechanical hybrid techniques

Besides the semi-active/semi-passive techniques, hybrid techniques as an alternative category to trade off between passive and active methods have also been developed in recent decades. In the study of Tang and Wang [132], several basic active-passive hybrid piezoelectric networks were analysed and compared. They pointed that larger electromechanical coupling leads to higher passive damping and, depending on the design and configuration, could also derive better active authority and overall performance. Additionally, a negative capacitance circuit (Figure 1.37) for increasing the electromechanical coupling coefficient was proposed and experimental verified. With adding this negative capacitance in the shunt circuit, the overall damping was significantly improved although it leads to larger optimal resistance, power requirement and reduces the voltage amplification effect around the circuit resonant frequency.

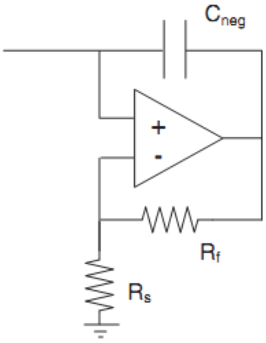

Figure 1.37. Circuit diagram of negative capacitance [132]

In order to obtain same performance as active control in multimodal vibration with significantly reduced the operative energy, Harari *et al.* [133] proposed a hybrid control method (Figure 1.38) which associates the active control with modal semi-active SSDI control. With the monomodal case and wide bandwidth excitation case study, it appeared that non significant interactions are observed between active and SSDI control in the hybrid approach. Meanwhile, the experiments under cantilever beam further confirmed that the hybrid control increases the damping performance and drastically lowers the operative energy requirement.

Tso *et al.* [49] combined the electromechanical active technique using piezoelectric elements with tuned vibration device to damp down all the interested resonant modes and minimize the spatial average mean square motion of vibrating structure. Analytical analysis proved the superior performance on global suppression of broadband vibration of this hybrid vibration absorber.

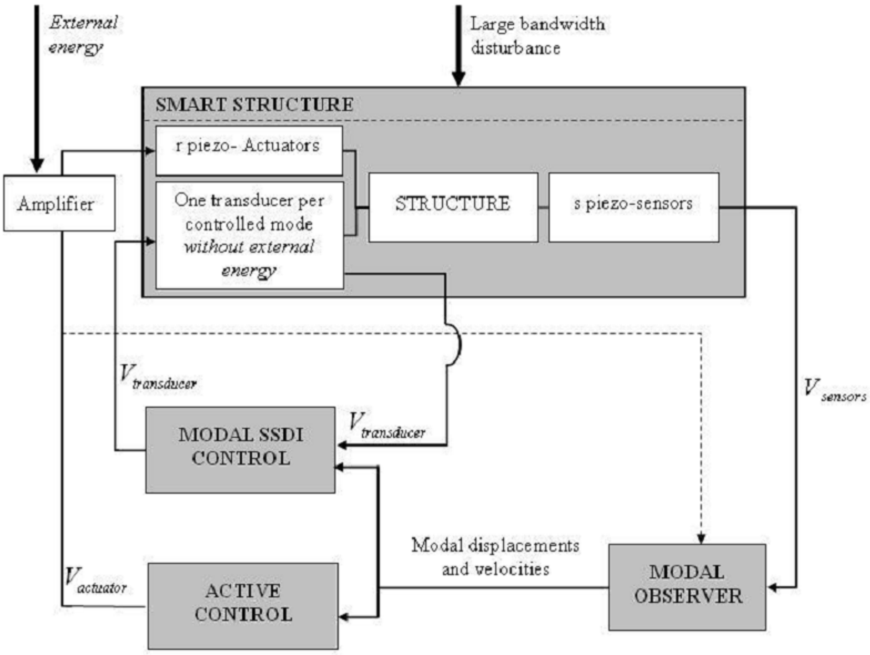

Figure 1.38. Strategy of hybrid control [133].

1.4. Conclusion

In this chapter, the main vibration treatments and systems are reviewed. The control principles of viscoelastic damping systems, particle damping systems, tuned dynamic devices and intelligent systems are briefly introduced. Piezoelectric materials as one type of intelligent materials which can convert the energy between mechanical and electrical forms attract lots of attentions for vibration control thanks to their features such as reliability, compactness, lightness and ease of implementation. Electromechanical control systems integrated with piezoelectric materials are briefly reviewed in passive, active, semi-passive/semi-active and hybrid aspects. Since this work is based on synchronized switch damping (SSD) approaches which are widespread and progressively developed for vibration control due to their simplicity, low power requirements, effective control performance and easy integration, the principles and development are introduced and reviewed in detail.

Chapter 2. Enhanced Synchronized Switch Damping on Inductor (SSDI) Strategy Based on Spatial Filtering

Due to the principles of switching on each extremum value, the synchronized switch damping (SSD) techniques have been proven to be less effective in multimodal vibration control. To improve the multimodal damping effectiveness, a nonlinear damping technique combining SSDI approach with spatial filtering based on the mode shapes of the vibrating structure is proposed in this chapter. For demonstration purpose, two control switches based on the sum and difference of the voltages of the piezoelectric elements and aiming at limiting different interested vibration modes are introduced. In order to verify the damping performance of the multimodal nonlinear damping technique based on spatial filtering, a clamped-clamped beam is used as an illustrative example. According to the mode shapes of the clamped-clamped beam, for attenuating the odd modes, two anti-symmetrically bonded patches are intermittently connected to a switching device composed of a digital switch and an inductor. This electronic switch is kept open except when the sum of the two piezovoltages reaches an extremum value. For limiting the even modes, two symmetrically bonded piezoelectric actuators are connected to the control switching device which is based on the voltage difference. A mathematical model based on finite element method is established for preliminary investigation. Numerical analysis is then experimentally validated. The further applications of the proposed damping technique are also discussed in this chapter.

2.1. Existing multimodal vibration control methods based on SSD techniques

As effective damping techniques for single mode vibration control, synchronized switch damping (SSD) approaches can achieve good control performance by properly phasing the piezovoltage and mechanical motion, thus increasing the converted energy and successfully dissipating the energy in mechanical system. However, it has also been proven that switching at each extremum of the reference signal (piezovoltage/displacement) is not an optimal algorithm of SSD techniques in multimodal vibration control case, since its principle only focuses on the highest detectable mode. Moreover, according to the control criterion of SSD approaches, the extracted energy from the vibrating structure by the piezoelectric patch is proportional to the square of the piezovoltage at the switching moment given as follows

$$E_{extracted} \propto \sum_{k \in N_s} V_k^{\ 2} \tag{2.1}$$

where V_k denotes the piezovoltage before the k^{th} switching action and N_s is the number of switching action.

Hence, there is a trade-off between switching actions and the piezovoltage as shown in Figure 2.1, which further illustrates that the degraded global damping performance of SSD approaches in multimodal control is attributed to the underprivileged lower modes which are most energetic. To enhance the damping effectiveness in multimodal vibration control, several ameliorations have been proposed.

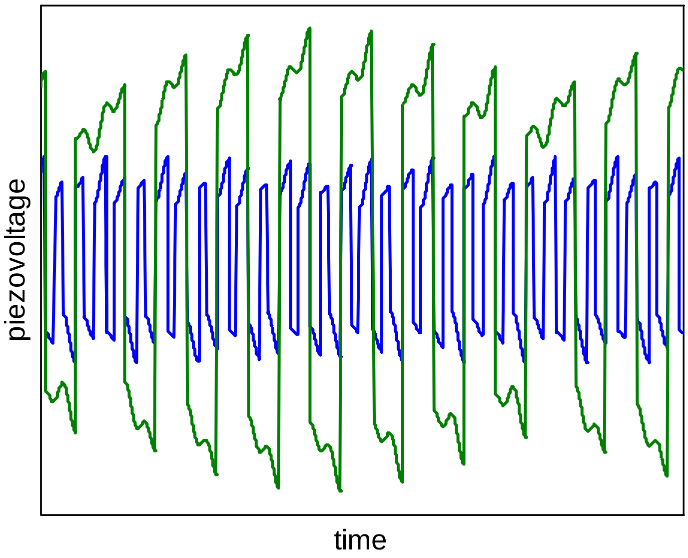

Figure 2.1. Illustration of the trade-off between piezovoltage and the number of switching actions.

Corr and Clark [120] firstly extended the SSD techniques for multimodal vibration control, in which the switch timing is determined according to the rate of energy change. When the product of the applied voltage and the sum of the voltage rates for the controlled modes given in Eq. (2.2) [134] is less than zero, the shunt switch will be shut for removing the energy from mechanical system.

$$P_{SM} = \sum_{j \in M} \alpha_j \dot{r}_j V \tag{2.2}$$

where α_j is the j^{th} macroscopic piezoelectric coefficient and $\dot{r}_j$ denotes the j^{th} velocity temporal coordinate. M is the set of modes to be controlled.

Although the multimodal damping effectiveness has been validated by numerical analysis and experimental measurements, filtering devices are necessary in this technique for selecting the controlled modes and obtaining the modal voltage for each controlled mode. Thus, it inevitably results in time shifts which may decrease the control performance.

A multimodal control algorithm based on probabilistic description of the piezovoltage for SSD techniques was then proposed by Guyomar and Badel [134] in order to optimize the energy dissipation in switching device without any structural information. A voltage threshold v_{min} expressed as Eq. (2.3) is determined with cumulative distribution function F during a preset observation time T_{es}.

$$\begin{gathered} F_{V^2}\left(v^2\right)=P\left[V^2\le v^2\right], \\ P\left[V^2>v_{\min}^2\right]=P_{sw}=1-F_{V^2}\left(v_{\min}^2\right) \end{gathered} \tag{2.3}$$

where P_{sw} is a fixed probability set by user.

Switching process will take place once the extremum occurs with exceeding the statistically probable value (Figure 2.2). It has been verified by simulation that both energy and displacement damping benefits from this probabilistic approach. Moreover, it has also been proven that this control law is insensitive to the boundary conditions and resonance frequencies drifts. Following the probabilistic approach, several statistical thresholds (Table 2.1) determined from average and standard deviation of voltage or displacement signal during a given time window, are employed for investigating the random vibration control effects with SSDI approach by Guyomar *et al.* [135]. Comparison on a clamped beam excited by random noise showed that although both probabilistic and statistical methods require a little knowledge of signals, the adjustment in the latter approach can be coarser. However, for obtaining the statistical threshold based on the corresponding signals, specific sensor needs to be collocated with piezoelectric patch.

By integration the self-powered control circuit proposed by Lallart *et al.* [117], the classical SSDI approach not only achieves the self-powering capability but also enhances its broadband damping effectiveness. Comparators as shown in Figure 1.29 are used to compare the piezovoltage and a reference voltage threshold on the purpose of detecting the proper time for voltage inversion (Figure 2.3 (a)). The electrical switch is disabled as the extremum value is less than the voltage threshold, thus allows improving the global multimodal control ability.

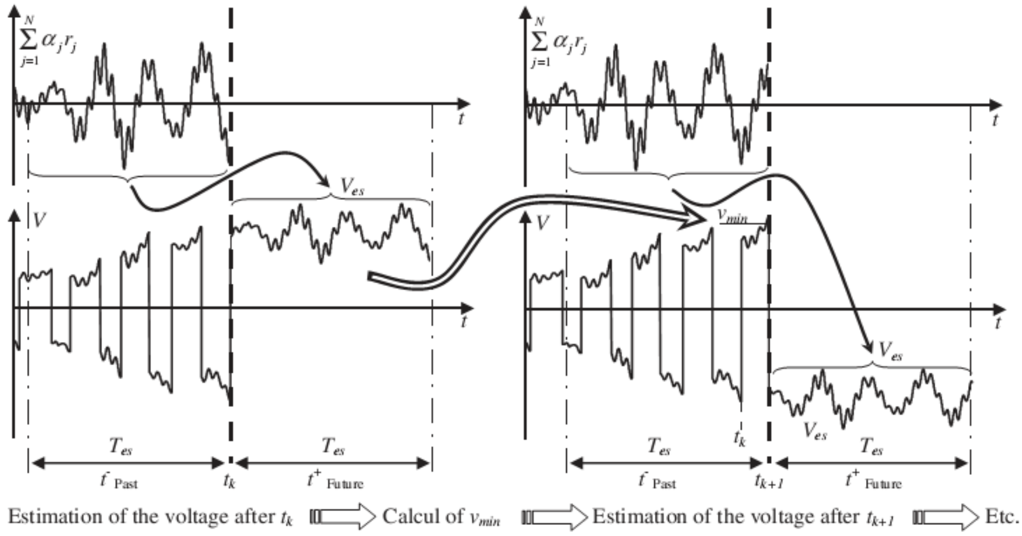

Figure 2.2. Estimation of the piezovoltage after an inversion process [134].

Table 2.1. Statistical thresholds in Guyomar's research.

Thresholds	definition equations	Function definitions
Voltage v_m^2	$v_m^2 = \mu_v^2 + \beta\sigma_v^2$	μ_v^2 : time average of the estimated square voltage σ_v^2 : standard deviation of the estimated square voltage
Deflection u_m	$u_m = \lvert\mu_u\rvert + \beta\sigma_u$	μ_u : time average of the deflection σ_u : standard deviation of the deflection
Root mean square x_m	$x_m = \beta\psi_x$	ψ_x : root mean square of a variable *x(t)* β: an arbitrary tuning coefficient

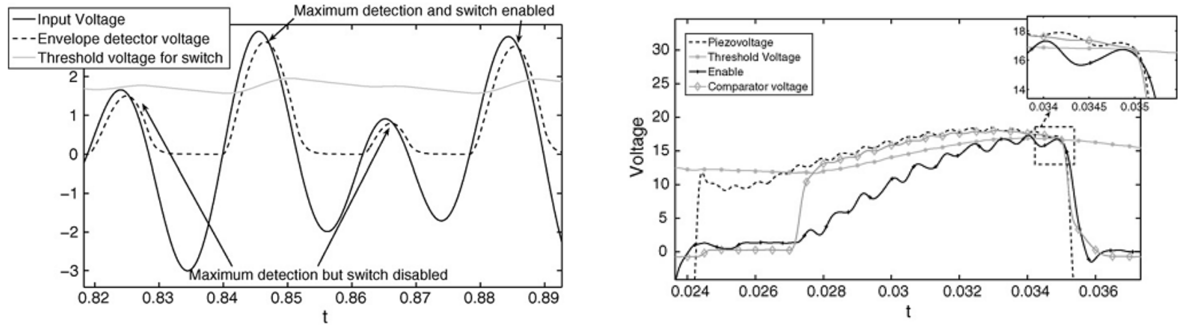

(a) (b)

Figure 2.3. (a) Waveforms of a maximum detector using envelope and threshold voltage and (b) control signals [117].

Similarly, displacement threshold [136] and converted energy threshold [137] for multimodal vibration control using SSD techniques were proposed by Ji *et al.*. In the former approach, the switching action takes place at the displacement extremum which is greater than the threshold calculated from average amplitude of latest ten switching points (Figure 2.4). Although the experimental validation confirmed the improvement of control performance for the first mode based on the displacement threshold, the damping effectiveness for second mode is slightly worse. Generally, the converted energy of a SSD system in a given time window can be expressed by

$$\int_0^T \alpha V_{sw} du = \frac{1+\gamma}{1-\gamma}\frac{\alpha^2}{2C_0}2n\overline{\left|\Delta u_j\right|}^2 \tag{2.4}$$

where γ is the inversion coefficient and C_0 is the capacitance of the piezoelectric patch. $2n$ defines the total number of switching actions in the given time window. $\overline{\left|\Delta u_j\right|}$ is the average effective distance between the neighbouring switching points. α is an arbitrary voltage constant used for normalization.

Although the converted energy depends on both the number of switching $2n$ and the average effective distance $\overline{\left|\Delta u_j\right|}$, it is more sensitive to the latter parameter. Thus, a threshold based on the effective distance can be set for switching detection. Comparative experiments were carried out with SSDI and adaptive SSDV approaches on a composite cantilever beam, which further confirmed the improvement in multimodal damping ability.

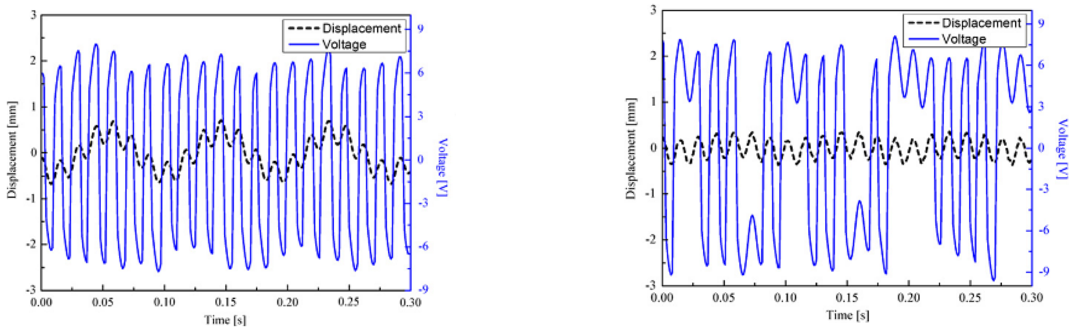

(a) (b)

Figure 2.4. Time response of the displacement and switched voltage on PZT with (a) classical SSDI and (b) SSDI based on displacement threshold approaches. [136]

Harari *et al.* [138] used a Luenberger observer to separate the modal variable from the signal of piezoelectric sensor in order to extend the SSD techniques to any type of excitation. Voltage inversion takes place on the extremum of the targeted modal displacement. Significant reduction and robustness were achieved and validated experimentally on a cantilever beam. However, interaction between controlled and uncontrolled modes was detected. Since the observer requires the identification of the modal characteristics, modal model is indispensable. Moreover, large amount of computation and high number of actuators and sensors are required in this method. Based on Harari's work, Richard *et al.* [139] proposed another control algorithm for triggering the switch named SSDI max. In this method, both the modal displacement extrema and the sign of voltage and its derivative are considered. If the voltage is positive and its derivative is negative when maximum modal displacement occurs, the switch is triggered immediately, or it should wait until this condition is fulfilled. Symmetric algorithm is used for the minimum modal displacement detection. By implementing this algorithm, control voltage for a targeted mode is artificially increased using the electric energy obtained from higher modes. Improvement in the damping for targeted mode was numerically demonstrated under bimodal and pulse excitations.

Several strategies aiming at improving the multimodal damping effectiveness of the SSD techniques are briefly introduced. These control methods are easy to implement and only low power is required for triggering the digital switch. It can be seen that most of the enhanced strategies are based on threshold detections, below which the control process is disabled. Moreover, these threshold criteria are obtained by time domain signal process according to the history of dynamical response in a given time window. In this chapter, a new enhanced SSDI approach based on the spatial filtering process is proposed.

2.2. Principle of enhanced SSDI approach based on spatial filtering

In this section, an enhanced SSDI approach based on spatial filtering is proposed aiming at reducing the multimodal vibration. The control principle and the switching algorithm will be demonstrated in detail for explaining the spatial filtering concept which can separate and filter the interested and untargeted modes respectively before controlling.

Modal filters and observers have been used for modal decomposition, however, the large computational requirements and significant amount of energy for driving the transducers may compromise the realistic applications. Different from the modal filtering which means the projection onto a field with predefined amplitude and phase distribution, spatial filtering means blocking of certain spatial frequencies, analogous to frequency filtering in electronics [140]. Generally, spatial filters implemented in vibration control [141] or damage detection [142] systems aiming at obtaining a single interested output by means of linear combinations are built from arrays of discrete sensors or continuous distributed sensors as shown in Figure 2.5.

In the proposed multimodal nonlinear damping technique using spatial filtering, the sensors used for detecting the switching moments are symmetrically or anti-symmetrically bonded according to the modal responses of the vibrating structure. Targeted modes and uninterested modes can be isolated and filtered from the sensing signal by the switching circuit connection (Figure 2.6). Due to aforementioned property of piezoelectric materials in Chapter 1, the sensors used for switching moment detection in this proposed enhanced nonlinear damping technique based on spatial filtering is dispensable, which can be replaced by the self-sensing actuators or shaped sensors.

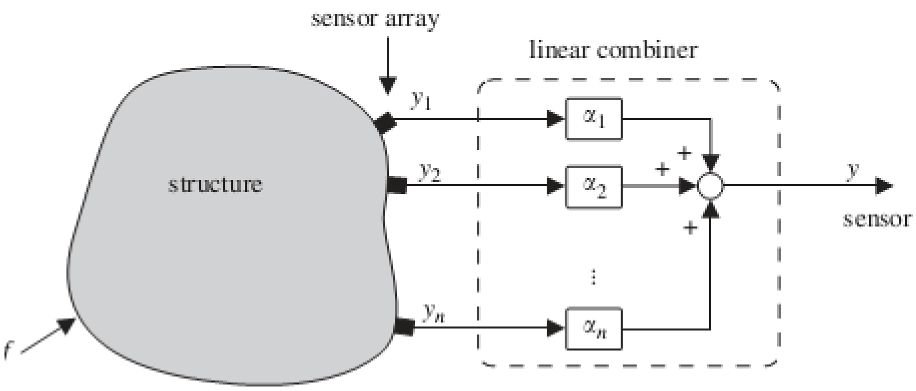

Figure 2.5. Representation of the spatial filter using *n* discrete sensors and a linear combiner [142].

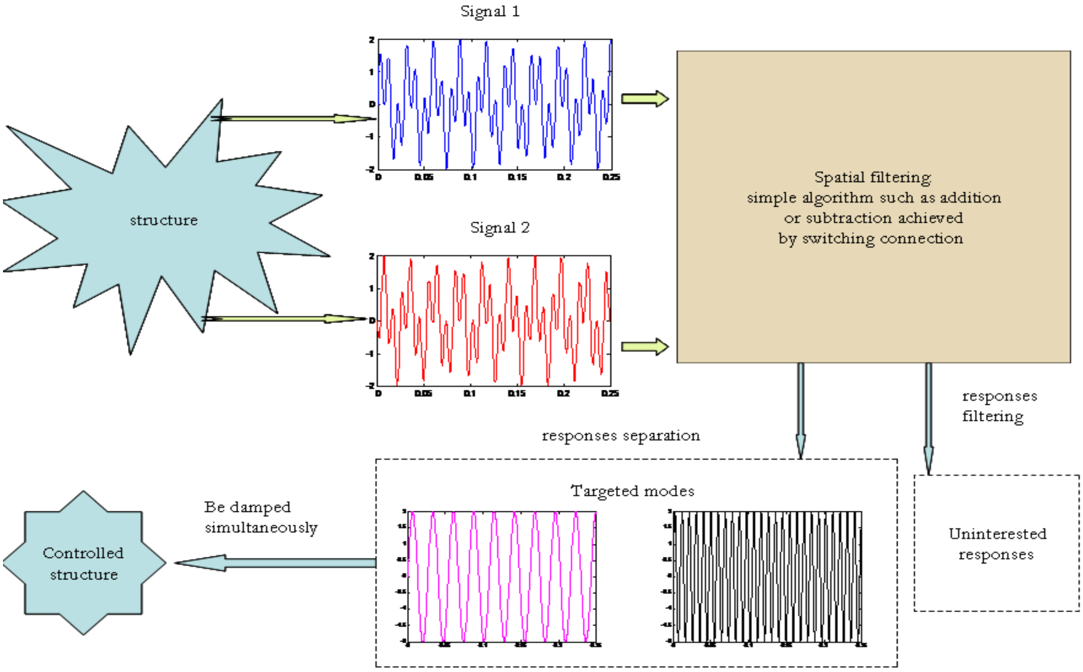

Figure 2.6. Spatial filtering concept in enhanced SSDI approach.

2.2.1. Mathematical modelling

In order to comprehensively demonstrate the spatial filtering concept and the control principle of the proposed multimodal nonlinear damping technique based on spatial filtering process, a clamped-clamped beam is used as an illustrative example. Four piezoelectric patches are symmetrically and anti-symmetrically bonded on the upper and lower surfaces of the beam close to its clamped ends. For simplicity, axes x_1, x_2 and x_3 are defined along the length, width and thickness of the beam, respectively (Figure 2.7).

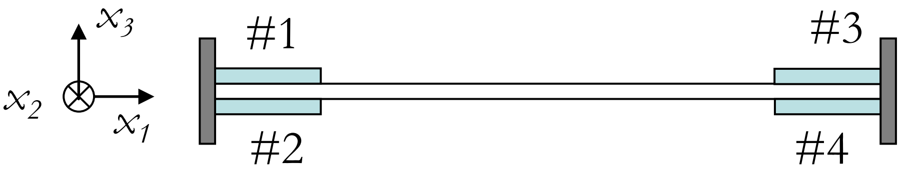

Figure 2.7. Illustrative example for multimodal nonlinear damping technique using spatial filtering.

Several assumptions are made for the mathematical modelling:

1). Investigated beam is governed by Euler-Bernoulli beam theory and the strain has only two dimensions ($S_2 = 0$ and $T_3 = 0$).

2). Piezoelectric material is regarded as a transversely isotropic material (∞-mm symmetry), thus the constitutive equations can be reduced as Eq. (2.5).

$$\begin{bmatrix} S_1 \\ S_2 \\ D_3 \end{bmatrix} = \begin{bmatrix} s_{11}^E & s_{12}^E & \sigma d_{31} \\ s_{12}^E & s_{11}^E & \sigma d_{31} \\ \sigma d_{31} & \sigma d_{31} & \varepsilon_{33}^T \end{bmatrix} \begin{bmatrix} T_{p1} \\ T_{p2} \\ E_3 \end{bmatrix} \tag{2.5}$$

where s^E corresponds to the mechanical compliance tensor of the piezoelectric element under constant electric field and ε^T is the electrical permittivity under constant stress. d_{31} is piezoelectric charge coefficient. T_p denotes the mechanical stress. E_3 and D_3 are the electric field intensity and electric displacement along x_3 direction, respectively. σ is the sign of piezoelectric constant which depends on the direction of polarization of the piezoelectric insert. In this research, it is assumed equal to 1 when the piezoelectric patch is bonded on the upper surface and -1 as the piezoelectric patches attached on the lower surface.

3). Polarization direction of piezoelectric patches is along the thickness of the beam. Electric field intensity in the piezoelectric patch is assumed constant and the beam serves as a common ground.

On the basis of these assumptions, the motion equation of the electromechanical beam can be given by Eq. (2.6) using finite element method [143] and the formulation in detail is given in Appendix.

$$[M]\{\ddot{d}\}+[C]\{\dot{d}\}+[K]\{d\}-[B_1]\{V_p\}=\{F(t)\} \tag{2.6}$$

where $\{d\}$ is the variables vector of electromechanical structures with two degree of freedoms, namely, deflection and slope for each node. M, C, K and V_p are mass, damping, stiffness and piezovoltage matrices. B_1 is the global force factor matrix assembling by

$$B_1^e = b_1 \int_0^l \left[H_{er}''\right]^T dx_1$$
$$\text{with } b_1 = \frac{\sigma d_{31} w}{t_p\left(s_{11}^E + s_{12}^E\right)} \int_{t_b}^{t_b+t_p} \left(x_3 - x_c\right) dx_3 \tag{2.7}$$

H_{er} is the Hermitian shape function. l is the length of one element. t_p and t_b denote the thickness of the piezoelectric patch and the beam respectively. w is the width of the investigated beam and the bonded piezoelectric patch, namely the width of the bending beam is same as that of the piezoelectric element. x_c is the position of neutral axis.

In order to simplify the electrical equation of the electromechanical beam, it is supposed that the piezoelectric patches are identical and the width and thickness are same. The i^{th} piezoelectric patch with its length L_{pi} is bonded at the position $x_{i0} \le x_1 \le x_{i0} + L_{pi}$ of the bending beam. Thus, the electric charge Q_i generated by the i^{th} piezoelectric element during the vibration can be expressed with the bending slope θ and piezovoltage V_{pi}:

$$Q_i = -\frac{w t_p \left(\sigma d_{31}\right)_i \theta\Big|_{x_{i0}}^{x_{i0}+L_{pi}}}{s_{11}^E + s_{12}^E} - \frac{w L_{pi}\left[\varepsilon_{33}^T\left(s_{11}^E + s_{12}^E\right) - 2 d_{31}{}^2\right]}{t_p\left(s_{11}^E + s_{12}^E\right)} V_{pi} \tag{2.8}$$

Then, the global electrical relationship can be given in matrix-vector notation by

$$\{Q\} = [B_2]\{d\} + [B_3]\{V_p\} \tag{2.9}$$

with B_2 assembled by

$$B_2^e = -\frac{w t_p d_{31}}{s_{11}^E + s_{12}^E}[\sigma] \cdot \int_0^l \left[H_{er}''\right] dx \tag{2.10}$$

and

$$B_3 = -\frac{w\left[\varepsilon_{33}^T\left(s_{11}^E + s_{12}^E\right) - 2 d_{31}{}^2\right]}{t_p\left(s_{11}^E + s_{12}^E\right)}\left[L_p\right] \tag{2.11}$$

where $[\sigma]$ and $\left[L_p\right]$ are diagonal matrices which respectively depend on the polarization and length of the bonded piezoelectric patches.

Thus, the dynamical relationships of the electromechanical beam can be demonstrated and summarized as

$$\begin{cases} [M]\{\ddot{d}\}+[C]\{\dot{d}\}+[K]\{d\}-[B_1]\{V_p\}=\{F(t)\} \\ \{Q\}=[B_2]\{d\}+[B_3]\{V_p\} \end{cases} \tag{2.12}$$

With this mathematical model which is also valid for any boundary conditions, the electromechanical behaviour of the investigated beam under external excitation can be predicted and simulated.

2.2.2. Classical SSDI technique

In the classical SSDI approach, each piezoelectric element is connected in parallel to a switching device which is composed of a digital switch S_w and an inductor L_{in} as shown in Figure 2.8.

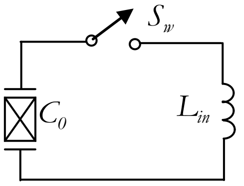

Figure 2.8. Control circuit of classical SSDI approach.

This switch is always kept open except the strain of piezoelectric patch reaches an extremum value. As it is in off state, the current in this control circuit is null. Therefore, the electrical relationship of the i^{th} piezoelectric patch holds

$$\dot{V}_{pi}=-\frac{t_p{}^2(\sigma d_{31})_i}{L_{pi}\left[\varepsilon_{33}^T\left(s_{11}^E+s_{12}^E\right)-2d_{31}{}^2\right]}\dot{\theta}\Big|_{x_{i0}}^{x_{i0}+L_{pi}} \tag{2.13}$$

With the null initial condition, the piezovoltage of i^{th} piezoelectric element can be expressed as:

$$V_{pi}=-\frac{t_p{}^2(\sigma d_{31})_i}{L_{pi}\left[\varepsilon_{33}^T\left(s_{11}^E+s_{12}^E\right)-2d_{31}{}^2\right]}\theta\Big|_{x_{i0}}^{x_{i0}+L_{pi}} \tag{2.14}$$

which can show that the piezovoltage varies with the displacement response in open circuit.

When an extremum is detected, the switch will be closed for half a period t_i (Eq. (2.15)) of the electrical oscillator constituted by the capacitance of the piezoelectric element and the inductor for voltage inversion.

$$t_i=\pi\sqrt{L_{in}C_0} \tag{2.15}$$

Compared with the vibration period of the electromechanical structure, the switching time is short enough to be considered as instantaneous switching so that there is no displacement variation during the inversion process. Consequently, the current flowing out of the i^{th} piezoelectric patch when the switch is closed is obtained as:

$$\dot{Q}_i = -\frac{wL_{pi}\left[\varepsilon_{33}^{T}\left(s_{11}^{E}+s_{12}^{E}\right)-2d_{31}^{\ 2}\right]}{t_p\left(s_{11}^{E}+s_{12}^{E}\right)}\dot{V}_{pi} \tag{2.16}$$

According to Eq. (2.16), the relationship of classical SSDI control circuit in on state can be presented by the differential equation:

$$\ddot{V}_{pi} = -\frac{1}{L_{in}C_{oi}}V_{pi} - \frac{\mathrm{R}}{L_{in}}\dot{V}_{pi} \text{ with } C_{0i} = \frac{wL_{pi}\left[\varepsilon_{33}^{T}\left(s_{11}^{E}+s_{12}^{E}\right)-2d_{31}^{\ 2}\right]}{t_p\left(s_{11}^{E}+s_{12}^{E}\right)} \tag{2.17}$$

where R denotes the resistance (losses) of the control circuit and C_{0i} is the clamped capacitance of the i^{th} piezoelectric patch.

Generally, the energy loss in the switching network (digital switch and inductor) is inevitable, thus the inversion process is imperfect. To preliminarily evaluate the damping performance, a voltage coefficient $\gamma\,(0 \le \gamma < 1)$ is introduced:

$$\gamma_{classical} = e^{-\frac{\pi \mathrm{R}}{2}\sqrt{\frac{C_0}{L_{in}}}} \tag{2.18}$$

2.2.3. Switching algorithm of the enhanced SSDI approach based on spatial filtering

It has been demonstrated in cited literature in (section 2.1) that the multimodal vibration control performance of the classical SSDI approach is diminished, since it focuses on the highest detectable frequency mode due to its principle which is besides not as electromechanically coupled as the first ones in general cases. In order to improve the damping effectiveness in multimodal vibration, a new switching algorithm based on spatial filtering will be presented. Two switching connections aiming at limiting the odd modes and even modes of the illustrative example (clamped-clamped beam) will be introduced.

Switching connection for odd modes

It can be easily found from Figure 2.9 that the displacement responses at the positions where boned the piezoelectric patches are same in odd modes and opposite in even modes. Thus, when the anti-symmetrically bonded patches such as #1 and #4 or #2 and #3 are connected in series as shown in Figure 2.10, the even modes of the voltage responses will be eliminated and the odd modes will be isolated, which is equivalent to a spatial filtering process. With this switching connection, the electric switch is always kept open except when the sum of the two piezovoltages reaches an extremum value. Consequently, Eqs. (2.13) and (2.14) are still valid when the switch is in off state.

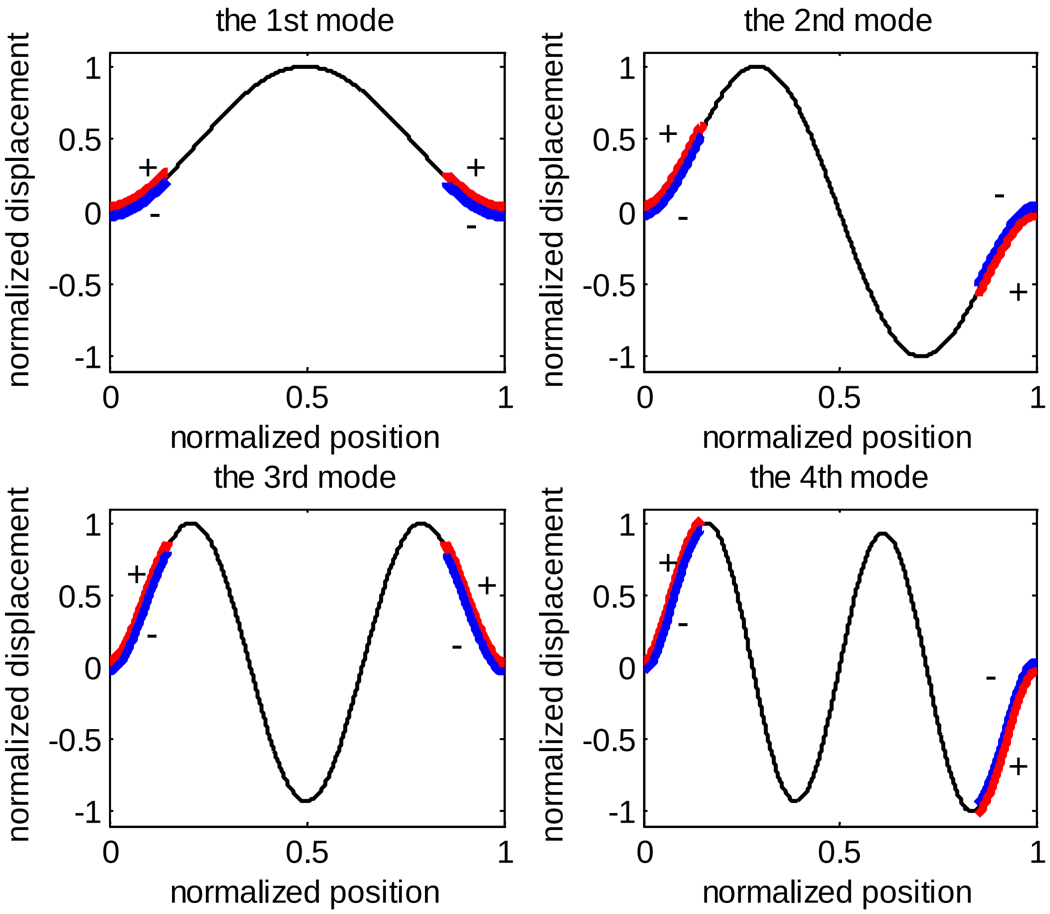

Figure 2.9. The first four mode shapes of a clamped-clamped beam (thick line: piezoelectric patches; thin line: host beam).

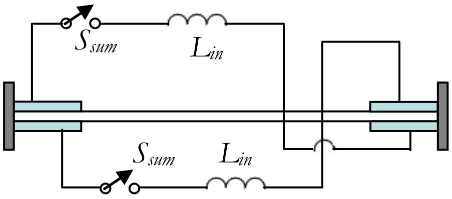

Figure 2.10. Switching connection for suppressing odd modes with enhanced SSDI approach based on spatial filtering.

As the extrema of the sum of the piezovoltages occur, the switch will be closed and at that moment, the capacitances of the two anti-symmetrically bonded piezoelectric patches and the inductor constitute an electrical oscillator. This switch will reopen after half a period of this oscillator until the sum of the piezovoltages is reversed. Supposing the piezoelectric patches are identical, the switching time can be expressed as:

$$t_i = \pi\sqrt{L_{in}\frac{C_0}{2}} \tag{2.19}$$

Since the switching time is short enough compared with the period of vibration, it can be considered that there is no displacement variation when the switch is in on state. Hence, the current flowing out of the i^{th} piezoelectric patch can be obtained from Eq. (2.16) and the following differential equation used to represent the control circuit with the switch on holds:

$$\begin{Bmatrix} \ddot{V}_{pi} \\ \ddot{V}_{pj} \end{Bmatrix} = \frac{1}{L_{in}C_0}\begin{bmatrix} -1 & -1 \\ -1 & -1 \end{bmatrix}\begin{Bmatrix} V_{pi} \\ V_{pj} \end{Bmatrix} - \frac{R}{L_{in}}\begin{Bmatrix} \dot{V}_{pi} \\ \dot{V}_{pj} \end{Bmatrix} \tag{2.20}$$

where the subscripts i and j denote the i^{th} and j^{th} piezoelectric patches which are anti-symmetrically attached and connected by the control switch device.

As in the previous discussion, the inversion is imperfect and the inversion coefficient in this case can be expressed as:

$$\gamma_{enhanced} = e^{-\frac{\pi R}{2}\sqrt{\frac{C_0}{2L_{in}}}} = \gamma_{classical}^{\sqrt{\frac{1}{2}}} > \gamma_{classical} \tag{2.21}$$

From the comparison, it can be found that the inversion coefficient with this switching algorithm is a bit higher than that in classical SSDI approach which allows slightly better damping performance in vibration control as the total piezoelectric capacitance is decreased from C_0 to $C_0/2$. Since this control switching is according to the sum signal of two anti-symmetrically bonded piezoelectric patches, hereinafter, it will be named as “sum switch”.

Switching connection for even modes

To suppress the even modes, the symmetrically bonded piezoelectric patches such as #1 and #3 or #2 and #4 are connected in series as shown in Figure 2.11 according to the mode shapes of the bending beam (Figure 2.9).

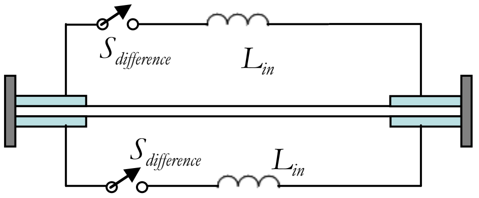

Figure 2.11. Switching connection for limiting even modes with enhanced SSDI approach based on spatial filtering.

Since this connection is equivalent to a spatial filtering process which can concentrate the even modes and filter the odd modes, therefore, the even modes can be effectively separated and damped. When this switching connection is integrated, the control switch is kept open except when the difference of the two piezovoltages reaches an extremum value. Thus, the electrical relationship of the i^{th} piezoelectric element in open circuit expressed as Eqs. (2.13) and (2.14) are still valid. When the extremum of the difference signal is detected, the symmetrically bonded patches will be connected to the switching device to induce the voltage inversion. The switching time is the same as in Eq. (2.19). The differential equations used to represented the control circuit as the switch is in on state are in the form of

$$\begin{Bmatrix}\ddot{V}_{pi}\\ \ddot{V}_{pj}\end{Bmatrix}=\frac{1}{L_{in}C_0}\begin{bmatrix}-1&1\\1&-1\end{bmatrix}\begin{Bmatrix}V_{pi}\\ V_{pj}\end{Bmatrix}-\frac{R}{L_{in}}\begin{Bmatrix}\dot{V}_{pi}\\ \dot{V}_{pj}\end{Bmatrix} \qquad (2.22)$$

The inversion coefficient in this case is same as that in the switching connection for odd modes suppression which is given by Eq. (2.21). For simplicity, this switching will be referred to as "difference switch" since its principle is due to the difference of the piezovoltages of two symmetrically attached patches.

Switching algorithm for suppression both odd and even modes

Based on the previous demonstration, both odd and even modes can be damped separately and simultaneously as two switching connections are integrated as shown in Figure 2.12.

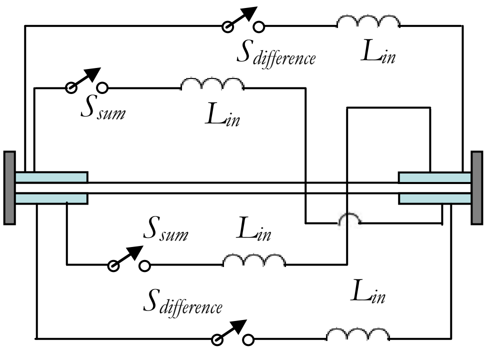

Figure 2.12. Switching connections for controlling odd and even modes simultaneously.

The sum switches and difference switches, which are respectively based on the sum and difference of the piezovoltages of the connected piezoelectric patches, work independently with these connections. Thanks to the spatial filtering process, the targeted and uninterested modes can be separated and filtered before damping, which allows elimination of dispensable switching actions and thus improving the multimodal vibration control performance.

The switching principles of classical SSDI approach and the enhanced nonlinear damping strategy based on spatial filtering are presented in this section. A new control algorithm based on the sum or difference signal of the piezovoltages of two anti-symmetrically or symmetrically attached patches is introduced. By integrating the sum and difference switches, the multimodal vibration can be separated and spatially filtered without any prejudicial interaction and the interested modes can be damped simultaneously. In order to preliminarily predict and evaluate the damping effectiveness of the enhanced strategy, the simulation of the illustrative example will be discussed in next section.

2.3. Simulations

In this section, the damping attenuation of classical SSDI technique and the enhanced nonlinear damping approach based on spatial filtering will be predicted according to the previously demonstrated mathematical model. A clamped-clamped beam with four piezoelectric patches attached close to the clamped ends on its upper and lower surfaces is simulated with MATLAB using home-made finite element analysis script. Since the first two modes are generally the most energetic ones, we only focus on the first two modes of the illustrative example in this section for demonstration purpose. The damping performances of classical SSDI technique and enhanced nonlinear damping approach using spatial filtering under monochromatic and multi-frequency excitations will be compared and discussed. The dimensional and material properties of the simulated electromechanical beam are summarized in Table 2.2 and Table 2.3.

Table 2.2. Dimensional and material properties of the clamped-clamped beam.

Young's modulus	$Y_b = 190\times10^9 Pa$	Poisson's ratio	$\nu_b = 0.21$	density	$\rho_b = 7875\, kg/m^3$
length	$L_b = 350\times10^{-3} m$	width	$w_b = 35\times10^{-3} m$	thickness	$t_b = 1.2\times10^{-3} m$

Table 2.3. Dimensional and material properties of piezoelectric patches.

Compliance in short circuit	$s_{11}^E = 10.66 \times 10^{-12}\ m^2/N$	length	$L_p = 30 \times 10^{-3}\,m$
	$s_{12}^E = -3.34 \times 10^{-12}\ m^2/N$		
Charge coefficient	$d_{31} = -108 \times 10^{-12}\ m/V$	thickness	$t_p = 0.4 \times 10^{-3}\,m$
Relative dielectric constant	$\varepsilon_{33}^T/\varepsilon_0 = 1150$	density	$\rho_p = 7650\,kg/m^3$

According to the given parameters, the first two resonance frequencies f_{1s} and f_{2s} of the electromechanical beam in open circuit are obtained at 66.45 *Hz* and 170.6 *Hz* based on the finite element modelling. Although there are several methods to introduce the damping matrix *C* such as calculated from experimental measurements or defined from the complex stiffness matrix etc., in this simulation, the Rayleigh damping (Eq. (2.23)) which is proportional to the mass and stiffness is used.

$$C = \beta_1 M + \beta_2 K \tag{2.23}$$

The proportional damping coefficients β_1 and β_2 listed in Table 2.4 are delicately chosen in this simulation to ensure the damping ratios (ζ_1=0.004 and ζ_2=0.0025) are same as those measured in the experiments which will be introduced in next section.

Table 2.4. Proportional damping coefficients used in simulation.

$\beta_1 = 3.31$	$\beta_2 = 2 \times 10^{-6}$

2.3.1. Damping effectiveness under monochromatic excitation

To discuss the single mode damping performances of the enhanced nonlinear damping approach using spatial filtering, a monochromatic excitation at one of the first two resonance frequencies is applied at the position $x_1 = 85 \times 10^{-3}\,m$ of the clamped-clamped beam.

The first mode control case

When an external force in forms of

$$F = \sin\left(\omega_{1s} t\right) \text{ with } \omega_{1s} = 2\pi f_{1s} \tag{2.24}$$

is applied, the four piezoelectric actuators are respectively connected to four control circuits and work independently (Figure 2.13) using classical SSDI technique. Since only the first mode is excited under this applied force, only two sum switches based on the sum of the piezovoltages of the anti-symmetrically attached patches are used for attenuation in the case of the enhanced SSDI strategy based on spatial filtering (Figure 2.10).

In order to qualitatively compare the damping effectiveness of these two control approaches, the same inductance value is chosen for each control circuit. The corresponding parameters for control switching in this simulation are listed in Table 2.5. The normalized displacement response at $x_1 = 257\times10^{-3}\,m$ with and without control are plotted in Figure 2. 14.

The attenuation defined by

$$Attenuation = 20\times\log_{10}\left(\frac{steady\ state\ amplitude\ with\ control}{steady\ state\ amplitude\ without\ control}\right) \tag{2.25}$$

obtained from the simulation results is listed in Table 2.6. It should be noted that the value of attenuation is negative as the vibration is reduced. Otherwise, the vibration is amplified.

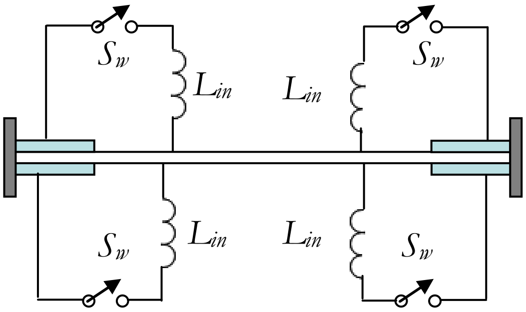

Figure 2.13. Switching connections using classical SSDI technique in simulation and experiments.

Table 2.5. Parameters for control switching in simulation.

	Classical SSDI approach	Strategy based on spatial filtering	
		Sum switch	Difference switch
L_{in}	0.7 H	0.7 H	0.7 H
t_i	0.0003 s	0.0002 s	0.0002 s
γ	0.8	0.82	0.82

Table 2.6. Attenuation of simulation under monochromatic and multi-frequency excitations.

	$F=\sin(\omega_{1s}t)$	$F=\sin(\omega_{2s}t)$	$F=\sin(\omega_{1s}t)+4\sin(\omega_{2s}t)$	Band-limited white noise
Classical SSDI technique	-19.91 dB	-19.36 dB	-12.6 dB	-2.49 dB
Strategy based on spatial filtering	-21.13 dB	-19.81 dB	-20.43 dB	-6.8 dB

Reduction of -19.91 *dB* and -21.13 *dB* for attenuating the first mode are respectively obtained with classical SSDI approach and the enhanced strategy based on spatial filtering. From this simulation, it can be easily found that both techniques can achieve good damping performance for control the single modal vibration. Moreover, the damping performance of the proposed strategy based on spatial filtering is slightly better than SSDI approach since the inversion coefficient of the proposed method is a litter bit greater than that of classical SSDI approach.

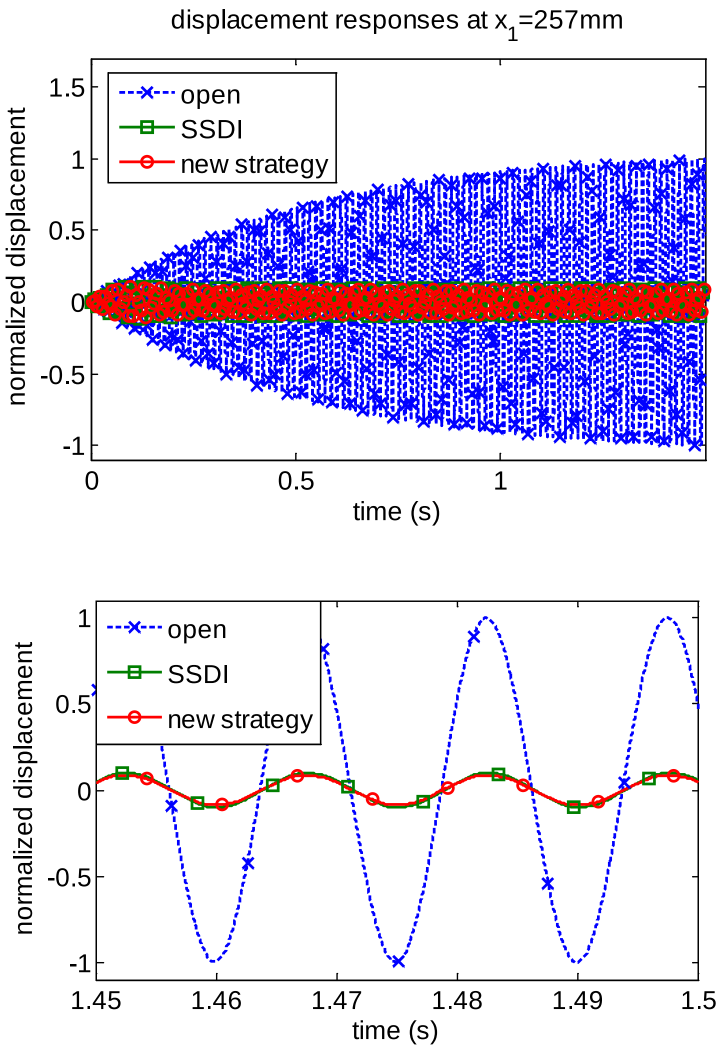

Figure 2. 14. Time responses at $x_1 = 257\times10^{-3}\,m$ with and without control under external excitation $F = \sin\left(\omega_{1s} t\right)$.

The second mode control case

Another single mode case under the external force

$$F = \sin\left(\omega_{2s} t\right) \text{ with } \omega_{2s} = 2\pi f_{2s} \tag{2.26}$$

is also simulated.

For damping the second mode, four control switches are implemented (Figure 2.13) with classical SSDI technique, and only the two difference switches based on the difference of piezovoltages of the symmetrically bonded piezoelectric patches are employed in the enhanced strategy (Figure 2.11). The corresponding parameters for control switching are same as that in the previous single mode case listed in Table 2.5. The normalized displacement responses at $x_1 = 257\times10^{-3}\,m$ with and without control are plotted in Figure 2.15. The obtained attenuation is given in Table 2.6. The amplitude of displacement response is limited by -19.36 *dB* in this case with original classical SSDI approach and -19.81 *dB* using the enhanced strategy based on spatial filtering. Slightly better damping is still found in the proposed strategy attributed to the greater inversion coefficient.

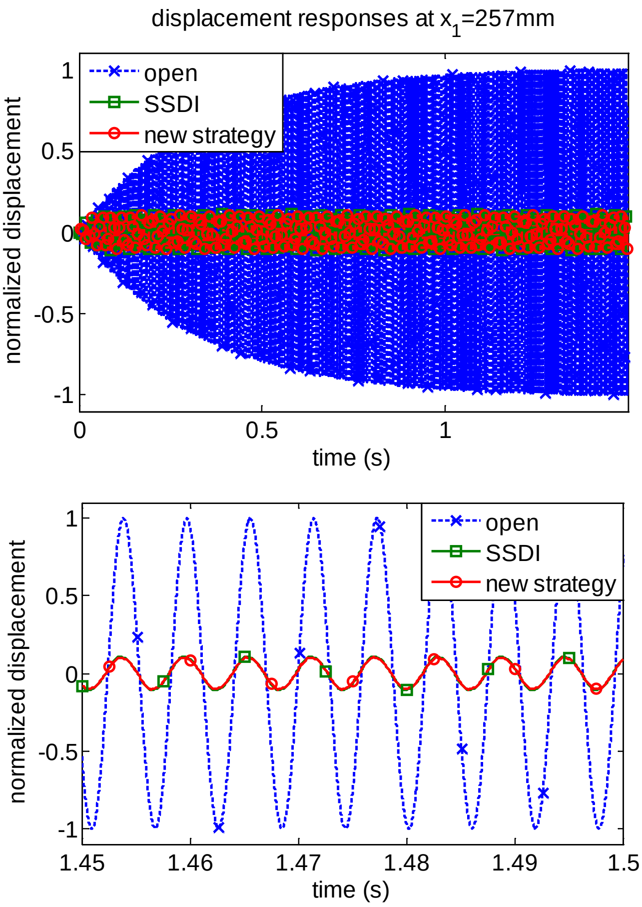

Figure 2.15. Time responses at $x_1 = 257\times10^{-3}\,m$ with and without control under external excitation $F = \sin\left(\omega_{2s} t\right)$.

According to the simulation results obtained under monochromatic excitation, it is further confirmed that both classical SSDI approach and the enhanced strategy based on spatial filtering can effectively damp the single modal vibration. Furthermore, the enhanced strategy shows slightly superior damping performance since the inversion coefficient is a bit greater than that in classical SSDI approach.

2.3.2. Damping effectiveness under multi-frequency excitation

Since the proposed nonlinear damping strategy based on spatial filtering aims at improving the multimodal damping effectiveness of SSDI approach, the dynamical responses of the illustrative example are simulated and discussed under multi-frequency excitation in this part. Typically, the most part of the energy is concentrated on the first two modes of the vibrating structure in multimodal vibration. Therefore, in this subsection, we focus on the first two modes vibration damping. The dynamical responses under bimodal and band limited white noise excitation will be simulated and compared using classical SSDI approach and the proposed enhanced nonlinear damping strategy based on spatial filtering.

Bimodal control case

In order to excite the first two modes of the clamped-clamped beam, a bimodal excitation

$$F = \sin\left(\omega_{1_s} t\right) + 4\sin\left(\omega_{2_s} t\right) \tag{2.27}$$

is applied at $x_1 = 85\times10^{-3}m$ of the beam, which is around a quarter of the overall length. Amplitude ratio is chosen as 4 to strengthen the response of the higher mode. Four control switches are used both in the classical SSDI case (Figure 2.13) and in the case of using proposed strategy based on spatial filtering (Figure 2.12). The corresponding parameters of control circuit are listed in Table 2.5. The dynamical responses at $x_1 = 257\times10^{-3}m$ obtained without control and controlled using classical SSDI approach or enhanced strategy based on spatial filtering are plotted in Figure 2.16.

In the bimodal case, the root mean square (RMS) value of the steady state displacement response is reduced by -12.6 *dB* using original SSDI technique. Meanwhile, -20.43 *dB* damping attenuation (Table 2.6) is achieved with the proposed nonlinear damping strategy based on spatial filtering, which exhibits superior multimodal control performance.

Typical voltage waveforms with original SSDI technique and the proposed enhanced strategy are exposed in Figure 2.17 and Figure 2.18.

From the voltage waveforms in open circuit and controlled cases, it can be noticed that the classical SSDI approach focuses on the second mode under the bimodal excitation, which is attributed to the control principle that the voltage inversion process takes place at each extremum occurrence. Hence, the second mode of the vibrating beam can be effectively damped. However, the damping performance for reducing the first vibration mode is deteriorated (Figure 2.19).

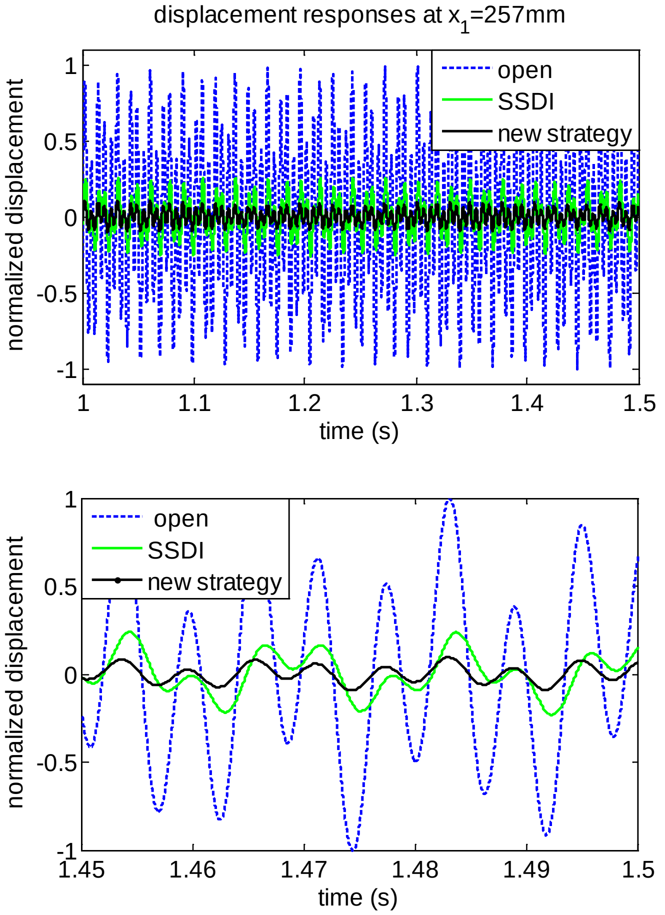

Figure 2.16. Time responses at $x_1 = 257\times10^{-3}\,m$ with and without control under bimodal excitation.

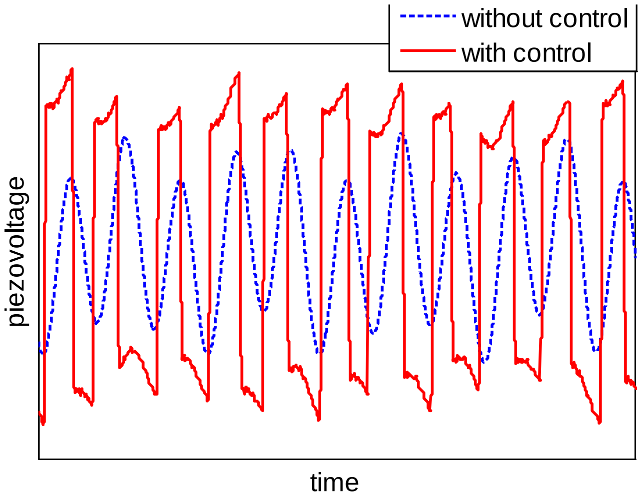

Figure 2.17. Voltage waveforms using classical SSDI technique.

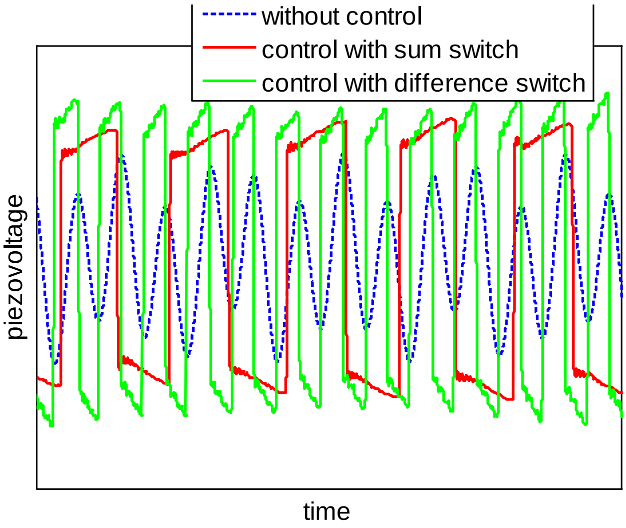

Figure 2.18. Voltage waveforms with enhanced nonlinear damping strategy using spatial filtering.

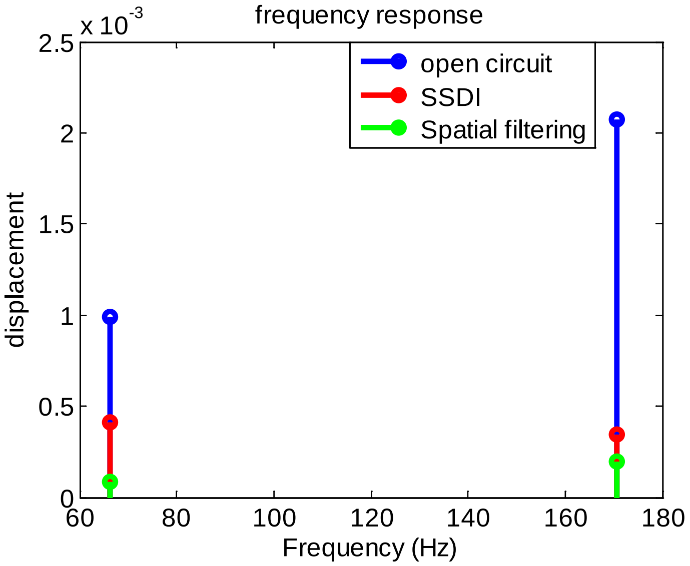

Figure 2.19. Frequency responses at $x_1 = 257 \times 10^{-3} m$ under bimodal excitation.

With the proposed strategy using spatial filtering, the first mode and the second mode can be respectively isolated by sum switch and difference switch. Therefore, by employing these two switches under the bimodal excitation, the first mode of the bending beam can be effectively suppressed by sum switch and simultaneously, the second mode can be significantly damped by the difference switch. From this comparison, it is preliminarily verified that the proposed nonlinear damping strategy based on spatial filtering is an effective multimodal control approach.

Band-limited white noise case

To further discussion the multimodal damping performance of the proposed nonlinear damping strategy based on spatial filtering, the dynamical responses of the electromechanical beam under band limited white noise (Figure 2.20) in the range of 10-210 Hz, allowing focus the first two modes, are simulated.

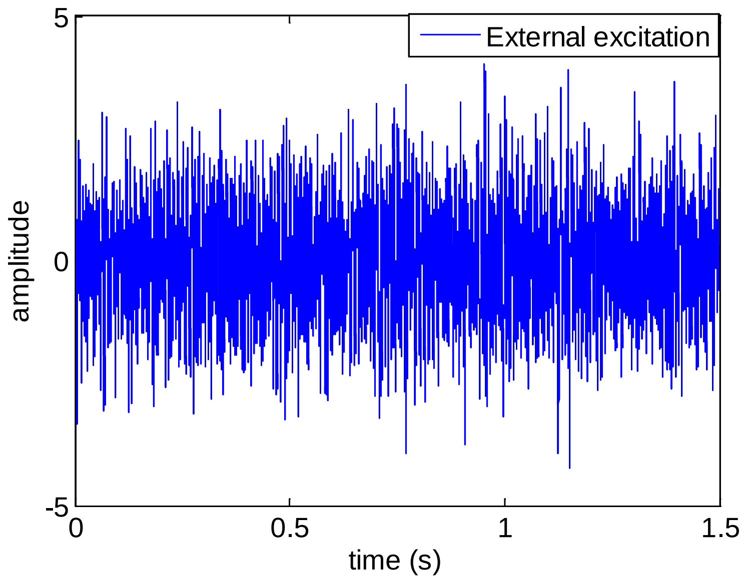

Figure 2.20. Band-limited white noise excitation given in simulation.

Figure 2.21 exposes the dynamical responses simulated under the band-limited white noise. From the responses comparison in time domain and frequency domain (Figure 2.22), it can be found that the proposed nonlinear damping technique using spatial filtering can effectively damp the first two modes by integrating the sum switch and difference switch, while with the original SSDI approach, only the second mode can be significantly damped.

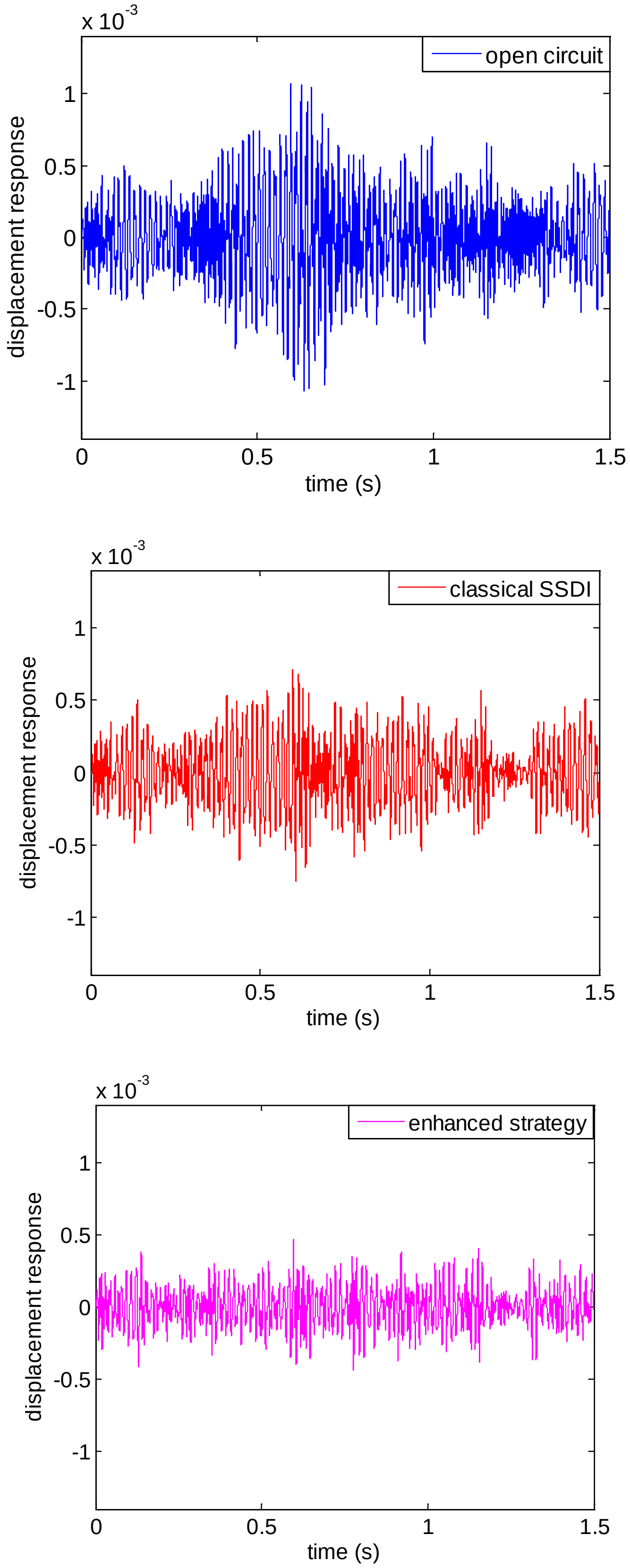

Figure 2.21. Simulation results at $x_1 = 257\times10^{-3}\,m$ in time domain measured under band-limited white noise.

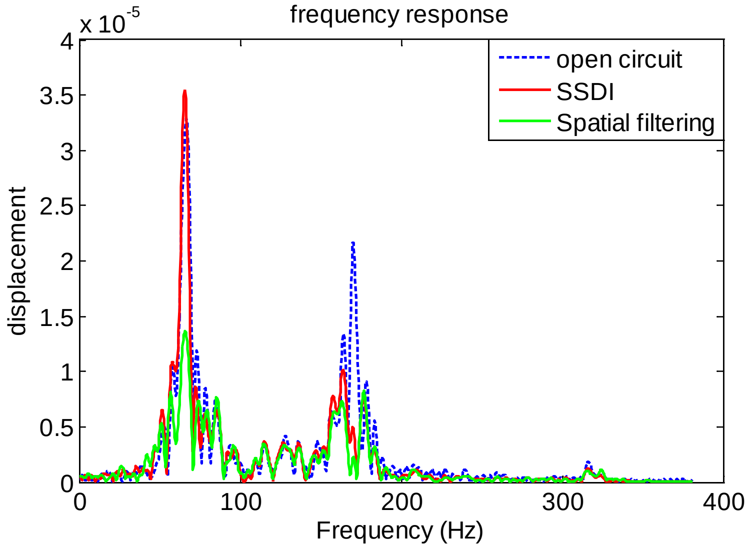

Figure 2.22. Responses at $x_1 = 257\times10^{-3}m$ obtained by Fast Fourier transform under band limited white noise.

From the simulation demonstration, it is further proven that although the classical SSDI technique is effective for single modal control, its damping performance is decreased in multimodal vibration due to its switching principle. To enhance the multimodal damping capability, sum switch and difference switch are integrated, which can isolate the concentrated modes and filter the uninterested modes according to the dynamical responses of the vibrating structure. Targeted modes can be effectively and simultaneously suppressed with this enhanced strategy, which outperforms to the classical SSDI technique. To validate the obtained simulation results and further confirm the multimodal damping performance of the enhanced strategy based on spatial filtering, the experiments are carried out. The details of the experiments will thus be described in the next section.

2.4. Experiments

To validate the simulated damping effectiveness of the enhanced nonlinear damping strategy based on spatial filtering, a clamped-clamped electromechanical beam is driven by monochromatic excitation, bimodal excitation and band-limited white noise. The dynamical responses measured in the experiments with different control techniques are investigated, compared and discussed.

2.4.1. Experimental setup

The schematic diagram of the experimental setup is depicted in Figure 2.23. A steel clamped-clamped beam is used as experimental sample. Four piezoelectric patches with same dimensions and properties are anti-symmetrically and symmetrically bonded on the upper and lower surfaces of the beam close to the clamped ends where the strain energy is relatively higher and better couplings appear for the mode of interest. The dimensions and materials properties are listed in Table 2.2 and Table 2.3. In order to implement the controller in real time, a Simulink/dSPACE system is employed to detect the control moments and generate the pulse control signal according to the control principles of the two techniques (classical SSDI and enhanced nonlinear damping strategy based on spatial filtering). Even though there are two circular sensors implemented in the experiments for sending the input signals (piezovoltages) into the dSPACE system, they can be replaced by self-sensing actuators, which is attributed to the unique traits of piezoelectric materials and the sensing dispensability in the control strategies (the piezoelectric inserts are almost kept in open circuit condition as the switching process is considered instantaneous). In addition, a displacement sensor is employed for displacement responses measurements.

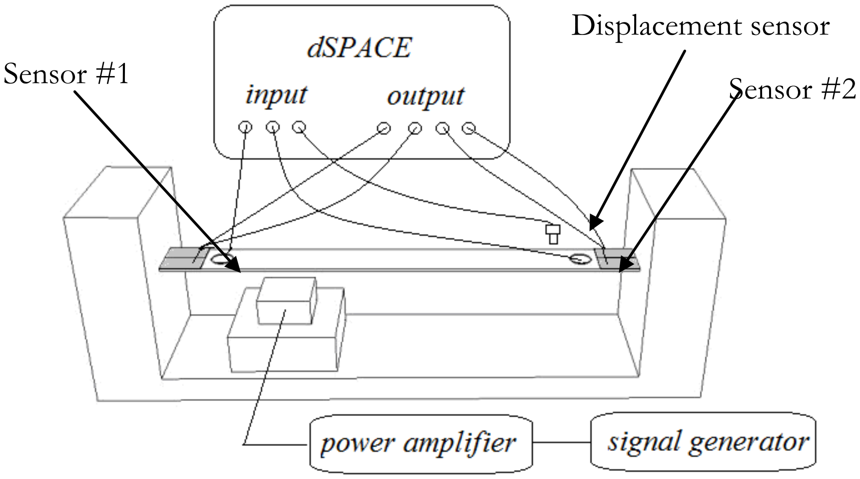

Figure 2.23. Schematic diagram of the experimental setup.

2.4.2. Experimental measurements under monochromatic excitation

The external force applied on the electromechanical beam is generated by a signal generator connected to a power amplifier system before sending to the electromagnet which is placed around a quarter of the overall length of the investigated beam. The first two resonance frequencies (f_{1e} and f_{2e}) of the experimental sample are measured at 66.5 *Hz* and 170.8 *Hz*, which closely approximate the simulation results ($f_{1s} = 66.45\,Hz$ and $f_{2s} = 170.6\,Hz$).

First mode control experiment

In order to damp the first mode, the switching connections shown as Figure 2.13 and Figure 2.10 are respectively integrated in classical SSDI approach case and enhanced nonlinear damping strategy based on spatial filtering. For the former approach, four control switches work independently and they are controlled by two command signals. For integrating the latter strategy, only one command signal is obtained from the dSPACE system for triggering the two sum switches. The general control algorithms in experiments for controlling the first mode are exposed in Figure 2.24 and Figure 2.25.

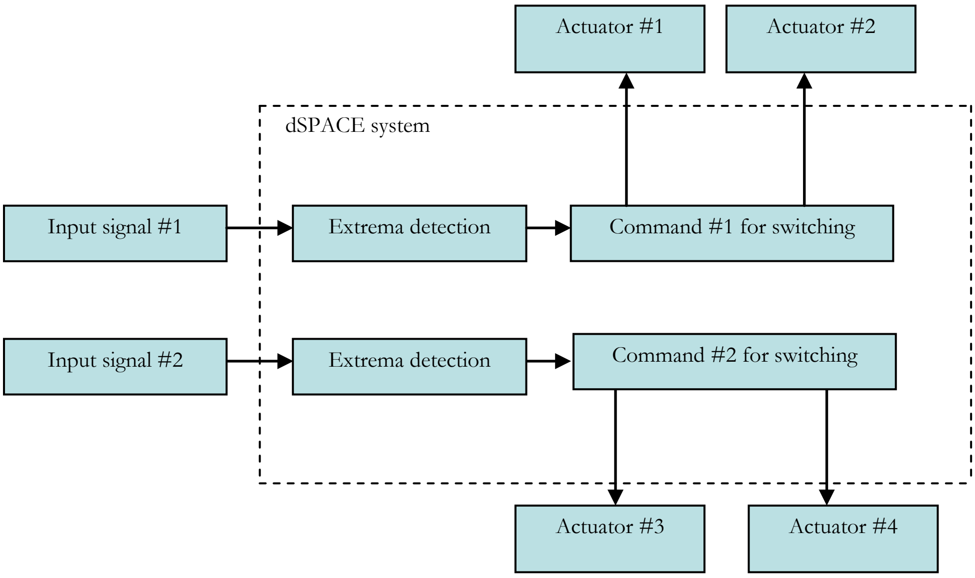

Figure 2.24. General control algorithm in experiments with classical SSDI technique in single mode cases.

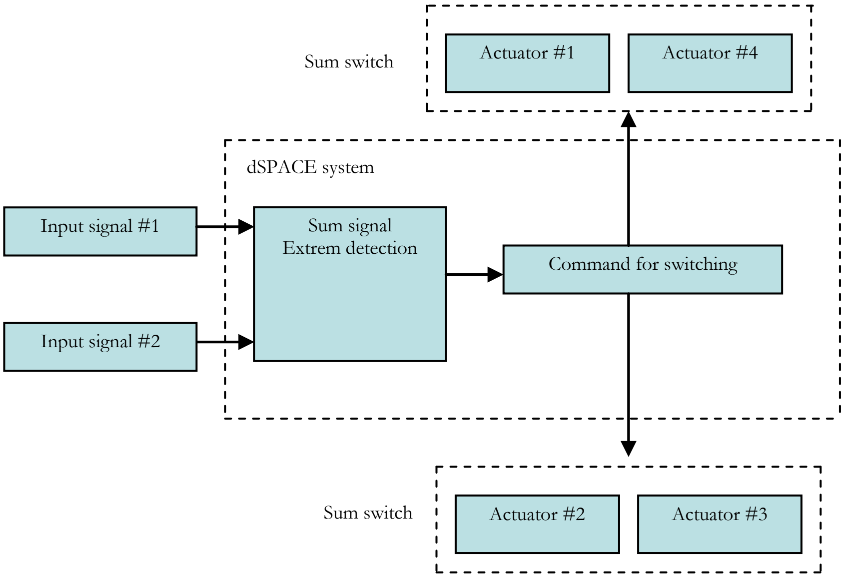

Figure 2.25. General control algorithm in experiment with enhanced strategy for controlling the first mode of clamped-clamped beam.

Corresponding switching parameters are summarized in Table 2.7. The dynamical frequency responses around the first resonance frequency obtained by displacement sensor at $x_1 = 257 \times 10^{-3} m$ with and without control are plotted in Figure 2.26. The damping attenuation varied with the frequency in the vicinity of the first resonance frequency using classical SSDI approach and the enhanced strategy are described in Figure 2.27.

Table 2.7. Parameters for control switching in experiments.

	Classical SSDI approach	Strategy based on spatial filtering	
		Sum switch	Difference switch
L_{in}	0.7 H	0.7 H	0.7 H
t_i	0.0004 s	0.0003 s	0.0003 s
γ	0.8	0.82	0.82

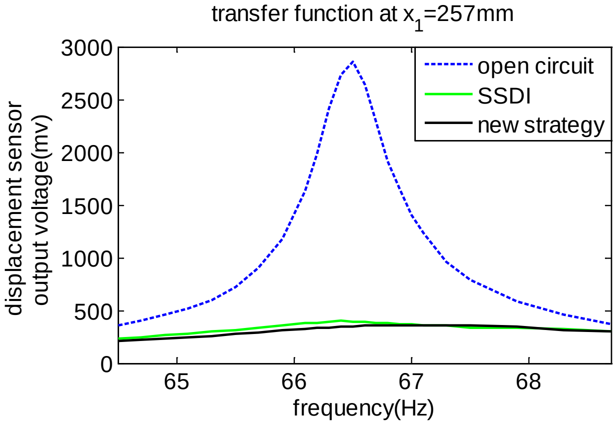

Figure 2.26. Frequency responses obtained in experiments around the first resonance frequency.

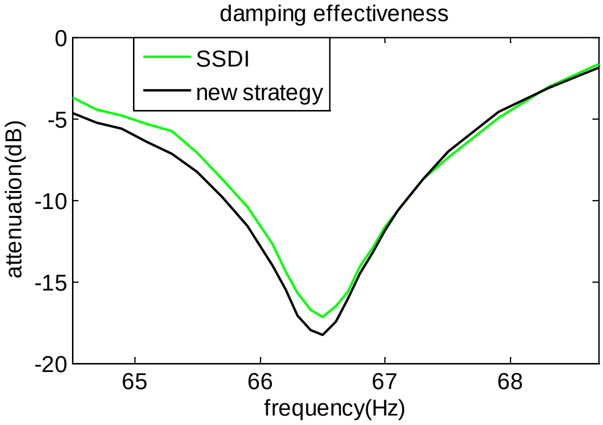

Figure 2.27. Damping attenuation obtained in experiments around the first resonance frequency.

Results show that both control strategies can successfully reduce the first mode of the vibrating beam and are in relatively good agreement with simulation results. The amplitude reduction of the displacement response at $x_1 = 257 \times 10^{-3} m$ is -17.19 *dB* with classical SSDI and -18.24 *dB* using enhanced strategy in this case. Even though the attenuation (Table 2.8) measured at the first resonance frequency shows a little bit less compared with that obtained in previously presented simulations, it is also proven that the two techniques can effectively damp the first mode vibration.

Table 2.8. Attenuation measurements in experiments.

	$F=\sin\left(\omega_{1e}t\right)$	$F=\sin\left(\omega_{2e}t\right)$	$F=\sin\left(\omega_{1e}t\right)+4\sin\left(\omega_{2e}t\right)$	Band-limited white noise
Classical SSDI technique	-17.19 *dB* *(simulation:* -19.91 *dB)*	-15.89 *dB* *(simulation:* -19.36 *dB)*	-10.28 *dB* *(simulation:* -12.6 *dB)*	-1.98 *dB* *(simulation:* -2.49 *dB)*
Strategy based on spatial filtering	-18.24 *dB* *(simulation:* -21.13 *dB)*	-18.65 *dB* *(simulation:* -19.81 *dB)*	-17.63 *dB* *(simulation:* -20.43 *dB)*	-6.8 *dB* *(simulation:* -6.8 *dB)*

Second mode control experiment

For limiting the second bending mode of the clamped-clamped beam, the switching connections with original SSDI technique and the enhanced nonlinear damping strategy are shown in Figure 2.13 and Figure 2.11. The general control algorithms for switching in the experiments are depicted in Figure 2.24 and Figure 2.28. In order to limit the second mode, difference signal of the piezovoltages is used for detecting switching moments in the enhanced approach. The dynamical response measurements obtained by displacement sensor in this case are plotted in Figure 2.29. Damping effectiveness varied with the frequency using different control methods are given in Figure 2.30.

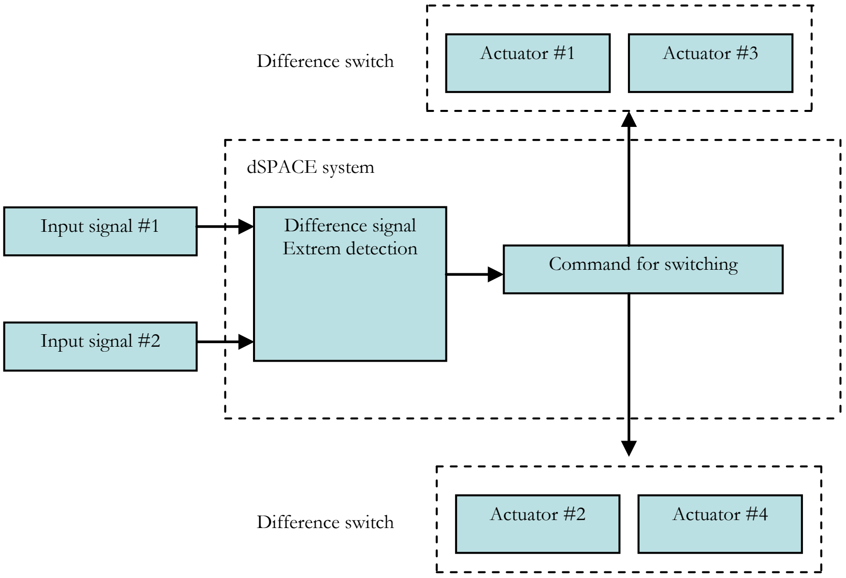

Figure 2.28. General control algorithm in experiment with enhanced strategy for controlling the second mode of clamped-clamped beam.

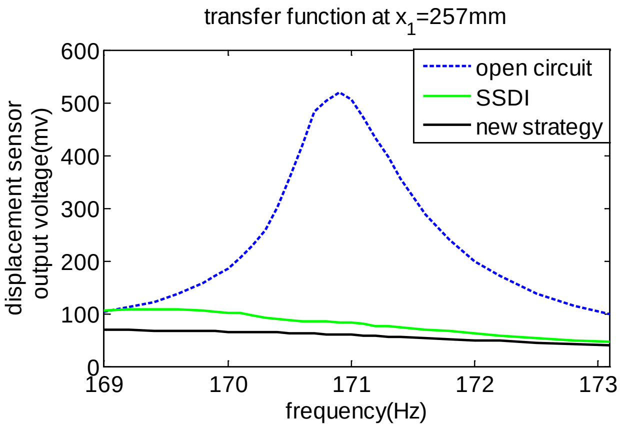

Figure 2.29. Frequency responses obtained in experiments around the second resonance frequency.

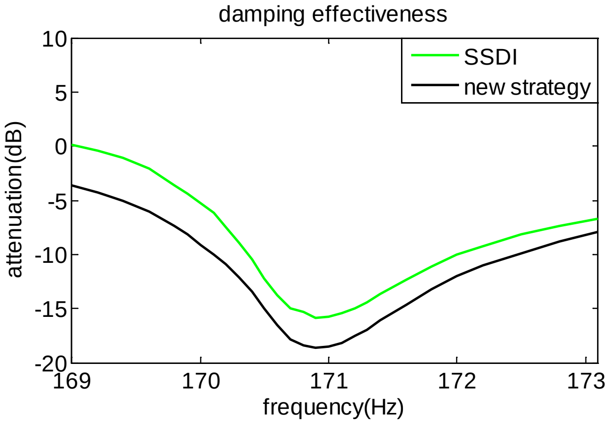

Figure 2.30. Damping attenuation obtained in experiments around the second resonance frequency.

-15.89 *dB* and -18.65 *dB* reduction of displacement amplitude at the second resonance frequency (Table 2.8) are respectively achieved with classical SSDI approach and the enhanced strategy based on spatial filtering. Compared with the simulation for single mode control, it is found that the numerical analyses are in good agreement with the experimental measurements although the damping performances achieved in experiments are slightly decreased, which may be attributed to mechanical nonlinearities in the experiments.

2.4.3. Experimental measurements under bimodal excitation

For validating the bimodal damping performance of the enhanced nonlinear damping strategy based on spatial filtering, the first two modes of the bending beam are excited by applying an external force at $x_1 = 85\times10^{-3}\,m$ with an amplitude ratio A_2/A_1 equal to four. It should be noted that in the bimodal case, the external excitation signal is implemented from dSPACE system which allows the output signal with two frequency components. Then, it is applied to the clamped-clamped beam by using the electromagnet. Control switching connections are shown in Figure 2.13 and Figure 2.12. Additionally, general algorithms with different control methods are briefly introduced in Figure 2.24 and Figure 2.31.

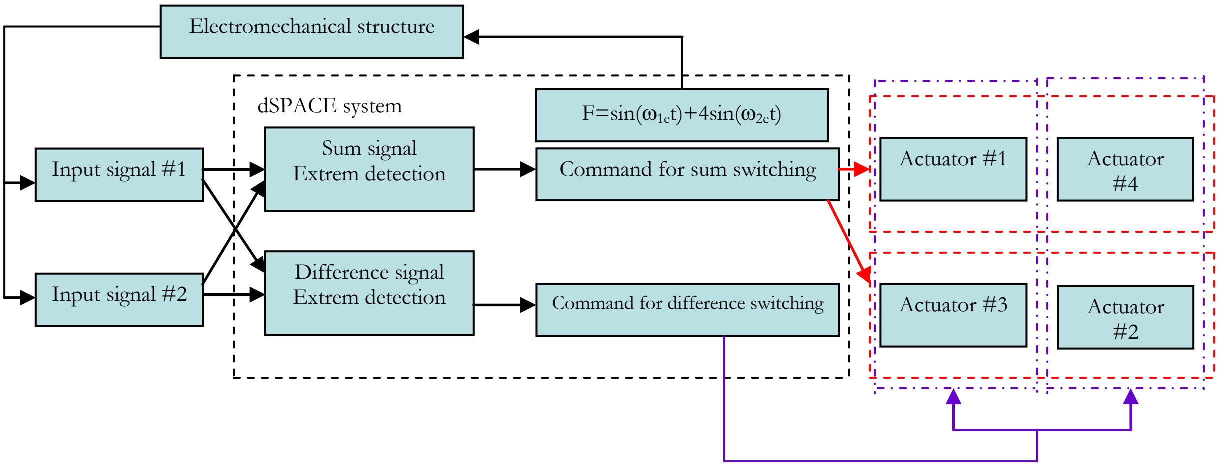

Figure 2.31. General control algorithm in experiment with enhanced strategy for bimodal control.

Figure 2.32 shows the dynamical responses measured by displacement sensor. From this figure and the attenuation calculated from the RMS values of the steady state responses given in Table 2.8, it can be easily found that superior bimodal damping performance of enhanced nonlinear damping strategy based on spatial filtering is achieved compared with classical SSDI approach, since the excited modes can be separated and filtered by the new switching connections, and then damped effectively and simultaneously with the sum and difference switches.

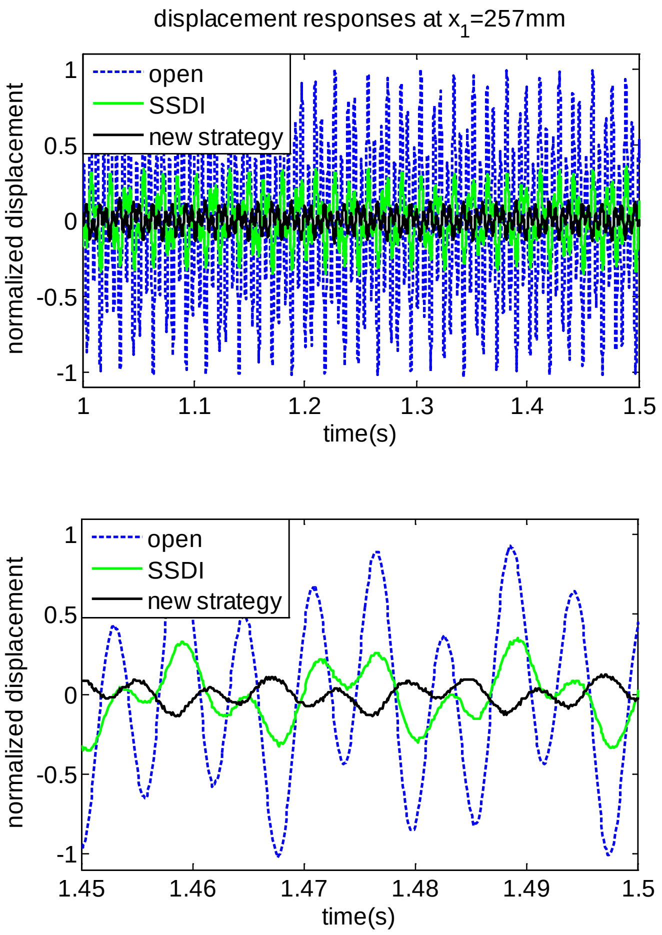

Figure 2.32. Experimental measurements at $x_1 = 257\times10^{-3}\,m$ with and without control under external excitation $F = \sin\left(\omega_{1e}t\right) + 4\sin\left(\omega_{2e}t\right)$.

2.4.4. Experimental measurements under band limited white noise

To further confirm that the enhanced strategy is effective for multimodal control, the experiments are conducted under band-limited white noise (Figure 2.33) in the range of 10 *Hz* to 210 *Hz*, hence allowing focusing on the first two modes of the investigated bending beam. Similar to the bimodal case, for implementing this excitation, the white noise signal is obtained from the dSPACE system with MATLAB script and then applied to the bending beam with electromagnet driver.

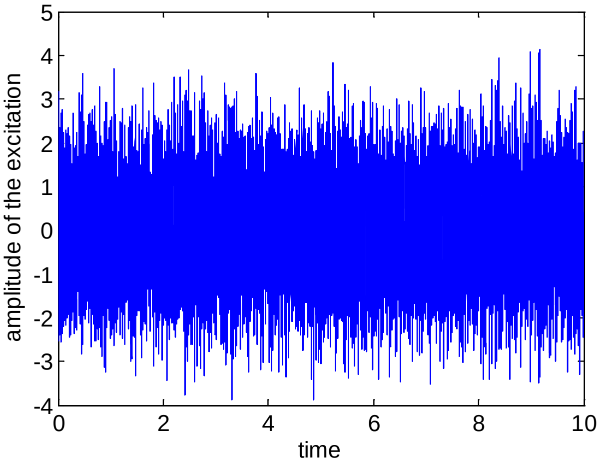

Figure 2.33. Band-limited white noise excitation.

Figure 2.34 and Figure 2.35 display dynamical responses in time domain and the corresponding frequency spectra, which further confirm that the enhanced nonlinear damping strategy using spatial filtering outperforms the classical SSDI technique in broadband vibration control. Damping attenuation as -4.57 *dB* at the first resonance frequency and -6.44 *dB* at the second resonance frequency are achieved with classical SSDI technique. Meanwhile, amplitude reductions of -13.9 *dB* in first mode and -14.95 *dB* in second mode are obtained as the enhanced strategy using spatial filtering is implemented. Although the multimodal damping performance of the enhanced nonlinear damping strategy based on spatial filtering is experimentally validated, it is found that the damping performances of two control methods are deteriorated compared with the results measured in single mode cases and bimodal case, which may result from the interfering signals or noise contained in the broadband excitation. Furthermore, the interfering signals may excite the higher modes of the vibrating structure as well, as shown in Figure 2.35 where the third mode around 323 *Hz* in the open case has been excited under this white noise. From the measured spectrum, it can be found that because of the existence of interfering signals and dispensable switching actions, there is no damping performance for the third mode when classical SSDI is implemented. Nevertheless, -7.86 *dB* reduction for limiting the third mode is obtained using the spatial filtering damping strategy since part of the interfering signals has been filtered before damping. Moreover, according to the mode shapes of the clamped-clamped beam, the odd modes can be isolated and damped by sum switches. Thus, even though the experiments only focused on the first two modes, the third mode can also be properly detected and attenuated by the employing sum switches once the first modes have been effectively damped.

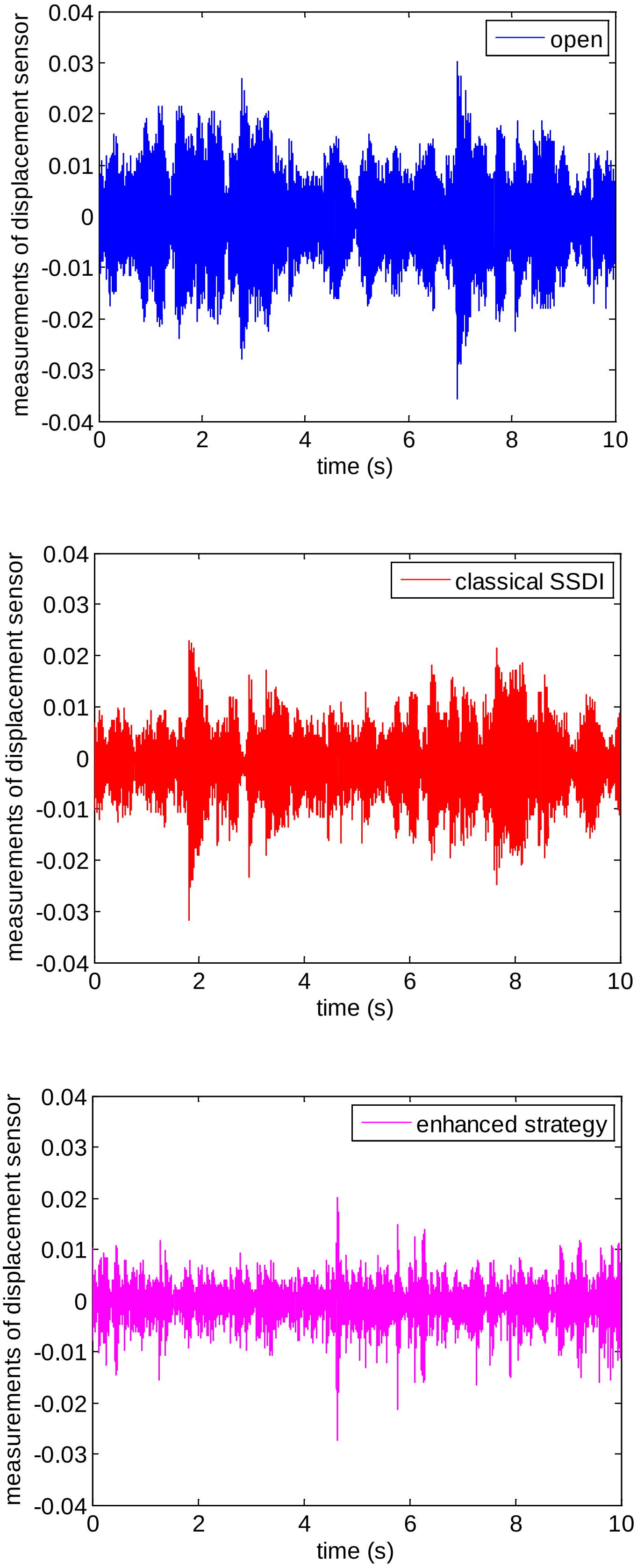

Figure 2.34. Dynamical responses in time domain measured under band-limited white noise.

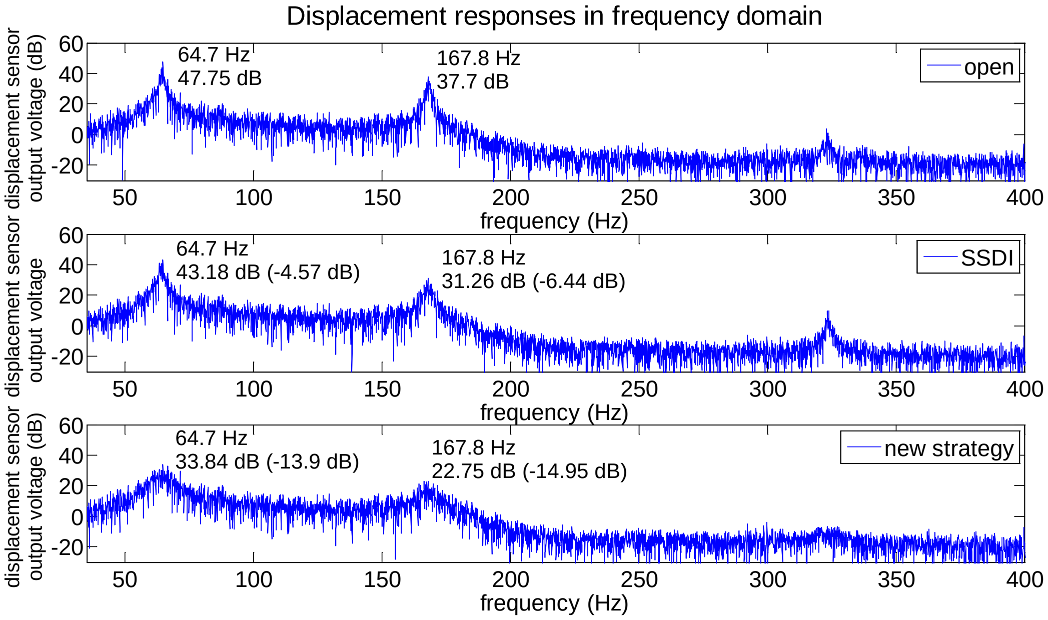

Figure 2.35. Experimental frequency spectra of uncontrolled and controlled cases under band limited white noise.

In this section, several experiments on a clamped-clamped steel beam under different excitations are carried out for validation of the numerical analyses and concept of spatial filtering. Single mode, bimodal and broadband vibration damping performances of the enhanced nonlinear damping strategy based on spatial filtering are investigated and discussed. Comparison with the classical SSDI technique demonstrates that the enhanced strategy allows better damping performance and maintains the characteristics of original SSDI approach such as simplicity, ease of implementation and low power requirement.

2.5. Further discussion

This section aims at pointing out the advantages and drawbacks of the enhanced nonlinear damping strategy using spatial filtering. Further investigations and applications of this method are discussed as well.

2.5.1. Extensibility of the enhanced nonlinear damping strategy based on spatial filtering

It should be pointed out that, although in the previous sections only the damping performances of a clamped-clamped bending beam used as an illustrative example are investigated and demonstrated, this enhanced nonlinear damping strategy based on spatial filtering can be either extended to other kinds of boundary conditions such as cantilever beam or to other vibrating structures like plates or shells. As the boundary condition or the investigated bending structure is changed, the control actuators implemented in this damping strategy should be placed anti-symmetrically or symmetrically according to the targeted vibration mode shapes in order to successfully isolate the interested modes and filter the untargeted modes. Moreover, the sum signal and difference signal of piezovoltages of two connected piezoelectric patches are essential for detecting the proper switching moments. However, along with the complexity of the vibrating structure, the integration of the spatial filtering damping strategy is more complex since the symmetrical and anti-symmetrical positions of the targeted modes are difficult to determine, thus the pre-design and theoretical modelling are indispensable.

In addition, it needs to be noted that this enhanced strategy is not restricted to reduce the dynamical responses of the first two modes of vibrating structure. Extensive application to any mode control with the spatial filtering damping strategy is feasible and can be considered. For instance, as shown in the experiments under band limited white noise excitation, the third mode (around 323 *Hz*) of the clamped-clamped beam is also excited. By employing the proposed nonlinear damping strategy based on spatial filtering, it is effectively suppressed by -7.86 *dB*. Nevertheless, as more targeted modes need to be damped, more piezoelectric actuators will be used to separate the concentrated modes and filter the useless responses. Whereas, accompanied by the increasing number of piezoelectric patches and implementation of switching control circuits, the damping effectiveness of each switching device may be decreased.

2.5.2 Feasibility and compatibility of the enhanced nonlinear damping strategy based on spatial filtering

As a feasible and compatible control strategy, the nonlinear damping technique based on spatial filtering can be combined with other strategies and approaches to achieve other capabilities which will be introduced in the following.

- **Self-sensing capability**

As previously discussed, for the enhanced strategy using spatial filtering, the sensors implemented to sending the input signals to the dSPACE system in experiments for switching moment detection are dispensable, since the SSDI approach is naturally self-sensing by its principle that the piezoelectric element is almost kept in open circuit. Thus, for realistic implementation, the sensors used in the proposed enhanced nonlinear damping strategy based on spatial filtering can be replaced by the self-sensing actuators (such as in simulations), shaped transducers or employed in cooperation with the self-sensing system proposed by Makihara *et al.* [123] to obtain the self-sensing capability, allowing simplifying the control system and reducing the number of piezoelectric patches.

• Self-powered capability

It is well known that the classical SSDI approach is a typical semi-passive approach with lower power requirement feature. The proposed enhanced strategy has inherited this attribution since the two methods are only differentiated by the control connections and switching algorithms while the basic principles are same (artificially obtained the phase shift between voltage and structural motion for increasing the damping). Thus, spatial filtering damping strategy can be designed with self-powering capability as well, by implementing the self-powered control block (Figure 1.28) proposed by Richard [116] or implementing the adaptive self-powered control block (Figure 1.29) proposed by Lallart [117]. Electronic breaker should be integrated in the spatial filtering switching connections such as in Figure 2.12 to ensure the control strategy possesses the capabilities of spatial filtering and self-powering.

• Spatial filtering cooperated with threshold detection

As proven in literature, the threshold detection based on SSDI approach is an alternative solution for improving the multimodal damping performance of classical SSDI. Hence, the combination of the proposed enhanced strategy based on spatial filtering and the threshold detection will broaden the application of these two strategies and acquire excellent multimodal damping capability. The control switching device implemented in the combined nonlinear damping strategy is disabled for voltage inversion until some conditions are fulfilled. In the combined nonlinear strategy, piezoelectric actuators are placed at the anti-symmetrical and/or symmetrical position based on the interested modes for spatial filtering process. Sum signal and/or difference signal of piezovoltages of the two connected patches will be used for detecting the switching moments. Moreover, threshold values will be achieved in accordance with different criteria as mentioned in references [117][134][135][136][137]. Control switch of the combined control technique is always kept open until an extremum occurs with a value that exceeds the computed threshold. At that moment, the corresponding piezoelectric patches will be connected into the control switching device for piezovoltage inversion.

To verify the broadband damping performance of this combined concept, the dynamical responses of the illustrative example under band-limited white noise in the range of 10 *Hz* to 610 *Hz* (exciting the first four modes) and pulse excitation are simulated and discussed. Displacement thresholds D_{thres_sum} and D_{thres_d} defined as Eq. (2.28) are introduced to detect the switching moments for sum switch and difference switch, respectively.

$$
\begin{aligned}
D_{thres\_sum} &= \beta_{sum} \cdot \frac{1}{N_s} \sum_{N_s} \left| disp._{ith} + disp._{jth} \right| && \textit{threshold for sum switch} \\
D_{thres\_difference} &= \beta_{difference} \cdot \frac{1}{N_d} \sum_{N_d} \left| disp._{ith} - disp._{jth} \right| && \textit{threshold for difference switch}
\end{aligned}
\tag{2.28}
$$

where β_{sum} and $\beta_{difference}$ are set by user. N_S and N_d are the number of calculated points (in simulation) or measured points (in experiments) in a given time window T_{es_sum} or $T_{es\_difference}$ for sum and difference switches. $disp._{ith}$ and $disp._{jth}$ are the displacement responses of the i^{th} and j^{th} piezoelectric elements.

Band-limited white noise

In this case study, a band-limited white noise (Figure 2.36) in the range of 10 *Hz* to 610 *Hz* which can drive the first four modes of the illustrative example is applied at the position $x_1 = 85 \times 10^{-3}\, m$. For preliminary investigation and verifying the combined concept, the parameters given in Table 2.9 are used to obtain the thresholds for sum and difference switches. Numerical dynamical responses at $x_1 = 257 \times 10^{-3}\, m$ without and with control are plotted in Figure 2.37. Damping effectiveness calculated from RMS value over the considered time window is listed in Table 2.10.

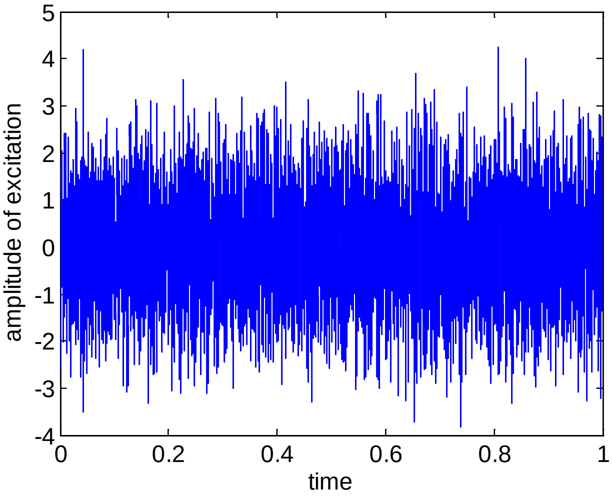

Figure 2.36. Band-limited white noise excitation in range of 10 *Hz* to 610 *Hz*.

Table 2.9. Parameters used for obtaining the thresholds in combined control strategy.

$\beta_{sum} = 0.8$	$T_{es\_sum} = 5 \cdot \frac{1}{2\pi f_{3s}}$	$L_{in} = 0.05H$	$\gamma_{classical} = 0.8$	$N_S = 12545$
$\beta_{difference} = 0.8$	$T_{es\_difference} = 5 \cdot \frac{1}{2\pi f_{4s}}$	$R = 307\Omega$	$\gamma_{enhanced} = 0.85$	$N_d = 7565$

*note: in the simulation the time step $dt = 1.25 \times 10^{-6}\, s$

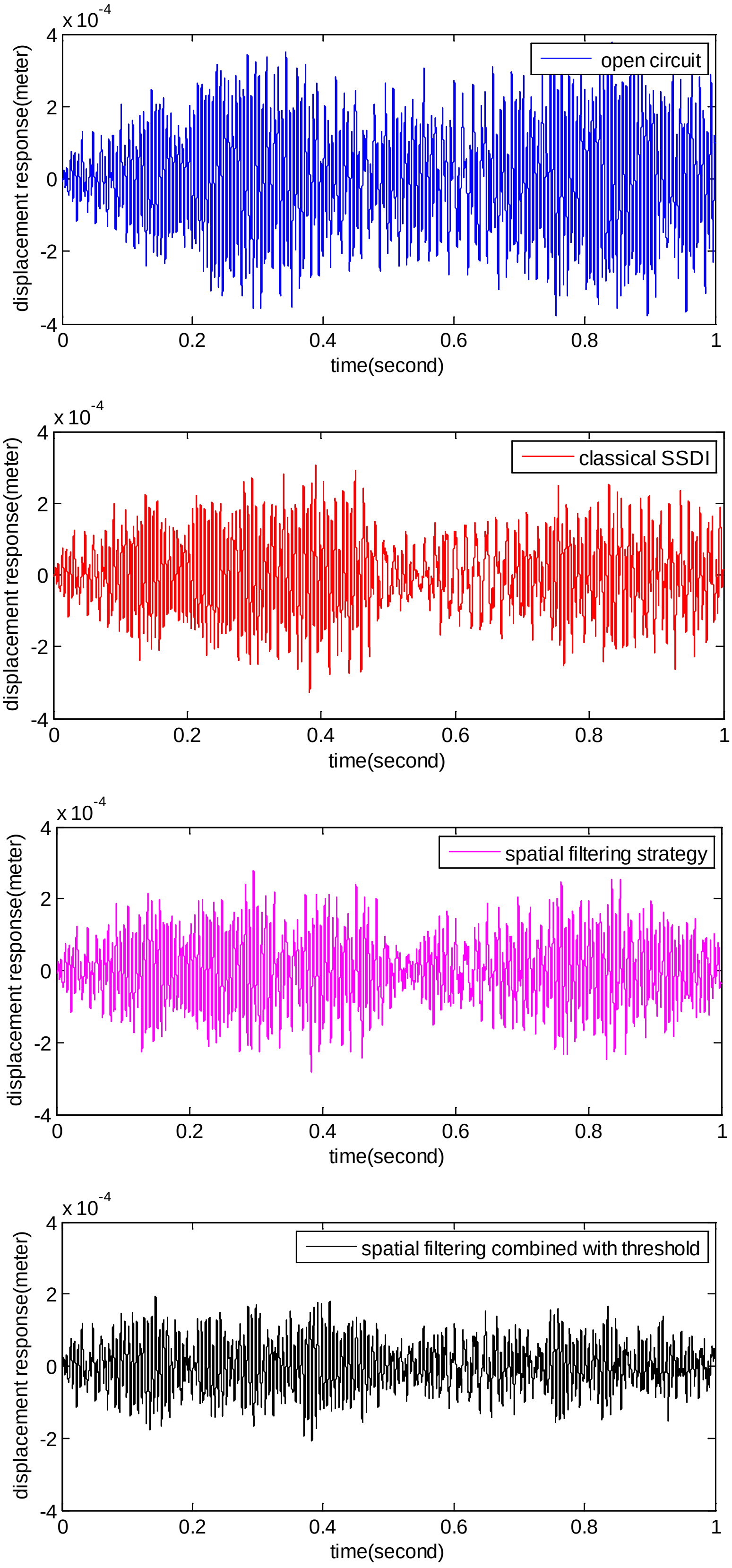

Figure 2.37. displacement responses at $x_1 = 257\times10^{-3}\,m$ under band-limited white noise excitation in range of 10 *Hz* to 610 *Hz*.

Table 2.10. Damping attenuation obtained from RMS value over the considered time window under band-limited white noise in the range of 10 *Hz* to 610 *Hz* with different control strategies.

Classical SSDI approach	Spatial filtering strategy	Spatial filtering & threshold
-3.15 dB	-4.16 dB	-7.31 dB

Significant damping effectiveness as -7.31 *dB* with the combined strategy is obtained, which verifies the feasibility of the multimodal control concept and confirms the excellent damping performance compared with the reduction -3.15 *dB* obtained in classical SSDI case and -4.16 *dB* achieved by the enhanced strategy based on spatial filtering. With this combined control strategy, the mode of interest can be separated through the spatial filtering process. Moreover, it can focus on the most energetic mode thanks to the threshold detection. To further discussing the broadband damping of the combined strategy, pulse control case is studied.

Pulse control case

In this case, a Gaussian-shaped pulse excitation given in Figure 2.38 is applied at $x_1 = 85 \times 10^{-3} m$ of the clamped-clamped beam. Dynamical responses at $x_1 = 257 \times 10^{-3} m$ in open circuit and controlled cases with different damping strategies are shown in Figure 2.39. Corresponding switching parameters are listed in Table 2.9. From these curves, it can be noticed that with the combined control strategy, the broadband dynamical response can be damped very quickly compared with the other two control methods.

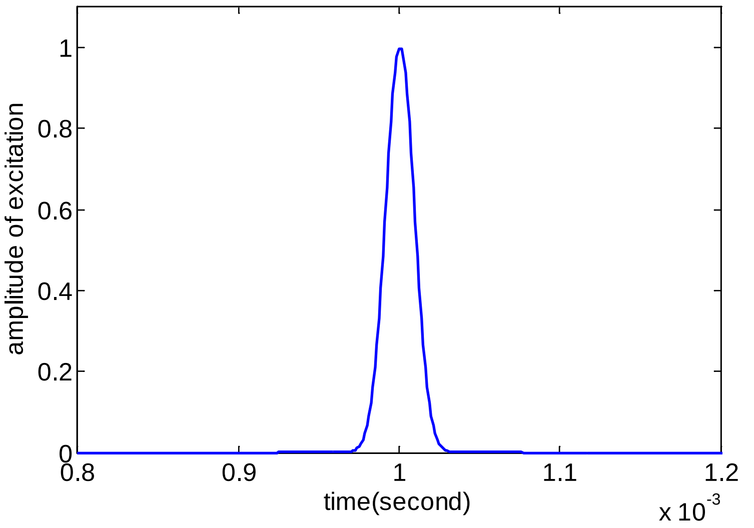

Figure 2.38. Pulse excitation.

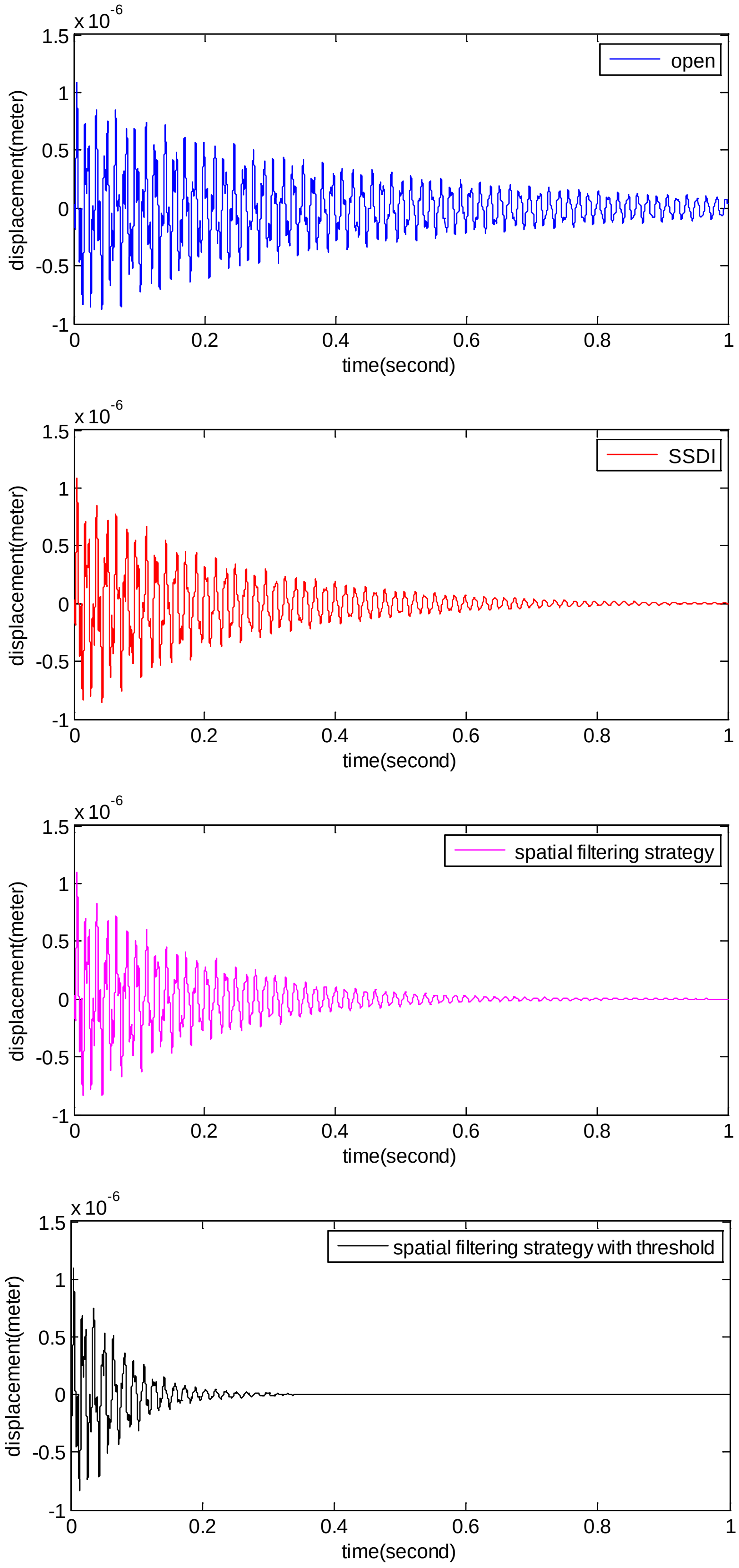

Figure 2.39. Displacement responses at $x_1 = 257 \times 10^{-3} m$ under pulse excitation

with $\beta_{sum} = \beta_{difference} = 0.8$.

In order to compare the damping performance, the attenuation obtained from the RMS value in the observed time history (1 second) is summarized in Table 2.11. From this comparison, it is obvious that the combined control strategy is superior to classical SSDI approach and the enhanced spatial filtering strategy under pulse excitation, as significant damping reduction of -5.99 dB is achieved. Meanwhile, only -2.02 dB and -2.94 dB are respectively obtained with classical SSDI and enhanced damping strategy based on spatial filtering. Since in the open case, the dynamical response is not negligible at the end of the considered time window, the damping performances obtained from RMS values are actually higher.

Table 2.11. Damping attenuation obtained from RMS value over the considered time window under pulse with different control strategies.

Classical SSDI approach	Spatial filtering strategy	Spatial filtering & threshold
-2.02 dB	-2.94 dB	-5.99 dB

To further confirm the excellent damping of the combined control strategy, the dynamical responses in frequency domain is exposed in Figure 2.40. Generally, the lower vibration modes are the most energetic ones, hence, only the first three modes are shown and discussed. Damping attenuation obtained for each mode with the three control methods are listed in Table 2.12.

Compared with the attenuation obtained as -4.3 *dB*, -8.9 *dB* and -7.6 *dB* in the case of classical SSDI technique and -8.28 *dB*, -12.34 *dB* and -4.28 *dB* with enhanced spatial filtering strategy, significant displacement reduction as -24.5 *dB*, -28.55 *dB* and -9.87 *dB* for the first three modes are achieved with the combined control strategy, which further validates the combined control concept and proves the control effectiveness of the improved control technique. Although the results for damping the first two modes with the enhanced damping strategy based on spatial filtering are still better than that obtained in original SSDI approach, it is found that for limiting the third mode, the latter is better than the former, which is attributed to the principle of SSDI approach that focuses on the highest detectable vibration mode. Moreover, since the third vibration mode is not the energetic mode under the pulse excitation, the global damping performance of classical SSDI technique is still inferior to the enhanced nonlinear damping strategy based on spatial filtering (Table 2.11).

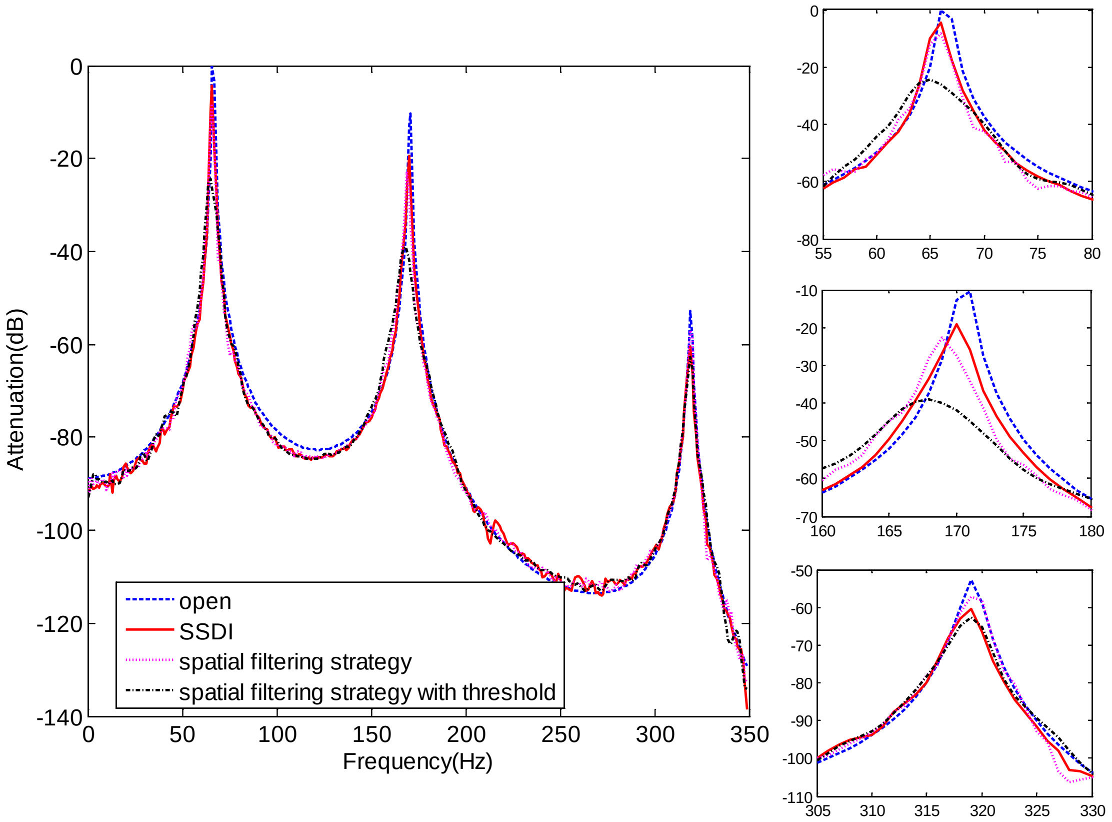

Figure 2.40. Dynamical responses at $x_1 = 257 \times 10^{-3} m$ in frequency domain under pulse excitation with $\beta_{sum} = \beta_{difference} = 0.8$.

Table 2.12. Damping attenuation obtained for the first three modes in pulse case.

	First mode	Second mode	Third mode
Classical SSDI approach	-4.3 *dB*	-8.90 *dB*	-7.6 *dB*
Spatial filtering strategy	-8.28 *dB*	-12.34 *dB*	-4.28 *dB*
Spatial filtering & threshold	-24.50 *dB*	-28.55 *dB*	-9.87 *dB*

Furthermore, it should be noted that the parameters β_{sum} and $\beta_{difference}$ can be chosen by the user for different control modes. As shown in Figure 2.41, with different threshold parameters, the global damping performance of the combined control strategy is different. In the particular studied range, the combined strategy outperforms to the other two control methods, which further confirms the broadband damping capability of the combined strategy. Although in this work, it is assumed that the threshold parameters β_{sum} and $\beta_{difference}$ are the same, the two parameters can be different to each other as well.

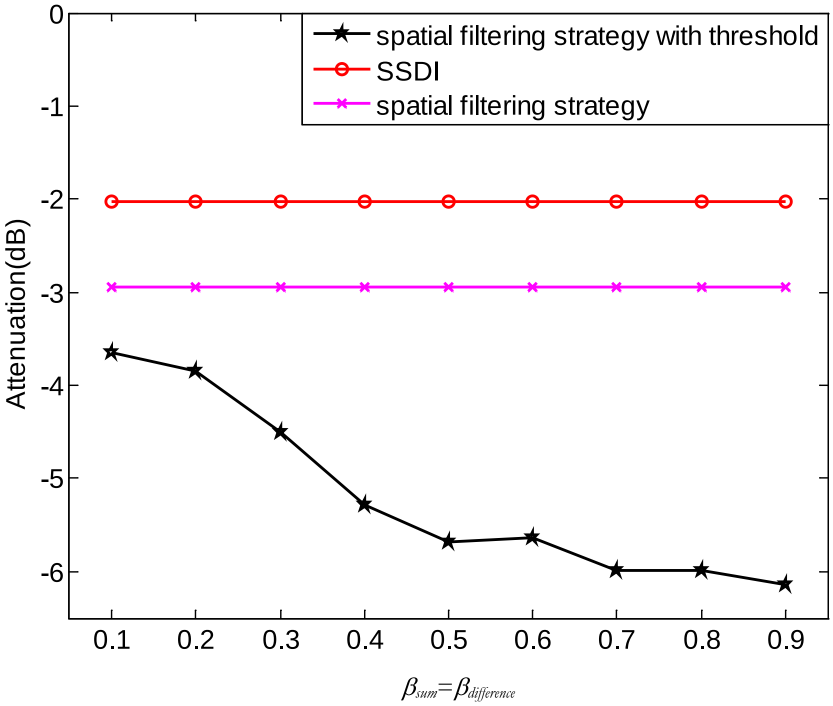

Figure 2.41. Global attenuation obtained in time domain with different β_{sum} and $\beta_{difference}$ under pulse excitation.

From the demonstration and discussion, it can be concluded that the proposed enhanced nonlinear damping strategy based on spatial filtering is an extensible multimodal vibration approach. Neither boundary condition nor the investigated structures can limit its application. Moreover, even though only the first two modes of the illustrative example are discussed in this work, it is not restricted to it and can be extended for any mode control. Furthermore, since it is feasible and compatible as well, it can be also combined with other techniques to achieve the self-sensing or self-powering capability. Additionally, in order to improve the multimodal damping performance and broadband control capability, this enhanced strategy can cooperate with threshold detection methods to extend their applications. Although it exhibits excellent damping in multimodal control, it still has some disadvantages if the vibrating structure is too complicated.

2.6. Conclusion

In this chapter, an enhanced nonlinear damping strategy based on spatial filtering for improving the multimodal damping performance of SSDI technique is presented. For demonstrating the control principle of this strategy, a clamped-clamped electromechanical beam is used as an illustrative example. Switching algorithm and connections aiming at reducing the vibrations of different modes are introduced. To preliminarily verify the damping performance, single mode control, bimodal control and band-limited white noise control are simulated with MATLAB home-made FEM script. Corresponding experiments are carried out for numerical validation. The main work in this chapter can be concluded as follows:

- In order to increase the multimodal damping performance of the SSDI approach, an enhanced nonlinear damping strategy based on spatial filtering is proposed. In this approach, the piezoelectric actuators need to be placed anti-symmetrically or symmetrically according to the targeted mode shapes of the vibrating structures. Two switches named as 'sum switch' and 'difference switch' are implemented in this enhanced strategy. For damping the odd modes of a clamped-clamped beam (illustrative example), the two anti-symmetrically bonded piezoelectric actuators are connected through a switching device made of a digital switch and an inductor, since the even vibration modes can be filtered by this connection. This switch is kept open except when an extremum of the sum signal of voltages of the two anti-symmetrically attached piezoelectric patches occurs. At that moment, the switch is closed for half a period of the electrical oscillator (constituted by the total capacitance of the piezoelectric patches and the inductor) until the sum piezovoltage is reversed. For suppressing the even modes of the clamped-clamped beam, the symmetrically bonded piezoelectric actuators are intermittently connected to a switching device for spatial filtering of the odd modes. Similarly, the switch is kept open except when the difference signal of piezovoltages of the two symmetrically attached piezoelectric patches reaches an extremum value. Once it occurs, the switch is triggered to close for half a period of the constituted electrical oscillator for the piezovoltage difference inversion. Thus, by implementing the sum and difference switches, both odd and even modes can be separated and damped simultaneously.

- Single modal vibration, bimodal vibration and band-limited white noise control performances of classical SSDI and the enhanced nonlinear damping strategy based on spatial filtering are simulated in MATLAB using a finite element model. From the single mode control results, it can be found that the two control strategies can effectively damp the excited mode. Nevertheless, the damping attenuation achieved by the enhanced strategy is a bit superior compared with the classical SSDI, since the inversion coefficient in the enhanced strategy is slightly greater. Furthermore, from the bimodal simulation results, it is shown that the proposed strategy can separate the modes of interest and spatially filter the uninterested mode before damping, which allows excellent bimodal damping performance, while the classical SSDI approach focuses on the highest detectable mode, hence degrading its performance in multimodal case. In order to further confirm this conclusion, the damping performance under the band-limited white noise in the range of 10 *Hz* to 210 *Hz*, allowing focusing on the first two bending modes are simulated and discussed. Corresponding results further prove that the enhanced nonlinear damping strategy based on the spatial filtering can effectively filter the interfering signal and obtain significant multimodal damping performance.

- Experiments on a clamped-clamped steel beam with piezoelectric patches under monochromatic excitation, bimodal excitation and band limited white noise excitation are carried out for validation of the concept and numerical analyses. From the comparison, it is shown that the simulation results and the experiment measurements are in good agreement. Thus, the multimodal damping performance of the enhanced nonlinear damping strategy based on spatial filtering is experimentally confirmed. Hence, it can be concluded that the enhanced strategy is an effective multimodal damping approach and outperform the classical SSDI approach, especially under wideband excitation.

- Further applications of the enhanced strategy based on spatial filtering are discussed. Due to its extensibility, it is can be implemented in other boundary conditions and structures. Additionally, it can also be extended for damping the higher modes (not only the first two modes). Since it is a feasible and compatible strategy, it can be combined with the self-sensing techniques, self-powered methods or threshold detection criteria to achieve self-sensing ability, self-powering capability and increase the multimodal damping performance. To further validate the feasibility of the enhanced damping strategy based on spatial filtering, a control method which combines spatial filtering (sum and difference signals) with time domain filtering (threshold applied to the previous signals) is simulated and discussed under band-limited white noise in the range of 10 *Hz* to 610 *Hz*, and pulse excitation. Corresponding simulated results not only verifies the feasibility of the spatial filtering nonlinear damping strategy but also validates the excellent multimodal damping ability and broadband control performance of this combined concept.

Chapter 3. Electromechanical Semi-passive Nonlinear Switch Tuned Mass Damper

As a typical passive control treatment, tuned dynamic devices (tuned vibration absorbers and tuned mass dampers) can effectively reduce the undesired vibration when their dynamic characteristics are properly tuned according to those of the primary structures. However, it has also been proven that tuned dynamic devices are sensitive to the changes of dynamic characteristics of the primary structure and less effective as it is mistuned. In order to improve the control effectiveness and robustness, some researches focused on combining this kind of devices with active controller, hybrid technique or semi-passive/semi-active strategies have been reported. In this chapter, an electromechanical semi-passive nonlinear tuned mass damper is proposed, which combines an electromechanical TMD featuring piezoelectric materials with the nonlinear Synchronized Switch Damping on Inductor (SSDI) semi-passive technique. The control principle of this nonlinear TMD is demonstrated using a Two-Degree of Freedom (TDOF) model and finite element approach. To validate this control concept and investigate the damping performance, experiments are carried out on a cantilever beam. A comparison of control effectiveness between purely mechanical TMD, electromechanical passive TMD and the proposed nonlinear semi-passive TMD is presented. Theoretical analyses and further application of this nonlinear TMD are also discussed in this Chapter.

3.1. Brief review of existing tuned vibration devices

Tuned vibration absorbers and tuned mass dampers have been extensively used in industrial and engineering applications to effectively damp undesired vibrations aiming at protecting the structures and extending their lifespan, such as limiting the vibrations induced by winds in buildings or subjected to earthquakes. Along with the development of intelligent materials, tuned vibration devices can be easily linked to other control methods (passive, active, hybrid and semi-passive/semi-active techniques) through electromechanical conversion.

An electromechanical passive absorber featuring piezoelectric materials has been investigated by Kim *et al.* [48], which is connected to a $R\|L$ parallel shunt circuit for artificially increasing the mechanical damping term. Although such passive tuned vibration devices are simply and easy to be implemented, they cannot adapt themselves to the changes of primary structures, thus leading to a deterioration of the control performance or exhibiting moderate control effectiveness. In order to counteract these drawbacks, active techniques have been implemented with tuned vibration devices for improving the control performance and robustness.

Bani-Hani [144] introduced an active TMD using robust neural network methodology for mitigating the wind induced vibrations of tall build. Two neural network models, respectively aiming at predicting and operating, function together for vibration control. The performance and robustness of this active TMD with stiffness uncertainty, time delay, measurements' noise and some sensor failure were presented, which further verified the effectiveness of this method.

Another active TMD merging the independent modal space control and TMD was proposed by Cazzulani *et al.*[145]. From the comparison of independent modal space control and positive position feedback, it is shown that this active TMD is able to achieve the same damping performance of positive position feedback control without increasing the low frequency response, spillover rejection and without causing quasi-static amplification. Furthermore, superior damping effectiveness is achieved compared with the classical TMD since the static preloads induced deformations are avoided in this method.

Kim *et al.* [48] numerically and experimentally analysed and compared the optimal design of passive and active vibration absorbers using piezoelectric materials, which further addresses the robustness of the active absorber. Duan and Or [79] developed a self-sensing vibration absorber as shown in Figure 3.1 for active vibration absorption. High tunability and good sensing capability and excellent absorbability were obtained in their study, which demonstrated the great promise for deploying this active absorber.

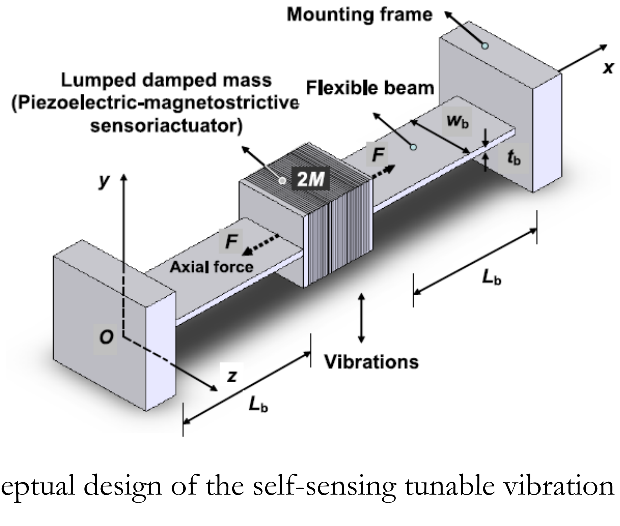

Figure 3.1. Conceptual design of the self-sensing tunable vibration absorber [79].

Significant damping attenuation and robustness of active tuned vibration devices are demonstrated and achieved in the cited literature. However, since a prescribed control algorithm and external power supply are required to generate the control force, the application of active

TMD is limited, especially during strong earthquakes which may result in power failure. Besides, the active TMD system is bulky and their operational cost is higher compared with the passive TMDs. Hence, to combine the simplicity of passive TMDs with the advantages of active TMDs such as broadband, excellent control performance and robustness, several semi-passive/semi-active TMD systems have been proposed.

Davis and Lesieutre [45] adjusted the effective stiffness of a vibration absorber by using a multiple and controllable piezoelectric capacitive shunt circuit, thus allowing tuning the resonance frequency in the range of its short and open circuit resonance frequencies.

The stiffness of the state-switched absorber (SSA) proposed by Cunefare *et al.* [44] as a descendant of TVA and TMD is changeable as well. In this approach, the switch is inactive until the relative displacement of SSA equals to zero for ensuring that the total energy of the system is the same before and after a switching event and avoiding mechanical transients. At that moment, this absorber instantaneously retunes to a new frequency. The performances of SSA and classical TVA under base excitation with two harmonic spectral components (Figure 3.2 (a)) were investigated by simulation and experiments, which indicated the potential of SSA for multi-frequency vibration control and proved its superior control performances (Figure 3.2 (b)).

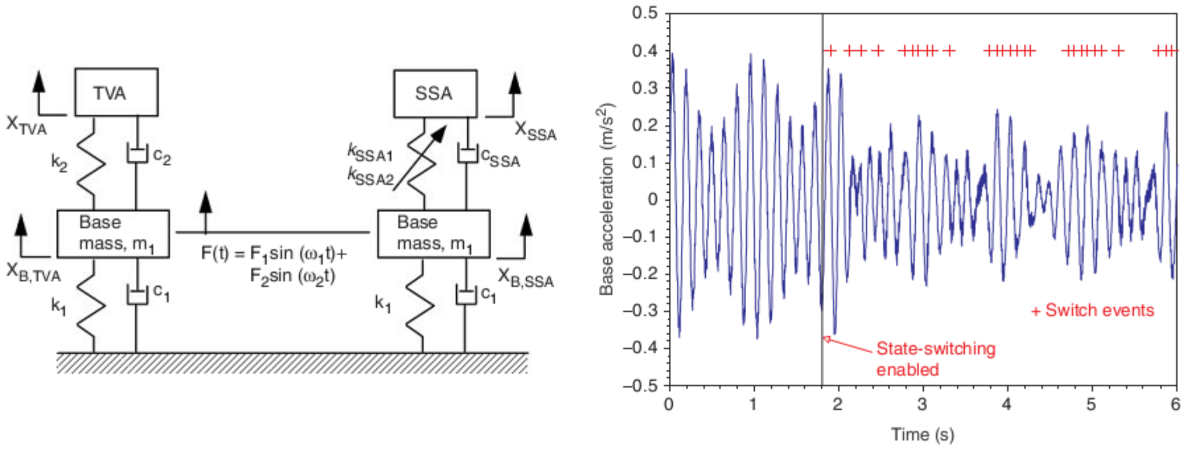

(a) (b)

Figure 3.2. (a) TVA and SSA attached to identical base system with identical forcing and (b) Base response for forcing frequencies of 4.5 and 5.5 Hz and TVA frequency of 7.2 Hz and SSA frequencies of 4.7 and 7.2 Hz [147].

Nagarajaiah and Sonmez [149] developed a semi-active control algorithm based on real-time frequency tracking of excitation by short time Fourier transform (Figure 3.3) for reducing the response of multi-story structures equipped with single or multiple semi-active independently variable stiffness (SAIVS) device (Figure 3.4).

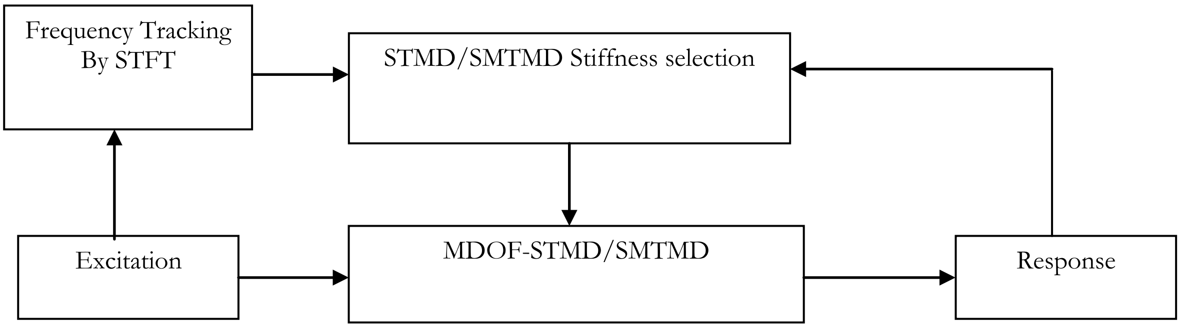

Figure 3.3. Control algorithm for adjusting the proper positioning of semi-active device [149].

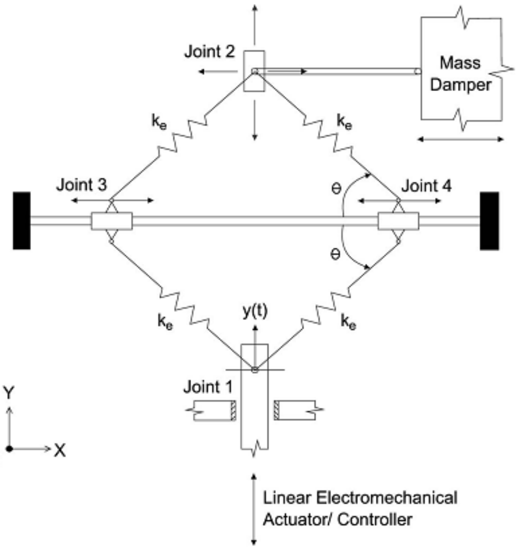

Figure 3.4. Schematic of the semi-active and independently variable stiffness (SAIVS) device [149].

This semi-active device can continuously and independently vary its stiffness by configuring the aspect ratio of the rhombus through a linear electromechanical actuator regulated by the controller. As the joints 1 and 2 (Figure 3.4) are in closest position, the device is tuned to its maximum stiffness. Similarly, when the joints 3 and 4 (Figure 3.4) are in closest position, the aspect ratio changes to open configuration which leads to the minimum stiffness. From the time responses obtained under harmonic, stationary and nonstationary excitation, it is concluded that the single and multiple semi-active TMD systems are superior to the passive TMD and multiple TMD systems and comparable to an active TMD with lower power consumption. Moreover, it can retune its frequency in real time thus allowing a distinct robustness against the dynamic characteristic changes of the primary structure.

Besides, it is known that once a linear TMD has an unintended nonlinearity, its performance will be significantly decreased (Figure 3.5 (a)). To tackle this problem, Eason *et al.* [150] proposed a configuration as retrofit of a TMD. As shown in Figure 3.5 (b), a SAIVS device aiming at removing the energy from a nonlinear TMD without diminishing its damping effectiveness is added in series with a passive TMD with small cubic stiffness nonlinearity. Based on the verification under random excitation, it is suggested that by adding a small SAIVS device, the operating range of TMD can be expanded without worrying about nonlinearities. Moreover, it is an efficient and cost-effective alternative to the original system.

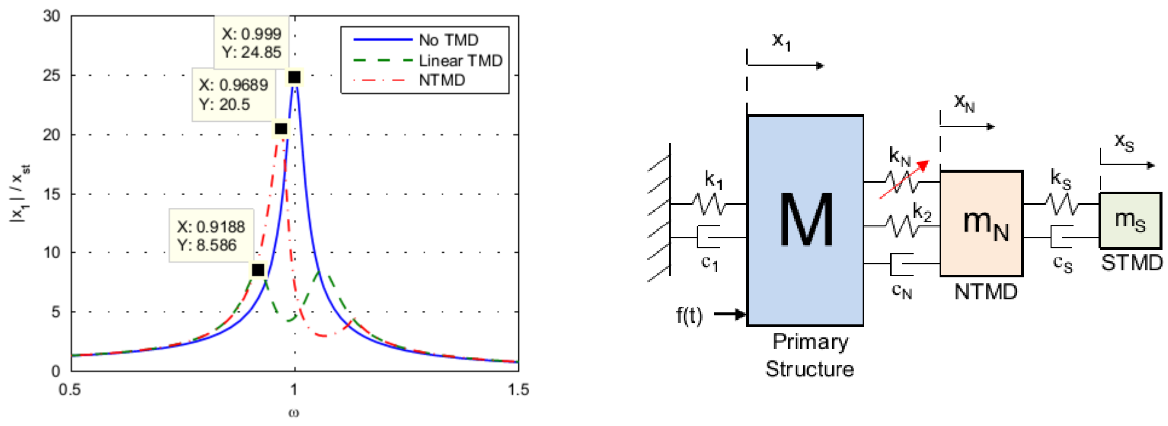

(a) (b)

Figure 3.5. (a) Primary structure frequency response curves and (b) Schematic of a primary structure with a nonlinear TMD and STMD in series [150].

Lin *et al.* [151] developed a semi-active piezoelectric friction TMD (Figure 3.6) which can adjust its slip force in response to the structure motion. By installing this device, the friction force can be regulated online. The effectiveness of this semi-active friction TMD was validated by the shacking table tests which also proved that this system can prevent a residual TMD stroke.

Ricciardelli *et al.* [152] presented a semi-active control strategy which uses an empirical algorithm for optimizing the control performance of TMD based on the measured response. Another semi-active approach depending on the structural response was proposed by Chey *et al.* [153] for effective retuning. Time history analyses concluded that the semi-active TMD is an effective way to limit earthquake damage with excellent robustness.

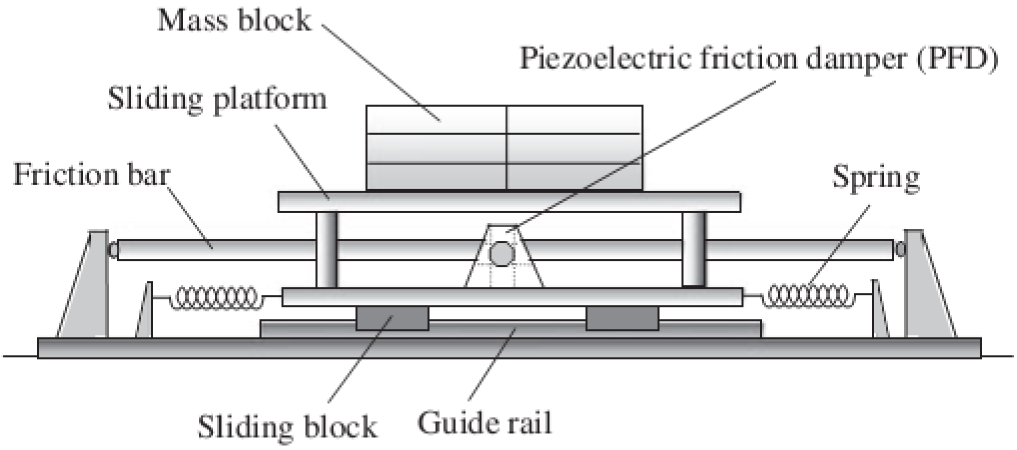

Figure 3.6. Schematic diagram of the SAF-TMD [151].

To enhance the damping performance and robustness of traditional tuned vibration devices, several kinds of semi-active systems have been reported. According to their investigations, it is shown that semi-active tuned vibration devices can obtain comparable damping performance as active TMD with lower energy requirement. Furthermore, it is insensitive to the dynamic characteristic changes of primary structure or frequency shift of environment since these semi-active devices are adaptive, thus allowing a potential for structural vibration suppression.

3.2. Theoretical analysis

For unambiguous demonstration, the TMD system such as traditional TMD which increases the damping of mechanism by mechanical to mechanical coupling is named as purely mechanical TMD (Figure 3.7). Meanwhile, the TMD which improves the damping performance by mechanical to mechanical coupling, as well as by electromechanical coupling is named as electromechanical TMD (Figure 3.8), such as the TMD featuring piezoelectric materials or other smart materials. In this section, a new semi-passive damping concept combining the electromechanical TMD featuring piezoelectric material with Synchronized Switch Damping on Inductor (SSDI) which can artificially increase the damping of system by integrating a switching circuit is presented for suppressing the response of vibrating structure, namely host structure. For detailed demonstration, a two-degree of freedom (TDOF) lumped mass model will be developed and used for explicating the control principles of the proposed semi-passive nonlinear TMD. The dynamical characteristics of purely mechanical TMD, electromechanical passive TMD and electromechanical semi-passive nonlinear TMD will be discussed and compared on the basis of the TDOF modelling. As an alternative numerical analysis method, a finite element model will be briefly introduced as well.

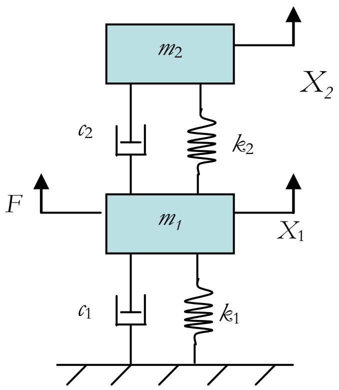

Figure 3.7. Purely mechanical TMD.

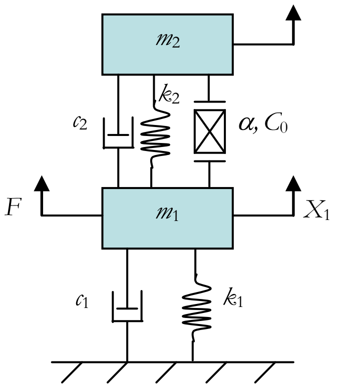

Figure 3.8. Electromechanical TMD.

3.2.1. Lumped model

In this subsection, a lumped mass model is developed to represent the vibrating structure and the system composed of a vibrating host structure and a TMD which is excited around one of its resonance frequencies. The principles of purely mechanical TMD, electromechanical passive TMD and the proposed electromechanical semi-passive nonlinear TMD will be introduced.

a) Host structure

Typically, the vibrating structure excited around one of its resonance frequencies can be simplified as a one degree of freedom system and represented by a single lumped mass with dynamical characteristics (stiffness k_1, damping c_1 and mass m_1). Thus, the motion equation of the vibrating structure under the external force F_1 can be expressed as

$$m_1\ddot{X}_1 + c_1\dot{X}_1 + k_1X_1 = F_1 \tag{3.1}$$

where $\ddot{X}$, $\dot{X}$ and X denote the acceleration, velocity and displacement responses in time domain under the external force F_1, respectively. The subscript *1* represents the vibrating structure (host structure).

When a sinusoidal external excitation $F_1(\omega) = \tilde{F}_1 e^{j\omega t}$ is applied, the above equation can be further written in frequency domain as:

$$\left(-\omega^2 m_1 + j\omega c_1 + k_1\right)\tilde{X}_1 = \tilde{F}_1 \tag{3.2}$$

Hence, the transfer function between the displacement of the host structure $\tilde{X}_1$ and the external force $\tilde{F}_1$ in frequency domain can be expressed as

$$\left(\frac{\tilde{X}_1}{\tilde{F}_1}\right)_{host\ only} = \frac{1}{\left(-\omega^2 m_1 + j\omega c_1 + k_1\right)} \tag{3.3}$$

b) Purely mechanical tuned mass damper (TMD)

Figure 3.7 depicts a TDOF model of a system composed of a traditional TMD attached to a vibrating host structure. As previous demonstration, for simplicities, the host structure and the TMD are respectively idealized as a single lumped mass characterised by stiffness *k*, damping *c* and mass *m*. Hence, the dynamical equations of this system under an external force can be given by

$$\begin{bmatrix} m_1 & 0 \\ 0 & m_2 \end{bmatrix}\begin{Bmatrix} \ddot{X}_1 \\ \ddot{X}_2 \end{Bmatrix} + \begin{bmatrix} c_1 + c_2 & -c_2 \\ -c_2 & c_2 \end{bmatrix}\begin{Bmatrix} \dot{X}_1 \\ \dot{X}_2 \end{Bmatrix} + \begin{bmatrix} k_1 + k_2 & -k_2 \\ -k_2 & k_2 \end{bmatrix}\begin{Bmatrix} X_1 \\ X_2 \end{Bmatrix} = \begin{Bmatrix} F_1 \\ 0 \end{Bmatrix} \tag{3.4}$$

The subscript *1* represents the host structure and *2* indicates the TMD.

When a sinusoidal external excitation at an angular frequency ω expressed by $F_1(\omega) = \tilde{F}_1 e^{j\omega t}$ is applied, the responses of the system in frequency domain can be obtained through

$$\left\{-\omega^2\begin{bmatrix} m_1 & 0 \\ 0 & m_2 \end{bmatrix} + j\omega\begin{bmatrix} c_1 + c_2 & -c_2 \\ -c_2 & c_2 \end{bmatrix} + \begin{bmatrix} k_1 + k_2 & -k_2 \\ -k_2 & k_2 \end{bmatrix}\right\}\begin{Bmatrix} \tilde{X}_1 \\ \tilde{X}_2 \end{Bmatrix} = \begin{Bmatrix} \tilde{F}_1 \\ 0 \end{Bmatrix} \tag{3.5}$$

Thus, the transfer function between the displacement of the host structure $\tilde{X}_1$ and the external force $\tilde{F}_1$ in frequency domain can then be expressed as:

$$\left(\frac{\tilde{X}_1}{\tilde{F}_1}\right)_{pure\ TMD} = \frac{1}{\left[\left(-\omega^2 m_1 + j\omega c_1 + k_1\right) + \dfrac{-\omega^2 m_2\left(j\omega c_2 + k_2\right)}{\left(-\omega^2 m_2 + j\omega c_2 + k_2\right)}\right]} \tag{3.6}$$

c) Electromechanical passive tuned mass damper (TMD)

Thanks to the development of intelligent materials, the dynamical characteristics of the system featuring smart materials are possible to be adjusted easily. Piezoelectric materials which couple the mechanical and electrical domains are suited to be used and implemented for vibration control attributed to its high integration capability, compactness, light weight and broad bandwidth. Thus, in our study, we concern with the performance of electromechanical TMD implementing piezoelectric materials as shown in Figure 3.8, although this concept of electromechanical semi-passive nonlinear TMD can integrate other smart materials. As a result of the electromechanical characteristic of piezoelectric materials, electrical charges appear on the two surfaces of the piezoelectric patch during the vibration, thus generating a piezovoltage. Then, the motion equations of the system featuring an electromechanical TMD can be represented by

$$\begin{bmatrix} m_1 & 0 \\ 0 & m_2 \end{bmatrix} \begin{Bmatrix} \ddot{X}_1 \\ \ddot{X}_2 \end{Bmatrix} + \begin{bmatrix} c_1+c_2 & -c_2 \\ -c_2 & c_2 \end{bmatrix} \begin{Bmatrix} \dot{X}_1 \\ \dot{X}_2 \end{Bmatrix} + \begin{bmatrix} k_1+k_2 & -k_2 \\ -k_2 & k_2 \end{bmatrix} \begin{Bmatrix} X_1 \\ X_2 \end{Bmatrix} + \begin{bmatrix} -\alpha \\ \alpha \end{bmatrix} V = \begin{Bmatrix} F_1 \\ 0 \end{Bmatrix} \tag{3.7}$$

with V the voltage between the two electrodes of the piezoelectric element. α denotes the force factor which is the ratio between force and the voltage due to inverse piezoelectric effect.

Moreover, the current I flowing out of the piezoelectric patch can be obtained by

$$I = \alpha\left(\dot{X}_2 - \dot{X}_1\right) - C_0\dot{V} \tag{3.8}$$

where C_0 is the clamped capacitance of the piezoelectric element.

It can be found from the above equations that when the piezoelectric element is in short circuit, the piezovoltage is null. In this case, the electromechanical TMD operates as a purely mechanical TMD without electromechanical coupling.

When the piezoelectric patch is in open circuit, the current I is null. Then, the Eq. (3.8) can be reduced as

$$C_0\dot{V} = \alpha\left(\dot{X}_2 - \dot{X}_1\right) \tag{3.9}$$

Hence, considering null initial conditions, the relationship between piezovoltage and relative displacement could be expressed by

$$V = \frac{\alpha}{C_0}\left(X_2 - X_1\right) \tag{3.10}$$

Then, the dynamical response equations of the system can be rewritten as

$$\begin{bmatrix} m_1 & 0 \\ 0 & m_2 \end{bmatrix} \begin{Bmatrix} \ddot{X}_1 \\ \ddot{X}_2 \end{Bmatrix} + \begin{bmatrix} c_1+c_2 & -c_2 \\ -c_2 & c_2 \end{bmatrix} \begin{Bmatrix} \dot{X}_1 \\ \dot{X}_2 \end{Bmatrix} + \begin{bmatrix} k_1+k_2' & -k_2' \\ -k_2' & k_2' \end{bmatrix} \begin{Bmatrix} X_1 \\ X_2 \end{Bmatrix} = \begin{Bmatrix} F_1 \\ 0 \end{Bmatrix} \tag{3.11}$$

with an equivalent stiffness $k_2' = k_2 + \dfrac{\alpha^2}{C_0}$.

From the previous demonstration, it can be easily found that the electromechanical TMD in open circuit also operates as a purely mechanical TMD with an increased stiffness $k_2 + \alpha^2 / C_0$ because of the electromechanical coupling.

In addition, the electromechanical TMD is an adaptive device and its resonance frequency is changeable by connecting the piezoelectric element to a shunt circuit. Generally, the shunt circuit is comprised of passive electrical components such as resistor, inductor and capacitor. Thus, the mechanical energy of the vibrating structure can be firstly transferred into electrical energy by piezoelectric material and then dissipated in the shunt circuit through Joule heating when using a resistor (Figure 3.9). Since huge value of inductance required in inductive shunt circuit, which compromises the realistic implementation, in this study, only the resistive shunt circuit is discussed.

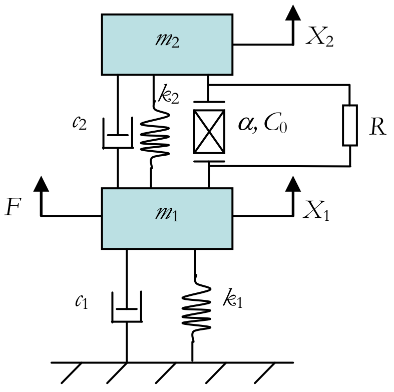

Figure 3.9. Electromechanical passive TMD.

Hence, the electrical relationship of this passive TMD shown in Figure 3.9 becomes

$$\frac{V}{R} = \alpha\left(\dot{X}_2 - \dot{X}_1\right) - C_0\dot{V} \tag{3.12}$$

where R denotes the resistance of the shunt circuit.

When the system is subjected to a sinusoidal external excitation $F_1(\omega) = \tilde{F}_1 e^{j\omega t}$, the above equation can be reduced to Eq. (3.13) by inserting the corresponding frequency responses $X_1(\omega) = \tilde{X}_1 e^{j\omega t}$, $X_2(\omega) = \tilde{X}_2 e^{j\omega t}$ and $V(\omega) = \tilde{V} e^{j\omega t}$.

$$\tilde{V} = \frac{j\omega\alpha R}{\left(1 + j\omega C_0 R\right)}\left(\tilde{X}_2 - \tilde{X}_1\right) \tag{3.13}$$

Then, the dynamical frequency responses of the system integrating the electromechanical passive TMD can be written in matrix-vector notation as

$$\left\{-\omega^2\begin{bmatrix} m_1 & 0\\ 0 & m_2\end{bmatrix} + j\omega\begin{bmatrix} c_1+c_2 & -c_2\\ -c_2 & c_2\end{bmatrix} + \begin{bmatrix} k_1+k_2 & -k_2\\ -k_2 & k_2\end{bmatrix} + \frac{j\omega\alpha^2 \mathrm{R}}{\left(1+j\omega C_0 \mathrm{R}\right)}\begin{bmatrix}1 & -1\\ -1 & 1\end{bmatrix}\right\}\begin{Bmatrix}\tilde{X}_1\\ \tilde{X}_2\end{Bmatrix} = \begin{Bmatrix}\tilde{F}_1\\ 0\end{Bmatrix} \tag{3.14}$$

The transfer function between the displacement of the host structure $\tilde{X}_1$ and the external force $\tilde{F}_1$ in frequency domain in this case can be expressed by

$$\left(\frac{\tilde{X}_1}{\tilde{F}_1}\right)_{electromechanical\ passive\ TMD} = \frac{1}{\left[-\omega^2 m_1 + j\omega c_1 + k_1 + \dfrac{-\omega^2 m_2\left(j\omega c_2 + k_2 + \dfrac{j\omega\alpha^2\mathrm{R}}{\left(1+j\omega C_0\mathrm{R}\right)}\right)}{\left[-\omega^2 m_2 + j\omega c_2 + k_2 + \dfrac{j\omega\alpha^2\mathrm{R}}{\left(1+j\omega C_0\mathrm{R}\right)}\right]}\right]} \tag{3.15}$$

As demonstrated in the literature, the electromechanical passive TMD can achieve optimum damping by integrating the optimal impedance R_{opt} which depends on the angular frequency of the vibration. Usually, the optimized R can be calculated by

$$\mathrm{R}_{opt} = \frac{1}{C_0\omega} \tag{3.16}$$

Hence, the dynamical frequency responses in optimized case can be obtained, yielding

$$\left\{-\omega^2\begin{bmatrix} m_1 & 0\\ 0 & m_2\end{bmatrix} + j\omega\begin{bmatrix} c_1+c_2 & -c_2\\ -c_2 & c_2\end{bmatrix} + \begin{bmatrix} k_1+k_2 & -k_2\\ -k_2 & k_2\end{bmatrix} + \frac{\left(1+j\right)\alpha^2}{2C_0}\begin{bmatrix}1 & -1\\ -1 & 1\end{bmatrix}\right\}\begin{Bmatrix}\tilde{X}_1\\ \tilde{X}_2\end{Bmatrix} = \begin{Bmatrix}\tilde{F}_1\\ 0\end{Bmatrix} \tag{3.17}$$

and the relationship between the displacement of the vibrating structure $\tilde{X}_1$ and the external force $\tilde{F}_1$ can be further written as

$$\left(\frac{\tilde{X}_1}{\tilde{F}_1}\right)_{optimal\ electromechanical\ passive\ TMD} = \frac{1}{\left[-\omega^2 m_1 + j\omega c_1 + k_1 + \left\{\dfrac{-\omega^2 m_2\left(j\omega c_2 + k_2 + \dfrac{\left(1+j\right)\alpha^2}{2C_0}\right)}{\left[-\omega^2 m_2 + j\omega c_2 + k_2 + \dfrac{\left(1+j\right)\alpha^2}{2C_0}\right]}\right\}\right]} \tag{3.18}$$

d) Electromechanical semi-passive nonlinear tuned mass damper (TMD)

In order to achieve superior damping effectiveness of TMD, the semi-passive SSDI approach is incorporated into the electromechanical TMD system as shown in Figure 3.10 to increase the transferred energy thus dissipating more mechanical energy of the host structure. Since the proposed TMD does not need external power to generate control force and only very lower energy is required for triggering the digital switch, this nonlinear TMD is a semi-passive device.

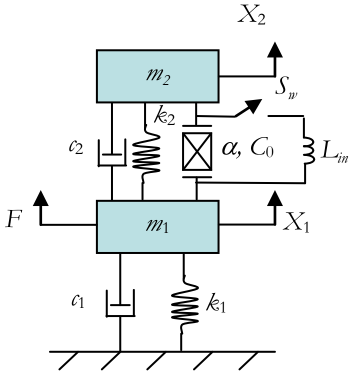

Figure 3.10. Electromechanical semi-passive nonlinear TMD.

As illustrated in Figure 3.10, a switching device composed of a digital switch S_w and an inductor L_{in} is connected in parallel with the piezoelectric patch of the TMD. Same as in classical SSDI approach, the switch is always kept open until the relative displacement/piezovoltage of the electromechanical TMD reaches an extremum value. When the switch is in off state, the current flowing from the piezoelectric patch is null. Thus, the equation of electrical relationship given by (3.9) is still valid in open circuit. Once an extremum value is detected, the switch will be triggered to close. At that moment, an electrical oscillator is constituted by the capacitance of the piezoelectric patch and the inductor. This switch is kept closed for half a period of the electrical oscillator t_i (Eq. (2.15)) for reversing the piezovoltage. It should be noted that the switching time is much shorter than the period of the motion of electromechanical TMD, thus it can be considered as an instantaneous voltage inversion process.

As demonstrated in last chapter, the voltage inversion is imperfect due to energy lost in the switching network (digital switch and inductor), thus, the voltage inversion coefficient γ ($0 \le \gamma < 1$) is introduced here which can be obtained from the absolute voltages before V_{before} and after V_{after} switching as well as from the electrical quality factor Q_e of the RLC circuit:

$$\gamma = \frac{V_{after}}{V_{before}} = e^{-\frac{\pi}{2Q_e}} \tag{3.19}$$

When SSDI approach is operating in steady state, the voltage can be decomposed into a voltage proportional to the displacement difference and a piecewise constant function H [126]

$$H = H_M sign\left(\dot{X}_2 - \dot{X}_1\right) \tag{3.20}$$

in phase with the displacement of the speed signals $\left(\dot{X}_2 - \dot{X}_1\right)$:

$$V = \frac{\alpha}{C_0}\left(X_2 - X_1\right) + H \tag{3.21}$$

Moreover, the magnitude H_M of the piecewise function H can be expressed similarly as [126]

$$H_M = \frac{1+\gamma}{1-\gamma}\frac{\alpha}{C_0}\left(X_2 - X_1\right)_M \tag{3.22}$$

where $\left(X_2 - X_1\right)_M$ denotes the magnitude of the displacement difference between the electromechanical semi-passive nonlinear TMD and the host structure.

When a sinusoidal external force is applied, the piecewise function can be expressed as the first harmonic approximation:

$$\tilde{H} = \frac{2}{T}\left[-\int_0^{\frac{T}{2}} He^{-j\omega t}dt + \int_{\frac{T}{2}}^{T} He^{-j\omega t}dt\right] = j\frac{4}{\pi}H_M \tag{3.23}$$

where T denotes the period and the ω is angular frequency.

Hence, according to the relationships given in Eqs. (3.21)-(3.23), the voltage response in frequency domain can be approximated by

$$\tilde{V} \approx \frac{\alpha}{C_0}\left(\tilde{X}_2 - \tilde{X}_1\right) + j\frac{4}{\pi}\frac{1+\gamma}{1-\gamma}\frac{\alpha}{C_0}\left(\tilde{X}_2 - \tilde{X}_1\right) \tag{3.24}$$

or

$$\tilde{V} \approx \left(\frac{\alpha}{C_0} + j\frac{4}{\pi}\frac{1+\gamma}{1-\gamma}\frac{\alpha}{C_0}\right)\begin{bmatrix}-1 & 1\end{bmatrix}\begin{bmatrix}\tilde{X}_1 \\ \tilde{X}_2\end{bmatrix} \tag{3.25}$$

Then, the general dynamical equations of this electromechanical semi-passive nonlinear TMD in frequency domain can be expressed as:

$$\left\{-\omega^2\begin{bmatrix} m_1 & 0 \\ 0 & m_2\end{bmatrix} + j\omega\begin{bmatrix} c_1 + c_2 & -c_2 \\ -c_2 & c_2\end{bmatrix} + \begin{bmatrix} k_1 + k_2 & -k_2 \\ -k_2 & k_2\end{bmatrix} + \left(\frac{\alpha^2}{C_0} + j\frac{4}{\pi}\frac{1+\gamma}{1-\gamma}\frac{\alpha^2}{C_0}\right)\begin{bmatrix} 1 & -1 \\ -1 & 1\end{bmatrix}\right\}\begin{Bmatrix}\tilde{X}_1 \\ \tilde{X}_2\end{Bmatrix} = \begin{Bmatrix}\tilde{F}_1 \\ 0\end{Bmatrix} \tag{3.26}$$

which can be further written by

$$\left\{-\omega^2\begin{bmatrix} m_1 & 0 \\ 0 & m_2\end{bmatrix} + j\omega\begin{bmatrix} c_1 + c_2 + \frac{4}{\pi}\frac{1+\gamma}{1-\gamma}\frac{\alpha^2}{C_0\omega} & -c_2 - \frac{4}{\pi}\frac{1+\gamma}{1-\gamma}\frac{\alpha^2}{C_0\omega} \\ -c_2 - \frac{4}{\pi}\frac{1+\gamma}{1-\gamma}\frac{\alpha^2}{C_0\omega} & c_2 + \frac{4}{\pi}\frac{1+\gamma}{1-\gamma}\frac{\alpha^2}{C_0\omega}\end{bmatrix} + \begin{bmatrix} k_1 + k_2 + \frac{\alpha^2}{C_0} & -k_2 - \frac{\alpha^2}{C_0} \\ -k_2 - \frac{\alpha^2}{C_0} & k_2 + \frac{\alpha^2}{C_0}\end{bmatrix}\right\}\begin{Bmatrix}\tilde{X}_1 \\ \tilde{X}_2\end{Bmatrix} = \begin{Bmatrix}\tilde{F}_1 \\ 0\end{Bmatrix} \tag{3.27}$$

The transfer function between the displacement of the vibrating structure $\tilde{X}_1$ and the external force $\tilde{F}_1$ of this electromechanical semi-passive TMD is then given as

$$\left(\frac{\tilde{X}_1}{\tilde{F}_1}\right)_{semi-passive} = \frac{1}{\left(-\omega^2 m_1 + j\omega c_1 + k_1\right) + \dfrac{-\omega^2 m_2\left[j\omega c_2 + j\frac{4}{\pi}\frac{1+\gamma}{1-\gamma}\frac{\alpha^2}{C_0} + k_2 + \frac{\alpha^2}{C_0}\right]}{\left[-\omega^2 m_2 + j\omega c_2 + j\frac{4}{\pi}\frac{1+\gamma}{1-\gamma}\frac{\alpha^2}{C_0} + k_2 + \frac{\alpha^2}{C_0}\right]}} \tag{3.28}$$

Compared with the previous demonstration of the purely mechanical TMD and electromechanical passive TMD, it can be easily found that by employing the SSDI approach in the electromechanical TMD device, the coupling is artificially increased. Thus, more mechanical energy of the vibrating host structure will be transferred into electrical energy attributed to the instantaneous switching process and then stored electrically on the piezoelectric element or dissipated in the switching circuit.

The two-degree of freedom (TDOF) model is developed to preliminarily analyze the dynamical responses of the vibrating host structure and/or TMD device in this subsection. Detailed principles of traditional purely mechanical TMD, electromechanical passive TMD and the proposed electromechanical semi-passive nonlinear TMD are addressed. Since the TDOF modelling is independent from the complexity of the host structure, it is a simple and easy method. To compare the damping effectiveness of the mentioned TMD devices, the investigation based on the TDOF modelling is discussed in the following subsection.

3.2.2. Preliminary dynamical response discussion

On the basis of the previous demonstration, the dynamical characteristics of purely mechanical TMD, electromechanical passive TMD and electromechanical semi-passive TMD systems can be preliminary investigated. Since for the electromechanical passive TMD device, the maximized transferred energy can be extracted and damped into the electrical circuit as the optimized resistance given in Eq. (3.16) is integrated, thus, hereinafter, only the optimal electromechanical passive TMD is considered. In order to simplify and generalize the transfer functions between the displacement of the primary structure and the external force, the following parameters are introduced:

$$\Omega = \frac{\omega}{\omega_1} \text{ with } \omega_1 = \sqrt{\frac{k_1}{m_1}} \tag{3.29}$$

$$r_\omega = \frac{\omega_2}{\omega_1} \text{ with } \omega_2 = \sqrt{\frac{k_2}{m_2}} \tag{3.30}$$

$$r_m = \frac{m_2}{m_1} \tag{3.31}$$

$$r_\zeta = \frac{\zeta_2}{\zeta_1} \text{ with} \zeta_1 = \frac{c_1}{2\sqrt{k_1 m_1}}, \zeta_2 = \frac{c_2}{2\sqrt{k_2 m_2}} \tag{3.32}$$

$$\kappa = \sqrt{\frac{\alpha^2}{C_0} \Bigg/ \left(k_2 + \frac{\alpha^2}{C_0}\right)} \tag{3.33}$$

Then, the normalized displacement responses of the primary structure $k_1\tilde{X}_1/\tilde{F}_1$ without and with the investigated TMD systems can be summarised as:

Host structure without TMD (or host only):

$$\left(\frac{k_1\tilde{X}_1}{\tilde{F}_1}\right)=\frac{1}{\left(-\Omega^2+j\Omega 2\zeta_1+1\right)} \tag{3.34}$$

Purely mechanical TMD:

$$\left(\frac{\tilde{X}_1}{F_1}\right)_{pure\ TMD}=\frac{1}{k_1\left[\left(-\Omega^2+j\Omega 2\zeta_1+1\right)+\dfrac{-\Omega^2 r_m r_\omega\left(j\Omega 2r_\zeta\zeta_1+r_\omega\right)}{\left(-\Omega^2+j\Omega 2r_\zeta\zeta_1 r_\omega+r_\omega{}^2\right)}\right]} \tag{3.35}$$

Optimal electromechanical passive TMD:

$$\left(\frac{\tilde{X}_1}{\tilde{F}_1}\right)_{optimal}=\frac{1}{k_1\left[-\Omega^2+j\Omega 2\zeta_1+1+\dfrac{-\Omega^2 r_m r_\omega\left(j\Omega 2r_\zeta\zeta_1+r_\omega+\dfrac{(1+j)}{2}\dfrac{\kappa^2}{\left(1-\kappa^2\right)}r_\omega\right)}{\left[-\Omega^2+j\Omega 2r_\zeta\zeta_1 r_\omega+r_\omega{}^2+\dfrac{(1+j)}{2}\dfrac{\kappa^2}{\left(1-\kappa^2\right)}r_\omega{}^2\right]}\right]} \tag{3.36}$$

Electromechanical semi-passive nonlinear TMD:

$$\left(\frac{\tilde{X}_1}{\tilde{F}_1}\right)_{semi-passive}=\frac{1}{k_1\left[\left(-\Omega^2+j\Omega 2\zeta_1+1\right)+\dfrac{-\Omega^2 r_m r_\omega\left[j\Omega 2r_\zeta\zeta_1+r_\omega+\dfrac{\kappa^2}{\left(1-\kappa^2\right)}r_\omega\left(1+j\dfrac{4}{\pi}\dfrac{1+\gamma}{1-\gamma}\right)\right]}{\left[-\Omega^2+j\Omega 2r_\zeta\zeta_1 r_\omega+r_\omega{}^2+\dfrac{\kappa^2 r_\omega{}^2}{\left(1-\kappa^2\right)}\left(1+j\dfrac{4}{\pi}\dfrac{1+\gamma}{1-\gamma}\right)\right]}\right]} \tag{3.37}$$

a) Damping performances of tuned TMD systems

Generally, a primary structure featuring TMD device is a lightly damped structure and it is considered as undamped structure in the classical vibration theory. To be more realistic, in this part, the damping ratios of the host structure as $\zeta_1 = 0.002$ and $\zeta_1 = 0.02$ will be considered and discussed. The TMD devices are supposed to be tuned at one of the resonance frequencies of the vibrating structure, namely $r_\omega = 1$. In order to compare and discuss the damping performance of each TMD system, the attenuation defined as

$$20\times\log_{10}\left(\frac{\max\left(Displacement\ amplitude_{with\ control}\right)}{\max\left(Displacement\ amplitude_{host\ only}\right)}\right) \tag{3.38}$$

is introduced. Same as introduced in last chapter, the value of attenuation is negative when the vibration is damped and positive as the vibration is magnified.

Figure 3.11 and Figure 3.12 expose the attenuation of tuned purely mechanical TMD device obtained with Ω in the range of 0~2 and varied with mass ratio r_m in the cases of different r_ζ. Typically, the mass ratio does not exceed a few percent of the host structure mass in civil applications, whereas along with the development of specific applications such as micro-electro-mechanical devices (MEMS), the mass ratio can be designed greater. Hence, in the discussion, it is chosen in the range of 10^{-5}~1.

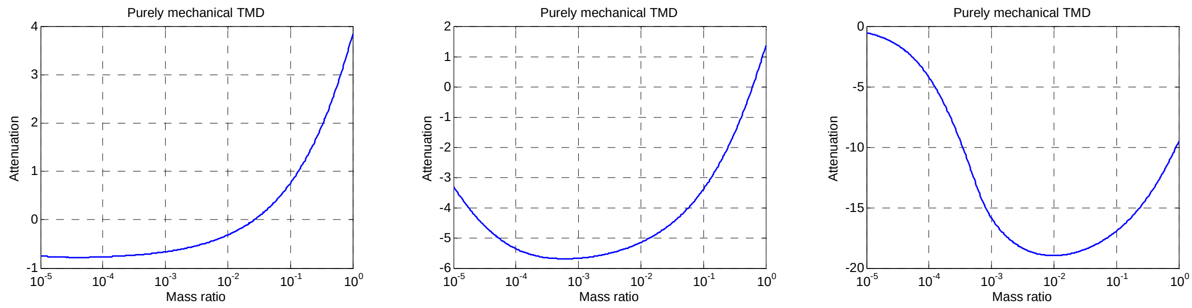

(a) $r_\zeta = 0.1$ (b) $r_\zeta = 1$ (c) $r_\zeta = 10$

Figure 3.11. Attenuation of tuned purely mechanical TMD varied with mass ratio r_m as ζ_1=0.002.

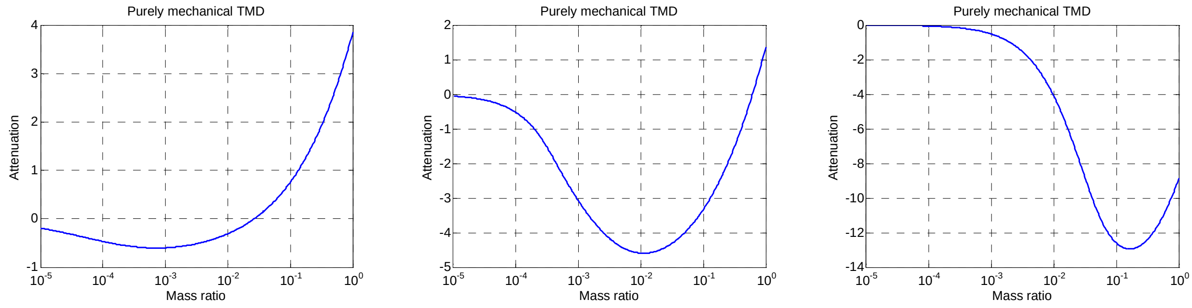

(a) $r_\zeta = 0.1$ (b) $r_\zeta = 1$ (c) $r_\zeta = 10$

Figure 3.12. Attenuation of tuned purely mechanical TMD varied with mass ratio r_m as ζ_1=0.02.

As shown in Figure 3.11 (a)-(b) and Figure 3.12 (a)-(b), when the low damping tuned purely mechanical TMD devices are installed, the dynamical responses of the host structure can be damped as the mass ratio r_ζ is lower than a specific value. After exceeding the specific mass ratio value, the global dynamical response of the primary structure may be amplified at some frequency bands instead of global reduction. However, the specific point of the mass ratio which gives the critical value is increasing as the damping ratio of the tuned purely mechanical TMD devices is increased. Thus, in the case of installing higher damping tuned purely mechanical TMD as shown in Figure 3.11 (c) and Figure 3.12(c), no critical mass ratio is found in the investigated mass ratio range although it would probably appear for greater mass ratio. Moreover, optimized mass ratio can be found from the plotted curves where the attenuation is lowest, allowing best damping performance of the tuned purely mechanical TMD, which is increased as the damping ratio of the tuned purely mechanical TMD increases. Furthermore, for limiting the vibration of primary structure, higher damping of tuned TMD devices can achieve better global damping performance as the mass ratio is a design variable. From the comparison, it can be easily found that the control effectiveness of tuned purely mechanical TMD is slightly better for limiting the vibration of less damped host structure, as the mechanical to mechanical enegy transfer is facilitated.

Corresponding attenuation of tuned optimal electromechanical passive TMD obtained with Ω in the range of 0~2, varied with mass ratio r_m and global coupling coefficient κ defined as Eq. (3.33) in the cases of different r_ζ is plotted in Figure 3.13 and Figure 3.14.

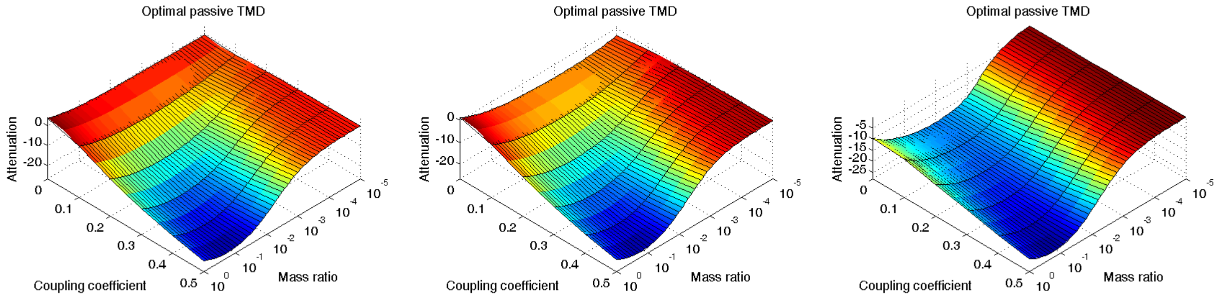

(a) $r_\zeta = 0.1$ (b) $r_\zeta = 1$ (c) $r_\zeta = 10$

Figure 3.13. Attenuation of tuned optimal electromechanical passive TMD varied with coupling coefficient κ and mass ratio r_m as ζ_t=0.002.

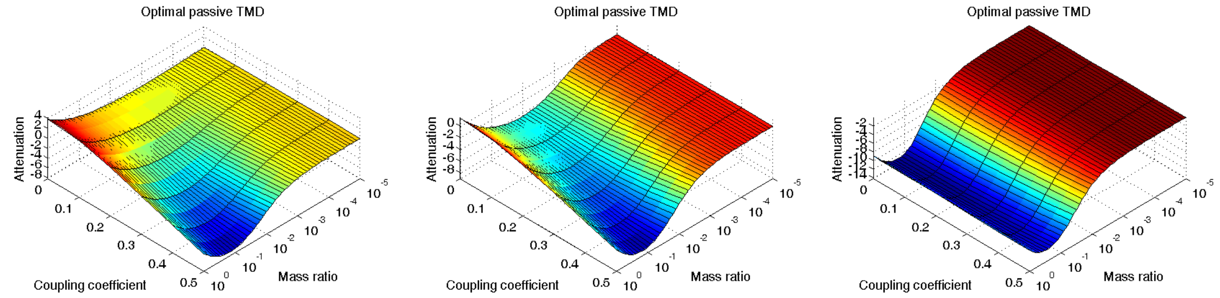

(a) $r_\zeta = 0.1$ (b) $r_\zeta = 1$ (c) $r_\zeta = 10$

Figure 3.14. Attenuation of tuned optimal electromechanical passive TMD varied with coupling coefficient κ and mass ratio r_m as ζ_t=0.02.

Similar as in the cases of using tuned purely mechanical TMD, the global damping performance is better when the higher damped tuned TMD device is employed and the damping effectiveness of tuned optimal electromechanical passive TMD is slightly superior to reduce the vibration of less damped primary structure. In addition, it can be found that it is very important to choose mass ratio as a design variable since in lower mass ratio range, the global the damping performance of tuned optimal electromechanical passive TMD is decreased with the increase of global coupling coefficient and the damping difference is decreased as the damping of primary structure increases. Meanwhile, the global damping performance of the tuned optimal electromechanical passive TMD is increased as coupling coefficient increases in the higher range of mass ratio which can be explained by the trade-off between mechanical to mechanical energy transfer and the electromechanical conversion (for low mass ratio, high coupling prevents the mechanical energy entering into TMD system). This conclusion can be further confirmed with Figure 3.15 and Figure 3.16.

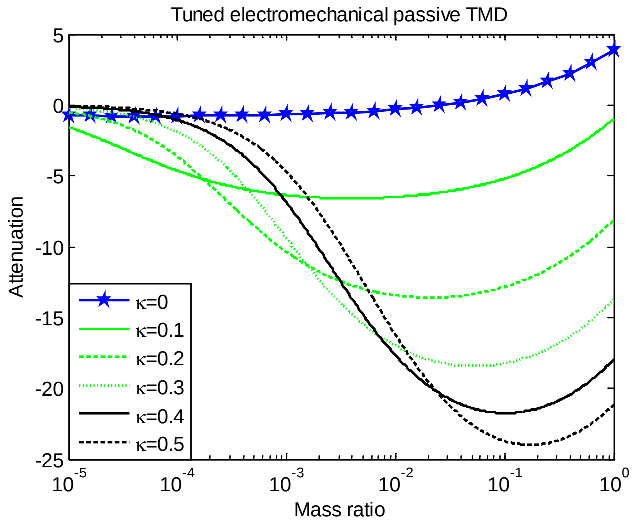

Figure 3.15. Attenuation of tuned optimal electromechanical passive TMD with r_ζ=0.1 and ζ_l=0.002.

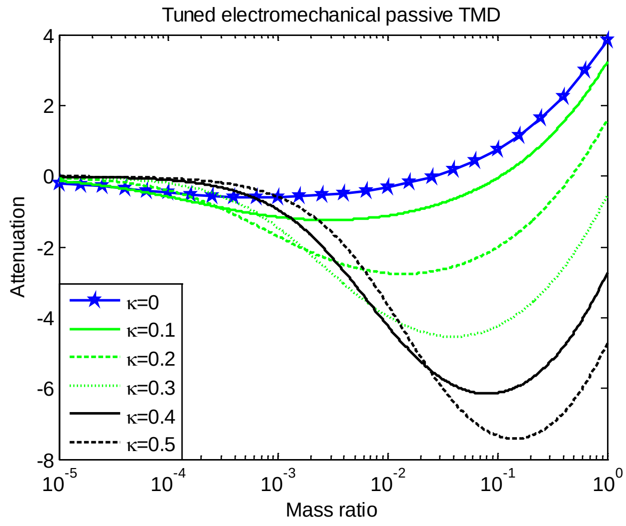

Figure 3.16. Attenuation of tuned optimal electromechanical passive TMD with r_ζ=0.1 and ζ_l=0.02.

Moreover, for limiting the vibration of primary structure with damping ratio ζ_l=0.02, it is less sensitive to the global coefficient in the case of using higher damping tuned electromechanical TMD compared with the corresponding TMD device with low damping coefficient.

In the higher damping (both primary structure and electromechanical TMD) case, no notable difference of global control performance (Figure 3.17) can be found between the electromechanical TMD and purely mechanical TMD, which is attributed to the extreme damping value of the particular case and most of the mechanical energy has been dissipated in the primary and TMD systems due to the high damping, thus there is no more extra energy needs to be damped by the electrical dissipation or storage.

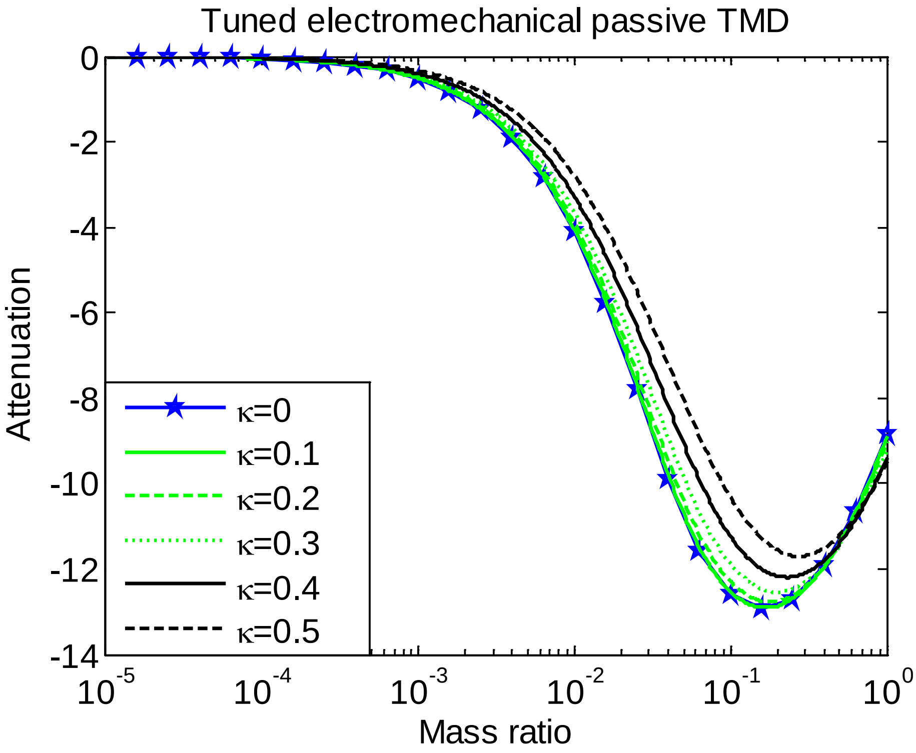

Figure 3.17. Attenuation of tuned optimal electromechanical passive TMD with r_ζ=10 and ζ_l=0.02.

Figure 3.18~Figure 3.21 expose the damping performance of tuned electromechanical semi-passive nonlinear TMD varied with the mass ratio r_m and global coupling coefficient κ. Different damping ratios of the employed tuned electromechanical semi-passive nonlinear TMD and different inversion coefficients γ are considered. When γ=0, there is no voltage inversion during the control process which is equivalent to Synchronized Switch Damping on Short circuit (SSDS) technique. From these results it can be found that the global control performance of tuned electromechanical semi-passive nonlinear TMD is better with greater damping coefficient of TMD device as the mass ratio is considered as a design variable.

For comparing the control performances of tuned electromechanical TMD devices, the details with different global coupling coefficients and voltage inversion coefficients are plotted in Figure 3.15~Figure 3.16 and Figure 3.22~Figure 3.25.

Same trend is found from the results that for lower mass ratio, the global the damping performance of tuned electromechanical semi-passive TMD is decreased as the global coupling coefficient increases and in higher mass ratio range, it is increased with the increase of global coupling coefficient.

Additionally, it is interesting to found that the global damping effectiveness of tuned electromechanical nonlinear switching TMD is very sensitive to the value of voltage inversion coefficient. When the latter is increased, the control performance of tuned electromechanical semi-passive TMD with lower global coupling coefficient is increased remarkably and the damping effectiveness of the tuned nonlinear switching TMD with higher global coupling is decreased dramatically. This phenomenon is totally different from the classical SSDI approach that intermittently connects the directly coupled piezoelectric patches to a switching device whose damping performance is monotonically increasing with the increase of voltage inversion coefficient [154]. Indeed, the two energy transfer processes (mechanical to mechanical and mechanical to electrical) lead to a trade-off to achieve the best performance, while by implementing the SSDI technique, the electromechanical conversion is artifitially increased. Thus, it can also be concluded that the proposed semi-passive nonlinear switching TMD does not always outperform the corresponding optimal electromechanical passive TMD, especially when the smart materials and the TMD are highly coupled and the voltage inversion coefficient is great. Hence, the voltage inversion coefficient γ is another very important parameter for design the proposed semi-passive nonlinear TMD.

Similar results as in previous cases are obtained as well that better control performance of the tuned electromechanical semi-passive nonlinear TMD can be achieved for attenuating lightly damped host structures.

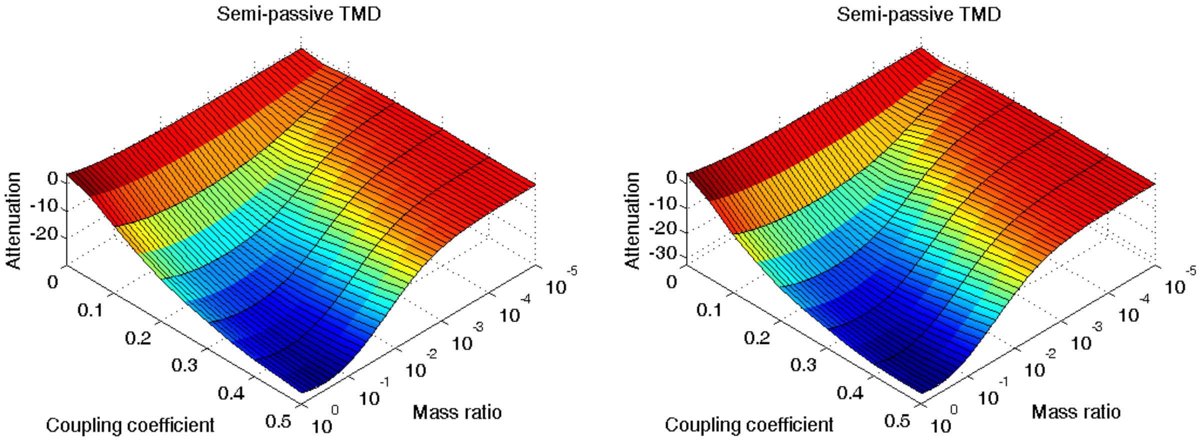

(1a) r_ζ=0.1 and γ=0

(2a) r_ζ=0.1 and γ=0.3

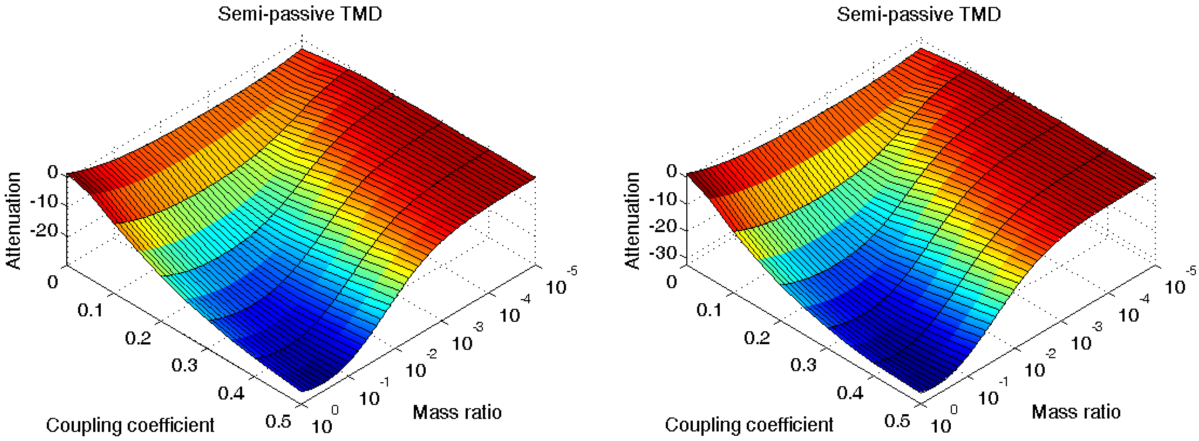

(1b) r_ζ=1 and γ=0

(2b) r_ζ=1 and γ=0.3

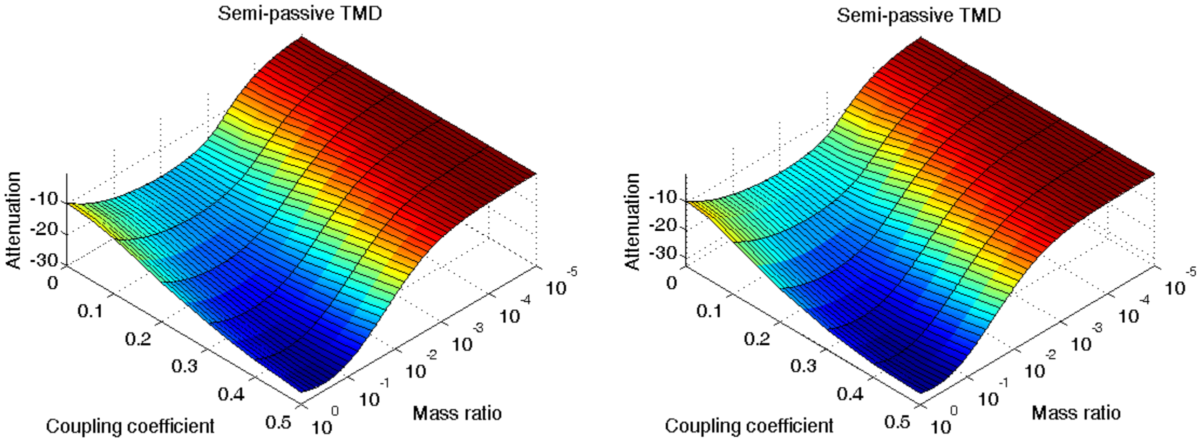

(1c) r_ζ=10 and γ=0

(2c) r_ζ=10 and γ=0.3

Figure 3.18. Attenuation of tuned electromechanical semi-passive nonlinear TMD varied with coupling coefficient and mass ratio in the cases of γ=0 and γ=0.3 as ζ_1=0.002.

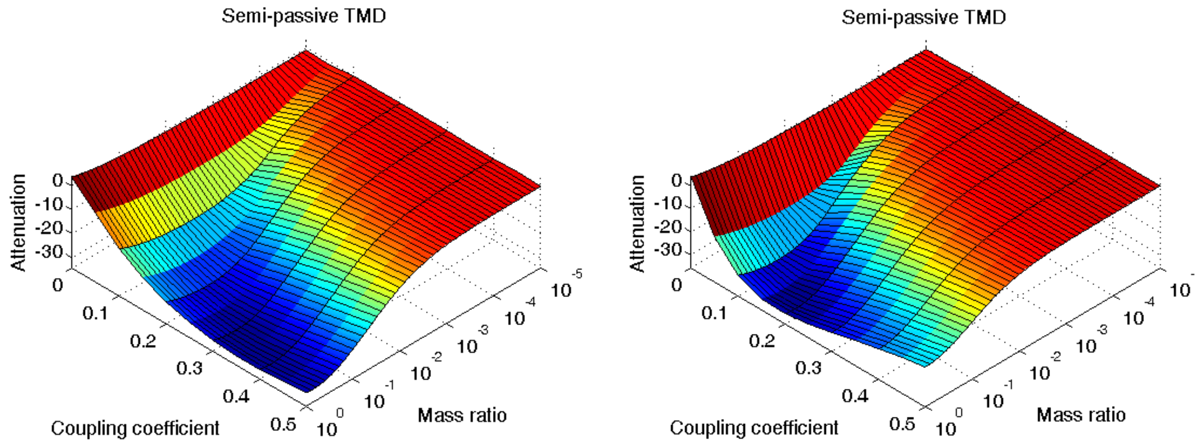

(1a) r_ζ=0.1 and γ=0.6 (1a) r_ζ=0.1 and γ=0.9

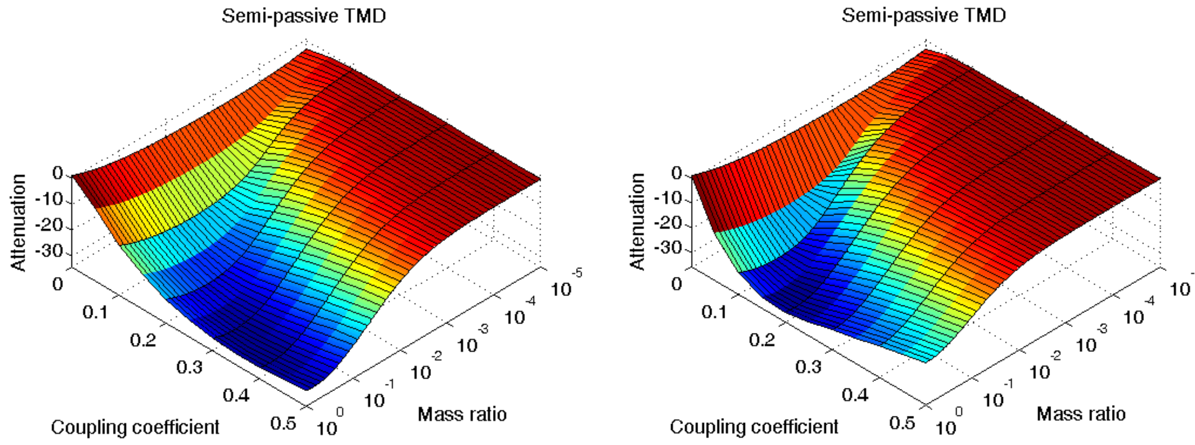

(1b) r_ζ=1 and γ=0.6 (2b) r_ζ=1 and γ=0.9

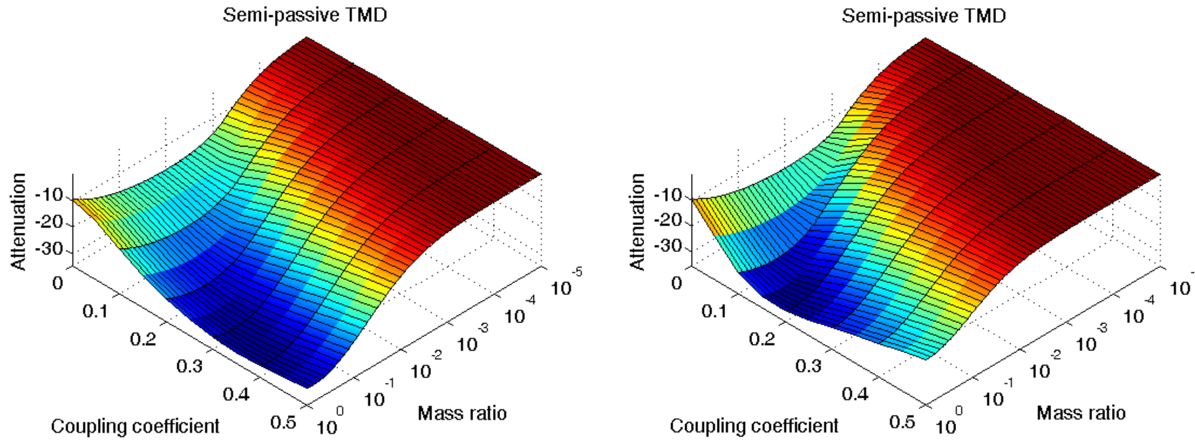

(1c) r_ζ=10 and γ=0.6 (2c) r_ζ=10 and γ=0.9

Figure 3.19. Attenuation of tuned electromechanical semi-passive nonlinear TMD varied with coupling coefficient and mass ratio in the cases of γ=0.6 and γ=0.9 as ζ_l=0.002.

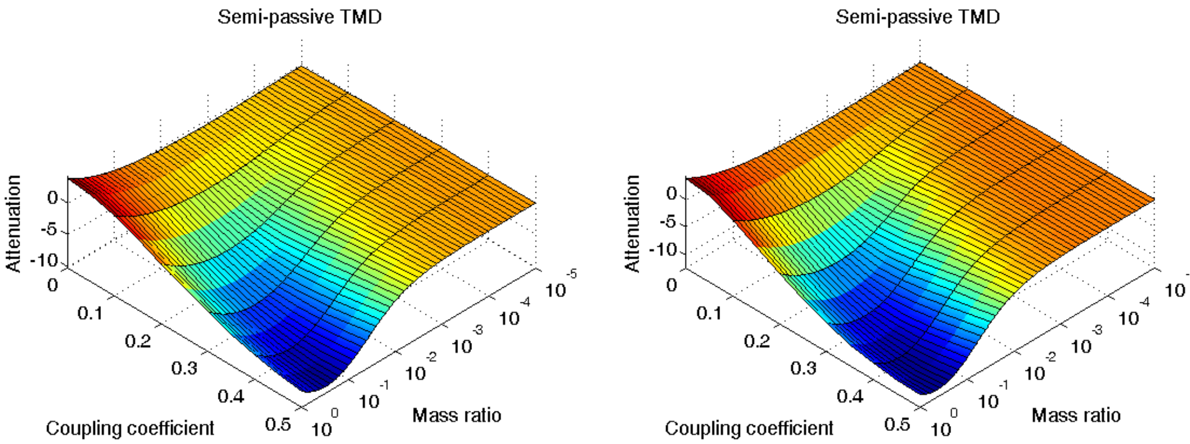

(1a) r_ζ=0.1 and γ=0

(2a) r_ζ=0.1 and γ=0.3

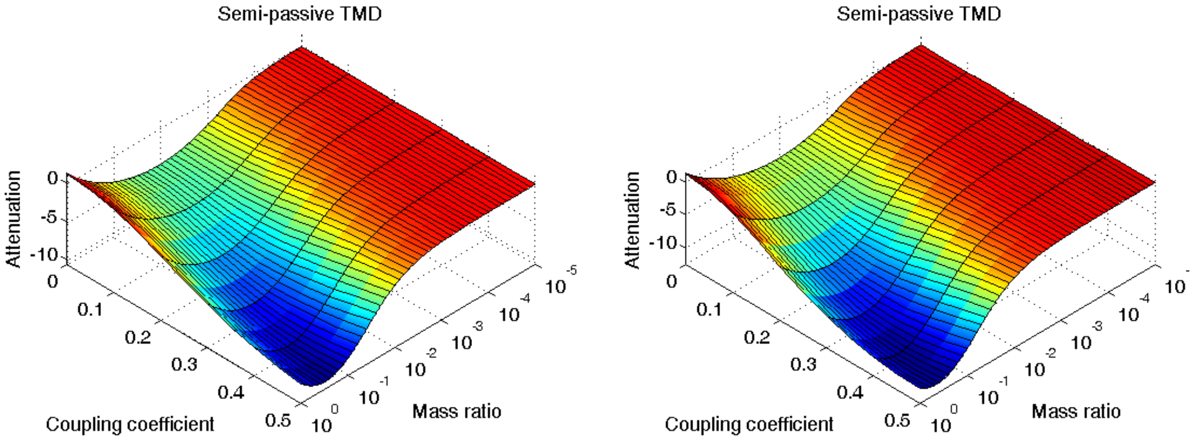

(1b) r_ζ=1 and γ=0

(2b) r_ζ=1 and γ=0.3

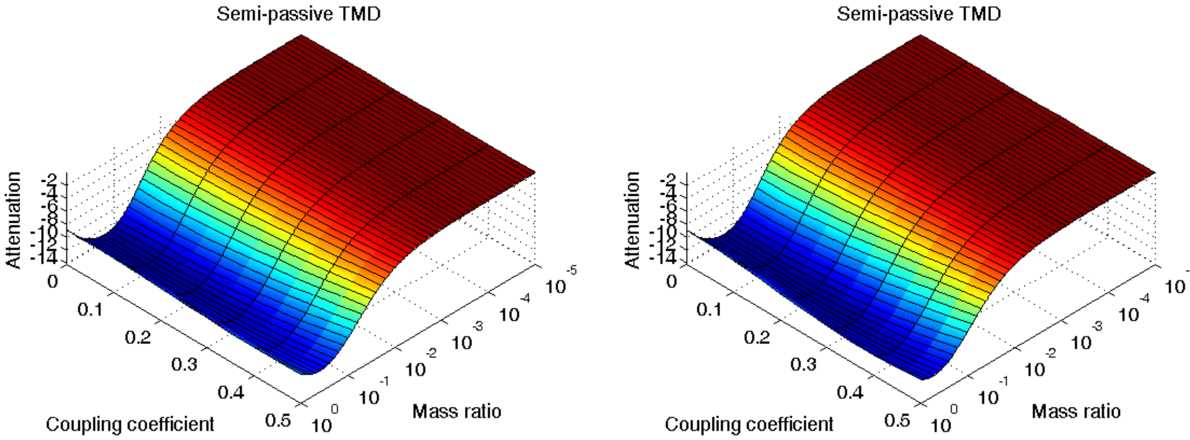

(1c) r_ζ=10 and γ=0

(2c) r_ζ=10 and γ=0.3

Figure 3.20. Attenuation of tuned electromechanical semi-passive nonlinear TMD varied with coupling coefficient and mass ratio in the cases of γ=0 and γ=0.3 as ζ_t=0.02.

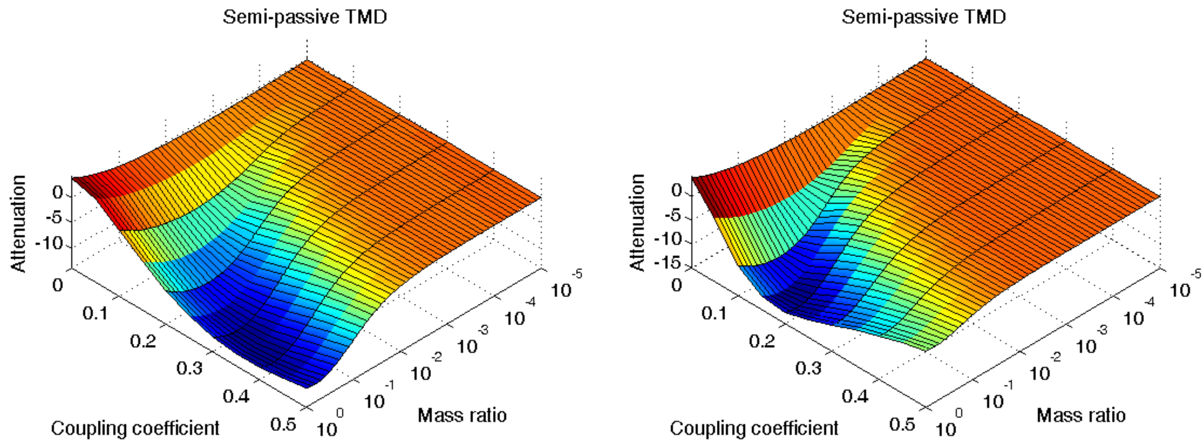

(1a) r_ζ=0.1 and γ=0.6 (2a) r_ζ=0.1 and γ=0.9

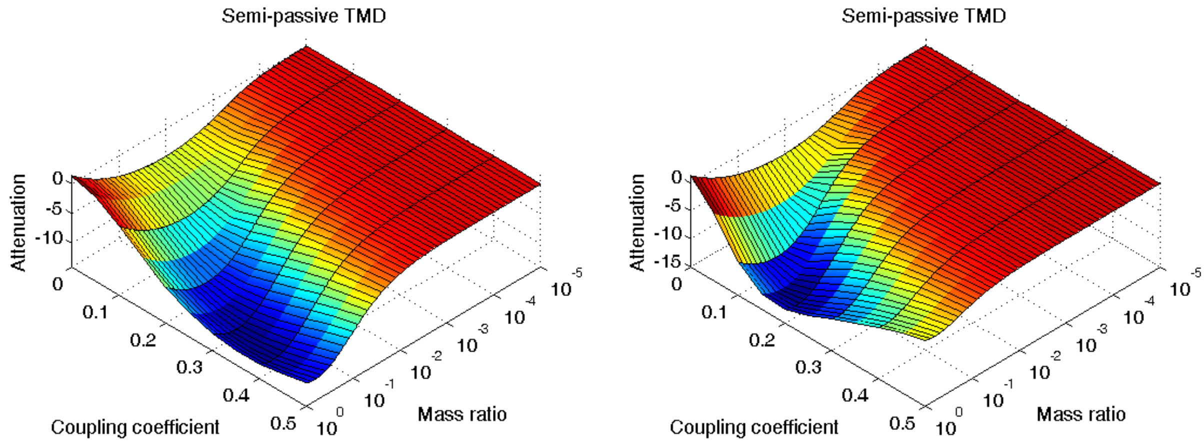

(1b) r_ζ=1 and γ=0.6 (2b) r_ζ=1 and γ=0.9

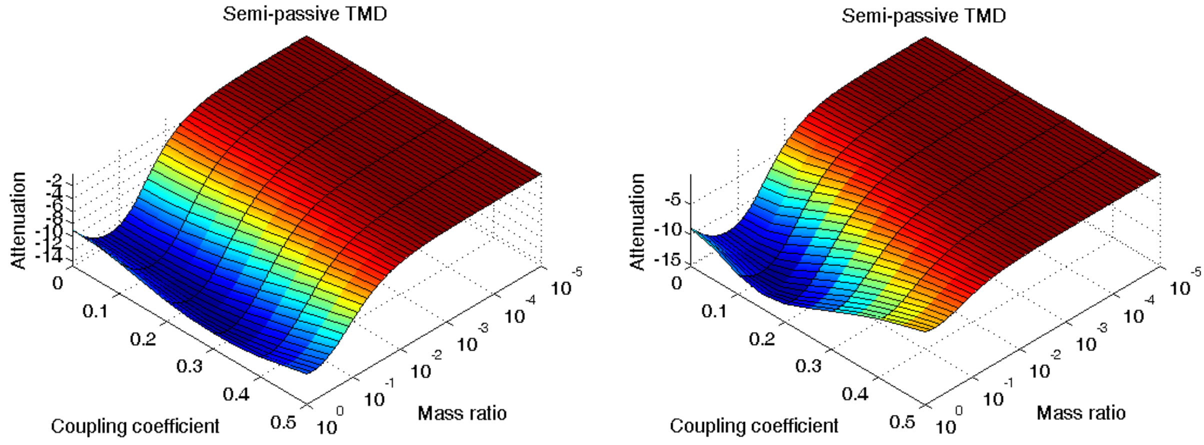

(1c) r_ζ=10 and γ=0.6 (2c) r_ζ=10 and γ=0.9

Figure 3.21. Attenuation of tuned electromechanical semi-passive nonlinear TMD varied with coupling coefficient and mass ratio in the cases of γ=0.6 and γ=0.9 as ζ_l=0.02.

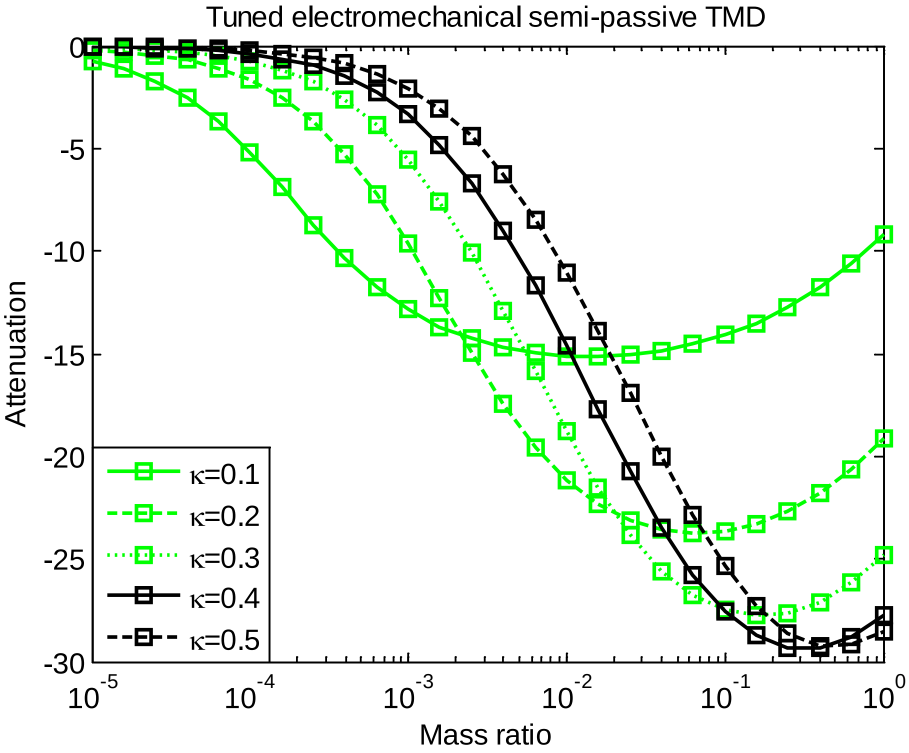

Figure 3.22. Attenuation of tuned electromechanical semi-passive nonlinear TMD with r_ζ=0.1 and γ=0.3 as ζ_t=0.002.

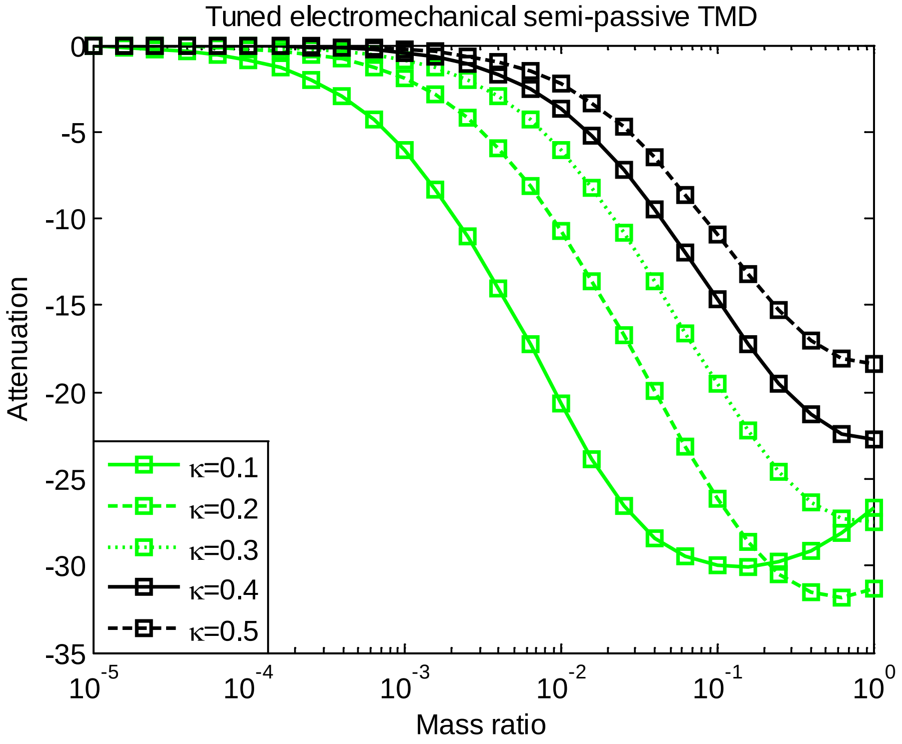

Figure 3.23. Attenuation of tuned electromechanical semi-passive nonlinear TMD with r_ζ=0.1 and γ=0.9 as ζ_t=0.002.

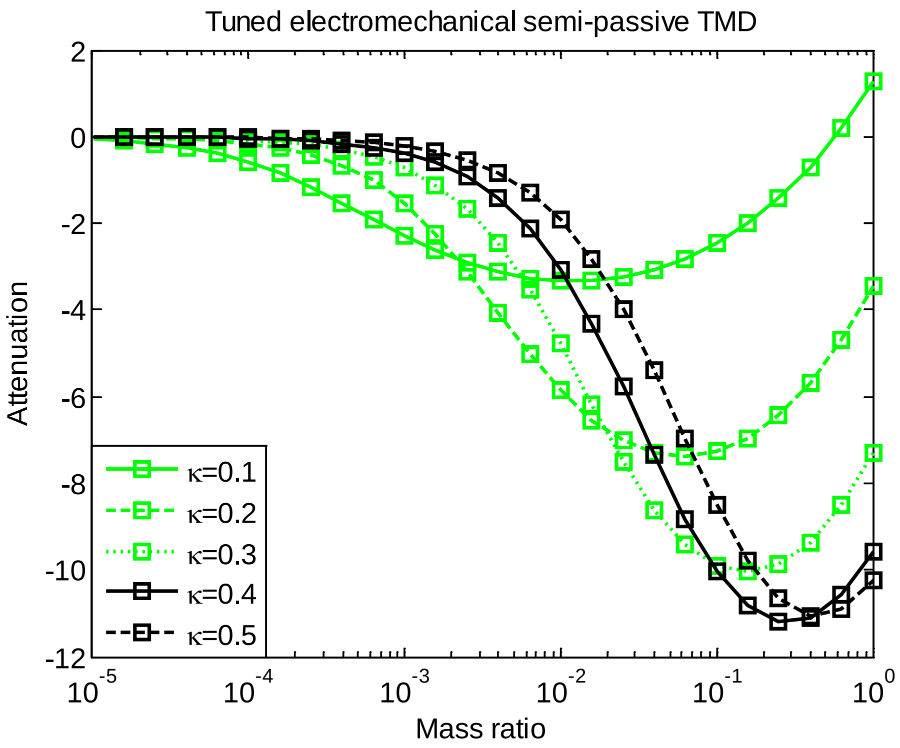

Figure 3.24. Attenuation of tuned electromechanical semi-passive nonlinear TMD with r_ζ=0.1 and γ=0.3 as ζ_l=0.02.

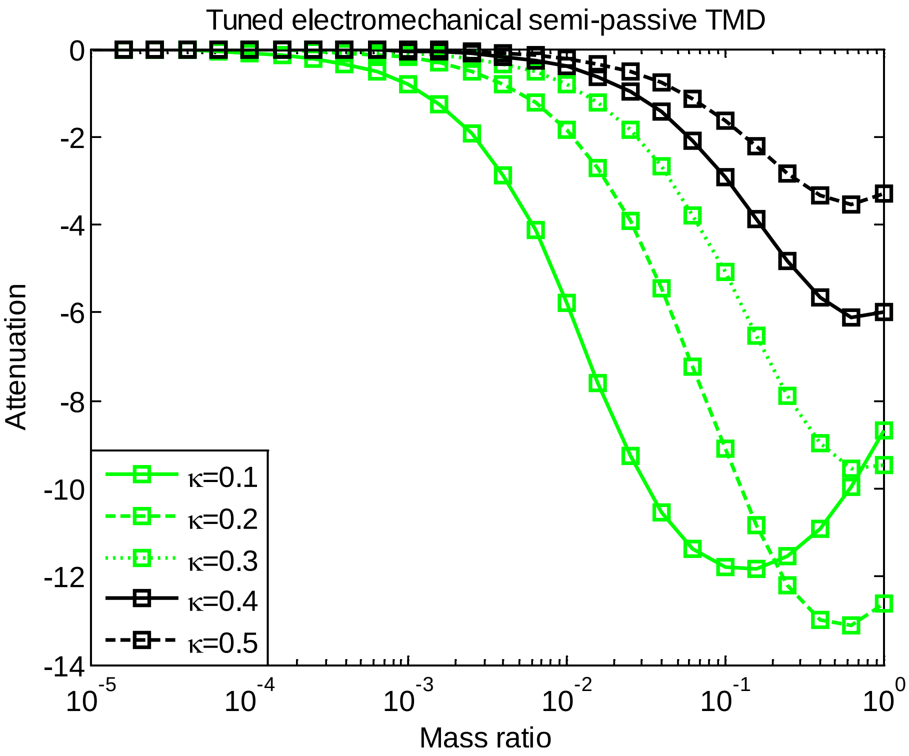

Figure 3.25. Attenuation of tuned electromechanical semi-passive nonlinear TMD with r_ζ=0.1 and γ=0.9 as ζ_l=0.02.

b) Damping performances of mistuned TMD systems

Generally, in realistic applications, the resonance frequency of the TMD device cannot be exactly tuned at the resonance frequency of the host structure and a frequency shift may be induced over the operative time as well. Hence, in this part, the damping performances of mistuned TMD devices with resonance frequency shifts of ±20% are considered and discussed. Control performances of the mistuned purely mechanical TMD devices with frequency ratios r_ω=0.8 and r_ω=1.2 for damping the host structure with ζ_1=0.002 and ζ_1=0.02 are respectively plotted in Figure 3.26 and Figure 3.27.

From the given results, it can be found that except the case of lightly damped TMD as r_ω=1.2, an optimal mass ratio can be found in the investigated range. Meanwhile, from the comparison of global damping performance in mistuned cases and tuned cases, it is suggested that for TMD design, it is better to ensure its resonance frequency lower than that of host structure in order to avoid the dramatical deterioration of global control effectivenss, especially when the tuned frequency can not be always achieved.

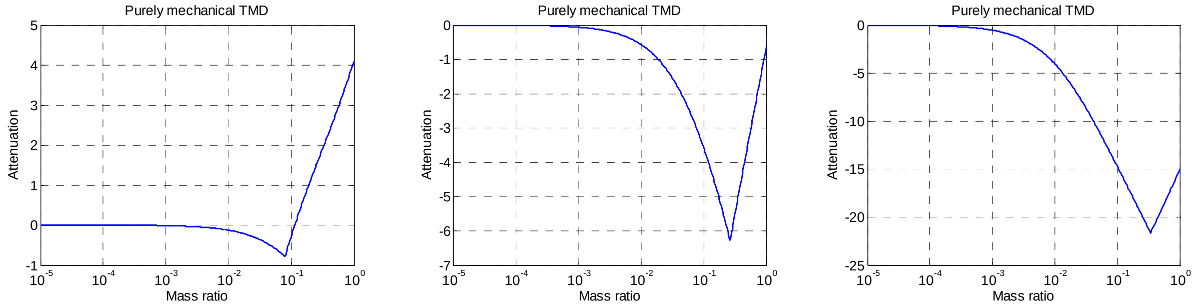

(1a) $r_\zeta = 0.1$ and r_ω=0.8 (1b) $r_\zeta = 1$ and r_ω=0.8 (1c) $r_\zeta = 10$ and r_ω=0.8

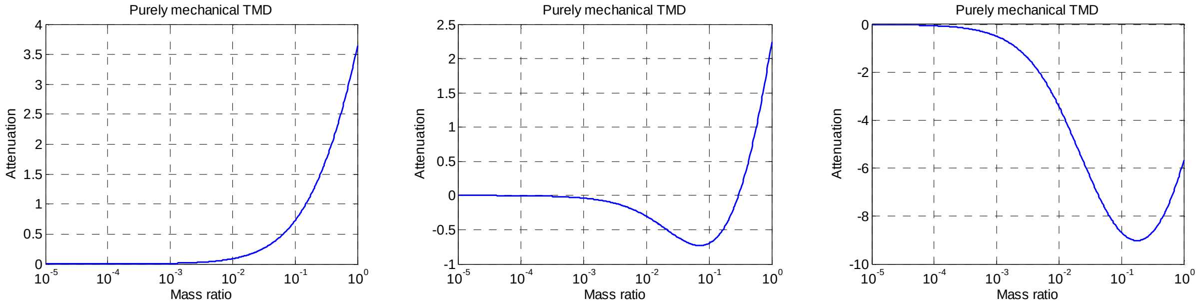

(2a) $r_\zeta = 0.1$ and r_ω=1.2 (2b) $r_\zeta = 1$ and r_ω=1.2 (2c) $r_\zeta = 10$ and r_ω=1.2

Figure 3.26. Attenuation of mistuned purely mechanical TMD varied with mass ratio r_m as ζ_1=0.002.

Furthermore, it should be noted that in this subsection, author focuses on the global damping performance instead of the control effectiveness at the resonance frequency of host structure, thus the obtained conclusion is effective in the investigated parameter ranges and may be a little bit different from the conclusions achieved in literature which focused on damping the vibration exactly at the particular resonance frequency of primary structure with a specific mass ratio.

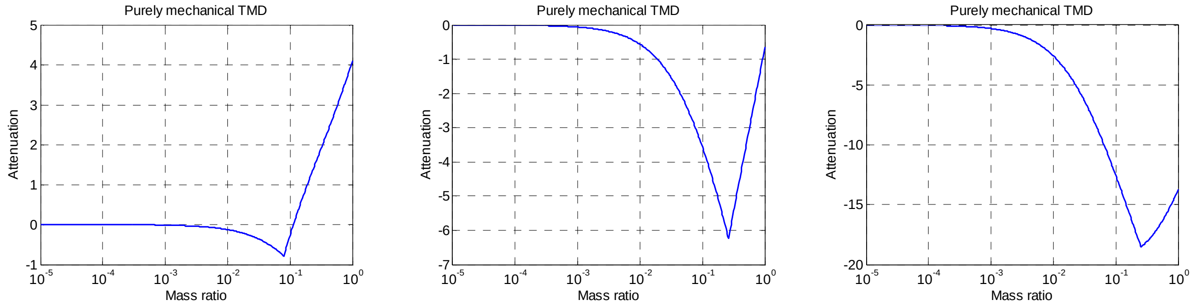

(1a) $r_\zeta = 0.1$ and r_ω=0.8 (1b) $r_\zeta = 1$ and r_ω=0.8 (1c) $r_\zeta = 10$ and r_ω=0.8

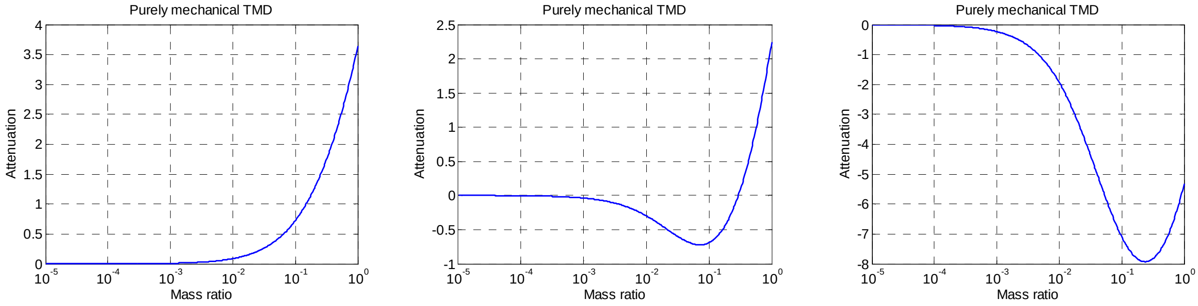

(2a) $r_\zeta = 0.1$ and r_ω=1.2 (2b) $r_\zeta = 1$ and r_ω=1.2 (2c) $r_\zeta = 10$ and r_ω=1.2

Figure 3.27. Attenuation of mistuned purely mechanical TMD varied with mass ratio r_m as ζ_t=0.02.

Similar conclusion is also obtained in the cases of using corresponding mistuned optimal electromechanical passive TMD and the results are exposed in Figure 3.28 and Figure 3.29. From the comparison of mistuned cases, it is found that the benefit of the mistuned optimal electromechanical passive TMD with r_ω=0.8 is experienced over a wider mass ratio range without global damping deterioration, thus allowing the pre-design of electromechanical passive TMD with a slightly lower frequency ratio. Moreover, the global damping performance of the mistuned optimal electromechanical passive TMD is more sensitive to a greater given mass ratio than a lower given mass ratio. Furthermore, mistuned TMD devices with higher damping are superior to the mistuned TMD systems with lower damping and the installed TMD systems are more effective to reduce the vibration of host structure with lower damping.

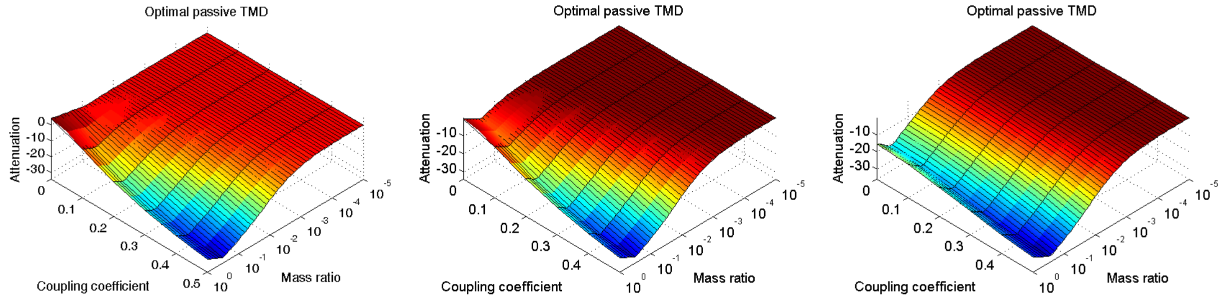

(1a) $r_\zeta = 0.1$ and r_ω=0.8 (1b) $r_\zeta = 1$ and r_ω=0.8 (1c) $r_\zeta = 10$ and r_ω=0.8

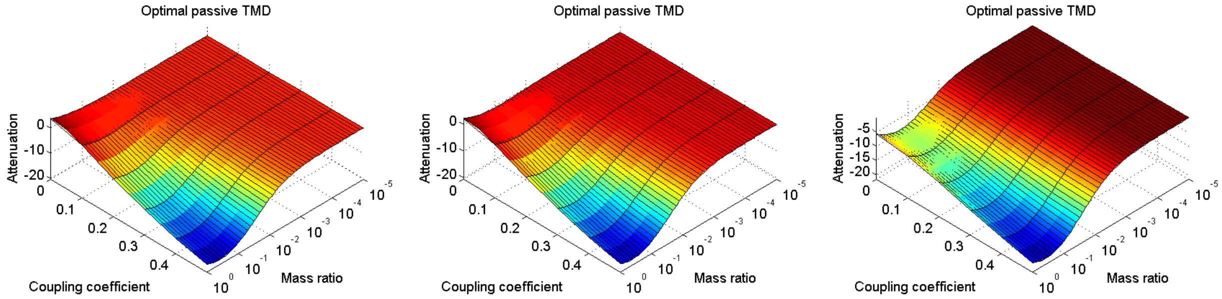

(2a) $r_\zeta = 0.1$ and r_ω=1.2 (2b) $r_\zeta = 1$ and r_ω=1.2 (2c) $r_\zeta = 10$ and r_ω=1.2

Figure 3.28. Attenuation of mistuned optimal electromechanical passive TMD varied with coupling coefficient κ and mass ratio r_m as ζ_1=0.002.

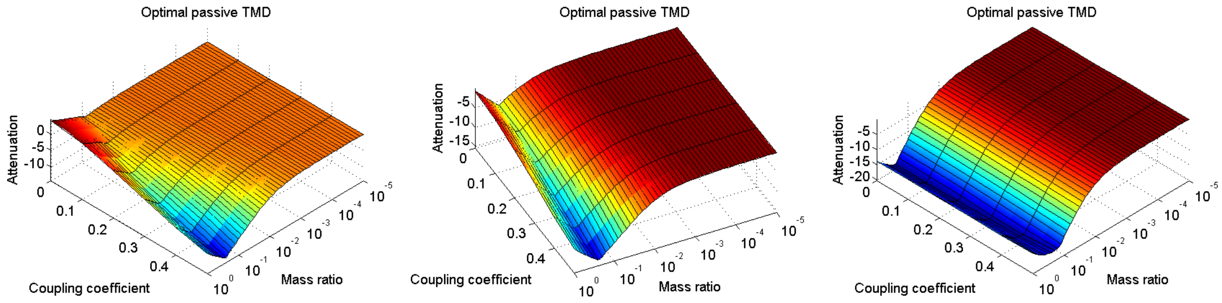

(1a) $r_\zeta = 0.1$ and r_ω=0.8 (1b) $r_\zeta = 1$ and r_ω=0.8 (1c) $r_\zeta = 10$ and r_ω=0.8

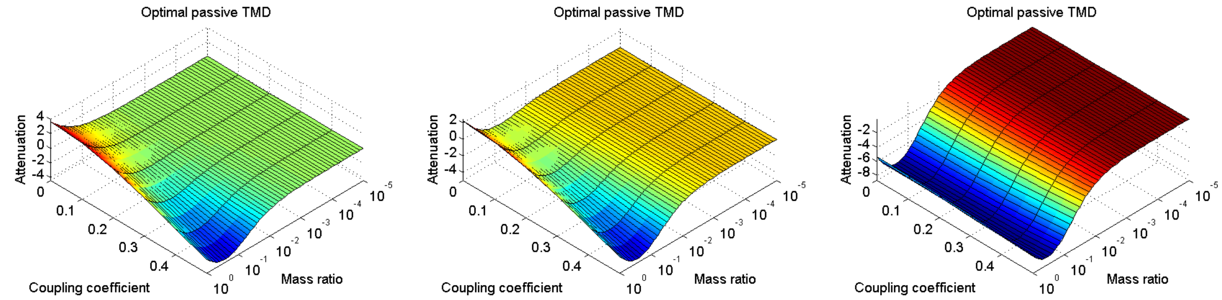

(2a) $r_\zeta = 0.1$ and r_ω=1.2 (2b) $r_\zeta = 1$ and r_ω=1.2 (2c) $r_\zeta = 10$ and r_ω=1.2

Figure 3.29. Attenuation of mistuned optimal electromechanical passive TMD varied with coupling coefficient κ and mass ratio r_m as ζ_1=0.02.

Different from purely mechanical TMD system in which only the mechanical to mechanical energy transfer occurs between host structure and TMD device, for the system featuring electromechanical TMD, the mechanical energy is not only transferred between vibrating structure and TMD device but also can be converted into electrical energy by the piezoelectric material, which contains more parameters for tuning the dynamical characteristics and leads to better control ability. Hence, it can be found that the electromechanical TMDs can achieve better control effectiveness even in mistuned cases compared with the purely mechanical TMDs except in the case where the damping of both primary structure and electromechanical TMD is high.

Figure 3.30~Figure 3.37 show the global attenuation obtained with mistuned electromechanical semi-passive nonlinear TMD devices varied with global coupling coefficient and mass ratio. Since the voltage inversion coefficient is a very important parameter, several values (γ=0, 0.3, 0.6, 0.9) are chosen for comparison.

In general, it also can be easily found that the global control effectiveness of mistuned electromechanical semi-passive nonlinear TMD with -20% resonance frequency shift in the investigated range is better then the counterpart TMD with +20% resonance frequency shift in the investigated parameters ranges. Although the vibration of host structure can effectively be damped by the mistuned electromechanical semi-passive nonlinear TMDs, the global control performance is dependent on the voltage inversion coefficient and global coupling coefficient as in the tuned cases (Figure 3.38~Figure 3.45). In the weak inversion cases in which the inversion coefficient value is small, the global control effectiveness of electromechanical nonlinear switching TMD is increased with the increase of coupling coefficient. Meanwhile, for the semi-passive TMD with excellement voltage inversion process, the control effectivenss is dramatically decreased with the increase of coupling coefficient in mass ratio range.

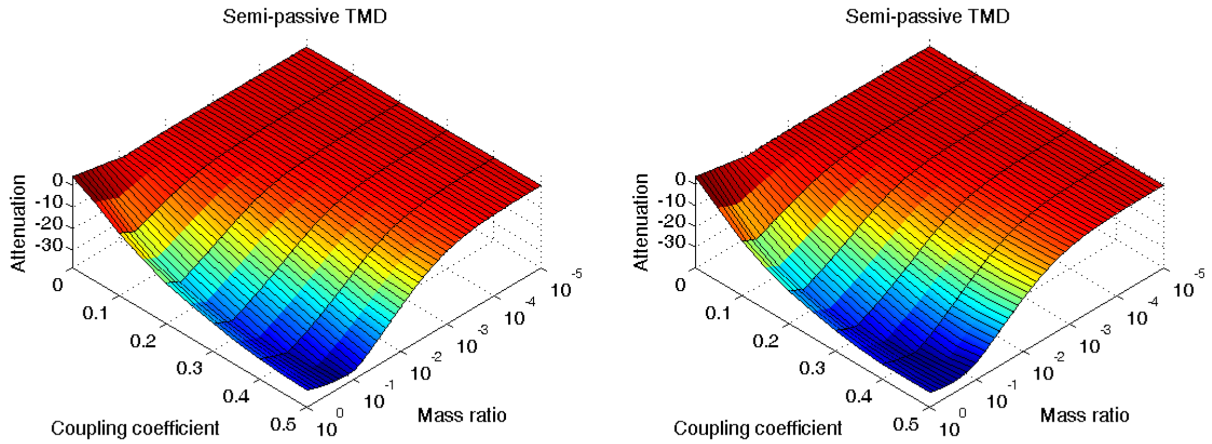

(1a) r_ζ=0.1 and γ=0 (2a) r_ζ=0.1 and γ=0.3

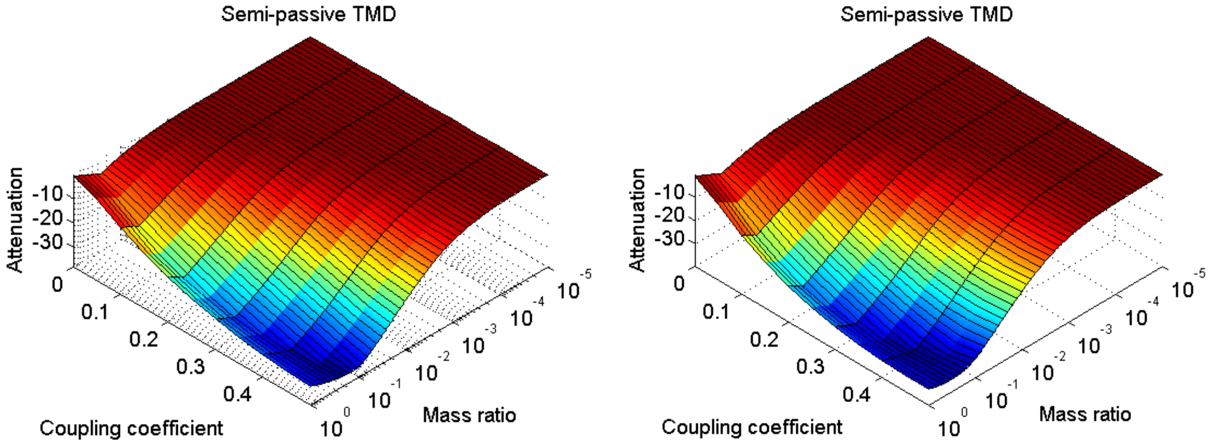

(1b) r_ζ=1 and γ=0 (2b) r_ζ=1 and γ=0.3

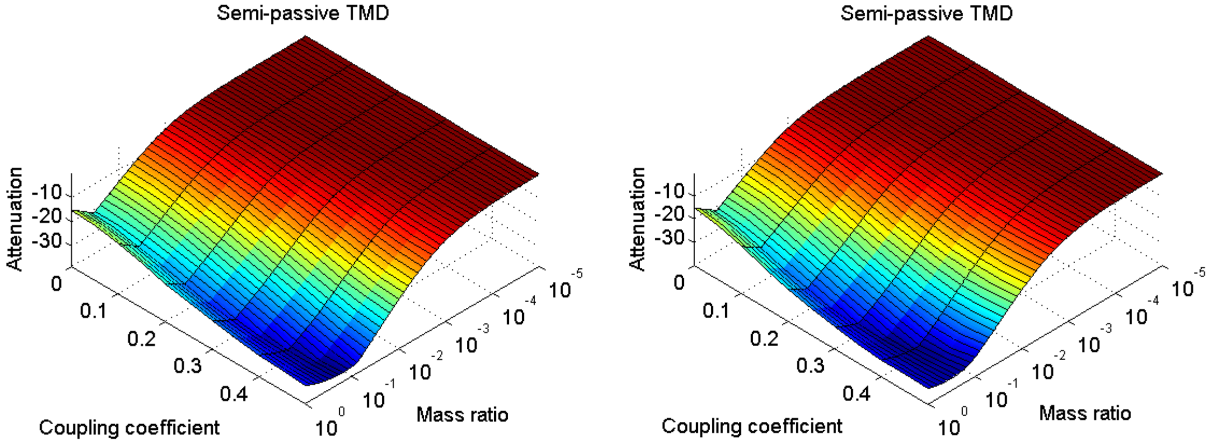

(1c) r_ζ=10 and γ=0 (2c) r_ζ=10 and γ=0.3

Figure 3.30. Attenuation of mistuned electromechanical semi-passive nonlinear TMD varied with coupling coefficient and mass ratio in the cases of γ=0 and γ=0.3 as ζ_t=0.002 and r_ω=0.8.

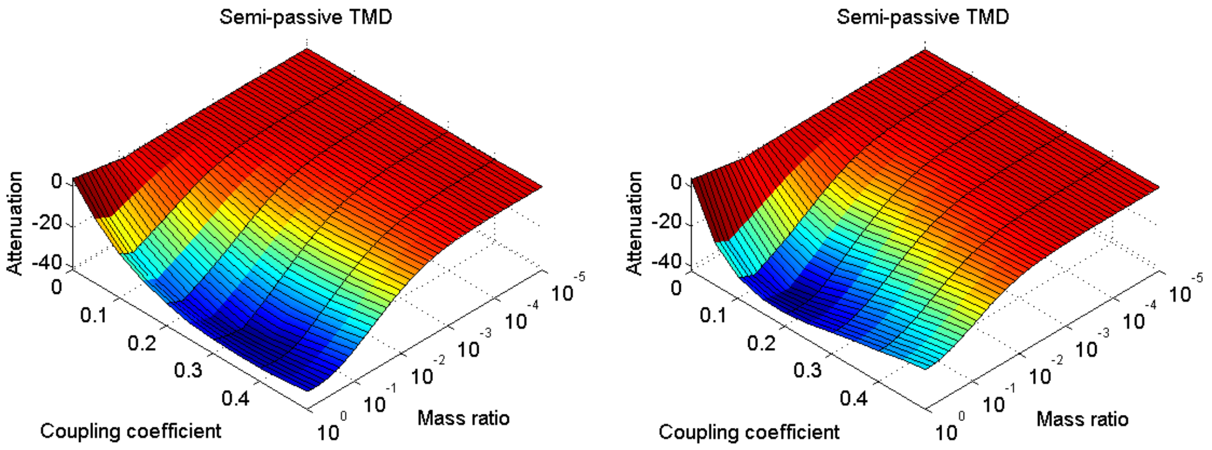

(1a) r_ζ=0.1 and γ=0.6 (2a) r_ζ=0.1 and γ=0.9

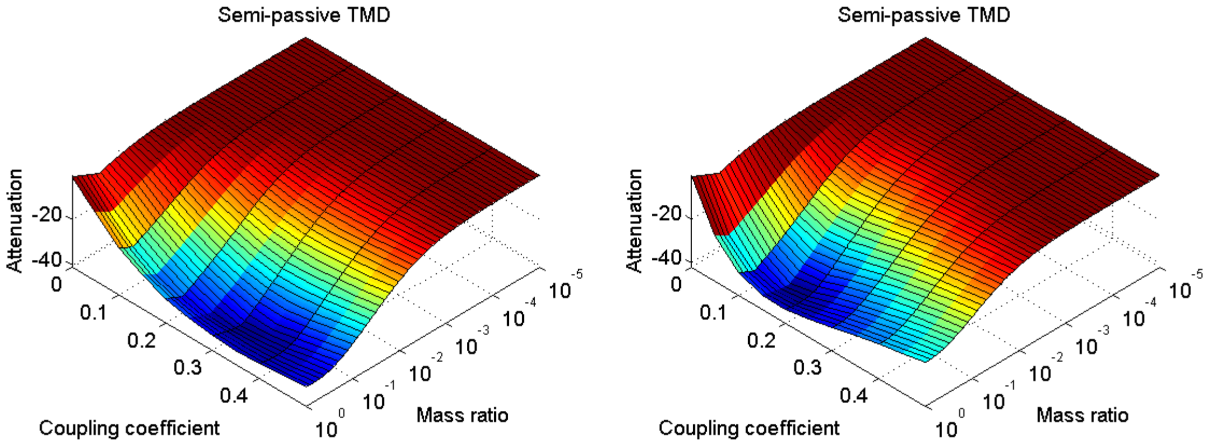

(1b) r_ζ=1 and γ=0.6 (2b) r_ζ=1 and γ=0.9

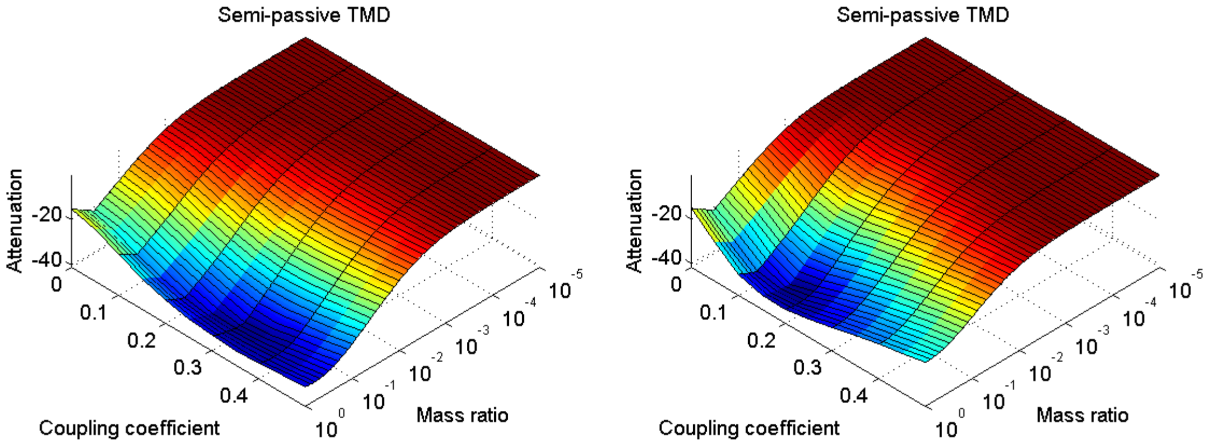

(1c) r_ζ=10 and γ=0.6 (2c) r_ζ=10 and γ=0.9

Figure 3.31. Attenuation of mistuned electromechanical semi-passive nonlinear TMD varied with coupling coefficient and mass ratio in the cases of γ=0.6 and γ=0.9 as ζ_t=0.002 and r_ω=0.8.

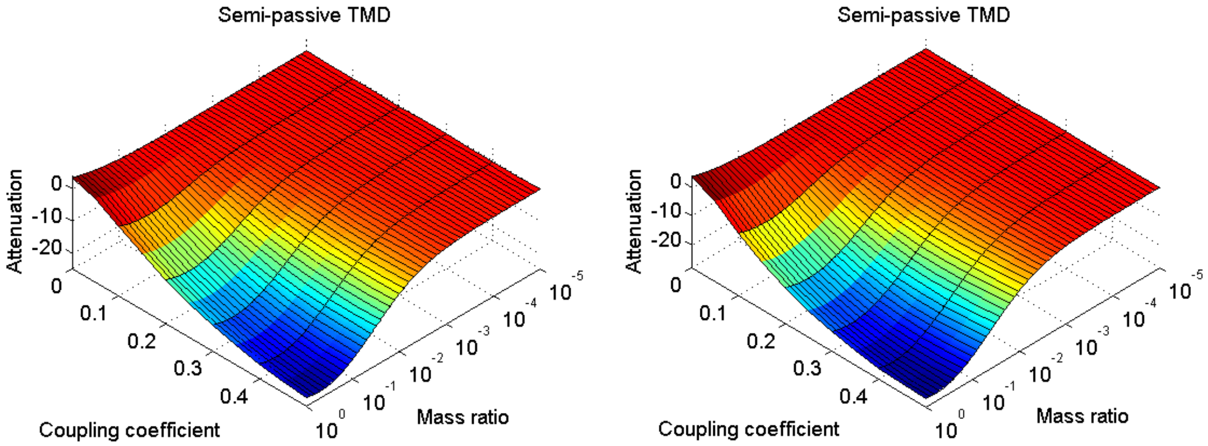

(1a) r_ζ=0.1 and γ=0 (2a) r_ζ=0.1 and γ=0.3

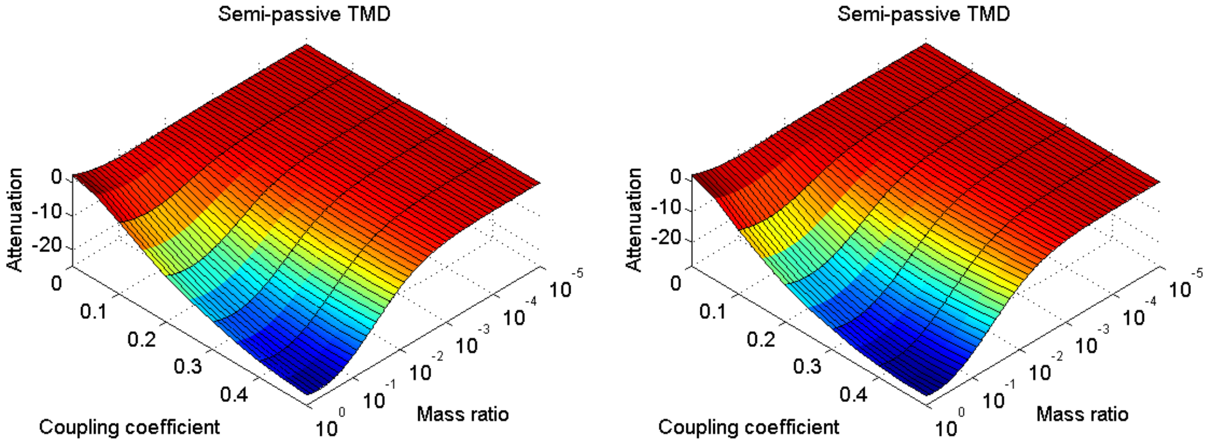

(1b) r_ζ=1 and γ=0 (2b) r_ζ=1 and γ=0.3

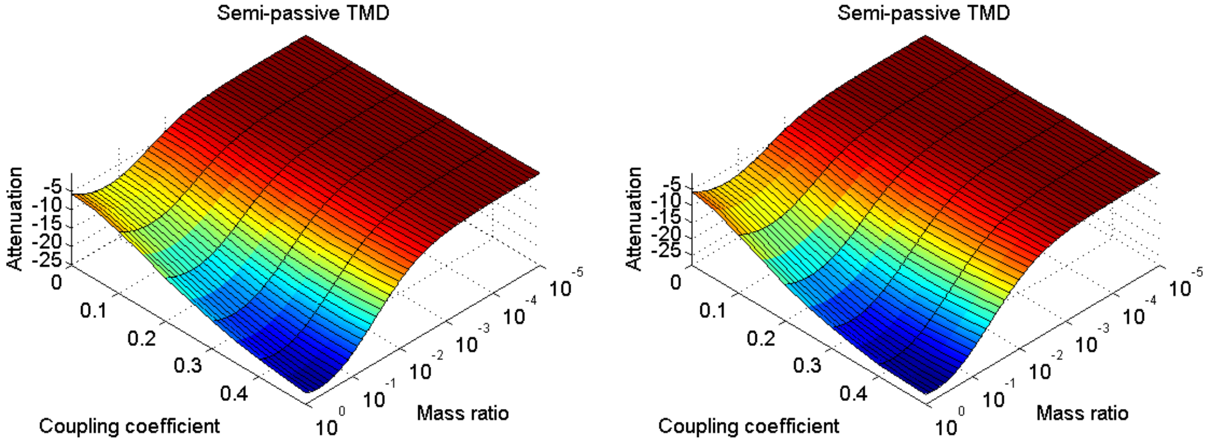

(1c) r_ζ=10 and γ=0 (2c) r_ζ=10 and γ=0.3

Figure 3.32. Attenuation of mistuned electromechanical semi-passive nonlinear TMD varied with coupling coefficient and mass ratio in the cases of γ=0 and γ=0.3 as ζ_1=0.002 and r_ω=1.2.

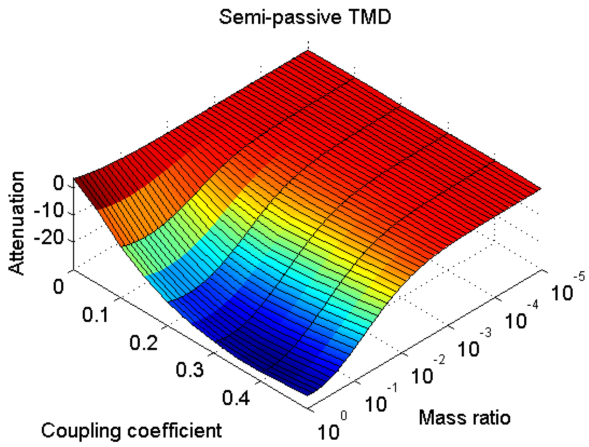

(1a) $r_\zeta=0.1$ and $\gamma=0.6$ (2a) $r_\zeta=0.1$ and $\gamma=0.9$

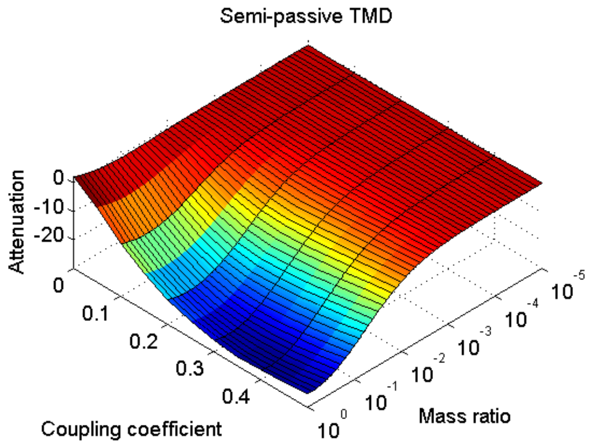

(1b) $r_\zeta=1$ and $\gamma=0.6$ (2b) $r_\zeta=1$ and $\gamma=0.9$

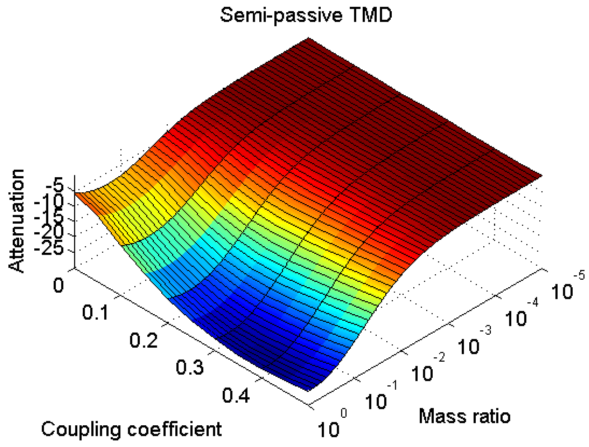

(1c) $r_\zeta=10$ and $\gamma=0.6$ (2c) $r_\zeta=10$ and $\gamma=0.9$

Figure 3.33. Attenuation of mistuned electromechanical semi-passive nonlinear TMD varied with coupling coefficient and mass ratio in the cases of $\gamma=0.6$ and $\gamma=0.9$ as $\zeta_t=0.002$ and $r_\omega=1.2$.

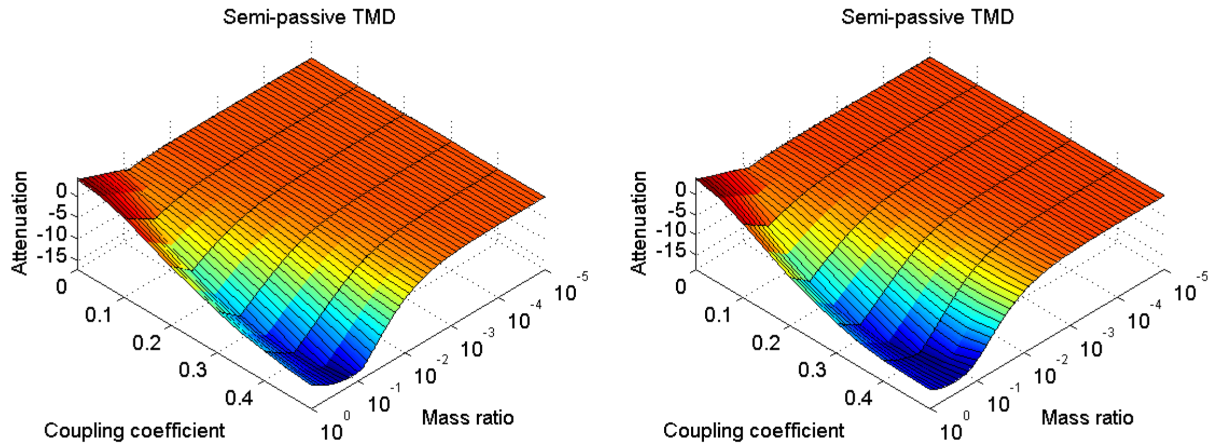

(1a) r_ζ=0.1 and γ=0 (2a) r_ζ=0.1 and γ=0.3

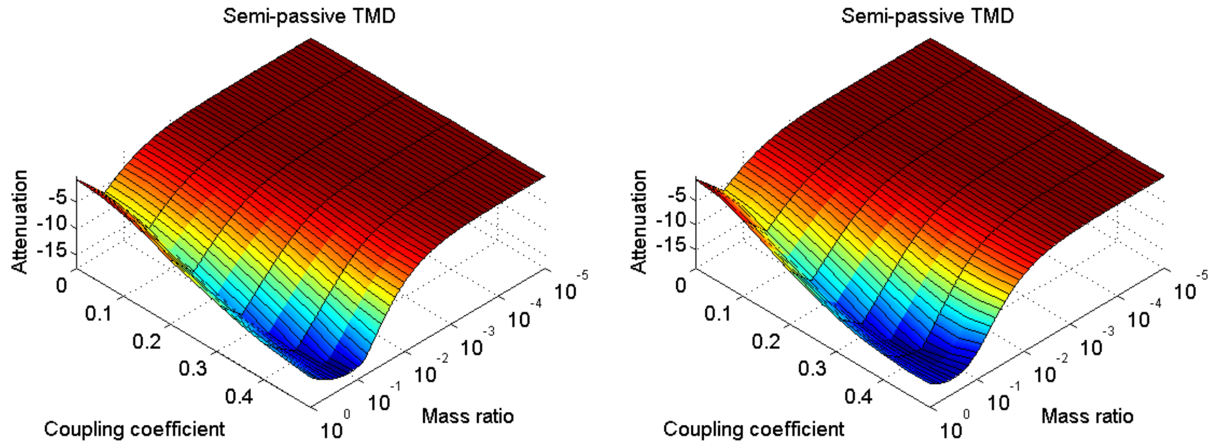

(1b) r_ζ=1 and γ=0 (2b) r_ζ=1 and γ=0.3

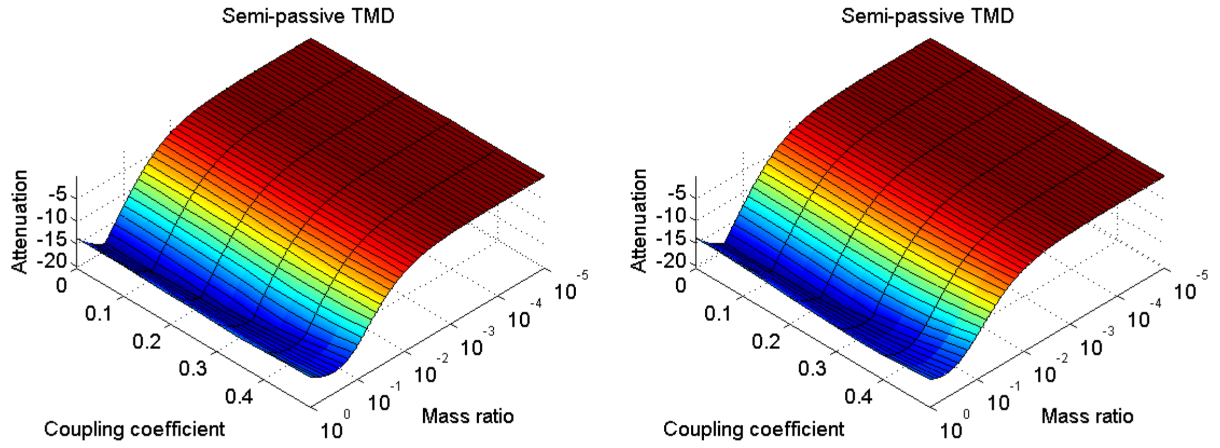

(1c) r_ζ=10 and γ=0 (2c) r_ζ=10 and γ=0.3

Figure 3.34. Attenuation of mistuned electromechanical semi-passive nonlinear TMD varied with coupling coefficient and mass ratio in the cases of γ=0 and γ=0.3 as ζ_t=0.02 and r_ω=0.8.

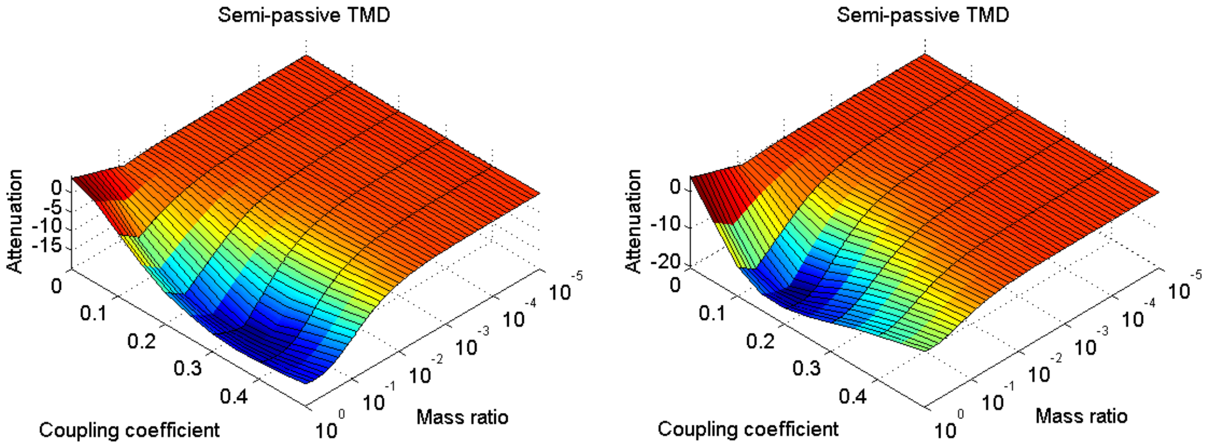

(1a) r_ζ=0.1 and γ=0.6 (2a) r_ζ=0.1 and γ=0.9

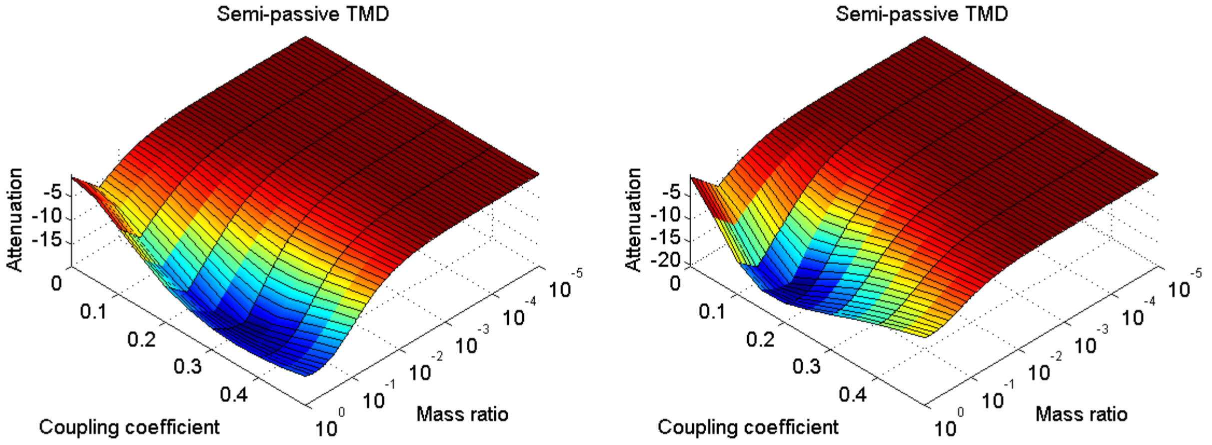

(1b) r_ζ=1 and γ=0.6 (2b) r_ζ=1 and γ=0.9

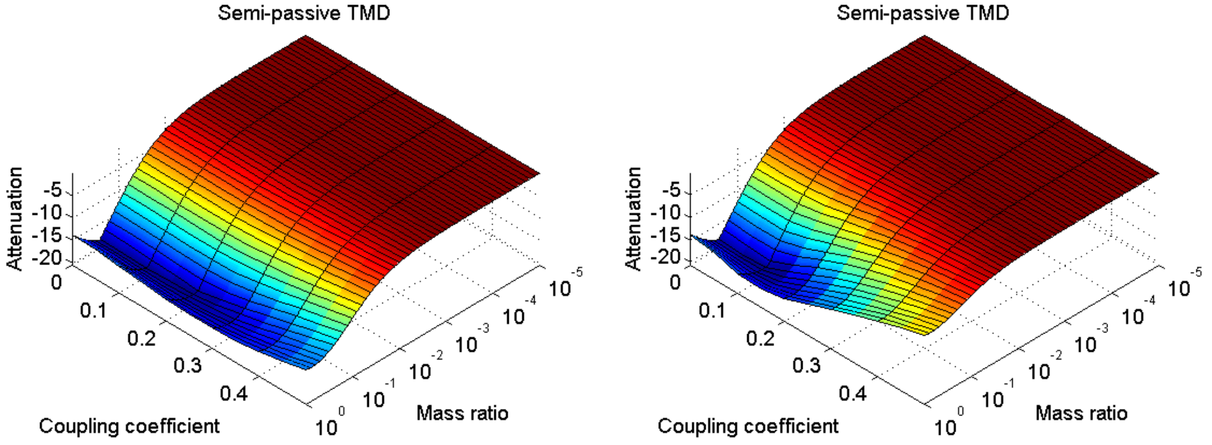

(1c) r_ζ=10 and γ=0.6 (2c) r_ζ=10 and γ=0.9

Figure 3.35. Attenuation of mistuned electromechanical semi-passive nonlinear TMD varied with coupling coefficient and mass ratio in the cases of γ=0.6 and γ=0.9 as ζ_t=0.02 and r_ω=0.8.

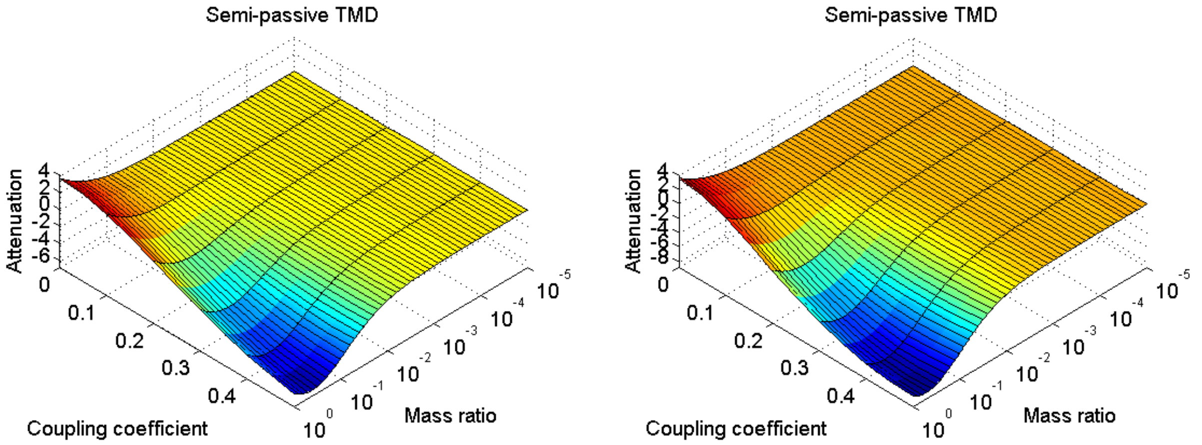

(1a) r_ζ=0.1 and γ=0 (2a) r_ζ=0.1 and γ=0.3

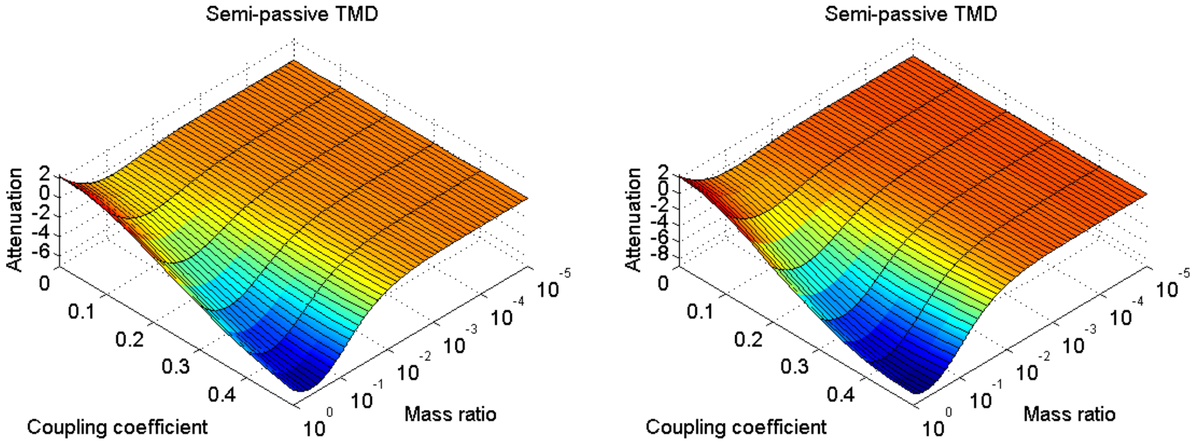

(1b) r_ζ=1 and γ=0 (2b) r_ζ=1 and γ=0.3

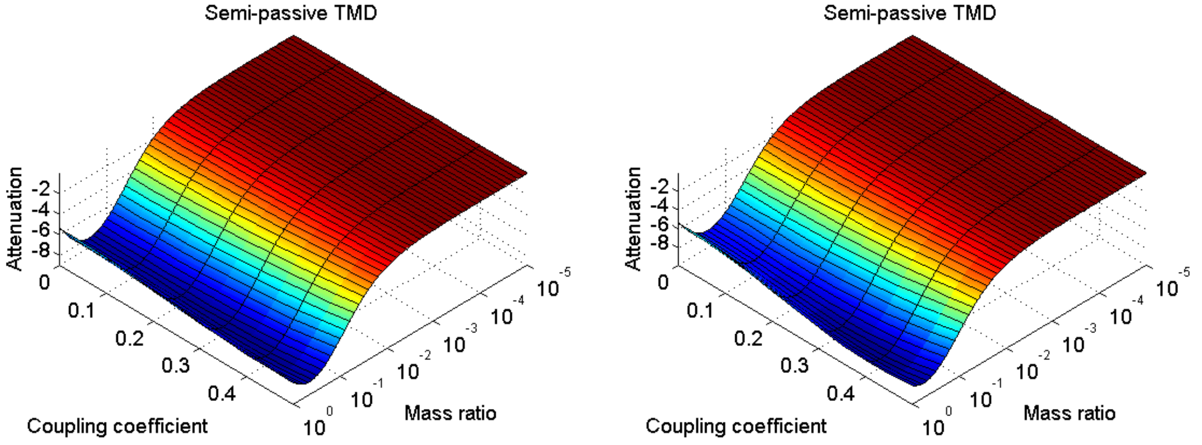

(1c) r_ζ=10 and γ=0 (2c) r_ζ=10 and γ=0.3

Figure 3.36. Attenuation of mistuned electromechanical semi-passive nonlinear TMD varied with coupling coefficient and mass ratio in the cases of γ=0 and γ=0.3 as ζ_l=0.02 and r_ω=1.2.

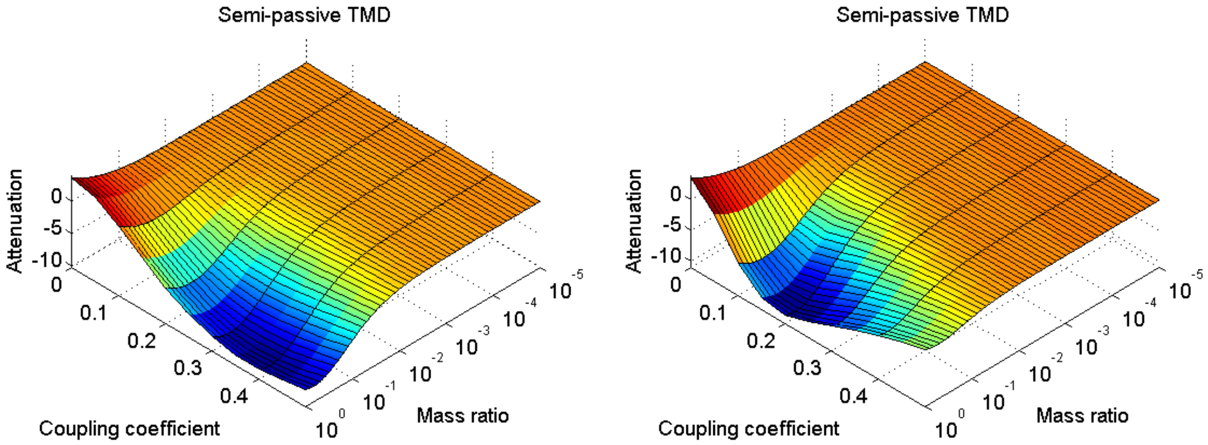

(1a) r_ζ=0.1 and γ=0.6 (2a) r_ζ=0.1 and γ=0.9

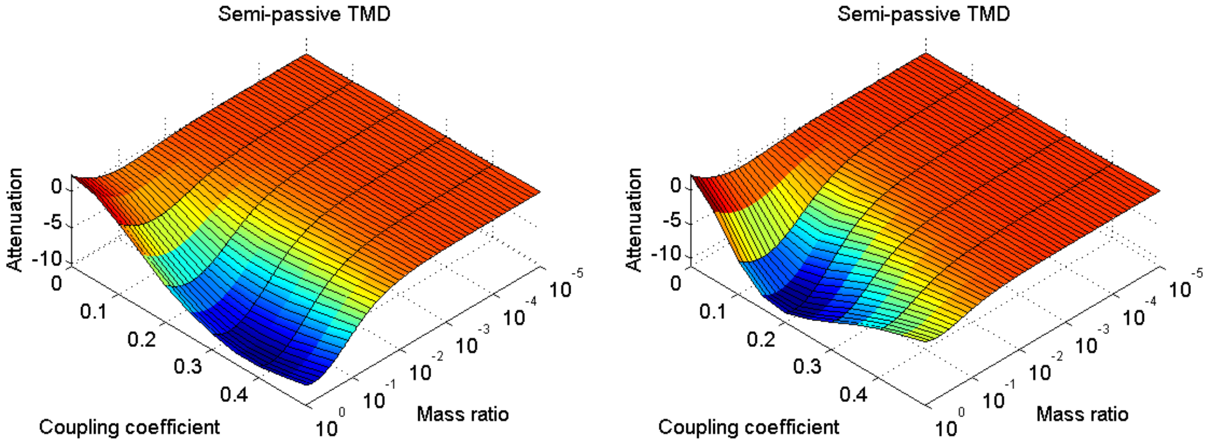

(1b) r_ζ=1 and γ=0.6 (2b) r_ζ=1 and γ=0.9

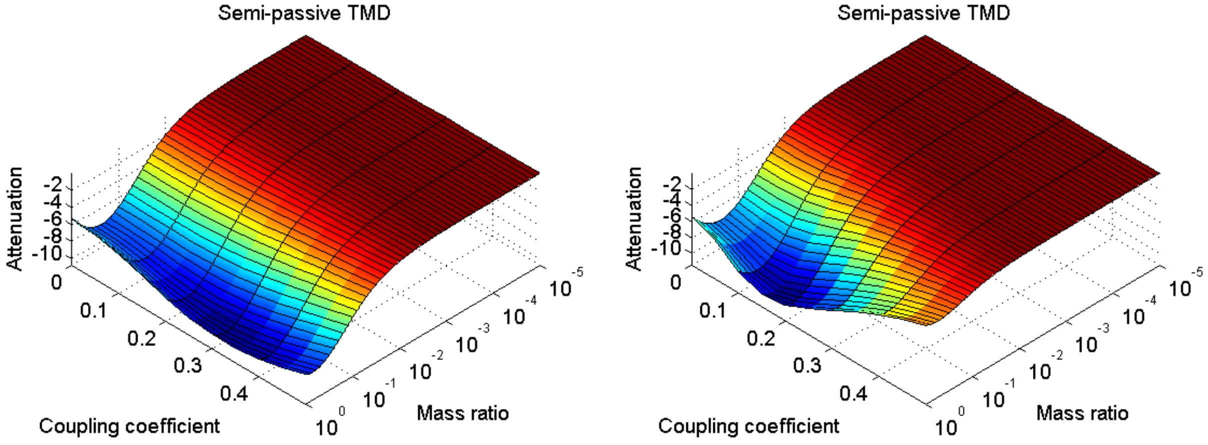

(1c) r_ζ=10 and γ=0.6 (2c) r_ζ=10 and γ=0.9

Figure 3.37. Attenuation of mistuned electromechanical semi-passive nonlinear TMD varied with coupling coefficient and mass ratio in the cases of γ=0.6 and γ=0.9 as ζ_t=0.02 and r_ω=1.2.

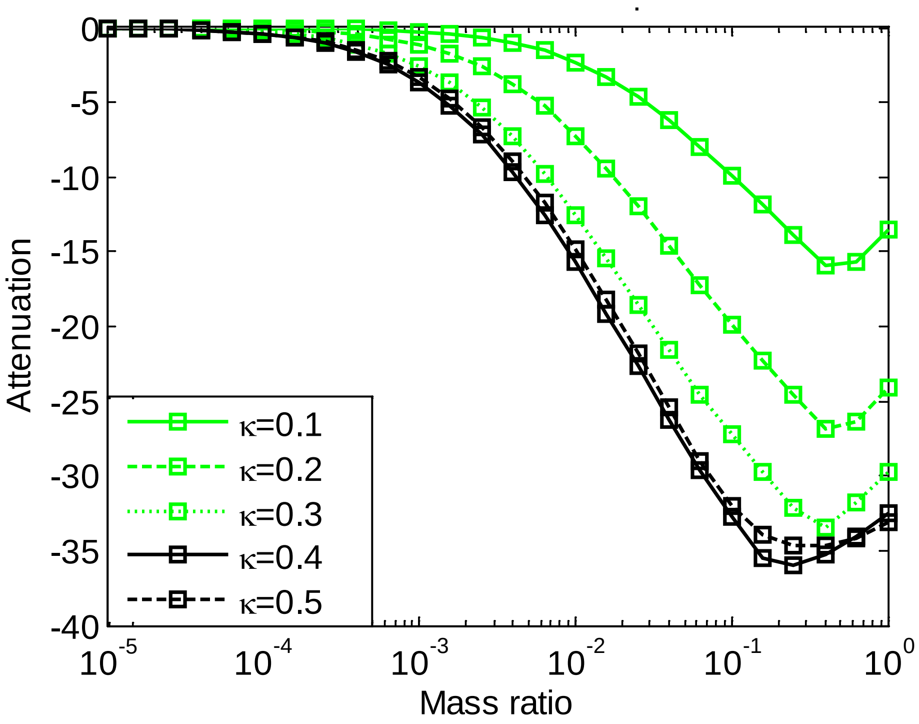

Figure 3.38. Attenuation of mistuned electromechanical semi-passive nonlinear TMD with

r_ζ=0.1 and γ=0.3 as ζ_t=0.002 and r_ω=0.8.

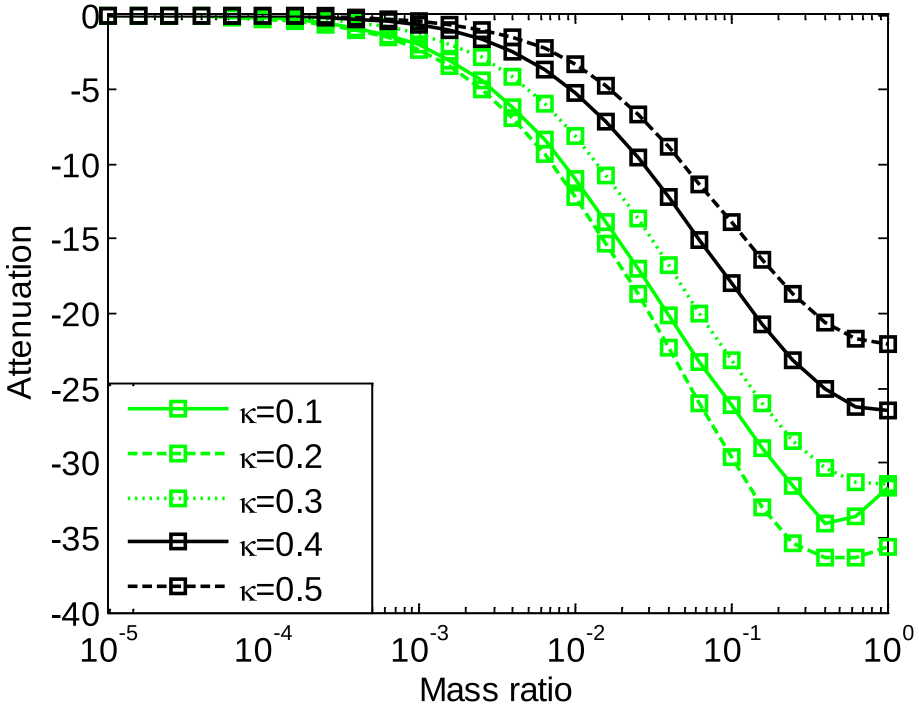

Figure 3.39. Attenuation of mistuned electromechanical semi-passive nonlinear TMD with

r_ζ=0.1 and γ=0.9 as ζ_t=0.002 and r_ω=0.8.

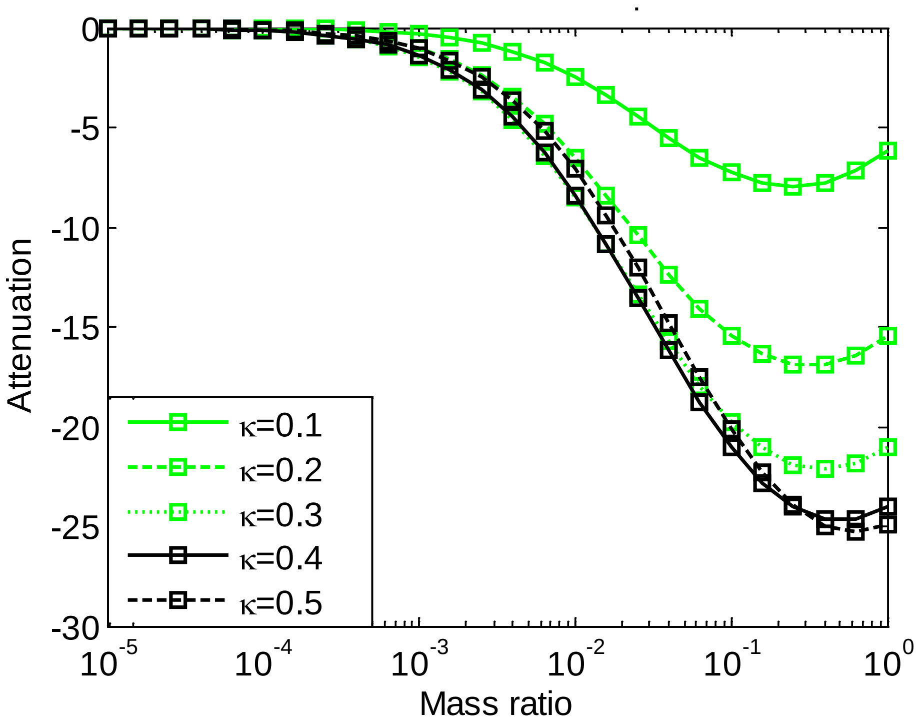

Figure 3.40. Attenuation of mistuned electromechanical semi-passive nonlinear TMD with r_ζ=0.1 and γ=0.3 as ζ_t=0.002 and r_ω=1.2.

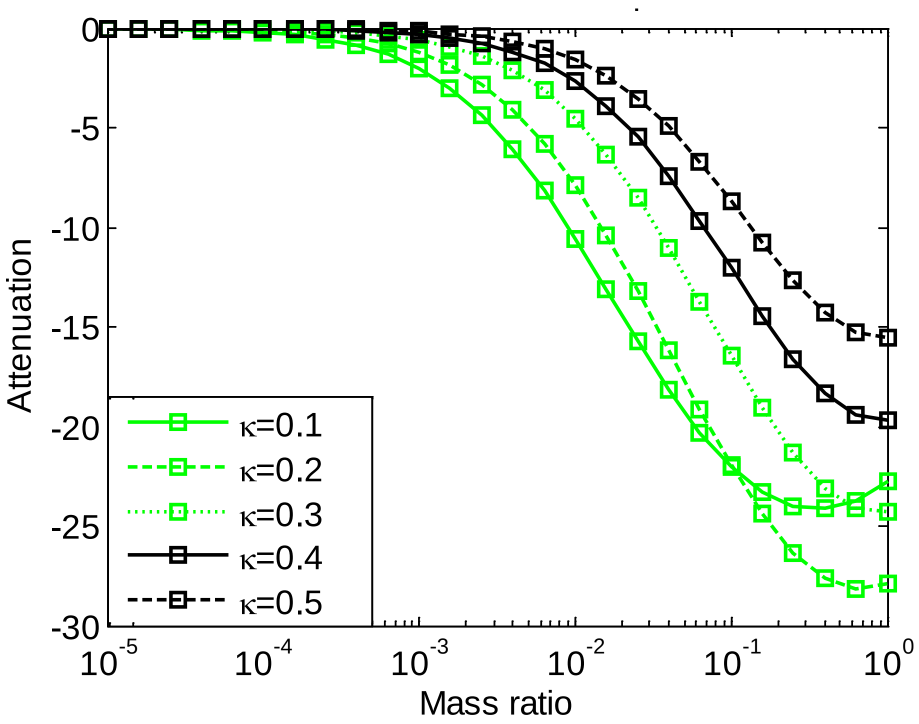

Figure 3.41. Attenuation of mistuned electromechanical semi-passive nonlinear TMD with r_ζ=0.1 and γ=0.9 as ζ_t=0.002 and r_ω=1.2.

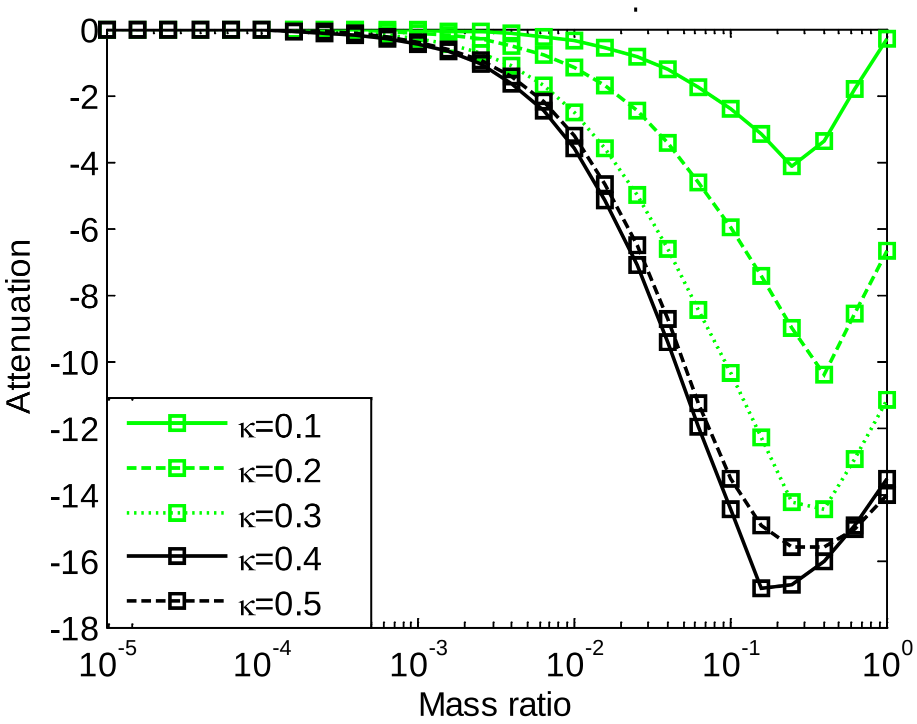

Figure 3.42. Attenuation of mistuned electromechanical semi-passive nonlinear TMD with r_ζ=0.1 and γ=0.3 as ζ_t=0.02 and r_ω=0.8.

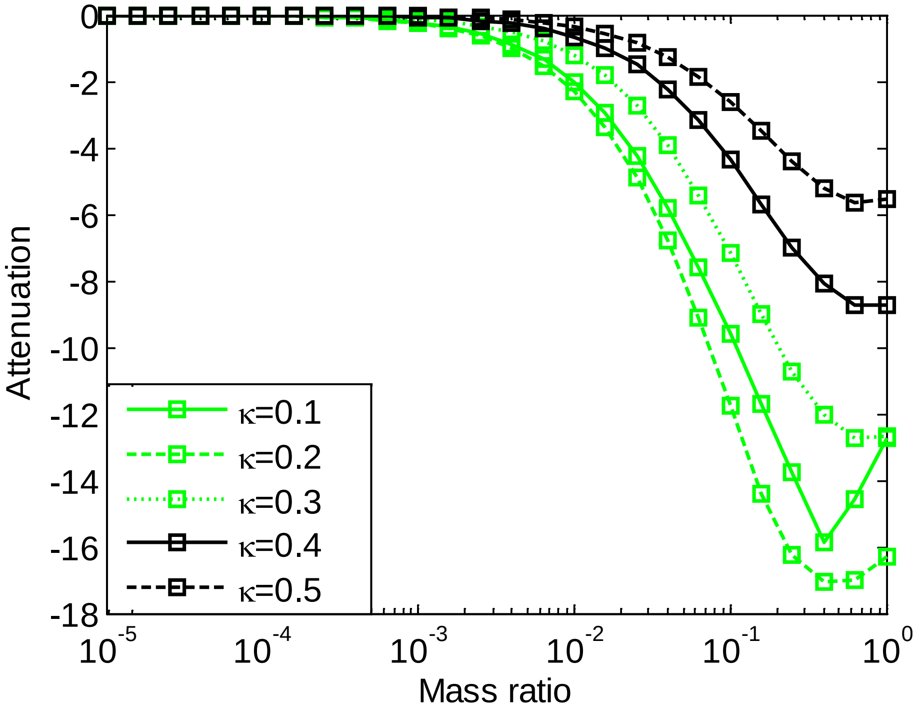

Figure 3.43. Attenuation of mistuned electromechanical semi-passive nonlinear TMD with r_ζ=0.1 and γ=0.9 as ζ_t=0.02 and r_ω=0.8.

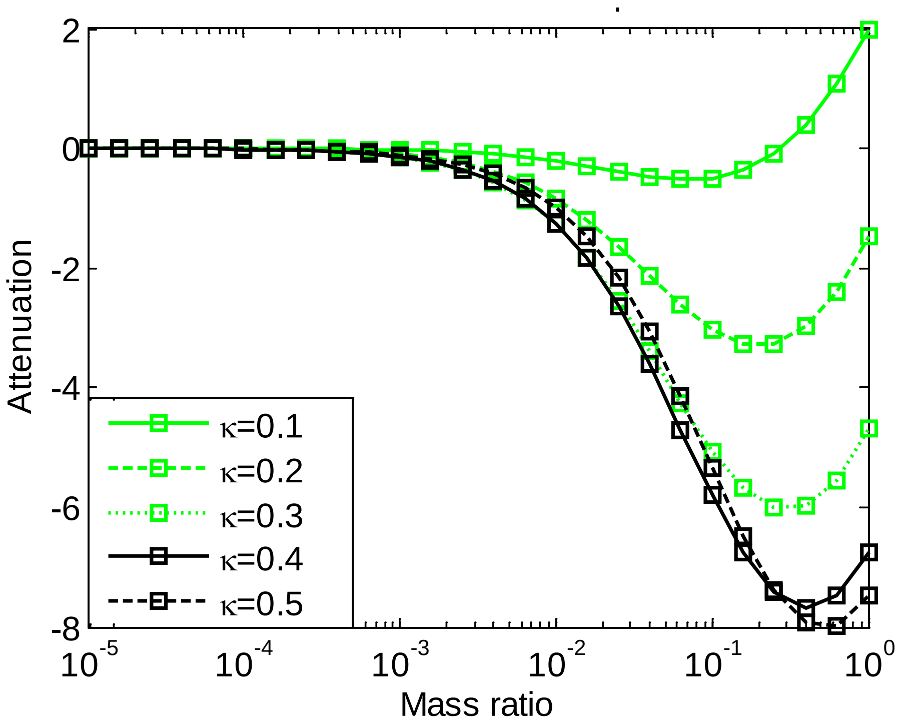

Figure 3.44. Attenuation of mistuned electromechanical semi-passive nonlinear TMD with r_ζ=0.1 and γ=0.3 as ζ_t=0.02 and r_ω=1.2.

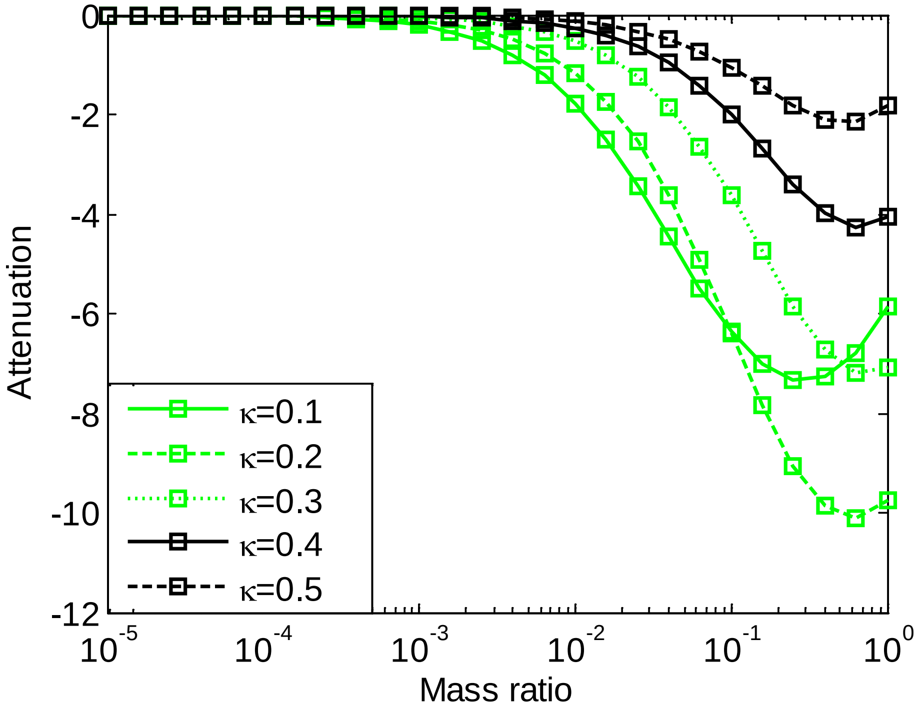

Figure 3.45. Attenuation of mistuned electromechanical semi-passive nonlinear TMD with r_ζ=0.1 and γ=0.9 as ζ_t=0.02 and r_ω=1.2.

Global control performances of the tuned and mistuned purely mechanical TMD, optimal electromechanical passive TMD and electromechanical semi-passive nonlinear TMD varied with mass ratio are simulated and discussed in this part with the developed TDOF model. From comparison, it can be found that the electromechanical TMD devices outperform the purely mechanical TMD except in the case where both primary structure and TMD with high damping. Although the control performance of electromechanical semi-passive nonlinear TMD devices can be superior to the electromechanical passive TMD systems, it is dependent on the voltage inversion coefficient and global coupling coefficient for some mass ratio ranges, which is different from the classical SSDI approach. Moreover, based on the results obtained in mistuned cases, it can be found that the TMD systems with a slightly lower resonance frequency ratio can damp the vibration in a wider mass ratio range without decreasing the global damping effectiveness. Thus, for pre-design of TMD, the resonance frequency of TMD can be devised a little bit lower.

Although the TDOF modelling is simple and easy compared with other modelling method, it is only feasible once the dynamical characteristics of the investigated system are acquired. Thus, as an alternative model for numerical analysis, finite element model is used as well for further discussion.

3.2.3. Finite element method model

A system composed of a cantilever beam (used as host structure) and an electromechanical TMD featuring piezoelectric material shown in Figure 3.46 is used as an illustrative example for demonstration and discussion. The two surfaces of the piezoelectric bimorph of the electromechanical TMD are connected in parallel. Since in this work, we only focus on the bending modes of the vibrating structure, same assumptions as in section 2.2.1. are made for simplicity. It should be noted that this finite element model is not restricted to the boundary conditions of the system. The global motion equation of the system equipped with the electromechanical TMD can be expressed by Eq. (2.6) as well.

Assuming the piezoelectric material is bonded at the position $x_0 \le x_1 \le x_0 + L_p$, then the electrical relationship of the electromechanical passive TMD holds:

$$\dot{V} = -\frac{t_p^2 d_{31}}{L_p\left[\varepsilon_{33}^T\left(s_{11}^E + s_{12}^E\right) - 2d_{31}^2\right]}\dot{\theta}\Big|_{x_0}^{x_0+L_p} - \frac{t_p\left(s_{11}^E + s_{12}^E\right)}{R w_2 L_p\left[\varepsilon_{33}^T\left(s_{11}^E + s_{12}^E\right) - 2d_{31}^2\right]}V \tag{3.39}$$

where w_2 denotes the width of the piezoelectric patch.

Furthermore, if the semi-passive SSDI approach is incorporated to the electromechanical TMD, the electrical relationships yield:

$$\begin{cases} \dot{V} = -\dfrac{t_p^2 d_{31}}{L_p\left[\varepsilon_{33}^T\left(s_{11}^E+s_{12}^E\right)-2d_{31}^2\right]}\dot{\theta}\Big|_{x_0}^{x_0+L_p} & \textit{open} \\ \dot{Q} = -\dfrac{wL_p\left[\varepsilon_{33}^T\left(s_{11}^E+s_{12}^E\right)-2d_{31}^2\right]}{t_p\left(s_{11}^E+s_{12}^E\right)}\dot{V} & \textit{switching} \end{cases} \tag{3.40}$$

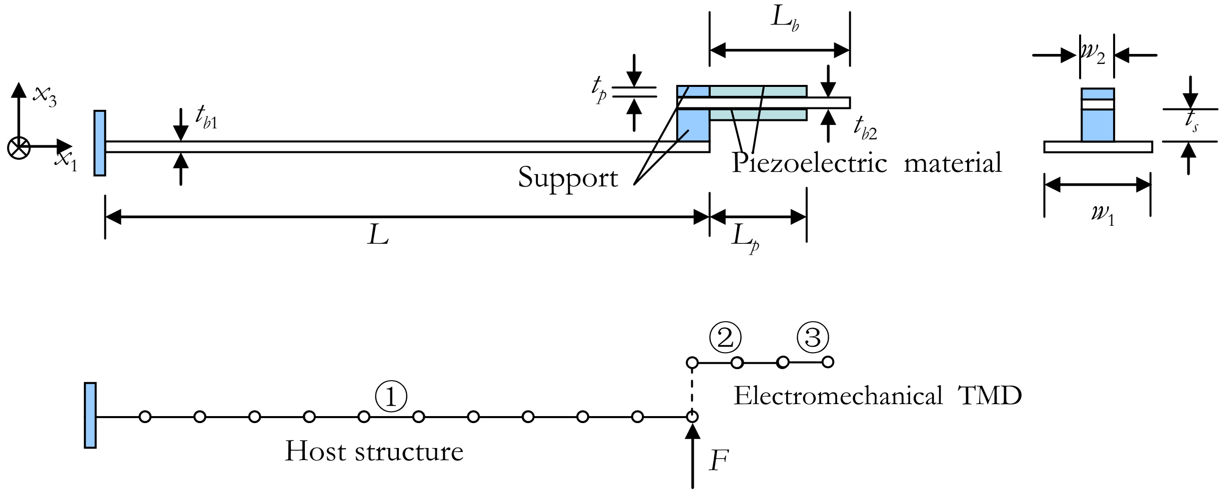

Figure 3.46. Investigated system featuring electromechanical TMD.

In this part, the principles of purely mechanical TMD, electromechanical passive TMD and the electromechanical semi-passive nonlinear TMD have been presented. A TDOF model and a finite element model are developed and introduced for analyzing the dynamical responses of the system comprising a host structure and a TMD device. Even though the finite element model is illustrated by a cantilever beam used as host structure, it can be extended to any boundary condition for predicting the damping performances of the installed TMD devices.

3.3. Experiments

To validate the proposed electromechanical semi-passive nonlinear TMD concept and compare the damping performances, experiments are carried out for investigation. The details of the physical experimental setup and procedure of experiments will be presented. Experimental measurements will be compared with the numerical analyses obtained from the TDOF model and finite element model as well. Since the electromechanical TMD in open circuit operates as an equivalent purely mechanical TMD, hereinafter, it is regarded as purely mechanical TMD for simplicity although it includes the electromechanical coupling as well.

3.3.1. Experimental setup

As shown in Figure 3.47, the experiments are performed on a steel cantilever beam with an electromechanical TMD attached to its free end. A smaller electromechanical beam, whose upper and lower surfaces are partially covered by piezoelectric material and connected in parallel for increasing the total capacitance, operates as an electromechanical TMD through an aluminium support. Several small-scale magnets are used to attach the aluminium support to the host steel beam and used as tip mass of the electromechanical TMD for initial tuning to ensure its resonance frequency is in the vicinity of the investigated resonance frequency of the host structure. External force $F = F_M \sin(\omega t)$ is generated by a signal generator and then applied to the end of the host structure through power amplifier and magnet driver. The relative velocity between the free end of the smaller electromechanical beam (namely the electromechanical TMD) and base is used as input signal measured by laser apparatus and displacement sensor for detecting the switching moment. In order to implement the controller in real time and obtained the command signal for switching, a dSPACE system is used.

The electromechanical characteristics of this system measured in the experiments are given in the Table 3.1. The dimension and material properties of host beam and electromechanical TMD device are respectively listed in Table 3.2 and Table 3.3.

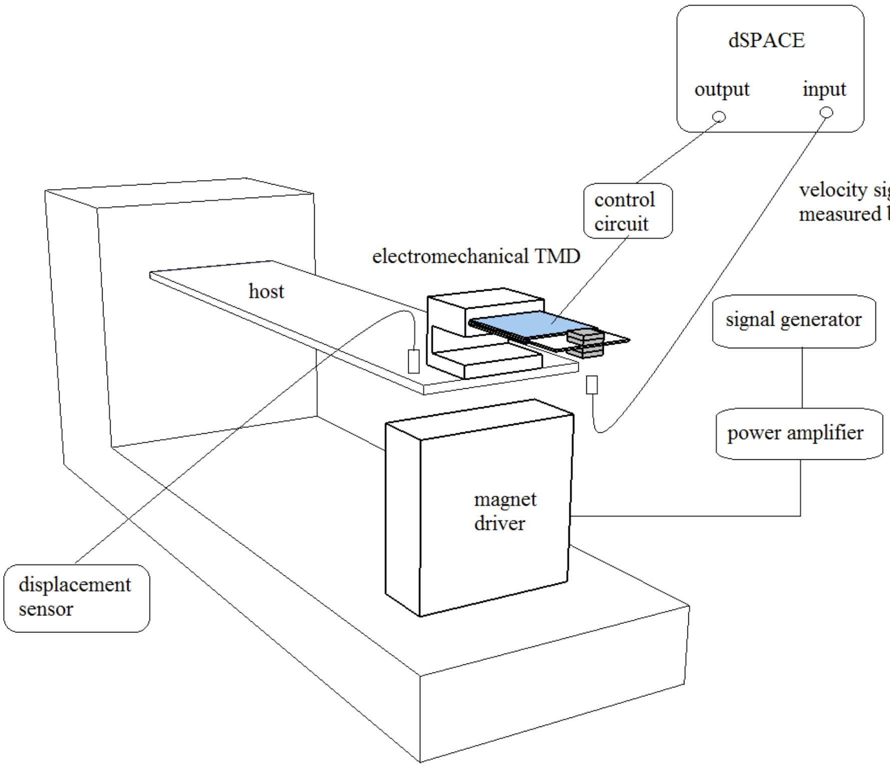

Figure 3.47. Experimental setup.

Table 3.1. Model parameters and characteristics measured in the experiments.

$m_1 = 0.012\,Kg$	$k_1 = 348.95\,N/m$	$Q_{M1} = 234$	$m_2 = 0.0012 Kg$	$k_2 = 39.12\,N/m$
$Q_{M2} = 16.38$	$\alpha = 6.5\times10^{-4}$	$C_0 = 380\times10^{-9}\,F$	$L_{in} = 0.6H$	$\gamma = 0.9$

Table 3.2. Dimensional and material properties of host beam.

Young's modulus	$Y_1 = 200\,Gpa$	Poisson's ratio	$\nu_1 = 0.24$
Density	$\rho_1 = 7870\,Kg/m^3$	Length	$L = 156\times10^{-3}\,m$
Width	$w_1 = 40\times10^{-3}\,m$	Thickness	$t_{b1} = 1\times10^{-3}\,m$

Table 3.3. Dimensional and material properties of electromechanical TMD.

<table>
<tr><td colspan="4">Substrate beam of TMD</td></tr>
<tr><td>Young's modulus</td><td>$Y_2 = 69\,Gpa$</td><td>Poisson's ratio</td><td>$\nu_2 = 0.33$</td></tr>
<tr><td>Density</td><td>$\rho_2 = 2700\,Kg/m^3$</td><td>Length</td><td>$L_b = 30\times10^{-3}\,m$</td></tr>
<tr><td>Width</td><td>$w_2 = 18\times10^{-3}\,m$</td><td>Thickness</td><td>$t_{b2} = 0.345\times10^{-3}\,m$</td></tr>
<tr><td colspan="4">Piezoelectric patch</td></tr>
<tr><td>Relative dielectric constant</td><td>$\varepsilon_{33}^T/\varepsilon_0 = 2021$</td><td>Thickness</td><td>$t_p = 0.041\times10^{-3}\,m$</td></tr>
<tr><td>Charge coefficient</td><td>$d_{31} = -129.6\times10^{-12}\,m/V$</td><td>Length</td><td>$L_p = 20\times10^{-3}\,m$</td></tr>
<tr><td rowspan="2">Compliance in short circuit</td><td>$s_{11}^E = 15.27\times10^{-12}\,m^2/N$</td><td rowspan="2">Density</td><td rowspan="2">$\rho_p = 7900\,Kg/m^3$</td></tr>
<tr><td>$s_{12}^E = -5.46\times10^{-12}\,m^2/N$</td></tr>
</table>

3.3.2. Experimental results

To examine and compare the damping performance of the proposed electromechanical semi-passive nonlinear TMD, the counterparts (purely mechanical TMD and electromechanical passive TMD with same dynamical parameters) are also investigated under the same external disturbance. Since the purpose of this research is to suppress the dynamical responses of the vibrating host structure under external force and preliminary discuss the possibility and potential of the proposed electromechanical semi-passive nonlinear TMD for damping the structural vibration, only the displacement response of the host structure will be measured and discussed. The normalized displacement response defined as

$$Displacement_{normalized} = \frac{Displacement}{\max\left(Displacement_{host\ only}\right)} \tag{3.41}$$

is used for qualitative analysis.

As exhibited in Figure 3.48 (a) and (b), after attaching the aluminium support at the free end of the host beam, the first resonance frequency of host structure is shifted from 34.19 Hz to 27.04 Hz while the response is slightly increased, since the dynamical mass is decreased. In order to initially tune the resonance frequency of the electromechanical TMD close to 27.04 Hz, four small-scale magnets are used as tip mass and attached at the free end of the electromechanical TMD. The fundamental resonance frequencies of electromechanical TMD are obtained as 27.8 Hz in short circuit and 28.8 Hz in open circuit after initial tuning.

As noted in last section, since the electromechanical TMD in open circuit can be regarded as an equivalent purely mechanical TMD, thus, the normalized displacement response of host structure with purely mechanical TMD (Figure 3.48 (c)) is referred to the measurements obtained by displacement sensor as the electromechanical TMD in open circuit. From the given curves, it can be found that after installing the purely mechanical TMD, the displacement response of the host structure is significantly reduced and accompanied by two smaller peaks at 23.5 Hz and 31.8 Hz.

In order to achieve optimized control performance, the optimal resistance given in Eq. (3.16) which varies with the frequency of the external excitation is chosen as the shunt circuit to magnify the damping effectiveness. Because inductively shunted electromechanical TMDs usually require unrealistic inductance value, only the resistive shunting is investigated and discussed here. The experimental measurements using the optimal electromechanical passive TMD with optimized resistance are plotted in Figure 3.48 (d). Compared with the results obtained with purely mechanical TMD, superior damping performance is achieved in this case.

Figure 3.48 (e) gives the normalized displacement response of the host beam in the case of featuring the proposed electromechanical semi-passive nonlinear TMD with excellent damping effectiveness. The inversion coefficient γ measured in this case is 0.9. It can be concluded from the comparison with purely mechanical TMD and the optimal electromechanical passive TMD that this electromechanical semi-passive nonlinear TMD outperforms the other TMDs and it can achieve much more pronounced damping performance. Moreover, the benefit of electromechanical semi-passive nonlinear TMD is experienced over a wider frequency range than the other counterparts.

Nevertheless, nonlinearities of the dynamical responses measured in experiments are found in Figure 3.48 (c)-(e), which may be attributed to the interactions of the host structure and the electromechanical TMD.

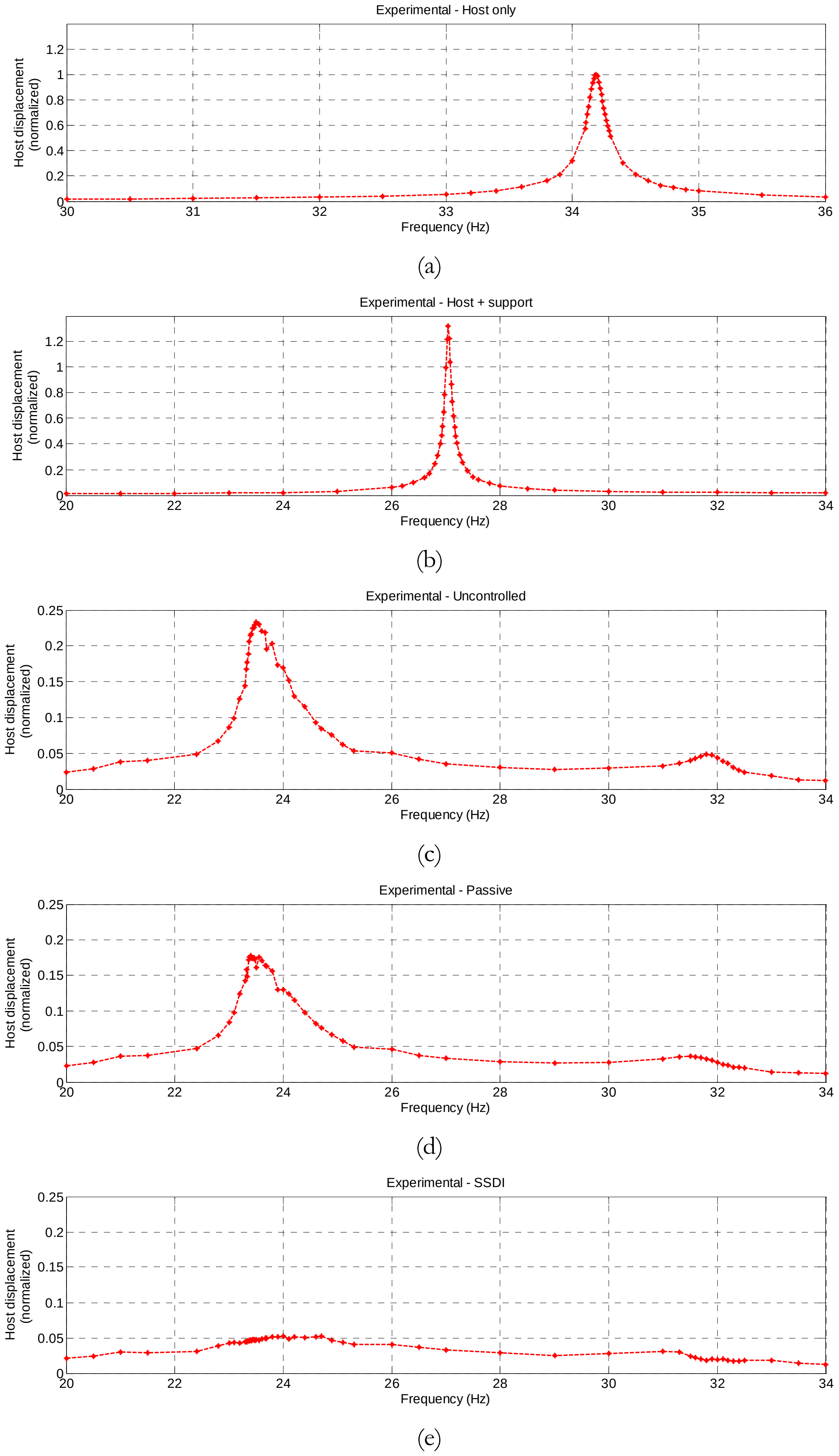

Figure 3.48. Experimental measurements of the host structure

In this part, the experiments conducted on a steel cantilever beam (host structure) are introduced. The experimental measurements obtained by the displacement sensor are plotted and compared. From the experiments, it is validated that the electromechanical semi-passive nonlinear TMD, combining the electromechanical TMD device and the semi-passive SSDI approach, provides the largest suppression of the resonant vibration amplitude of the host structure compared with the cases of using purely mechanical TMD and optimal electromechanical passive TMD with same dynamical parameters.

3.3.3. Comparison with theoretical analysis for harmonic response

To further investigate the damping performances of the TMD devices, the dynamical displacement response of the host beam and the damping attenuation of each TMD will be evaluated by the TDOF model and the finite element model with MATLAB and compared with the experimental results.

a) Simulation by the TDOF model

Same model parameters and characteristics measured in experiments which are summarized in Table 3.1, are used in the TDOF simulation. The normalized displacement response of the host structure subjected to the external force $F = F_M \sin(\omega t)$ without TMD is plotted in Figure 3.49 (a). Compared with the dynamical response given in Figure 3.49 (b), it can be found that after attaching the aluminium support to the tip end, the resonance frequency of the host beam is shifted from 34.2 Hz to 27.14 Hz with slight response increase due to the increase of dynamical mass, which is very close to the measurements obtained in experiments. To damp the dynamical response of host structure, the fundamental resonance frequency of the electromechanical TMD is initially tuned in this TDOF model. The normalized displacement responses of the host structure with purely mechanical TMD, optimal electromechanical passive TMD and electromechanical semi-passive nonlinear TMD are given in Figure 3.49 (c)-(e). It is obvious that the dynamical response of the vibrating beam is significantly attenuated by employing the TMD device. It should be noted that in the case of using optimal electromechanical passive TMD, the implemented resistance is varied with the external angular frequency as given in Eq. (3.16). In addition, the inversion coefficient γ in the case of using electromechanical semi-passive nonlinear TMD equals to 0.9 which is same as that obtained in the experiments.

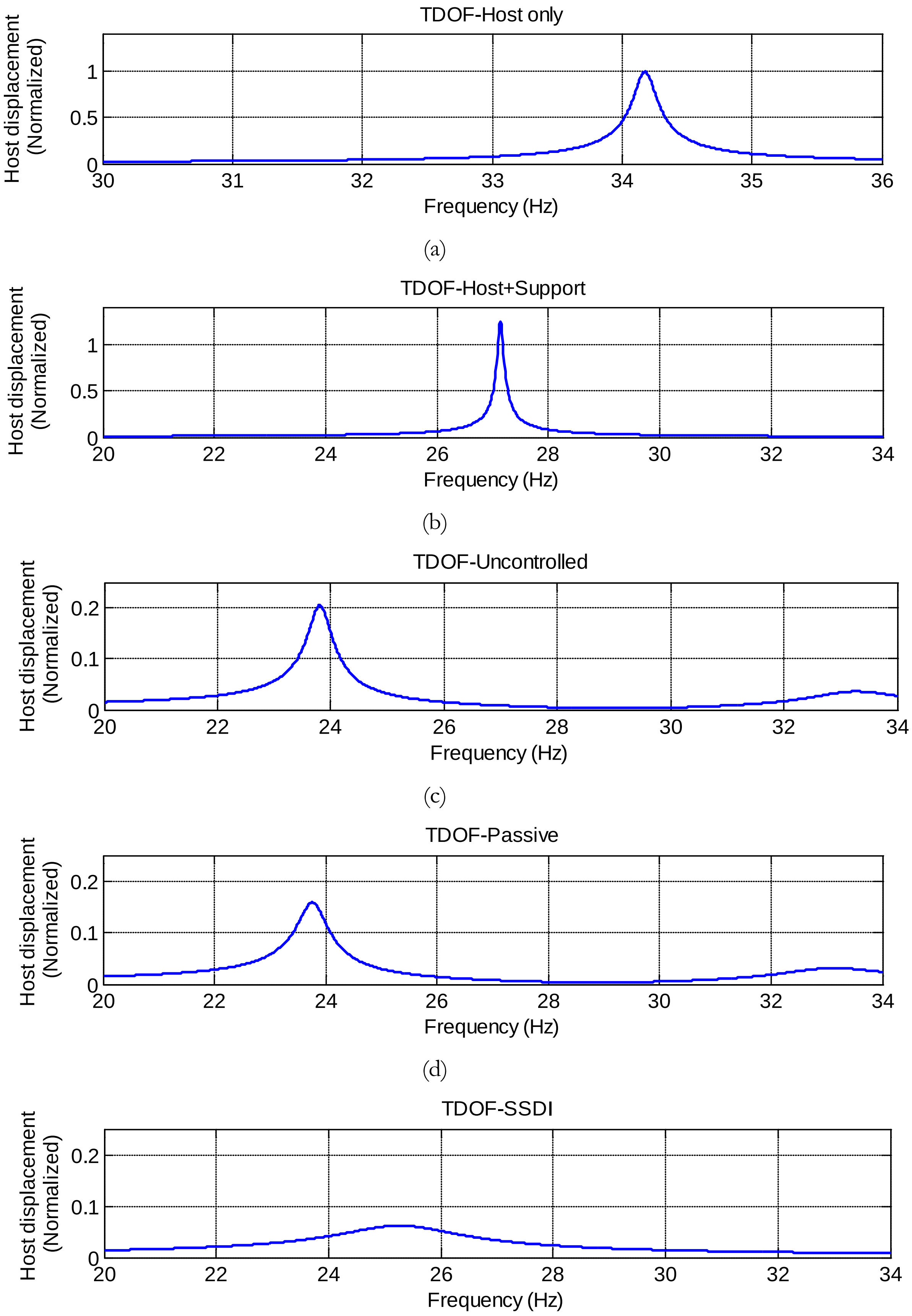
TDOF-Host only

TDOF-Host+Support

TDOF-Uncontrolled

TDOF-Passive

TDOF-SSDI

(a)

(b)

(c)

(d)

(e)

Figure 3.49. Simulation results with TDOF model.

From the TDOF simulation results, it is confirmed that the proposed electromechanical semi-passive nonlinear TMD can obtained the superior damping performance, which are in good agreement with the experimental results. However, a slight difference is found from the curves given in Figure 3.48 (e) and Figure 3.49 (e) as there is only one peak in the TDOF modelling while two peaks appear in experiments. This difference can be explained by the first harmonic assumption demonstrated in TDOF modelling with Eqs. (3.23)-(3.24).

b) Simulation by the finite element model

To further confirm the conclusions obtained from TDOF modelling, the cantilever beam with a TMD device attached at its free end is also simulated by the alternative finite element model. The dimensional and material properties of the simulated system are listed in Table 3.2 and Table 3.3, which are same as the experimental measurements. In order to obtain the same mechanical quality factor as that in experiments, the damping coefficients of Rayleigh damping C are delicately chosen, which are given in Table 3.4. For simplicity, the aluminium support and the small-scale magnets used for attaching are considered as a tip mass which is added to the last element of the host beam in this model. The normalized displacement responses of host beam obtained by finite element model are plotted in Figure 3.50 (a)-(e).

Table 3.4. Damping coefficients used in finite element modelling.

$\beta_1 = 2.4$	$\beta_2 = 1\times 10^{-4}$

It can be seen from the curves that the simulation results obtained from the finite element model are in good agreement with those acquired in experiments even though the simulation is slightly smaller than the experimental results probably due to the nonlinearities in the measurements. Although the purely mechanical TMD and optimal electromechanical passive TMD can successfully suppress the vibration of host beam, the electromechanical semi-passive nonlinear TMD achieves the best damping performance. Moreover, compared with the TDOF modelling, it can be seen that the finite element model is better than the TDOF model in the case of installing the electromechanical semi-passive nonlinear TMD since there is no first harmonic approximation in modelling development, which therefore allows taking into account harmonics generated by the switching process. For easy comparison, the damping attenuation defined as Eq. (3.38) is summarized in Table 3.5.

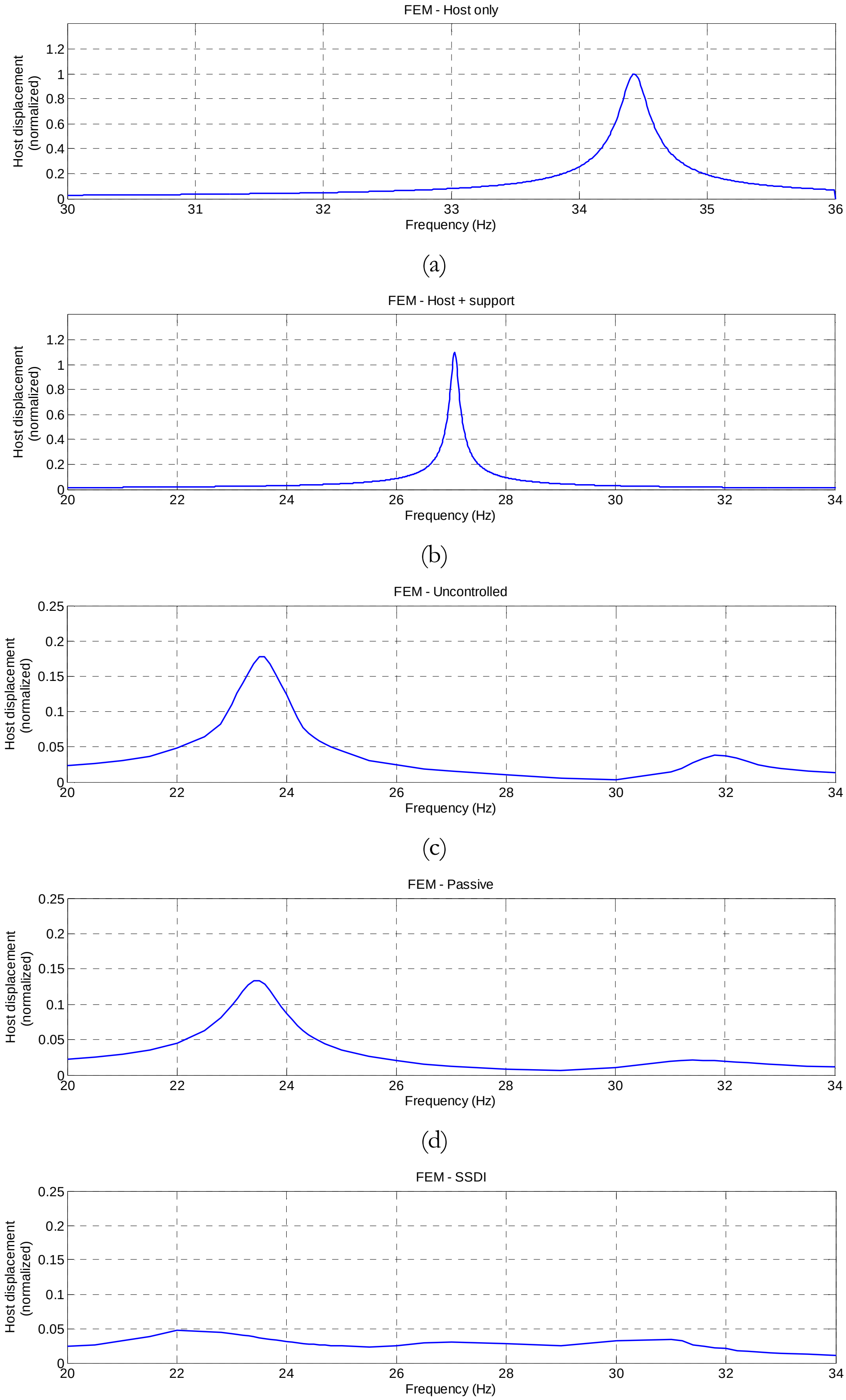

(a)

(b)

(c)

(d)

(e)

Figure 3.50. Simulation results with FEM model.

Table 3.5. Damping attenuation obtained with TMD systems

	Purely mechanical TMD	Optimal electromechanical passive TMD	Electromechanical semi-passive nonlinear TMD
Experiments	-12.65 *dB*	-15.01 *dB*	-25.60 *dB*
TDOF	-13.76 *dB*	-16.02 *dB*	-24.18 *dB*
FEM	-14.98 *dB*	-17.48 *dB*	-26.55 *dB*

It can be seen from the comparison that the electromechanical semi-passive nonlinear TMD outperforms to the purely mechanical TMD and optimal electromechanical passive TMD since by combining the semi-passive SSDI technique with TMD device, more mechanical energy of the host structure can be converted into electrical energy and dissipated in the switching circuit due to the voltage inversion process. Moreover, TDOF and finite element modelling have been proven as effective numerical analysis methods which can be used for predicting the damping performance or further discussion.

Figure 3.51 exposes the normalized frequency responses obtained in directly coupled cases through the finite element method in frequency domain (with first harmonic approximation for SSDI), in which the same piezoelectric actuator is directly bonded on the host structure. Compared with the normalized responses obtained by electromechanical TMD devices, it can be found that excellent damping ability of TMD systems are demonstrated as the attenuation is achieved as -25.60 *dB* with the proposed semi-passive nonlinear TMD while less than 10 *dB* is obtained by classical SSDI approach in the directly coupled case, which is attributed to the better energy transfer processes (mechanical energy transferred from host structure to TMD, electromechanical coupling between the piezoelectric patch and TMD) in the electromechanical TMD systems and low coupling in directly coupled cases. Hence, the proposed electromechanical semi-passive nonlinear TMD device is a very good alternative for damping the vibration of lightly coupled host structure.

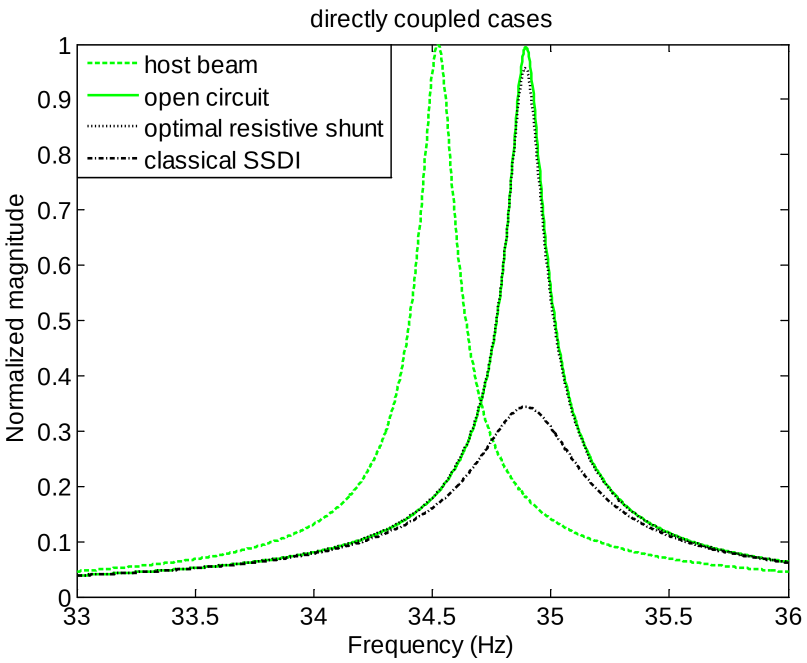

Figure 3.51. Normalized frequency responses with directly coupled piezoelectric patch.

To validate the superior damping performance of the proposed electromechanical semi-passive nonlinear TMD, the experiments are performed on a steel cantilever beam (host structure) with a TMD attached at its free end. Purely mechanical TMD, optimal electromechanical passive TMD and electromechanical semi-passive TMD are respectively investigated. Numerical analyses obtained from the TDOF model and finite element model are also demonstrated. From the results, it is obvious that the experimental measurements are in accordance with the simulation results. Moreover, the dynamical response of the host structure can be effectively damped by implementing the TMD devices. Since in the case of using electromechanical semi-passive nonlinear TMD, more mechanical energy of host structure can be transferred into electrical energy form by the artificial voltage inversion process and then dissipated in the electrical switching circuit, this semi-passive nonlinear TMD is superior to the purely mechanical TMD and optimal electromechanical passive TMD with a wider frequency benefit. The effectiveness of TDOF model and finite element model has been experimentally validated. Hence, they can be used for effectively predicting the damping performance of systems.

3.4. Further discussion

Further investigation is demonstrated in this part to extend the application of the proposed electromechanical semi-passive nonlinear TMD. Although the experiments are only conducted on the cantilever beam, the proposed electromechanical semi-passive nonlinear TMD device is not restricted to the host structure and boundary conditions. Hence, it can be extended to damp the vibration of any arbitrary host structures (such as plate or shell, etc.) under other boundary conditions (clamped-clamped, etc.) as it is put at areas where can experience maximum acceleration of the interested vibration modes. Moreover, it should be pointed that this study is a preliminary investigation of the proposed adaptive electromechanical semi-passive nonlinear TMD. Nevertheless, it can be intensively and extensively used for vibration control. Future works would be focused on the following three aspects.

3.4.1. Optimization of design parameters

Optimization of the proposed electromechanical semi-passive nonlinear TMD can be further investigated on the basis of TDOF modelling and/or finite element method. The effects of the location, mass ratio, damping ratio and voltage inversion coefficient of electromechanical semi-passive nonlinear TMD can be further studied and optimized according to the objective functions. Although in this study, author only focuses on the global damping performances of the electromechanical semi-passive nonlinear TMD in the given parameter (mass ratio, angular frequency of external excitation, global coupling coefficient and voltage inversion coefficient) ranges, the global attenuation in wider investigated ranges or the damping performance at the resonance frequency of the vibrating host structure can be further studied and optimized. Even though the mass ratio is regarded as one of variables, the design variables of the proposed electromechanical semi-passive TMD can be changed and chosen according to the realistic applications and objective optimal functions.

As shown in Figure 3.52, different from the classical SSDI approach in which the control effectiveness is monotonically increasing with the increase of inversion coefficient (greater inversion coefficient leads to better damping performance), there is an optimal range of inversion coefficient (around 0.82 for the experimental sample) of the electromechanical semi-passive nonlinear TMD. Such an effect can be attributed to the double energy conversion (mechanical to mechanical and then mechanical to electrical) that leads to a trade-off for achieving good performance. In particular, a high electromechanical conversion effect (for example large γ) would prevent mechanical energy entering within the TMD, so that host to TMD mechanical energy transfer would be compromised, yielding degraded damping effect. Hence, the dynamical response of the primary structure is decreased and then increased with the increase of γ as shown in Figure 3.53.

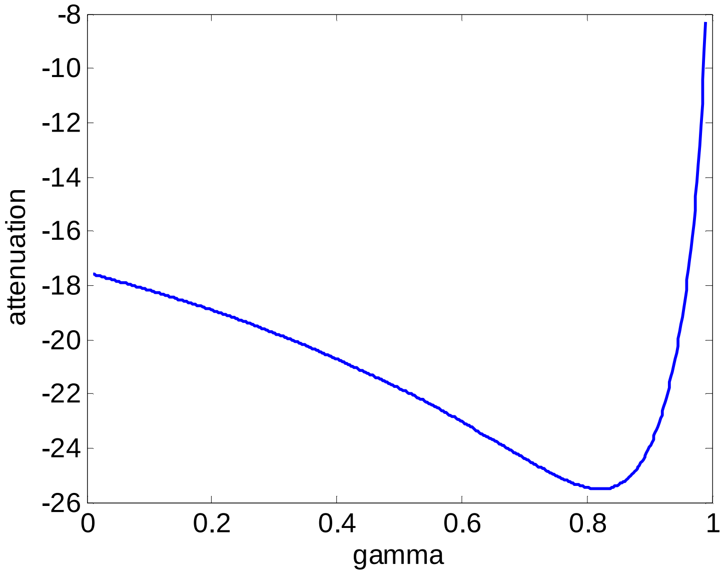

Figure 3.52. Attenuation of the experimental sample varied with voltage inversion coefficient.

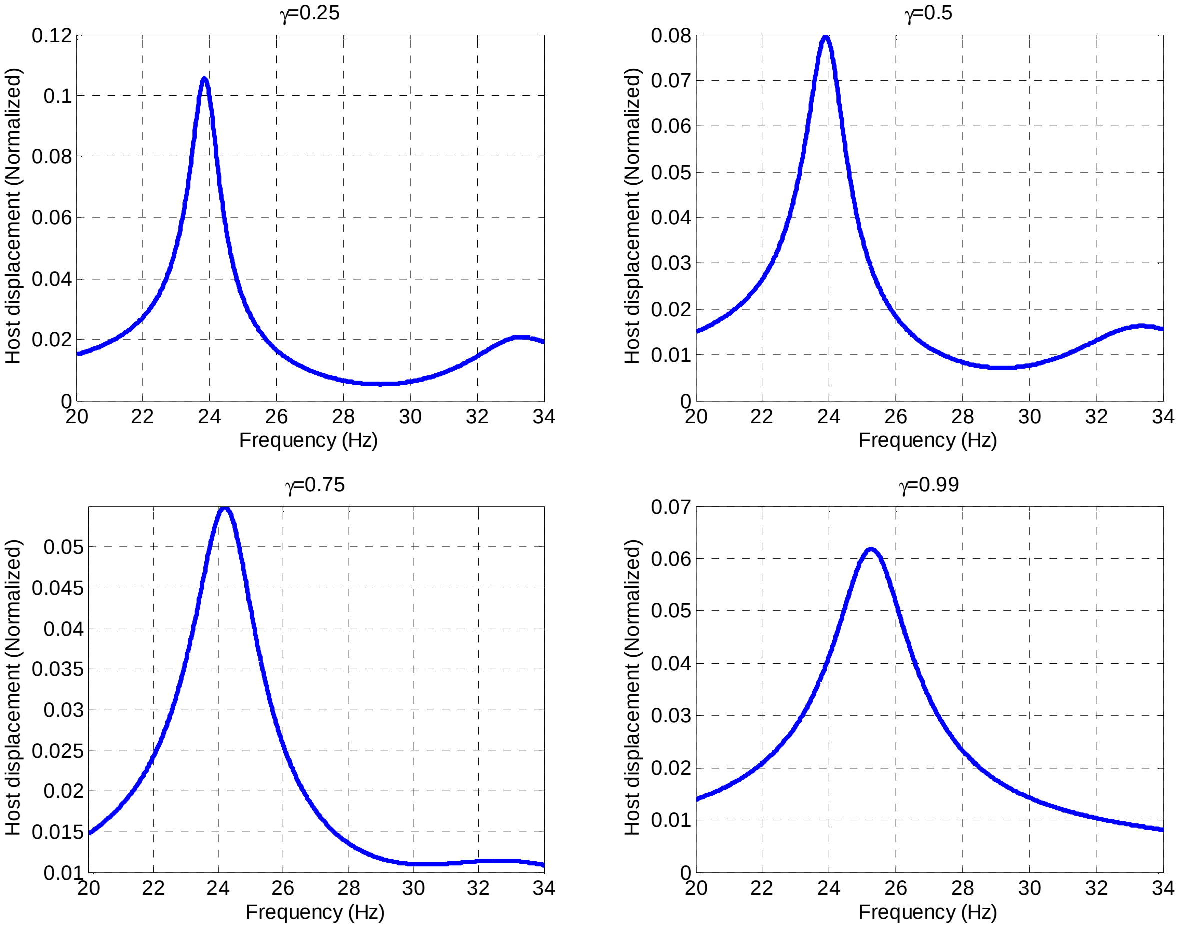

Figure 3.53. Dynamical responses of host structure using electromechanical semi-passive TMD with different inversion coefficient.

3.4.2. Multimodal/broadband control

Even though in this chapter, only the control effectiveness of proposed electromechanical semi-passive nonlinear TMD in the vicinity of the one resonance frequencies of host structure is demonstrated, in order to achieve multimodal/broadband vibration control performance, it can be combined with other multimodal control techniques.

Aiming at limiting multimodal/ broadband vibration of host structure, the threshold detection criteria [117][134][135][136][137] can be employed in the electromechanical semi-passive nonlinear TMD, which the control switching action is disabled until some conditions are fulfilled. Digital switch in this case should be kept open until the relative displacement of electromechanical semi-passive nonlinear TMD reaches an extremum value and it exceeds the computed threshold. At that moment, the piezoelectric element of the TMD is connected to the control circuit for voltage inversion for half a period of the electrical oscillator.

Moreover, the multimodal/broadband control ability can also be achieved by installing multiple electromechanical semi-passive nonlinear TMD devices. In this case, the locations, damping ratios, mass ratios, coupling coefficients and inversion coefficients of the multiple electromechanical semi-passive nonlinear TMD devices need to be chosen by pre-design (using TDOF model or finite element model) in order to obtained effective damping performance with interactions. Thus, compared with the previous method combined with threshold detection, the multiple electromechanical semi-passive nonlinear TMD devices may be relatively complex. In addition, the multiple electromechanical semi-passive nonlinear TMD devices can be combined with the enhanced nonlinear strategy based on spatial filtering (introduced in Chapter 2) for broadband control through the energy transformation between TMD devices.

3.4.3. Self-powered electromechanical semi-passive nonlinear TMD

Since the proposed electromechanical semi-passive nonlinear TMD succeeds to the traits of classical SSDI technique such as low energy requirement and ease of implementation, thus, it can be devised with self-powered capability by implementing the self-powered control block (Figure 1.28) proposed by Richard [116] or implementing the adaptive self-powered control block (Figure 1.29) proposed by Lallart [117] to eliminate the energy requirement for switch control.

3.5. Conclusion

In this chapter, an electromechanical semi-passive nonlinear TMD aiming at achieving superior damping performance for limiting the vibration of host structure is proposed, which combined the electromechanical TMD with the semi-passive nonlinear technique (SSDI). TDOF model is developed for introducing the control principle of the proposed semi-passive nonlinear TMD. Damping performance of purely mechanical TMD, electromechanical passive TMD and electromechanical semi-passive nonlinear TMD are preliminary investigated on the basis of TDOF modelling. Finite element modelling as an alternative analysis method is briefly introduced. Experiments are conducted on the cantilever beam to validate the control effectiveness of the proposed electromechanical semi-passive nonlinear TMD, which is in good agreement with the numerical analyses and confirms the better control capability of the proposed TMD. The main work in this chapter can be summarized as follows:

- In order to achieve superior damping performance, an adaptive electromechanical semi-passive nonlinear TMD is proposed based on the semi-passive control technique SSDI. For effectively damping the vibration of host structure, the piezoelectric patches of the proposed electromechanical semi-passive nonlinear TMD is kept open until the relative displacement between the TMD device and the host structure or the piezovoltage reaches an extremum value. At that moment, the digital switch of the control circuit is closed and the piezoelectric patch of the TMD and the inductor of the switching device will constitute an electrical oscillator. This switch will reopen after half a period of this electrical oscillator until the piezovoltage is reversed. This voltage inversion process is very short compared with the motion period and yields an artificial electromechanical coupling increase. The control principles of purely mechanical TMD, electromechanical TMD and the proposed electromechanical semi-passive nonlinear TMD are introduced in detail based on the TDOF modelling and finite element modelling. For the preliminary investigation of each TMD, the global control performances of tuned and mistuned TMD systems varied with mass ratio are demonstrated. From the results obtained in tuned cases, it can be found that the higher damping TMD systems can result in better damping effectiveness in the given mass ratio range. Moreover, TMD systems are more effective for reducing the vibration of the host structure with lower damping. Globally, from the comparison of tuned purely mechanical TMD and the tuned optimal electromechanical passive TMD, the latter is superior to the former. Additionally, with the increasing of global coupling coefficient, global damping effectiveness is increased in relatively higher mass ratio range. According to the results obtained with tuned electromechanical semi-passive nonlinear TMD, it is found that for the semi-passive nonlinear TMD with lower inversion coefficient, the global damping performance is better as the global coupling coefficient is increased. However, for the semi-passive nonlinear TMD with higher inversion coefficient, the global damping capability is firstly increased and then decreased with the increase of global coupling coefficient, which is different from directly coupled cases where a greater inversion coefficient leads to better control performance. Thus, the voltage inversion coefficient is a very important parameter for the proposed semi-passive nonlinear TMD with a given global coupling coefficient. Furthermore, the global control performance of the mistuned TMD systems with ±20% resonance frequency shift (between the host structure and TMD) are demonstrated as well. From the comparison, it can be found that the optimal mass ratio is increased for the mistuned TMD systems with -20% resonance frequency shift and decreased with the corresponding mistuned TMD systems with +20% resonance frequency shift without notable global damping performance difference. Thus for the pre-design of TMD devices, the resonance frequency of the TMD can be delicately devised a slightly lower without global control performance deterioration.

- In order to validate the excellent damping performance of the proposed electromechanical semi-passive nonlinear TMD, experiments are conducted on a cantilever beam (host structure) with a TMD device attached at its free end. The control effectiveness of electromechanical passive TMD in open circuit (operating as purely mechanical TMD), optimal electromechanical passive TMD and the proposed electromechanical semi-passive nonlinear TMD is obtained and compared. Numerical analyses based on the TDOF model and finite element model are achieved as well. From the experimental measurements and theoretical results, it can be found that the obtained results are in good agreement, which shows the superior damping effectiveness of the electromechanical semi-passive nonlinear TMD and confirms that the proposed adaptive TMD outperforms the purely mechanical TMD and electromechanical passive TMD as the inversion coefficient is in a propriate range.

- Further applications and future works of the electromechanical semi-passive nonlinear TMD are discussed. Based on the demonstrated preliminary investigation, the design variables such as the location, mass ratio, damping ratio and voltage inversion coefficient can be further optimized according to the objective function (global damping performance, control ability at the resonance frequency of the host structure, etc.) in order to achieve better effectiveness. Moreover, this adaptive TMD can be extended for multimodal/broadband control by employing the threshold detection criteria, using multiple electromechanical semi-passive nonlinear TMD systems or the combination of multiple electromechanical semi-passive nonlinear TMD systems with enhanced nonlinear strategy based on spatial filtering. Since the proposed concept inherits the low power requirement characteristic of SSDI technique, it can be devised as a self-powered electromechanical semi-passive nonlinear TMD.

Chapter 4. Wave attenuation of Periodic Structures Featuring Nonlinear Interfaced Piezoelectric Patches

Periodic structures which consist of a number of identical elements in an identical manner are capable of propagating the elastic waves along the periodic structures over specific frequency bands named "pass bands" and the waves within the other frequency bands, namely "stop bands", can be filtered and blocked. The attenuation of wave propagation due to structural periodicity is distinctly different from the damping effect since the former results from impedance changes in the structural physical or geometrical properties and the latter is due to energy losses. In order to tune the width and location of the pass and stop bands, the combinations of periodic structures with active control techniques, passive shunting circuits and/or hybrid methods have been reported. In this chapter, periodic structures featuring the semi-passive nonlinear SSDI technique have been studied for vibration control purposes. The attenuation and localization of wave propagation with different connections (independently switching circuit and interconnection between cells) are respectively investigated based on finite element method and transfer matrix method. To validate the numerical analyses, experiments are conducted on a clamped-clamped beam. Numerical and experimental results show that the nonlinear interface not only dramatically increases the damping ability of the periodic structures in stop bands but also significantly enlarges the stop bands width, which allows good abilities for efficiently damping the mechanical vibration and attenuating the elastic waves over a wider frequency band.

4.1. Brief review of existing research combined the periodic structures with control techniques

Different from the damping strategies that use energy losses over entire frequency spectra, the elastic waves can be significantly attenuated in stop bands of the periodic structures while for other frequencies, it remains unchanged. In order to tune the width and location of the bands, some research combining periodic structures and other techniques for vibration control and/or noise attenuation purposes have been reported, thanks to the development of intelligent materials which allows ease of implementation.

Baz [155] demonstrated the utility of the active control capabilities in tuning the spectral width and locations of pass and stop bands according to the external excitation. Numerical examples studies on the aperiodicity showed that increasing the level of control randomness can extend the spectral width of a stop band into the adjacent propagation zones.

Shunted piezoelectric patches were periodically placed along rods (Figure 4.1) to control the longitudinal wave propagation by Thorp *et al.* [156]. Simulation results indicated that the resistive shunting can introduce damping in the periodic structure, thus providing the wave attenuation outside the stop bands. The width and location of the stop bands are significantly influenced as an inductance is connected in series to the resistive shunting circuit. Moreover, by proper tuning of the shunting circuit, additional stop bands can be produced over any frequency band. Furthermore, adding disorder to the shunting parameters can extend the upper boundary of the stop band at the considered tuning frequency. The amplitude decay is enhanced with the increase of disorder level.

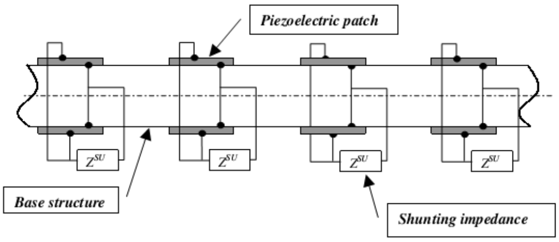

Figure 4.1. Periodic rod with periodic shunted piezoelectric patches [156].

In their succeeding work, they extended this concept to attenuate the wave propagation in fluid-loaded shells with periodic shunting piezoelectric rings [157] (Figure 4.2). Numerical analyses based on finite element model were performed both for in vacuo and fuild-loaded shells, which showed the effectiveness of this periodic shells in generating an additive stop band at the tuned frequency of the inductive-resistive shunting circuit. However, the location of the stop band is independent from the effect of fluid-loading, which indicates the robustness of this vibration control treatment with respect to the structural/environmental changes.

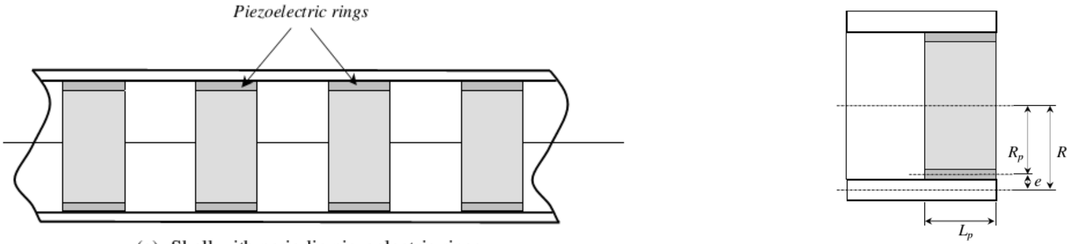

(a) -Shell with periodic piezoelectric rings

(b) – Main dimensions of ring and shell

Figure 4.2. Schematic diagram of considered periodic shell and unit cell [157].

Spadoni *et al.* [158] numerically studied the wave propagation attenuation and vibration reduction for plates with periodic shunted piezoelectric patches, which attenuates the waves and limits the vibrations without specifically targeting the structural modes. The simulation results illustrated the strong broadband characteristics of this concept which is contrast with the narrow band effect obtained with single resistive-inductive shunting circuit.

Optimization for allowing maximization or minimization of wave transmissibility between passive and active distributed beam has been introduced by Collet *et al.* [159]. Wave effects of negative capacitance shunts, negative capacitance optimization and resistive-capacitive impedance optimization were investigated. It is concluded that implementing efficient shunt circuits can induce a total absorption or reflection of propagating waves. Moreover, the shunts with negative capacitance are far from the instability point and guarantee the global stability and robustness.

Normal and oblique wave propagation and localization in piezoelectric and piezomagnetic layered periodic structures were considered by Pang et al. [160]. Numerical results obtained by transfer/ stiffness matrix methods showed that the width of gaps is determined by the differences between material constants.

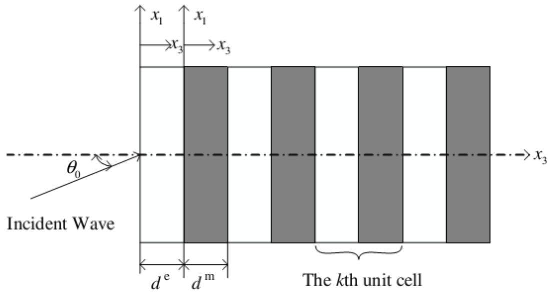

Figure 4.3. Schematic diagram of the piezoelectric and piezomagnetic layered periodic structure [160].

Casadei *et al.* [161] experimentally designed a periodic layout using resistive-inductive shunting for broadband vibration reduction of a flexible isotropic cantilever plate (Figure 4.4). Significant broadband attenuation confirmed the broadband control effectiveness of this simply and low computational concept. Generally, the periodical resonant shunts are much more effective for attenuating the wave at medium-high frequencies. Thus, in order to reduce the vibration along a broad frequency spectra, hybrid arrays of resistive-inductive shunt and negative impedance capacitance for suppressing the vibration of plate were further investigated numerically and experimentally by this group [162]. Two different electrical arrangements (Figure 4.5) were tested with corresponding unit cell configurations. Experimental results verified the control effectiveness and robustness of the periodic hybrid arrays.

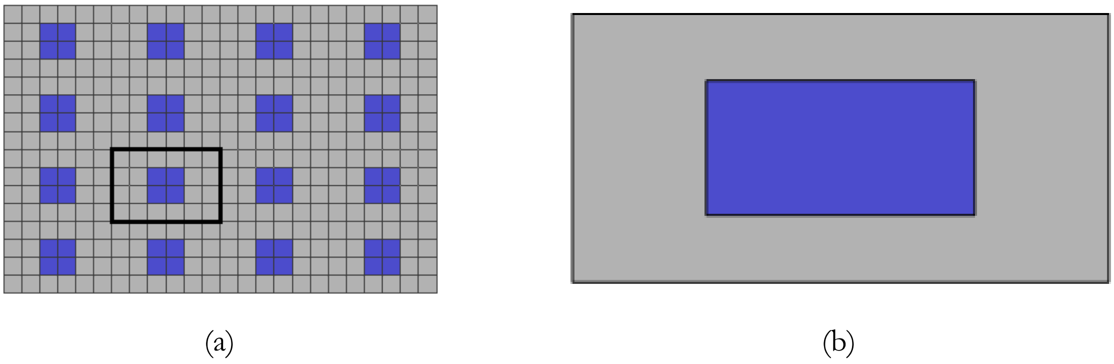

Figure 4.4. Schematic of the FE discretization of a periodic plate (a) and unit cell of the periodic plate configuration (b) [161].

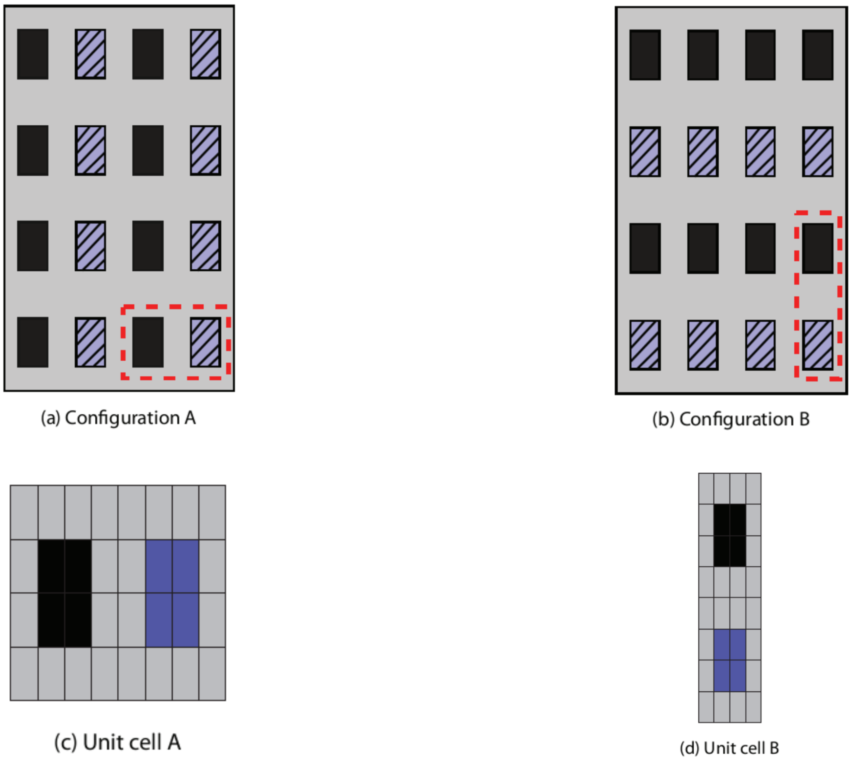

Figure 4.5. Configurations (a) A and (b) B chosen to realize a finite periodic assembly and the corresponding unit cells of (c) A and (d) B, respectively [162].

Low frequency band gaps induced by arrays of resonant shunts with Antoniou's circuit which can produce large ideal inductance were experimental investigated on beams (Figure 4.6) by Wang *et al.* [163]. They pointed out that the band gaps induced by resistive-inductive shunted PZT patches is composed of may tiny Bragg band gaps (Figure 4.7) and the maximum attenuation is located at a frequency higher than the resonance frequency of the shunting circuit.

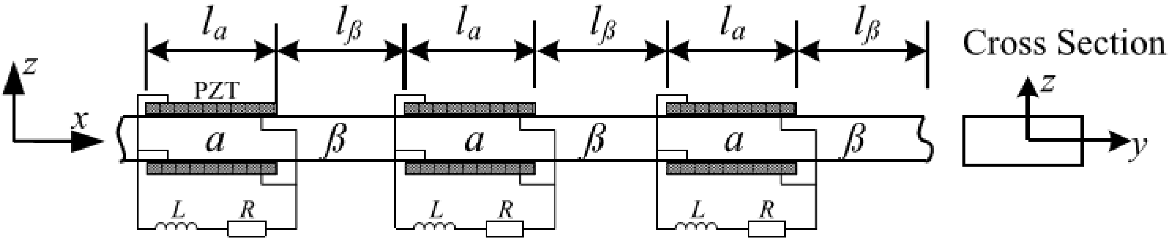

Figure 4.6. Beam with arrays of resonant shunts [163].

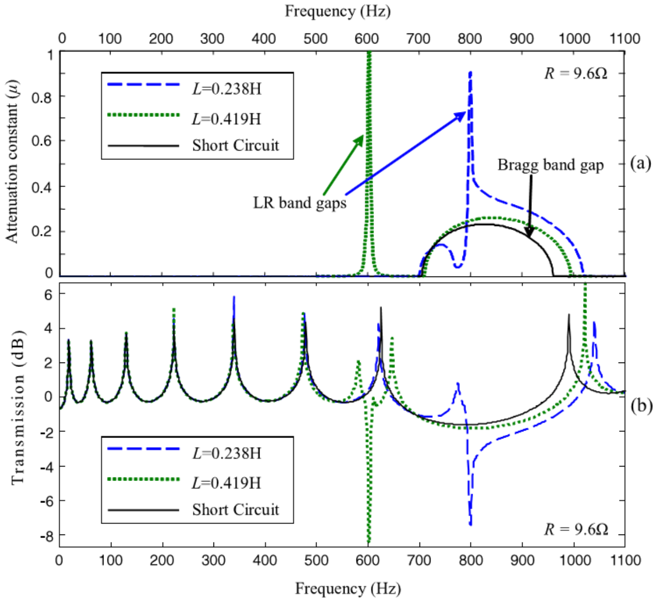

Figure 4.7. Calculated attenuation constants and transmission factor of the one-dimensional phononic crystals composed of an epoxy beam and different arrays of the resonant shunts with R=9.6 Ω [163].

Subsequently, the vibration attenuation achieved by enhanced resonant shunting circuits integrated into the periodic arrays (Figure 4.8) was demonstrated as well [164]. From the comparison of passive resonant shunting circuits, it was shown that the enhanced resonant shunting circuits can evidently increase the attenuations around the locally resonant band gaps (Figure 4.9). Furthermore, wider attenuation frequency range can be obtained by combination with different enhanced resonant shunting circuits (Figure 4.10) since aperiodicity is intentionally induced.

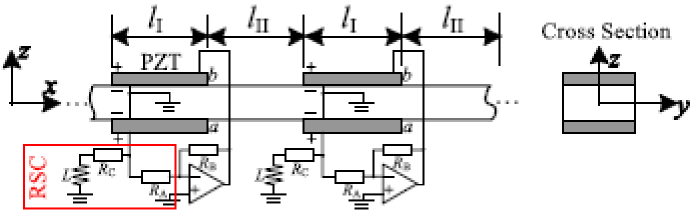

Figure 4.8. Beam with arrays of PZT patches and enhanced resonant shunting circuits [164].

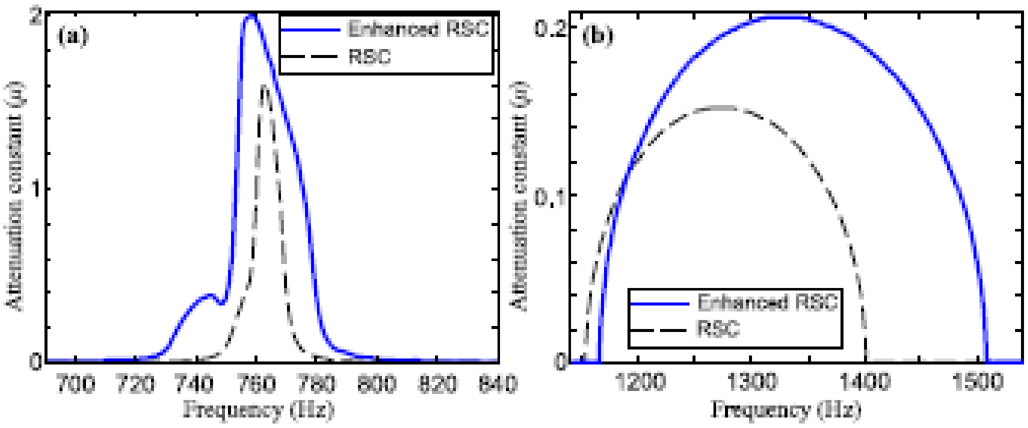

Figure 4.9. Comparison of the calculated attenuation constants of a 1D photonic crystal with RSC (dashed lines) and the other with enhanced RSC (solid lines). The two sub-figures in different frequency ranges correspond to the (a) locally resonant and (b) Bragg scattering band gaps [164].

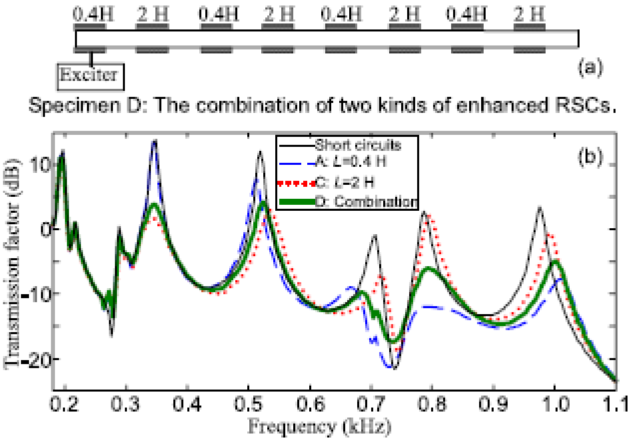

Figure 4.10. (a) Sketch of specimen D where a combination of two kinds of enhanced RSCs is involved. The inductance in half of the RSCs is set as L=0.4 H, while that in the other half is set as L=2H. (b) Measured transmissions [164].

Airoldi and Ruzzene [165] illustrated the wave propagation in beams through periodic multi-branch shunts proposed by Wu [87], which can be tuned to target several vibration modes of the beam. Simulation results obtained by finite element model and experimental measurements showed that the attenuation band can be enlarged by the feasible and effective periodic multi-resonant shunting.

Periodic structures featuring piezoelectric arrays were briefly introduced in this section. Significant wave attenuation can be achieved and the band gaps can be tuned by integrating the passive or active shunting circuits. Although the elastic wave can be reduced by using negative impedance capacitance and/or Antoniou's circuits in lower frequency spectra, the integrated inductance is still relatively larger compared with that used in semi-passive nonlinear SSDI strategy. Hence, in the following part, a nonlinear interfaced periodic structure combining the SSDI technique with periodic bending structures will be proposed. Wave attenuation and damping performance of this periodic structure featuring nonlinear interfaced piezoelectric elements will be further introduced and discussed.

4.2. Theoretical analysis: coupled finite element method and transfer matrix

The detailed principle of the proposed approach for attenuation the wave propagation and responses of the periodic structures by the nonlinear interfaced piezoelectric patches is demonstrated in this part based on the theoretical model coupled finite element method and transfer matrix. The logical ider of this modelling consists of using finite elment method to be able to obtain the transfer matrix of a single unitary cell, which is then used to study the cell combination.

4.2.1. Motion equation of one cell based on finite element method

Generally, the periodic structure fundamentally consists of a number of identical sub-structures or periodic cells as shown in Figure 4.11. For simplicity, only the periodic electromechanical beam with featuring piezoelectric element is considered in this study. However, the proposed strategy can be integrated in other intelligent systems such as electromagnetic systems.

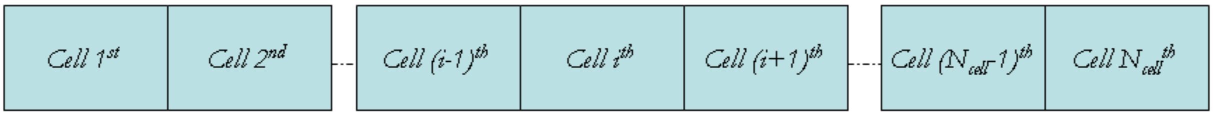

Figure 4.11. Periodic structure.

It is supposed that the periodic structure is constituted by N_{cell} cells and each cell can be divided into n elements. Based on the finite element method, the motion relationships in frequency domain of the i^{th} cell (Figure 4.12) considered as a small Euler-Bernoulli beam can be expressed by

$$\left\{-\omega^2[m]+[k]\right\}\begin{Bmatrix}\tilde{d}_0^{\,i}\\ \vdots\\ \tilde{d}_j^{\,i}\\ \vdots\\ \tilde{d}_n^{\,i}\end{Bmatrix}=[A]\begin{Bmatrix}\tilde{d}_0^{\,i}\\ \vdots\\ \tilde{d}_j^{\,i}\\ \vdots\\ \tilde{d}_n^{\,i}\end{Bmatrix}=\begin{Bmatrix}\tilde{P}_0^{\,i}\\ \vdots\\ \tilde{P}_j^{\,i}\\ \vdots\\ \tilde{P}_n^{\,i}\end{Bmatrix} \tag{4.1}$$

where the superscript i denotes the matrices for the i^{th} cell. $[m]$ is the mass matrix and $[k]$ denotes the stiffness matrix. $\tilde{d}$ is the displacement and slope vector in frequency domain. $\tilde{P}$ refers to the frequency domain force and moment vector. The subscript j (j =0… n) of these vectors denotes the j^{th} element of the cell. ω is the angular frequency.

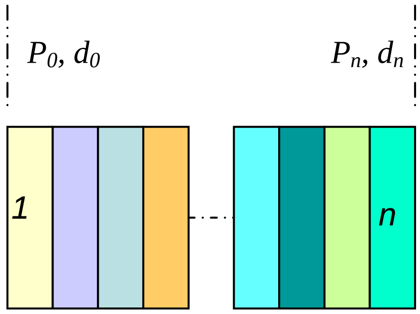

Figure 4.12. Diagram of a single cell.

For the electromechanical cell integrating piezoelectric material, the electric charge is generated between the electrodes and the piezovoltage can be generated due to the piezoelectric effect during the vibration. Thus, the dynamical relationship of the electromechanical cell with piezoelectric patches can be expressed as follows:

$$[A]\begin{Bmatrix}\tilde{d}_0^{\,i}\\ \vdots\\ \tilde{d}_j^{\,i}\\ \vdots\\ \tilde{d}_n^{\,i}\end{Bmatrix}-[B_1]\begin{Bmatrix}\tilde{V}_1^{\,i}\\ \vdots\\ \tilde{V}_{j_p}^{\,i}\\ \vdots\\ \tilde{V}_{np}^{\,i}\end{Bmatrix}=\begin{Bmatrix}\tilde{P}_0^{\,i}\\ \vdots\\ \tilde{P}_j^{\,i}\\ \vdots\\ \tilde{P}_n^{\,i}\end{Bmatrix} \tag{4.2}$$

where the $\tilde{V}_{j_p}$ denotes the voltage in frequency domain of the j_p^{th} piezoelectric patch and *np* is the number of piezoelectric patches in the i^{th} electromechanical cell.

As demonstrated in Chapter 2, the electrical relationship of each piezoelectric patch in open circuit can be expressed as Eq.(2.13). Supposing identical piezoelectric patches are used, thus with the null initial condition, the piezovoltages of the i^{th} electromechanical cell can be written in matrix-vector notation:

$$\left[V^i\right]=\left[B_4\right]\left\{d^i\right\} \tag{4.3}$$

where $\left[B_4\right]$ can be obtained as

$$\left[B_4\right]=b_4\cdot\int_0^l\left[H''\right]dx \text{ with } b_4=-\frac{{t_p}^2 d_{31}}{L_p\left[\varepsilon_{33}^T\left(s_{11}^E+s_{12}^E\right)-2{d_{31}}^2\right]} \tag{4.4}$$

Hence, Eq. (4.2) can be further simplified as

$$\left\{\left[A\right]-\left[B_1\right]\left[B_4\right]\right\}\begin{Bmatrix}\tilde{d}_0^{\,i}\\ \vdots\\ \tilde{d}_j^{\,i}\\ \vdots\\ \tilde{d}_n^{\,i}\end{Bmatrix}=\begin{Bmatrix}\tilde{P}_0^{\,i}\\ \vdots\\ \tilde{P}_j^{\,i}\\ \vdots\\ \tilde{P}_n^{\,i}\end{Bmatrix} \text{ or } \left[A_{open}\right]\begin{Bmatrix}\tilde{d}_0^{\,i}\\ \vdots\\ \tilde{d}_j^{\,i}\\ \vdots\\ \tilde{d}_n^{\,i}\end{Bmatrix}=\begin{Bmatrix}\tilde{P}_0^{\,i}\\ \vdots\\ \tilde{P}_j^{\,i}\\ \vdots\\ \tilde{P}_n^{\,i}\end{Bmatrix} \tag{4.5}$$

As the piezoelectric patches are all in short circuit, the dynamical relations of i^{th} electromechanical cell is same as Eq. (4.1), namely, $\left[A_{short}\right]=\left[A\right]$.

It is well known that the converted electrical energy can be dissipated through shunting circuits composed of passive electrical components (resistor, inductor and capacitor). Hence, if the j_p^{th} piezoelectric patch piezoelectric patch is connected to a resistance R_{j_p}, according to Eq.(2.9) the electrical relationship for the investigated electromechanical cell can be expressed by

$$\left\{\tilde{V}_p^{\,i}\right\}=\left\{\left[I\right]-j\omega diag\left(\left[\mathrm{R}_1 \quad \ldots \quad \mathrm{R}_{j_p} \quad \ldots \quad \mathrm{R}_{np}\right]\right)\left[B_3\right]\right\}^{-1}\cdot j\omega diag\left(\left[\mathrm{R}_1 \quad \ldots \quad \mathrm{R}_{j_p} \quad \ldots \quad \mathrm{R}_{np}\right]\right)\left[B_2\right]\left\{\tilde{d}^i\right\} \tag{4.6}$$

When same the resistors are integrated, the above equation can be simplified as

$$\left\{\tilde{V}^i\right\}=\left(\left[I\right]-\mathrm{R}j\omega\left[B_3\right]\right)^{-1}\cdot j\omega\mathrm{R}\left[B_2\right]\left\{\tilde{d}^i\right\}=\left[B_5\right]\left\{\tilde{d}^i\right\} \tag{4.7}$$

Thus, the motion equation yields

$$\left\{\left[A\right]-\left[B_1\right]\left[B_5\right]\right\}\begin{Bmatrix}\tilde{d}_0^{\,i}\\ \vdots\\ \tilde{d}_j^{\,i}\\ \vdots\\ \tilde{d}_n^{\,i}\end{Bmatrix}=\begin{Bmatrix}\tilde{P}_0^{\,i}\\ \vdots\\ \tilde{P}_j^{\,i}\\ \vdots\\ \tilde{P}_n^{\,i}\end{Bmatrix} \text{ or } \left[A_{passive}\right]\begin{Bmatrix}\tilde{d}_0^{\,i}\\ \vdots\\ \tilde{d}_j^{\,i}\\ \vdots\\ \tilde{d}_n^{\,i}\end{Bmatrix}=\begin{Bmatrix}\tilde{P}_0^{\,i}\\ \vdots\\ \tilde{P}_j^{\,i}\\ \vdots\\ \tilde{P}_n^{\,i}\end{Bmatrix} \tag{4.8}$$

Once the optimal resistance given as Eq. (3.16) is connected, the Eq. (4.9) is valid.

$$\left[B_5\right]_{opt} = \frac{-j\left[B_3\right]^{-1}\left[B_2\right]}{\left(1+j\right)} \tag{4.9}$$

As the proposed nonlinear interfaced periodic cell is implemented, namely combining the electromechanical periodic cell with the semi-passive nonlinear technique SSDI, the piezovoltage of each piezoelectric patch under harmonic excitation can be decomposed as the sum of two functions (one is proportional to the displacement and the other is a crenel function h_{j_p}). Thus, the following relationship holds

$$\left[V^i\right] = \left[B_4\right]\left(\left\{d^i\right\} + \left\{h^i\right\}\right) \tag{4.10}$$

Taking a similar approach than presented in [126] by the approximation of first harmonic yields the crenel function can be written as

$$\left\{h^i\right\} = \frac{4j}{\pi} diag\left(\frac{1+\gamma_{j_p}}{1-\gamma_{j_p}}\right)\left\{d^i\right\} \tag{4.11}$$

Thus, the piezovoltages of the i^{th} electromechanical cell yields Eq. (4.12) under monochromatic excitation:

$$\left[V^i\right] = \left[B_4\right]\left(\left[I\right] + \frac{4j}{\pi} diag\left(\frac{1+\gamma_{j_p}}{1-\gamma_{j_p}}\right)\right)\left\{d^i\right\} = \left[B_6\right]\left\{d^i\right\} \tag{4.12}$$

leading to the motion equation as:

$$\left\{\left[A\right]-\left[B_1\right]\left[B_6\right]\right\}\begin{Bmatrix}\tilde{d}_0^{\,i}\\ \vdots \\ \tilde{d}_j^{\,i} \\ \vdots \\ \tilde{d}_n^{\,i}\end{Bmatrix} = \begin{Bmatrix}\tilde{P}_0^{\,i}\\ \vdots \\ \tilde{P}_j^{\,i} \\ \vdots \\ \tilde{P}_n^{\,i}\end{Bmatrix} \text{ or } \left[A_{ssdi}\right]\begin{Bmatrix}\tilde{d}_0^{\,i}\\ \vdots \\ \tilde{d}_j^{\,i} \\ \vdots \\ \tilde{d}_n^{\,i}\end{Bmatrix} = \begin{Bmatrix}\tilde{P}_0^{\,i}\\ \vdots \\ \tilde{P}_j^{\,i} \\ \vdots \\ \tilde{P}_n^{\,i}\end{Bmatrix} \tag{4.13}$$

4.2.2. Transfer matrix between periodic cells

Once the dynamical relationship of one electromechanical periodic cell obtained in the form:

$$\left[A_{condition}\right]\left\{\tilde{d}^i\right\} = \left\{\tilde{P}^i\right\} \tag{4.14}$$

with $\left[A_{condition}\right]$ equals to $\left[A_{short}\right]$, $\left[A_{open}\right]$, $\left[A_{passive}\right]$ or $\left[A_{ssdi}\right]$ according to the electrical conditions (short circuit, open circuit, resistive shunt circuit or synchronized switch), the transfer matrix between the periodic cells can be achieved as follows.

Eq. (4.14) can be rearranged for separation of the extreme vectors and internal vectors:

$$\begin{bmatrix} a_{00} & a_{0n} & a_{0j} \\ a_{n0} & a_{nn} & a_{nj} \\ a_{j0} & a_{jn} & a_{jj} \end{bmatrix} \begin{Bmatrix} \tilde{d}_0^{\,i} \\ \tilde{d}_n^{\,i} \\ \tilde{d}_j^{\,i} \end{Bmatrix} = \begin{Bmatrix} \tilde{P}_0^{\,i} \\ \tilde{P}_n^{\,i} \\ \tilde{P}_j^{\,i} \end{Bmatrix} \tag{4.15}$$

with the matrices a_{kk} being part of the matrix $A_{condition}$

$$A_{condition} = \begin{bmatrix} a_{00} & a_{0j} & a_{0n} \\ a_{j0} & a_{jj} & a_{jn} \\ a_{n0} & a_{nj} & a_{nn} \end{bmatrix} \tag{4.16}$$

Considering there is no external loads (moment and force) applied within the cell, namely,

$$\left\{\tilde{P}_j^{\,i}\right\} = 0, j \in [1 \ldots n-1] \tag{4.17}$$

the expression of the extreme displacement and slope vectors as the function of the extreme force and moment vectors yields, according to Guyan's reduction,:

$$\begin{bmatrix} a_{00} - a_{0j} a_{jj}^{-1} a_{j0} & a_{0n} - a_{0j} a_{jj}^{-1} a_{jn} \\ a_{n0} - a_{nj} a_{jj}^{-1} a_{j0} & a_{nn} - a_{nj} a_{jj}^{-1} a_{jn} \end{bmatrix} \begin{Bmatrix} \tilde{d}_0^{\,i} \\ \tilde{d}_n^{\,i} \end{Bmatrix} = \begin{bmatrix} \alpha_{11} & \alpha_{12} \\ \alpha_{21} & \alpha_{22} \end{bmatrix} \begin{Bmatrix} \tilde{d}_0^{\,i} \\ \tilde{d}_n^{\,i} \end{Bmatrix} = \begin{Bmatrix} \tilde{P}_0^{\,i} \\ \tilde{P}_n^{\,i} \end{Bmatrix} \tag{4.18}$$

Hence, the relationships between the vectors of the right side and left side can be obtained by re-arranging the Eq. (4.18), yielding

$$\begin{bmatrix} -\alpha_{12}^{-1}\alpha_{11} & \alpha_{12}^{-1} \\ \alpha_{21} - \alpha_{22}\alpha_{12}^{-1}\alpha_{11} & \alpha_{22}\alpha_{12}^{-1} \end{bmatrix} \begin{Bmatrix} \tilde{d}_0^{\,i} \\ \tilde{P}_0^{\,i} \end{Bmatrix} = \begin{Bmatrix} \tilde{d}_n^{\,i} \\ \tilde{P}_n^{\,i} \end{Bmatrix} \tag{4.19}$$

Since the displacement and slope vectors are continuous between cells and the force and moment exerted on the right side of the i^{th} electromechanical cell is opposite to those exerted on the left side of the $(i+1)^{th}$ electromechanical cell, it allows formulating the transfer matrix between cells such as:

$$\begin{bmatrix} -\alpha_{12}^{-1}\alpha_{11} & \alpha_{12}^{-1} \\ -\alpha_{21} + \alpha_{22}\alpha_{12}^{-1}\alpha_{11} & -\alpha_{22}\alpha_{12}^{-1} \end{bmatrix} \begin{Bmatrix} \tilde{d}_0^{\,i} \\ \tilde{P}_0^{\,i} \end{Bmatrix} = \begin{Bmatrix} \tilde{d}_n^{\,i} \\ \tilde{P}_n^{\,i} \end{Bmatrix} = [T] \begin{Bmatrix} \tilde{d}_0^{\,i} \\ \tilde{P}_0^{\,i} \end{Bmatrix} \tag{4.20}$$

where

$$[T] = \begin{bmatrix} t_{11} & t_{12} \\ t_{21} & t_{22} \end{bmatrix} \tag{4.21}$$

denotes the transfer matrix between cells.

In order to have a clear view of the propagation aspect within the medium, each eigenvalue λ can be written as

$$\lambda_i = e^{jk_{bi}L}, i \in [1,2,3,4] \tag{4.22}$$

with L the cell length and k_b the complex wavenumber.

Four waves can be identified as follow according to the values of the complex wave number:

•Evanescent wave travelling in the left direction (k_{bi} is pure imaginary and it is negative)

•Evanescent wave travelling in the right direction (k_{bi} is pure imaginary and it is positive)

•Propagating wave travelling in the left direction (k_{bi} is complex with its real part unequal to zero and it is negative)

•Propagating wave travelling in the right direction (k_{bi} is complex with its real part unequal to zero and it is positive)

In order to have a clear view of the kind of wave, the following notation is used for eigenvalue:

$$\lambda = e^{\eta + j\delta} \tag{4.23}$$

where $\eta + j\delta$ is the propagation constant with η denoting the logarithmic decay of the vectors and δ denoting the phase difference between cells.

4.3. Theoretical analysis and experimental validation

In this section, the comparative wave attenuation performance of the electromechanical periodic structure using either resistive shunting or the nonlinear SSDI interface will be discussed. The global relationships of the investigated periodic bending beam under different boundary conditions will be briefly introduced. In order to validate the theoretical analyses, corresponding experiments are conducted on a clamped-clamped beam.

4.3.1. Preliminary discussion of wave attenuation performance

Wave attenuation performance of an electromechanical periodic cell as shown in Figure 4.13 is demonstrated based on the finite element method with the parameters given in Table 4.1 and Table 4.2 which are same as those in the experimental section 4.3.3.

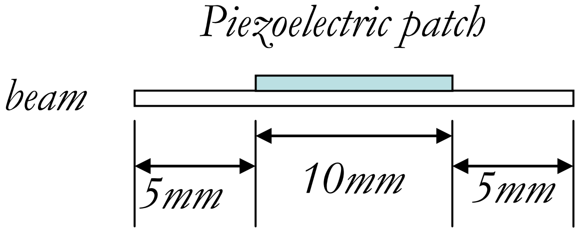

Figure 4.13. Investigated electromechanical periodic cell.

In order to obtain the band figure, the structural damping matrix is not considered in this subsection. Only considering the positive direction, the real part and imaginary part of propagation constant of the investigated electromechanical periodic cell in different cases (open, resistive shunting circuit and nonlinear SSDI interfaced cases) are plotted in Figure 4.14. For comparative purpose, the corresponding results of evanescent wave are given in Figure 4.15.

Table 4.1. Dimensional and material properties of beam.

Young's modulus	$Y_b = 190\times10^9\,Pa$	Poisson's ratio	$\nu_b = 0.21$	density	$\rho_b = 7875\,kg/m^3$
length	$L_b = 20\times10^{-3}\,m$	width	$w_b = 40\times10^{-3}\,m$	thickness	$t_b = 0.61\times10^{-3}\,m$

Table 4.2. Dimensional and material properties of piezoelectric patch.

Compliance in short circuit	$s_{11}^E = 10.66\times10^{-12}\,m^2/N$ $s_{12}^E = -3.34\times10^{-12}\,m^2/N$	length	$L_p = 10\times10^{-3}\,m$
Charge coefficient	$d_{31} = -108\times10^{-12}\,m/V$	thickness	$t_p = 0.6\times10^{-3}\,m$
Relative dielectric constant	$\varepsilon_{33}^T/\varepsilon_0 = 1150$	density	$\rho_p = 7650\,kg/m^3$

It can be found from the given results that with the periodic configuration, the electromechanical periodic structure has the capability of filtering the waves in some frequency spectra within stop bands. Even though the electromechanical periodic cell with piezoelectric patch in open circuit operates as purely mechanical periodic structure (namely without smart materials and energy conversion), the wave attenuation ability is superior to that in short circuit case. For implementing the resistive shunting, optimal resistance varied with the external angular frequency and expressed by Eq.(4.9) is used. As shown in Figure 4.14, propagating wave is slightly attenuated within pass bands as the resistive shunt circuit is employed since in this case the converted electrical energy is dissipated. Superior wave attenuation is achieved as the nonlinear switching interface is featured. From the comparison of the results obtained in other cases, it can be found that not only the magnitude of the logarithmic decay is much higher within the stop bands, but stop bands also appear over a much wider frequency band almost containing the whole frequency spectrum. This phenomenon is attributed to the adaptive SSDI technique which can artificially increase the coupling coefficient by nonlinear voltage inversion process. Meanwhile, phase constant δ is not significant affected by the nonlinear switching interface as shown in Figure 4.14 (b). It is also interesting to note that although the η of the evanescent wave is reduced by featuring the switching interface as shown in Figure 4.15 (a), it is still much higher compared to the propagating wave.

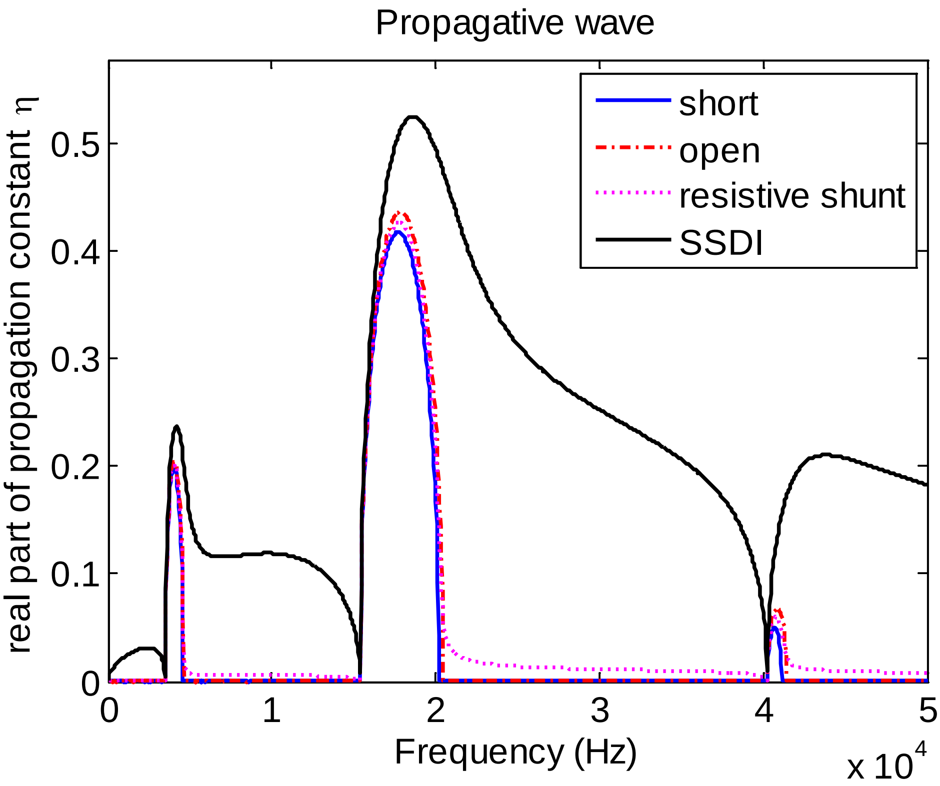

(a)

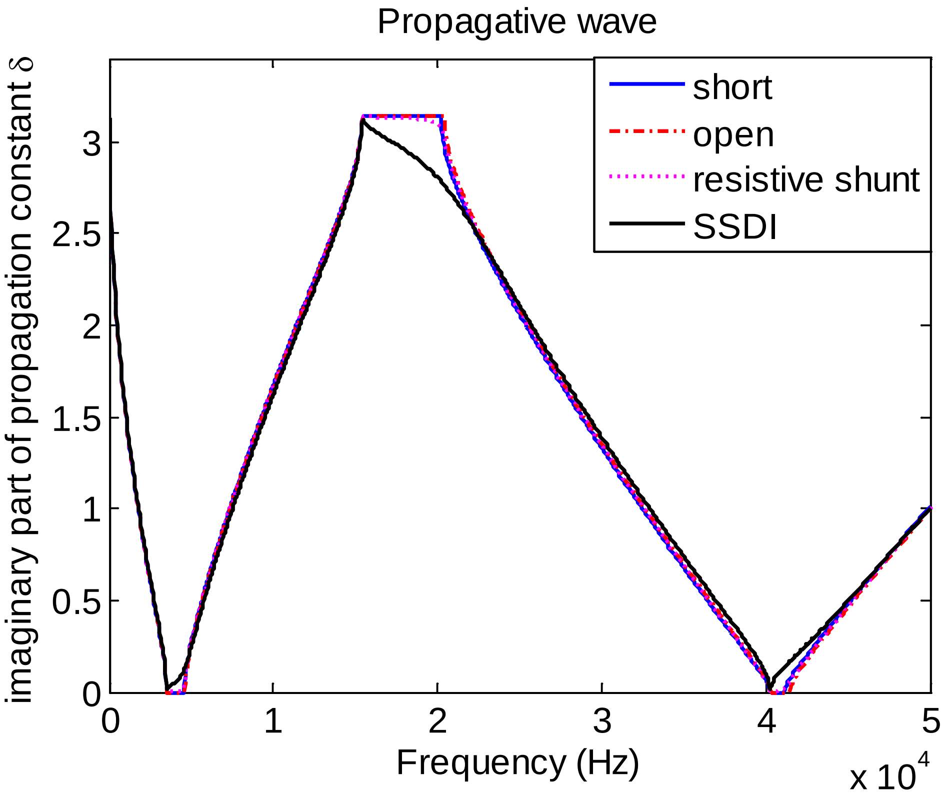

(b)

Figure 4.14. Real part (a) and imaginary part (b) of propagation constant of propagating wave.

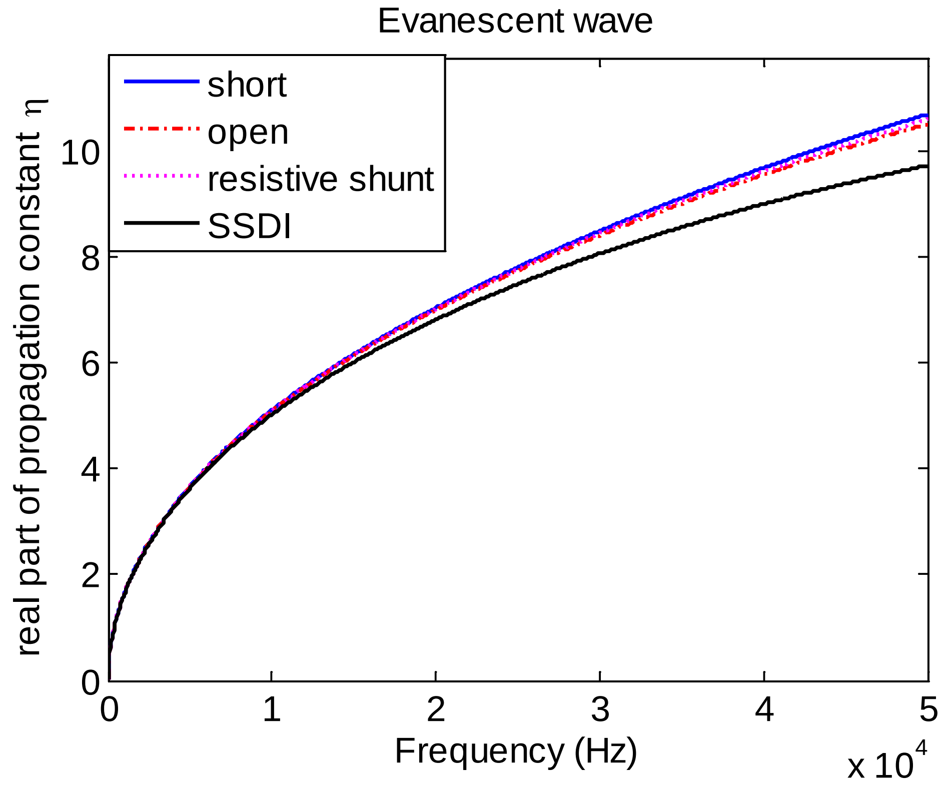

(a)

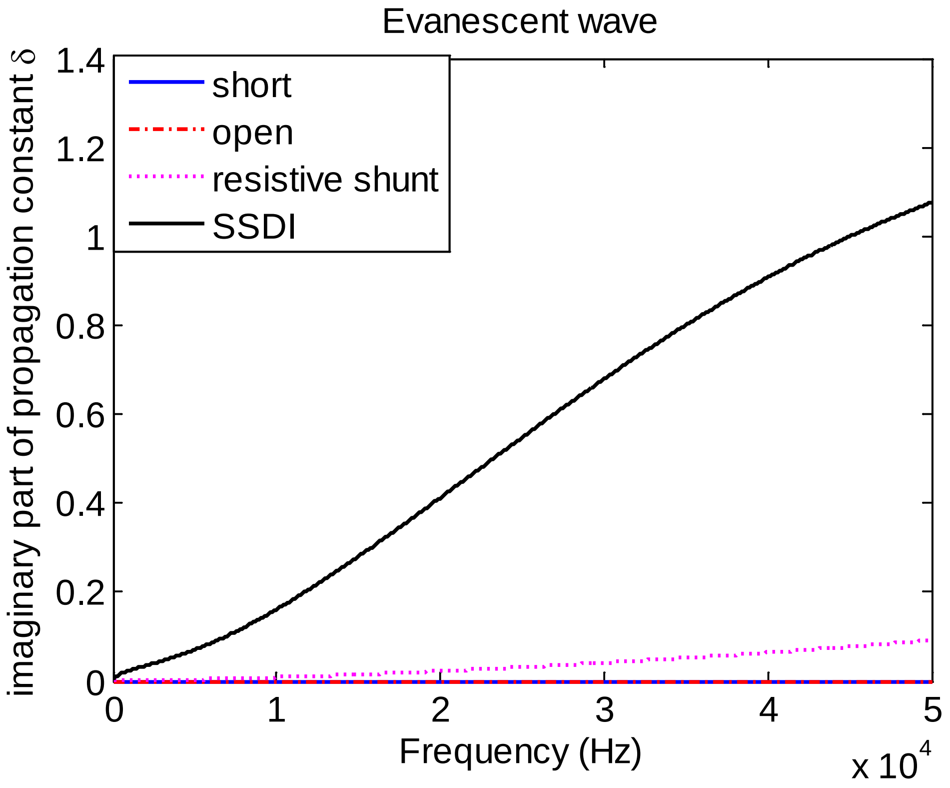

(b)

Figure 4.15. Real part (a) and imaginary part (b) of evanescent wave.

In order to investigate the effect of voltage inversion process for wave attenuation, the logarithmic decay obtained under different inversion coefficients is exhibited in Figure 4.16. From the results, it can be concluded that the logarithmic decay is increasing as the voltage inversion coefficient increases which demonstrates that the elastic waves can be much more effectively attenuated with higher inversion coefficient.

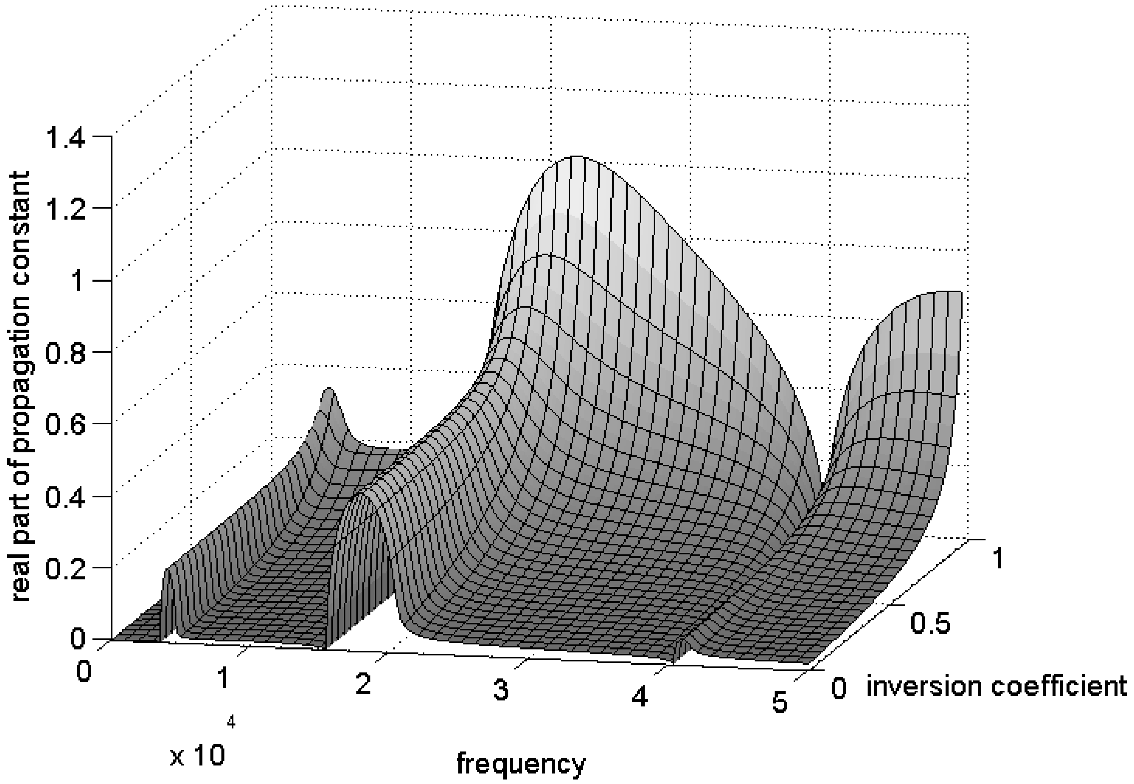

Figure 4.16. Real part of propagation constant varied with inversion coefficient.

4.3.2. Global relationships under different boundary conditions

This subsection proposes to examine the case of an electromechanical periodic structure featuring piezoelectric materials with fixed boundary conditions (clamped-clamped and cantilever cases). Global relationships under the interested boundary condition will be briefly introduced for obtaining the corresponding responses based on transfer matrix method.

Clamped-clamped case

It is assumed here that the considered structure is a clamped-clamped electromechanical periodic beam consisting of N_{cell} cells and the external force F is applied between the N^{th} and the $(N+1)^{th}$ cells. Under these boundary conditions, the fixed ends feature a zero vector of displacement and slope and extert external force and moment on the structure as well, respectively noted as $\tilde{P}_0=\begin{bmatrix}\tilde{F}_0 & \tilde{M}_0\end{bmatrix}^t$ and $\tilde{P}_{N_{cell}}=\begin{bmatrix}\tilde{F}_{N_{cell}} & \tilde{M}_{N_{cell}}\end{bmatrix}^t$ with the vector $\tilde{P}_i$ of the applied force $\tilde{F}_i$ and moment $\tilde{M}_i$, where the subscripts 0 and N_{cell} respectively denote the left and right ends of the electromechanical periodic structure. According to the linearity of the system, the displacement, slope, force and moment vectors at any point i may be obtained from:

$$\begin{Bmatrix}\tilde{d}_i\\ \tilde{P}_i\end{Bmatrix}=[T]^i\begin{Bmatrix}0\\ \tilde{P}_0\end{Bmatrix}+[T]^{(i-N)}\begin{Bmatrix}0\\ \tilde{P}_e\end{Bmatrix} \tag{4.24}$$

with $\tilde{P}_e=\begin{bmatrix}F & 0\end{bmatrix}^t$ (i.e. no external moment is exerted on the electromechanical periodic beam) and the boundary condition $\tilde{d}_0=0$.

Based on the above equation, the vectors of the right end can be obtained according to the vector of the left end and the external vector $\tilde{P}_e$ with boundary condition $\tilde{d}_{N_{cell}}=0$, which holds the form as:

$$\begin{Bmatrix}0\\ \tilde{P}_{N_{cell}}\end{Bmatrix}=[T]^{N_{cell}}\begin{Bmatrix}0\\ \tilde{P}_0\end{Bmatrix}+[T]^{(N_{cell}-N)}\begin{Bmatrix}0\\ \tilde{P}_e\end{Bmatrix} \tag{4.25}$$

Hence, solving Eq. (4.25), the force and moment vectors of the fixed ends can be written as a function of the external force and moment vector as:

$$\begin{aligned}\tilde{P}_0&=-\left(t_{12}^{\{N_{cell}\}}\right)^{-1}t_{12}^{\{N_{cell}-N\}}\tilde{P}_e\\ \tilde{P}_{N_{cell}}&=\left[-t_{22}^{\{N_{cell}\}}\left(t_{12}^{\{N_{cell}\}}\right)^{-1}t_{12}^{\{N_{cell}-N\}}+t_{22}^{\{N_{cell}-N\}}\right]\tilde{P}_e\end{aligned} \tag{4.26}$$

where the matrices $t_{ij}^{\{N_{cell}\}}$ and $t_{ij}^{\{N_{cell}-N\}}$ are the 2 by 2 constitutive matrices of $T^{N_{cell}}$ and $T^{(N_{cell}-N)}$ respectively expressed as:

$$\begin{aligned}T^{N_{cell}}&=\begin{bmatrix}t_{11}^{\{N_{cell}\}} & t_{12}^{\{N_{cell}\}}\\ t_{21}^{\{N_{cell}\}} & t_{22}^{\{N_{cell}\}}\end{bmatrix}\\ T^{\{N_{cell}-N\}}&=\begin{bmatrix}t_{11}^{\{N_{cell}-N\}} & t_{12}^{\{N_{cell}-N\}}\\ t_{21}^{\{N_{cell}-N\}} & t_{22}^{\{N_{cell}-N\}}\end{bmatrix}\end{aligned} \tag{4.27}$$

Cantilever case

For the cantilever case, the general relationship given as Eq. (4.24) is still valid, with the boundary condition $\tilde{d}_0 = 0$ resolving in a similar way as demonstrated in the clamped-clamped case, the vectors at the point where external vector applied can be expressed as

$$\begin{Bmatrix} \tilde{d}_N \\ \tilde{P}_N \end{Bmatrix} = [T]^N \begin{Bmatrix} 0 \\ \tilde{P}_0 \end{Bmatrix} + \begin{Bmatrix} 0 \\ \tilde{P}_e \end{Bmatrix} \tag{4.28}$$

Since the vectors of the right side of this case can be obtained by

$$\begin{Bmatrix} \tilde{d}_{N_{cell}} \\ \tilde{P}_{N_{cell}} \end{Bmatrix} = [T]^{\{N_{cell}-N\}} \begin{Bmatrix} \tilde{d}_N \\ \tilde{P}_N \end{Bmatrix} \tag{4.29}$$

with $\tilde{P}_{N_{cell}} = 0$, it yields

$$\begin{gathered} \tilde{P}_0 = -\left(t_{21}^{\{N_{cell}-N\}} t_{12}^{\{N\}} + t_{22}^{\{N_{cell}-N\}} t_{22}^{\{N\}} \right)^{-1} \left(t_{22}^{\{N_{cell}-N\}} \right) \tilde{P}_e \\ \tilde{d}_{N_{cell}} = \left\{ -\left(t_{11}^{\{N_{cell}-N\}} t_{12}^{\{N\}} + t_{12}^{\{N_{cell}-N\}} t_{22}^{\{N\}} \right) \left(t_{21}^{\{N_{cell}-N\}} t_{12}^{\{N\}} + t_{22}^{\{N_{cell}-N\}} t_{22}^{\{N\}} \right)^{-1} \left(t_{22}^{\{N_{cell}-N\}} \right) + t_{12}^{\{N_{cell}-N\}} \right\} \tilde{P}_e \end{gathered} \tag{4.30}$$

In this section, the dynamical responses based on transfer matrix method under different boundary conditions as clamped-clamped case and cantilever case are briefly introduced. General equation for obtaining the vectors of interested points of the electromechanical periodic structure is given. Based on the above formulation, corresponding vectors of the targeted cells can be obtained easily. In order to validate the wave attenuation discussed in the previous subsection, experiments are carried out on a clamped-clamped electromechanical beam with four investigated cells. The details will be explained in the following subsection.

4.3.3. Experimental validation

Aiming at validating the previously exposed principles, experiments are conducted on a clamped-clamped periodic beam consisting of 4 electromechanical periodic cells as depicted in Figure 4.17. The dimension and material properties of the beam and piezoelectric inserts are summarized in Table 4.1 and Table 4.20.

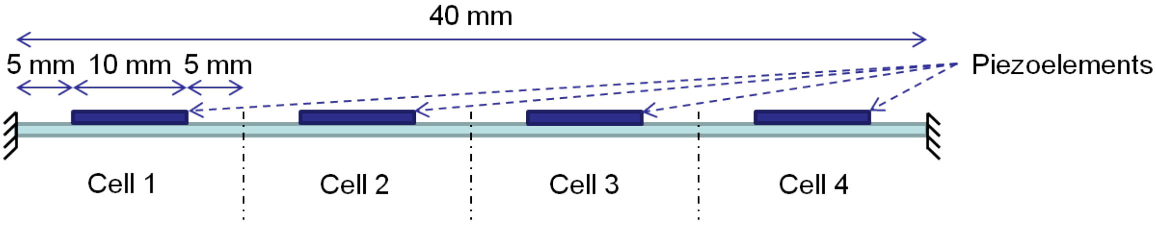

Figure 4.17. Experimental sample of electromechanical periodic structure.

The test set-up shown in Figure 4.18 consists of the electromechanical periodic beam excited at approximately a quarter of its length by an electromagnet (for applying external force) driven by a function generator through a power amplifier. Switching command signal is obtained from a dSpace system for controlling a dedicated switching circuit although the latter can be made self-powered as introduced in literature [116] and [117]. Additionally, a laser vibrometer is employed for monitoring the displacement at three quarter of the beam length.

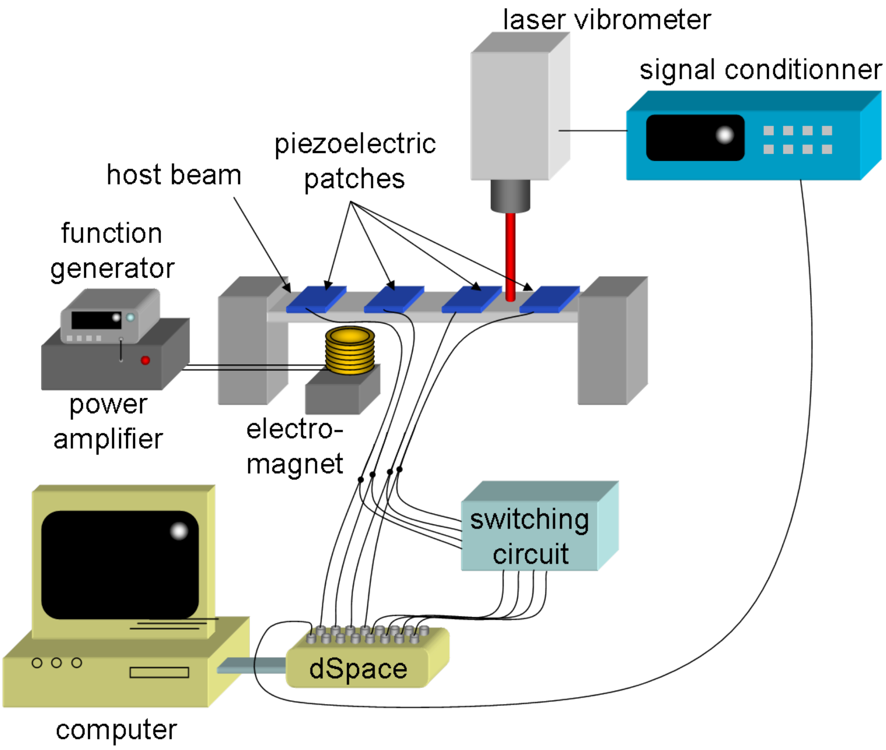

Figure 4.18. Experimental setup for electromechanical periodic structure.

For preliminary investigation, the Rayleigh damping which is proportional to the mass matrix and stiffness matrix is considered for modelling as demonstrated in previous chapters. In order to match the damping coefficient obtained in experiments, the damping coefficients are deliberately chosen as summarized in

Table 4.3. Voltage inversion coefficient γ is equal to 0.4, which is quite low compared with the classical values reported in literature, but which is explained the use of the digital dSpace interface that has a finite and discrete time step, thus not allowing controlling finely the inversion time, while for controlling the high frequency mode, the inversion time has to be quite short.

Table 4.3. Damping coefficients used for modelling the electromechanical periodic structure.

$\beta_1 = 4$	$\beta_2 = 1.5 \times 10^{-6}$

For comparison purpose, displacement magnitudes with piezoelectric inserts in open circuit, connected to resistive shunting (with the resistance chosen as the optimal value for the first bending mode) and SSDI switching circuit are experimentally measured and depicted in Figure 4.19. The attenuation obtained in each case for damping the first three modes is summarized in Table 4.4. Corresponding responses obtained by simulation are exposed by Figure 4.20 and the simulated attenuation is listed in Table 4.5.

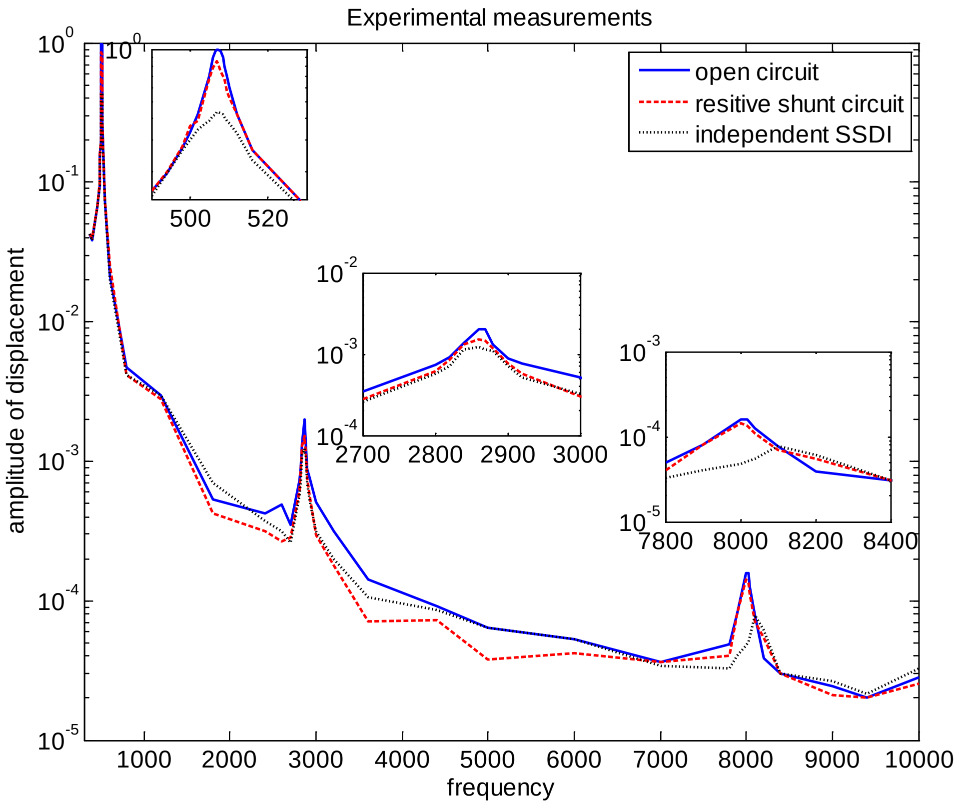

Figure 4.19. Experimental measurements of clamped-clamped electromechanical periodic structure.

Table 4.4. Attenuation obtained in the experiments of electromechanical periodic structure.

	Resistive shunting circuit	SSDI
1st mode	-1.41 *dB*	-7.13 *dB*
2nd mode	-2.43 *dB*	-4.28 *dB*
3rd mode	-0.92 *dB*	-5.26 *dB*

Globally, a good agreement can be found between the experimental measurements and the theoretical analyses, although the second mode is significantly lower in the experiments, which can be attributed to the external force applied by electromagnet which is not exactly located between the interfaces of the two cells and can not be exactly seemed as a point force as in the simulation.

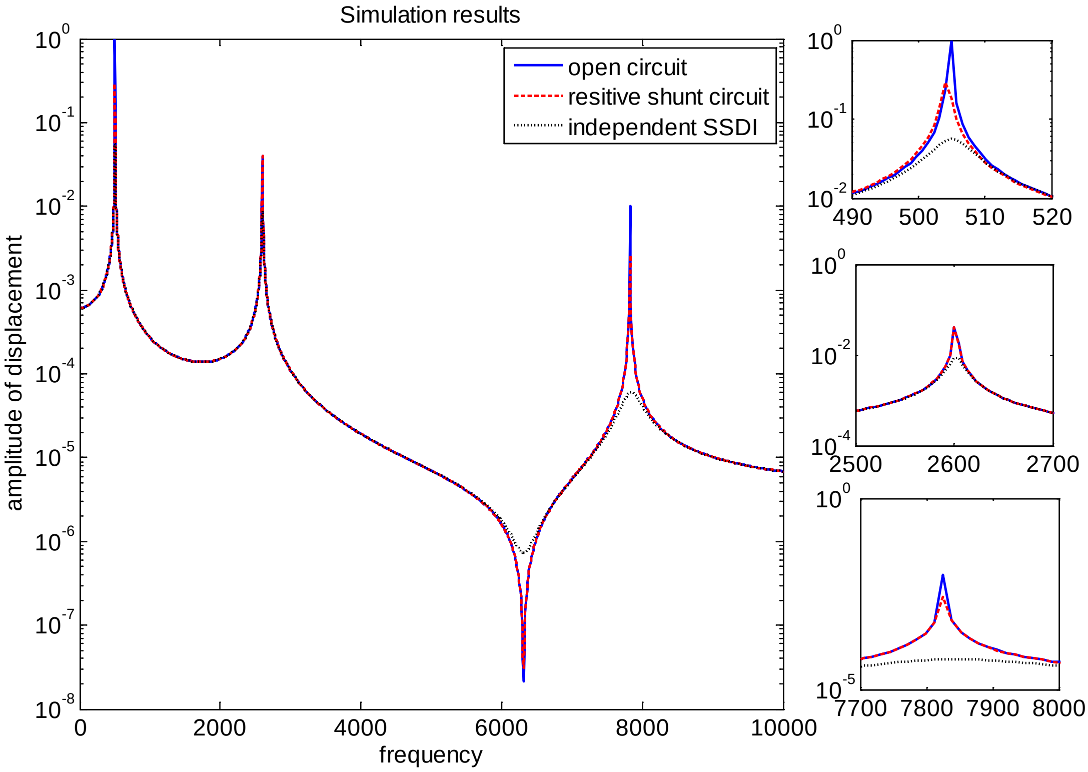

Figure 4.20. Simulation results of clamped-clamped electromechanical periodic structure.

Table 4.5. Attenuation obtained in the simulation of electromechanical periodic structure.

	Resistive shunting circuit	SSDI
The 1st mode	-2.67 *dB*	-9.39 *dB*
The 2nd mode	-0.11 *dB*	-1.48 *dB*
The 3rd mode	-0.09 *dB*	-3.24 *dB*

Relatively speaking, the damping performance summarized in Table 4.4 and Table 4.5 shows good agreement between theoretical and experimental results, except for the better performance of the resistive shunt for the second mode in the experiment which may be due to the higher mechanical quality factor while in the theoretical investigation it is assumed lower based on Rayleigh damping law. Moreover, since the parameters as the capacitances of the piezoelectric patches and the inversion coefficient in each switching circuit are not exactly same, aperiodicity of the structure will be induced due to the differences between cells, which allows a better damping effectiveness in the experiments. Furthermore, superior performance of the nonlinear switching interface for providing higher damping along a larger bandwidth is confirmed.

In this section, the wave attenuation of an electromechanical periodic cell in the open circuit, connected to resistive shunt and featuring the proposed nonlinear switching interface is discussed. Corresponding results shown that with the nonlinear SSDI technique, the propagating wave can be effectively attenuated in a wider frequency bands. To obtain the dynamical responses based on the transfer matrix method, the general relationships between periodic cells under different boundary conditions are briefly introduced. Experiments are carried out for validating the effective damping performance of the proposed nonlinear periodic structure. From the comparison results, it can be further confirmed the periodic nonlinear switching interface can effectively attenuate the vibration.

4.4. Discussion and extensions

Based on the previous demonstration, electromechanical periodic structures which are capable of spatially filtering waves within some frequency bands can be further investigated. Although in this chapter, only a clamped-clamped electromechanical periodic beam is experimentally studied, it can be extended to other boundary conditions or other kind of structure (such as plates [158][161][162]) for effectively attenuating the elastic waves and damping the vibration since the nonlinear SSDI technique is an adaptive method which is not restricted to boundary conditions, frequency bands and kind of structure . Future works would be focused as follows.

4.4.1. Periodic structure with interconnection between cells

In this part, a particular emphasis is put on the possibility of interconnecting the electrical parts as well.Wave attenuation and damping performance of periodic structure with electrical interconnection between cells (Figure 4.21) can be further investigated.

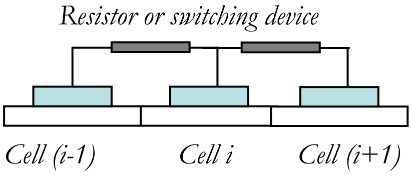

Figure 4.21. Periodic structure with interconnection between cells.

As the adjacent cells are connected through a resistance *R*, then the following relationships hold:

$$I_i + I_p = I_{i+1} \tag{4.31}$$

$$V_p = V_{i+1} \tag{4.32}$$

$$V_i = V_p + RI_i \tag{4.33}$$

Inserting $I_p = [B_2]\{\dot{d}^i\} + [B_3]\dot{V}_{i+1}$ into Eq.(4.31), it yields

$$I_i + [B_2]\{\dot{d}^i\} + [B_3]\dot{V}_{i+1} = I_{i+1} \tag{4.34}$$

Since Eq. (4.33)can be rewritten as

$$\dot{V}_i - R\dot{I}_i = \dot{V}_{i+1}, \tag{4.35}$$

inserting it into the Eq. (4.34), the current flowing from the i^{th} cell can be further expressed by

$$I_{i+1} = I_i + [B_2]\{\dot{d}^i\} + [B_3]\dot{V}_i - R[B_3]\dot{I}_i \tag{4.36}$$

Then, the electrical relationships between two adjacent cells can be obtained as:

$$\begin{Bmatrix} V_{i+1} \\ I_{i+1} \end{Bmatrix} = \begin{bmatrix} 1 & -R \\ 0 & 1 \end{bmatrix} \begin{Bmatrix} V_i \\ I_i \end{Bmatrix} + \begin{bmatrix} 0 & 0 \\ [B_3] & -R[B_3] \end{bmatrix} \begin{Bmatrix} \dot{V}_i \\ \dot{I}_i \end{Bmatrix} + \begin{Bmatrix} 0 \\ [B_2] \end{Bmatrix} \{\dot{d}^i\} \tag{4.37}$$

and the corresponding electrical responses in frequency domain are given by:

$$\begin{Bmatrix} \tilde{V}_{i+1} \\ \tilde{I}_{i+1} \end{Bmatrix} = \begin{bmatrix} 1 & -R \\ j\omega[B_3] & 1 - j\omega R[B_3] \end{bmatrix} \begin{Bmatrix} \tilde{V}_i \\ \tilde{I}_i \end{Bmatrix} + \begin{Bmatrix} 0 \\ j\omega[B_2] \end{Bmatrix} \{\tilde{d}^i\} \tag{4.38}$$

On the basis of the motion equation (Eq. (4.2)) and electrical equations, the dynamical responses for the interconnected electromechanical periodic cells can be summarized as:

$$\begin{Bmatrix} \{\tilde{P}^i\} \\ \tilde{V}_{i+1} \\ \tilde{I}_{i+1} \end{Bmatrix} = \begin{bmatrix} [A] & -[B_1] & R[B_1] \\ 0 & 1 & -R \\ j\omega[B_2] & j\omega[B_3] & 1 - j\omega R[B_3] \end{bmatrix} \begin{Bmatrix} \{\tilde{d}^i\} \\ \tilde{V}_i \\ \tilde{I}_i \end{Bmatrix} \tag{4.39}$$

For the case of interconnecting by nonlinear switching device, the resistance *R* can be replaced by the global impedance under first harmonic assumption of the switching circuit to obtain the dynamical relationships between cells. With these relationships, wave attenuation and damping performance of the interconnected electromechanical periodic cell can be further investigated.

In order to obtain the global impedance in the case of interconnection with SSDI switching device, the electrical relationships are derived as follows on the basis of Norton theorem. Since the parameters of the periodic cells are identical, introducing the clamped capacitance of each piezoelectric patch C_0, the equivalent circuit shown in Figure 4.23 can be used to represent the connection shown in Figure 4.22.

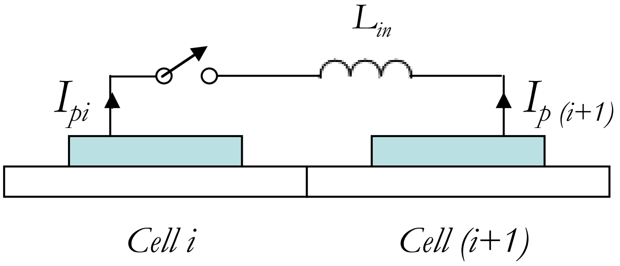

Figure 4.22. Periodic structure with nonlinear switching interconnections.

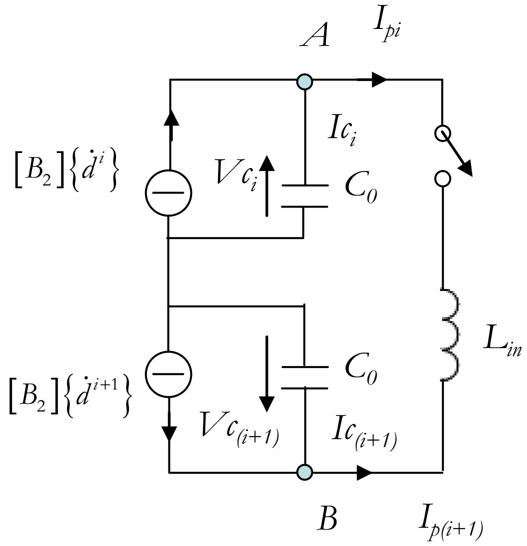

Figure 4.23. Equivalent circuit of periodic cells with nonlinear switching interconnections.

Then, by short-circuiting the branch *AB*, the current I_{Norton} flowing from *A* to *B* by using Norton theorem can be obtained as:

$$I_{Norton} = [B_2]\{\dot{d}^i\} - Ic_i = Ic_{(i+1)} - [B_2]\{\dot{d}^{i+1}\} \tag{4.40}$$

and the following voltage relationship holds as well,

$$Vc_i = Vc_{(i+1)} \tag{4.41}$$

which can be further expressed as

$$\frac{1}{j\omega C_0} Ic_i = \frac{1}{j\omega C_0} Ic_{(i+1)} \tag{4.42}$$

yielding

$$Ic_i = Ic_{(i+1)} \tag{4.43}$$

Inserting the above equation into Eq. (4.40), the current I_{Norton} is simplified as:

$$I_{Norton}=\frac{1}{2}\left(\left[B_2\right]\left\{\dot{d}^i\right\}-\left[B_2\right]\left\{\dot{d}^{i+1}\right\}\right)=\frac{1}{2}\left[B_2\right]\left(\left\{\dot{d}^i\right\}-\left\{\dot{d}^{i+1}\right\}\right) \tag{4.44}$$

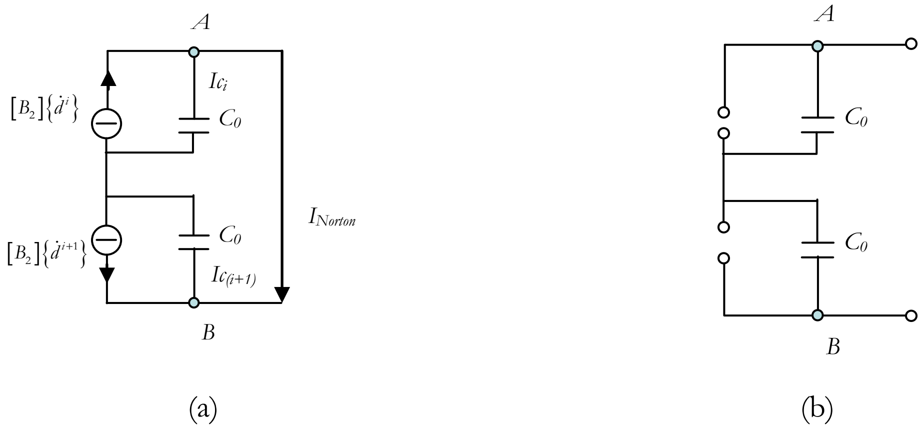

Figure 4.24. Networks of (a) the short-circuit current and (b) the equivalent capacitance.

Removing the sources and replacing with open circuit state (Figure 4.24(b)), the equivalent capacitance of the interconnection is obtained as:

$$C_{equivalent}=\frac{C_0}{2} \tag{4.45}$$

Thus, the pure optimal resistance can be expressed by

$$R_{opt}=\frac{2}{C_0\omega} \tag{4.46}$$

Similar as the previous demonstration, in the case of interconnection by nonlinear switching device, when the SSDI approach is operating in steady state, the voltage across A and B can be regarded as the superposition of a voltage V_{linear} which is proportional to the relative displacement and a crenel function H (Figure 4.25) and expressed as

$$V_{AB}=V_{linear}+H \tag{4.47}$$

with

$$V_{linear}=V_0\cos\left(\omega t\right) \tag{4.48}$$

and

$$H=H_M sign\left(\dot{V}_{linear}\right) \tag{4.49}$$

which can also be represented by Fourier series as

$$H=-H_M\cdot\frac{4}{\pi}\sum_{n_k=1}^{\infty}\sin\left(\left(2n_k-1\right)\omega t\right) \tag{4.50}$$

As introduced in [126], the amplitude of the crenel function can be written using the piezovoltages before and after switching action or expressed by the inversion coefficient γ:

$$H_M = \frac{V_{before} + V_{after}}{2} = \frac{1+\gamma}{1-\gamma} V_0 \tag{4.51}$$

Hence, the voltage across A and B can be simplified with first harmonic approximation:

$$V_{AB} \approx V_0 \cos(\omega t) - \frac{4}{\pi}\frac{1+\gamma}{1-\gamma} V_0 \sin(\omega t) \tag{4.52}$$

and the voltage V_{AB} in frequency domain can be further written as

$$V_{AB} \approx \left(1 + \frac{4j}{\pi}\frac{1+\gamma}{1-\gamma}\right) V_{linear}(\omega) \tag{4.53}$$

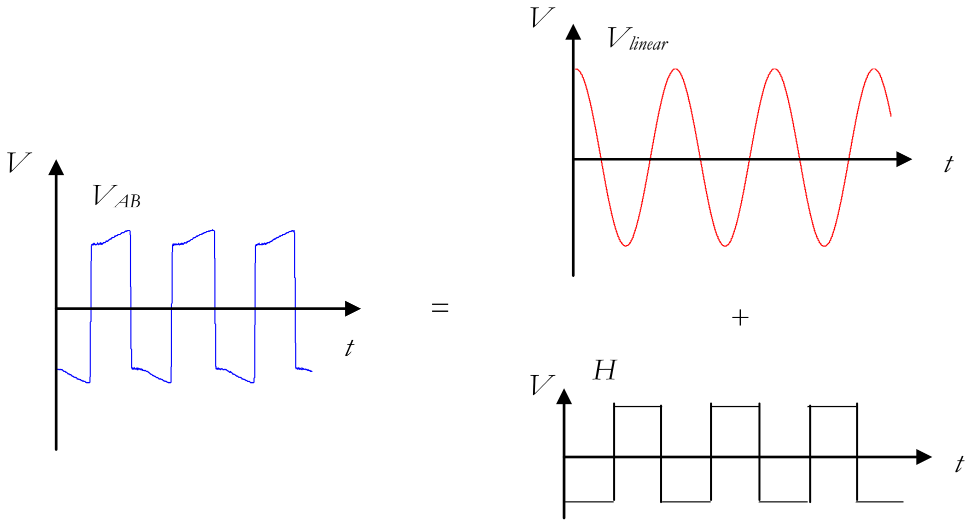

Figure 4.25. Schematic decomposition of piezovoltage across A and B.

In a similar way, the current flowing from A to B and given as:

$$\begin{aligned} I(t) &= -C_{equivalent}\frac{dV_{AB}}{dt} = C_{equivalent}(1+\gamma)V_{before}\sum_i (-1)^i \delta\left(t - \frac{T_{period}}{2} i\right) \\ &= I_0 \sum_i (-1)^i \delta\left(t - \frac{T_{period}}{2} i\right) \end{aligned} \tag{4.54}$$

where T_{period} denotes the period, can be approximated by its first harmonic by:

$$I_{AB} = \frac{2\omega}{\pi} I_0 \cos(\omega t) \tag{4.55}$$

Inserting

$$V_{before} = \frac{2V_0}{1-\gamma} \tag{4.56}$$

into (4.54) and replacing I_0 into Eq. (4.55) yields

$$I_{AB} = \frac{4\omega}{\pi}\frac{1+\gamma}{1-\gamma}C_{equivalent}V_{linear}(\omega) \tag{4.57}$$

On the basis of the previous demonstration, the equivalent impedance Z in the case of interconnection with nonlinear switch device can be obtained:

$$Z = \frac{V_{AB}}{I_{AB}} = \frac{\left(1+\frac{4j}{\pi}\frac{1+\gamma}{1-\gamma}\right)}{\frac{4\omega}{\pi}\frac{1+\gamma}{1-\gamma}C_{equivalent}} = \frac{\pi(1-\gamma)}{4\omega(1+\gamma)C_{equivalent}} + \frac{j}{\omega C_{equivalent}} \tag{4.58}$$

which can be rewritten as

$$Z = \frac{\pi(1-\gamma)}{2\omega(1+\gamma)C_0} + \frac{2j}{\omega C_0} \tag{4.59}$$

It should be noted that since for the case of interconnecting by nonlinear switching device, the equivalent capacitance is less than the clamped capacitance of each piezoelectric patch (similar as using the nonlinear switching technique with spatial filtering expressed in chapter 2), the corresponding inversion coefficient γ is greater than that in the independently switching case, yielding

$$\gamma = \gamma_{independent}^{\sqrt{\frac{1}{2}}} > \gamma_{independent} \tag{4.60}$$

The wave attenuation of the periodic cell as shown in Figure 4.13 with interconnection by resistor and nonlinear switching device are plotted in Figure 4.26 and Figure 4.27. From the comparison of the obtained results of the independently connected cases demonstrated in section 4.3.1 (Figure 4.14 and Figure 4.15), it can be found that for the lower frequency range the global control performance of the interconnection cases are less effective although the inversion coefficient in the interconnected case is a little bit greater than that in the independent case, which is due to that the wavelength is greater than the length of periodic cell. Meanwhile, for attenuating the wave propagation in higher frequency spectra, the case of interconnecting by nonlinear switching case outperforms the corresponding independent switching case, which may be attributed to the better energy flow control for the particular periodic cell and can be affected by the length of the periodic cell or other investigated parameters. Moreover, extra wave attenuation frequency ranges (such as the one in $f \in \left[2\times10^4 \quad 3\times10^4\right]$) which may be induced by the particular electrical boundary conditions are found in the interconnection cases. Since it is a preliminary investigation, the effects of interested paramters and the optimal wave attenuation performance can be further studied in the future works.

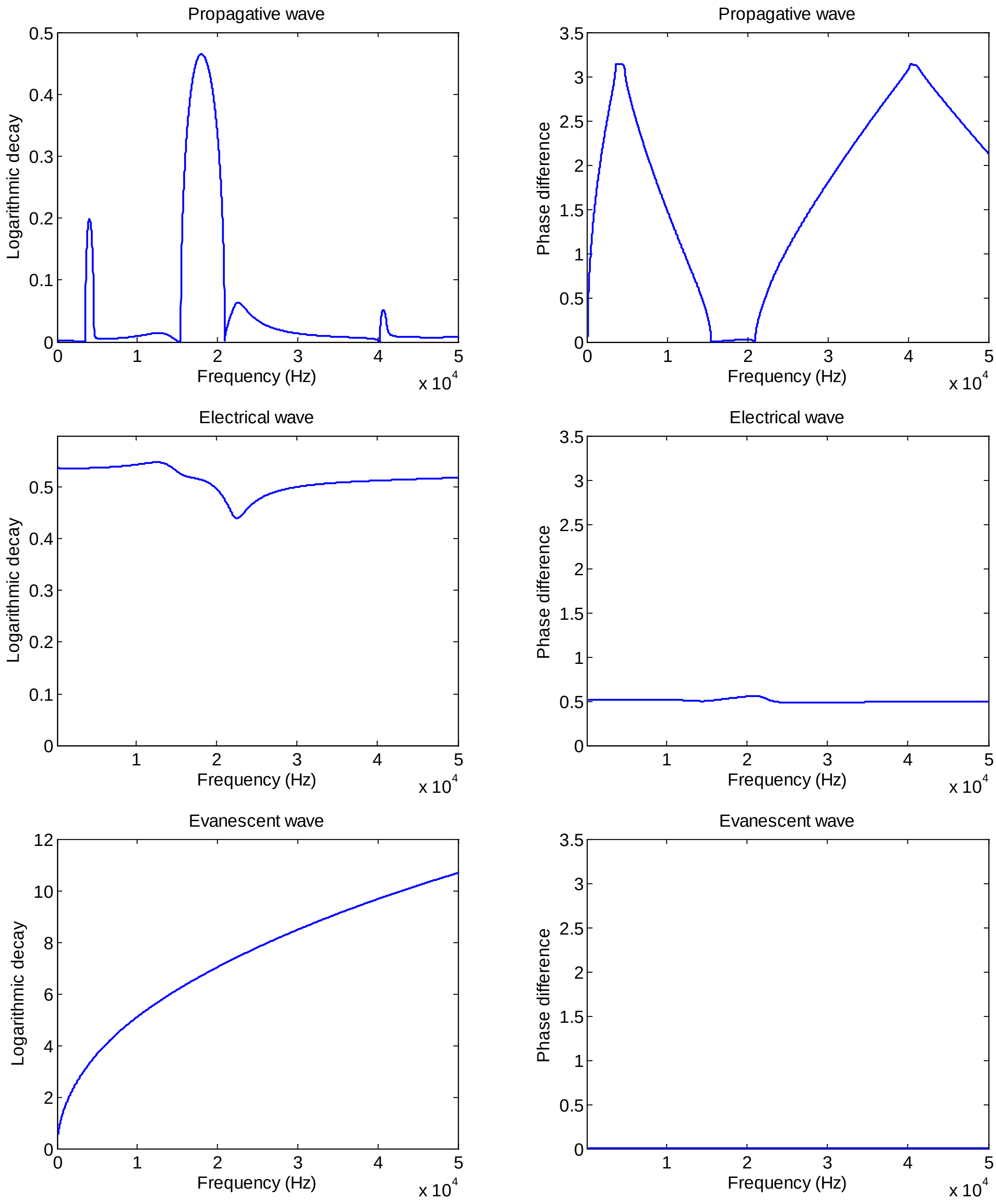

Figure 4.26. Wave propagation of the periodic structure interconnected with optimal resistor.

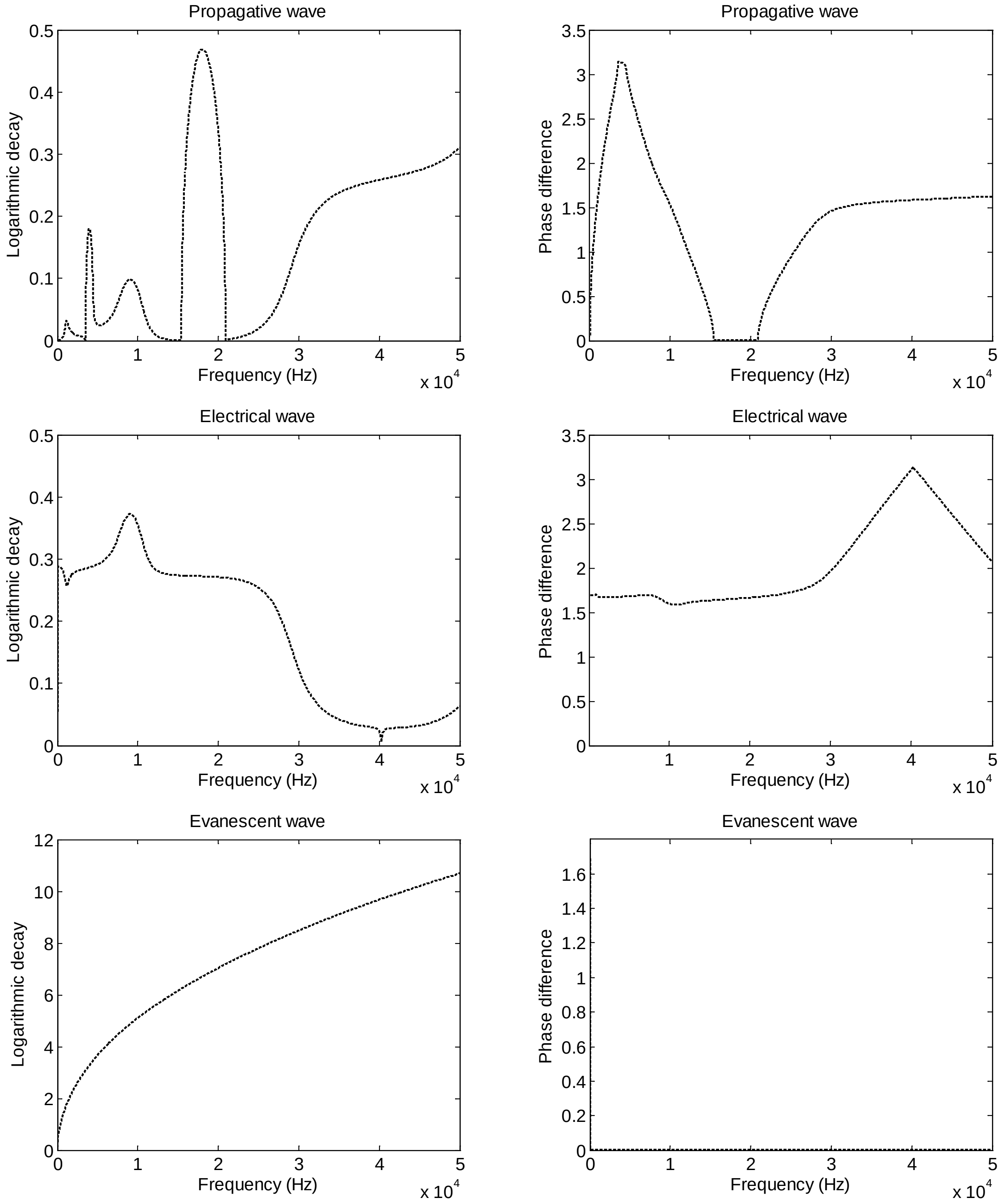

Figure 4.27. Wave propagation of the periodic structure interconnected with nonlinear switching device (*$\gamma=0.38$*).

4.4.2. Effects of aperiodicity of inversion coefficient γ

It is known that wave attenuation of the periodic structure will be affected by the aperiodicity which may induced by differences in physical dimensions or material properties between cells or intentionally introduced by control gain of active periodic cell or different shunting parameters as illustrated in Figure 4.10. Inversion coefficient as an important parameter in SSDI technique can be further studied although the wave attenuation varied with its value has shown in last section. Since the aperiodicity of the periodic structure can lead to better results in some frequency bands, the effects of aperiodicity of the inversion coefficient for independent switched periodic cells and/or interconnected periodic cells may provide another design method for vibration reduction purposes.

4.4.3. Wave attenuation for lower frequency bands

As it is mentioned in the research of Casadei *et al.* [161], periodic resistive shunting is effective for wave attenuation and vibration reduction in mid-higher frequency spectra. Although this study focused on attenuating the propagating wave and limiting the vibration in relatively high frequency with the proposed nonlinear switching periodic interface, this damping strategy can also be extended for lower frequency spectra since the SSDI approach is an adaptive strategy which is independent to the external excitation frequency.

4.5. Conclusion

In this chapter, the periodic structure featuring nonlinear switching interface is introduced for preliminary demonstrating the wave attenuation along the periodic structure and for vibration reduction purpose. Finite element method coupled with transfer matrix method is introduced for investigating the periodic structure. In order to compare the wave attenuation effects and the damping performance, the cases of piezoelectric patch in open circuit, connected to resistive shunt and featuring the proposed nonlinear interface have been studied and discussed. Experiments are carried out on a clamped-clamped electromechanical periodic beam for validating the theoretical discussion. Relatively good agreements are achieved between experiments and simulation which further confirm the excellent damping ability of the proposed nonlinear switching periodic interface. The main work in this chapter can be summarized as follows:

- It is known that periodic structures can attenuate and confine the wave within specific frequency bands without changing the characteristic of the elastic waves in other frequency bands, which is able to spatially filter the waves. In order to effectively attenuate the propagating waves and limit vibrations, the periodic structure is combined with the nonlinear switching SSDI technique. Transfer matrix based on the relationships between the elements of each cell obtained with finite element method is introduced. Formulation as the piezoelectric patch in open circuit case, connected to resistive shunting circuit and the proposed nonlinear switching device is derived.

- For preliminary investigation, the wave attenuation of an electromechanical periodic cell with one piezoelectric patch is discussed with different electrical conditions (short circuit, open circuit, resistive shunting circuit and nonlinear switching device). From the obtained band gaps, it can be found that with the periodic configuration, the electromechanical periodic structure has the capability of spatially filtering the waves within stop bands. Moreover, wave attenuation ability is increased in open circuit compared with the results obtained in the case of short circuit. Although within the stop bands, the real part of propagation constant does not evidently change as optimal resistive shunt circuit is employed; the elastic wave is attenuated within pass bands due to the energy dissipation. Wave attenuation ability is significantly increased with a wider stop bands when using the proposed nonlinear switching interface, which is due to the voltage inversion process of the SSDI technique that can artificially increase the coupling coefficient. Additionally, wave attenuation varied with voltage inversion coefficient is further discussed. From the results, it can be concluded that the attenuation ability of the electromechanical periodic structure is increasing with the inversion coefficient. Dynamical responses of the periodic cells under different conditions (clamped-clamped and cantilever cases) are briefly introduced. Aming at discussing the global damping performance of the electromechanical periodic structure featuring nonlinear switching interface, experiments are conducted on a clamped-clamped electromechanical periodic structure which consists of four electromechanical periodic cells. From the experimental results and the simulation analyses, it can be found that the results are in good agreement which further confirms the excellent performance of the proposed technique, since the switching approach allows a significant enlargement of the stop bands thus yielding a larger attenuation bandwidth. Furthermore, due to the adaptive nonlinear process, the voltage is artificially increased with a phase reduction between voltage and speed, therefore artificially increasing the coupling coefficient and the damping ability.

- Future works of the electromechanical periodic structure featuring nonlinear switching interface are discussed. Wave attenuation and damping performance of the interconnected electromechanical periodic cells can be further investigated based on the relative derivation. In addition, the effects of aperiodicity of the inversion coefficient can be further discussed with the independent nonlinear periodic interface and/or with the interconnected electromechanical periodic cells. Furthermore, as the nonlinear switching technique (SSDI) is an adaptive control method, it can be combined with periodic structure for damping the vibration and attenuating the wave in lower frequency spectra.

Chapter 5. Conclusion and perspectives

The main achievements of this thesis are the developments and extensions for broadband vibration control of Synchronized Switch Damping on Inductor (SSDI) technique. Multimodal nonlinear strategy based on spatial filtering according to the mode shapes of the vibrating structure, combination of the spatial filtering with threshold detection obtained by time domain signal process for broadband vibration attenuation, electromechanical nonlinear TMD and electromechanical periodic structures featuring nonlinear switching interface are proposed and discussed.

In the first chapter, main vibration treatments and damping systems are deeply reviewed. Control principles and developments of viscoelastic damping treatments, particle damping systems, tuned dynamic devices and intelligent control systems are briefly introduced. Due to the coupling properties of smart materials, electrorheological fluids, magnetorheological fluids, magnetostrictive materials, electrostrictive materials, shape memory alloys and piezoelectric materials are extensively implemented into the vibration control system for sensing and/or responding in a useful manner. Additionally, electromechanical systems equipped with piezoelectric materials which have the capability to couple the electrical field and mechanical field, are comprehensively reviewed in passive, active, semi-passive/semi-active and hybrid aspects. Electromechanical semi-passive/semi-active control strategies allowing excellent damping performance compared to passive strategies with much lower power requirements than active approaches, simplicity and light weight attracted a lot of attention in the last two decades, expecially for the synchronized switch damping (SSD) approaches.

Although the classical SSDI strategy has been proven to be an effective damping strategy for single mode vibration control, the over-frequent switching actions in multimodal vibration environment will decrease its control performance due to the control principle which allows the switching action occuring at each detectable extremum. In order to improve the multimodal control effectiveness of classical SSDI technique, an enhanced nonlinear damping strategy based on spatial filtering is proposed in the second chapter.

According to the mode shapes of the vibrating structure, piezoelectric actuators should be placed anti-symmetrically and/or symmetrically in the proposed enhanced spatial filtering strategy. Two switches (sum switch and difference switch) aiming at different vibration modes are introduced. A clamped-clamped beam is used as an illustrative example for demonstrating the control principles. In order to damp the odd modes of the clamped-clamped beam, the two anti-symmetrically bonded piezoelectric actuators are connected through a switching device (same as classical SSDI switching device composed of an inductor and a digital switch) for spatially filtering the even modes before switching. This switch is always kept open except when an extremum of the sum of the piezovoltages occurs. At that moment, the switch is closed for half a period of the electrical oscillator (constituted by the total capacitance of the piezoelectric patches and the inductor) until the sum piezovoltage is reversed. In a similar way, in order to attenuate the even modes, symmetrically bonded piezoelectric actuators are intermittently connected to a switching device which is based on the piezovoltage difference for spatial filtering of the odd modes. Thus, as the sum and difference switches are employed, both odd and even modes can be separated and damped simultaneously.

It is concluded from the theoretical investigation and experimental validation under monochromatic excitation, bimodal excitation and band limited white noise excitation that the enhanced nonlinear damping strategy based on the spatial filtering can effectively filter the uninterest modes and damp the targeted modes. Moreover, from the comparison with classical SSDI technique, it is further comfirmed that the enhanced nonlinear spatial filtering strategy outperforms the classical SSDI approach, especially under wideband excitation.

Aiming at attenuating the broadband vibration, the proposed enhanced strategy based on spatial filtering is combined with time domain filtering (threshold detection). Simulation results obtained under band-limited white noise in the range of 10 *Hz* to 610 *Hz*, and pulse excitation not only validate the excellent multimodal damping ability and broadband control performance of this combination but also verify the feasibility of the enhanced spatial filtering strategy.

In the third chapter, an electromechanical semi-passive nonlinear TMD, in which mechanical energy is not only transferred between vibrating structure and TMD device but also can be converted as electromechanical energy by the piezoelectric materials, is proposed for reducing the vibration of host structure. Piezoelectric patches of this electromechanical semi-passive nonlinear TMD is intermittently connected to a switching device (same as in classical SSDI strategy) for voltage inversion as the extremum value of relative displacement between the TMD device and the host structure or the piezovoltage is detected.

Global control performances of tuned and mistuned TMD systems (purely mechanical TMD, optimal electromechanical passive TMD and electromechanical semi-passive nonlinear TMD) varied with mass ratio are discussed. Generally, higher damping TMD systems can obtain better damping effectiveness in the investigated mass ratio range and the TMD systems are more effective for limiting the vibration of lightly damped host structure. Different from directly coupled cases where a greater inversion coefficient leads to better control performance, for the proposed semi-passive nonlinear TMD, global damping performance is dependent to the higher voltage inversion coefficient and global coupling coefficient. It is also found that the mass ratio is a very important design parameter. Moreover, different from the mistuned TMD systems with +20% resonance frequency shift, in which the control effectiveness is dramatically decreased, global damping performance of TMD systems with -20% resonance frequency shift is still excellent in the investigated parameters ranges.

For validating the excellent damping performance of the proposed electromechanical semi-passive nonlinear TMD, experiments are carried out on a cantilever beam (host structure) with a TMD device attached at its free end. Numerical analyses based on the TDOF model and finite element model are in good agreement with the experiments measurements, which show the superior damping effectiveness of the electromechanical semi-passive nonlinear TMD in the comparison of purely mechanical TMD and electromechanical passive TMD systems.

Electromechanical periodic structure featuring nonlinear switching interface is proposed in the fourth chapter aiming at effectively attenuating the propagating waves and limiting vibrations. From the wave attenuation of an electromechanical periodic cell obtained in different cases (short circuit, open circuit, resistive shunt circuit and nonlinear switching interface), it can be found that the wave attenuation ability and damping capability of the electromechanical periodic cell are significantly improved due to the voltage inversion process of the SSDI technique which artificially increases the coupling coefficient. Moreover, attenuation ability of the electromechanical periodic structure is increasing with the inversion coefficient.

Experimental results and the simulation analyses obtained with a clamped-clamped electromechanical periodic structure composed of four electromechanical periodic cells are in good agreement. It can be concluded that integrating the nonlinear switching interface in electromechanical periodic structure allows a significant enlargement of the stop bands due to the adaptive nonlinear process, thus yielding larger wave attenuation and vibration reduction.

Future work would focus on the following aspects:

1) Although the simulation results showed the excellent broadband vibration control effectiveness of the combination of enhanced spatial filtering strategy with threshold detection, experimental validation will be carried out for further comfirmation. The proposed enhanced nonlinear strategy based on spatial filtering will be extended to more complex vibrating structures such as plates for verifying its feasibility and effectiveness.

2) In the framework of efficient multimodal vibration damping systems, the use of a distributed network of electromechanical TMDs would be a very promising field. As an example, the use of algorithms based on the previously proposed spatial filtering technique applied to electromechanical TMD network would be a possible field of investigation. Additionally, since the voltage inversion coefficient is an important design variable for the proposed electromechancial TMD, the future work will also focus on optimizating the inversion coefficient with other given parameters.

3) Wave attenuation and control effectiveness of the interconnected electromechanical periodic cells will be further studied since the artifially spatial filtering process may be induced by the connections as introduced in the enhanced spatial filtering strategy. Moreover, effects of aperiodicity induced by inversion coefficient will be investigated as the inversion coefficient is an important parameter for the nonlinear damping strategy.

Bibliographie / References

[1] Singiresu S. Rao, Mechanical vibrations, fifth edition, 2011

[2] http://www.healthline.com/natstandardcontent/alt-vibration-healing

[3] "whole body vibration good practice guide"

[4] Z. Yang and L. Yan, effects of passenger seat stiffness on the impact responses of human body during aircraft force-landing, Journal of Vibration and Shock, 2009

[5] L. Yan, Z. Yang and H. Luo, analysis on impact response of seated human body, Journal of Vibration and Shock, 2010

[6] C. A. Gallimore, "passive viscoelastic constrained layer damping application for a small aircraft landing gear system", thesis, (2008)

[7] B. C. Nakra, vibration control in machines and structures using viscoelastic damping, Journal of sound and vibration, 1998

[8] H. Ghoneim, electromechanical surface damping using constrained layer and shunted piezoelectric, Proc. SPIE Smart Structures and Materials, 1993, Vol. 1919

[9] S.W. Kung and R. Singh, vibration analysis of beams with multiple constrained layer damping patches, Journal of Sound and Vibration, 1998, 212 (5),781-805

[10] Y.C. Hu and S.C. Huang, the frequency response and damping effect of three-layer thin shell with viscoelastic core, Computers and Structures, 2000, 76, 577-591

[11] C. H. Park and A. Baz, vibration control of bending modes of plates using active constrained layer damping, Journal of Sound and Vibration, 1999, 227(4), 711-734

[12] M. C. Ray and A. Baz, control of nonlinear vibration of beams using active constrained layer damping, Journal of Vibration and Control, 2001, 7: 539-549

[13] C. Chantalakhana and R. Stanway, active constrained layer damping of clamped-clamped plate vibrations, Journal of Sound and Vibration, 2001, 241(5), 755-777

[14] S. H. Zhang and H. L. Chen, a study on the damping characteristics of laminated composites with integral viscoelastic layers, Composite Structures, 2006, 74, 63-69

[15] S. F. Masri and T. K. Caughey, on the stability of the impact damper, Trans ASME, J. Appl. Mech., 1966, 33(3):586-592

[16] Z. Xu, M. Y. Wang and T. Chen, Particle damping for passive vibration suppression: numerical modelling with experimental verification, ASME Design Engineering Technical Conferences and Computers and Information in Engineering Conference, 2003

[17] A. Papalou and S. F. Masri, an experimental investigation of particle dampers under harmonic excitation, Journal of Vibration and Control, 1998, 4:361-379

[18] B. L. Fowler, E. M. Flint and S. E. Olson, design methodology for particle damping, SPIE Smart Structures and Materials, 2001, Vol. 4331

[19] Z. Xu, M. Y. Wang and T. Chen, Particle damping for passive vibration suppression: numerical modelling with experimental verification, ASME Design Engineering Technical Conferences and Computers and Information in Engineering Conference, 2003

[20] Z. Xu, M. Y. Wang and T. Chen, particle damping for passive vibration suppression: numerical modelling and experimental investigation, Journal of Sound and Vibration, 2005, 279:1097-1120

[21] K. S. Marhadi and V. K. Kinra, particle impact damping: effect of mass ratio, material, and shape, Journal of Sound and Vibration, 2005, 283:433-448

[22] X. Bai, L. M. Keer, Q. J. Wang and R. Q. Snurr, investigation of particle damping mechanism via particle dynamics simulations, Granular Matter, 2009, 11:417-429

[23] Z. Lu, S. F. Masri and X. Lu, parametric studies of the performance of particle dampers under harmonic excitation, Structural control and health monitoring, 2011, 18:79-98

[24] K. W. Chan, W. H. Liao, M. Y. Wang and P. K. Choy, experimental studies for particle damping on a bond arm, Journal of Vibration and Control, 2006, 12: 297-312

[25] H. Frahm, Device for damping vibrations of bodies, 1911. U.S. patent No.989.958

[26] G. C. Marano, S. Sgobba, R. Greco and M. Mezzina, robust optimum design of tuned mass dampers devices in random vibration mitigation, Journal of Sound and Vibration, 2008, 313: 472-492

[27] G. C. Marano and G. Quaranta, Robust optimum criteria for tuned mass dampers in fuzzy environments, Applied Soft Computing, 2009, 9: 1232-1243

[28] G. C. Marano, R. Greco and B. Chiaia, a comparison between different optimization criteria for tuned mass dampers design, Journal of Sound and Vibration, 2010, 329: 4880-4890

[29] L. Zuo and S. A. Nayfeh, minimax optimization of multi-degree-of-freedom tuned mass dampers, Journal of Sound and Vibration, 2004, 272: 893-908

[30] L. Zuo and S. A. Nayfeh, the two-degree-of-freedom tuned mass damper for suppression of single mode vibration under random and harmonic excitation, Transactions of the ASME Journal of Vibration and Acoustics, 2006, Vol. 128: 56-65

[31] S. Krenk and J. Høgsberg, tuned mass absorbers on damped structures under random load, Probabilistic Engineering Mechanics, 2008, 23: 408-415

[32] N. Hoang, Y. Fujino and P. Warnitchai, optimal tuned mass damper for seismic applications and practical design formulas, Engineering Structures, 2008, 30: 707-715

[33] G. Bekdaş and S. M. Nigdeli, Estimating optimum parameters of tuned mass damper using harmony search, Engineering Structures, 2011, 33: 2716-2723

[34] O. F. Tigli, optimum vibration absorber (tuned mass damper) design for linear damped system subjected to random loads, Journal of Sound and Vibration, 2012, 331: 3035-3049

[35] A. Kareem and S. Kline, performance of multiple mass dampers under random loading, Journal of Structural Engineering, 1995, 121: 348-361

[36] L. Zuo and S. A. Nayfeh, optimization of the individual stiffness and damping parameters in multiple-tuned-mass-damper systems, Journal of Vibration and Acoustics, 2005, Vol. 127: 77-83

[37] L. Zuo, effective and robust vibration control using series multiple tuned mass dampers, Journal of Vibration and Acoustics, 2009, Vol. 131, 031006

[38] C. Li and B. Zhu, estimating double tuned mass dampers for structures under ground acceleration using a novel optimum criterion, Journal of Sound and Vibration, 2006, 298: 280-297

[39] D. Stăncioiu and H. Ouyang, structural modification formula and iterative design method using multiple tuned mass dampers for structures subjected to moving loads, Mechanical Systems and Signal Processing, 2012, 28: 542-560

[40] P. Bonello, M. J. Brennan, S. J. Elliott, J. F. V. Vincent and G. Jeronimidis, designs for an adaptive tuned vibration absorber with variable shape stiffness element, Proceedings of the royal society A, 2005, 461: 3955-3976

[41] P. Bonello, M. J. Brennan and S. J. Ellliott, vibration control using an adaptive tuned vibration absorber with a variable curvature stiffness element, Smart Materials and Structures, 2005, 14: 1055-1065

[42] F. Weber, C. Boston and M. Maślanka, an adaptive tuned mass damper based on the emulation of positive and negative stiffness with an MR damper, Smart Materials and Structures, 2011, 20, 015012

[43] D. Hrovat, P. Barak and M. Rabins, semi-active versus passive or active tuned mass dampers for structural control, Journal of Engineering Mechanics, 1983, Vol. 109, No. 3: 691-705

[44] K. A. Cunefare, S. De Rosa, N. Sadegh and G. Larson, state-switched absorber for semi-active structural control, Journal of Intelligent Material Systems and Structures, 2000, Vol. 11: 300-310

[45] C. L. Davis and G. A. Lesieutre, an actively tuned solid-state vibration absorber using capacitive shunting of piezoelectric stiffness, Journal of Sound and Vibration, 2000, 232 (3): 601-617

[46] H. R. Owji, A. H. N. Shirazi and H. H. Sarvestani, a comparison between a new semi-active tuned mass damper and an active tuned mass damper, Procedia Engineering, 2011, 14: 2779-2787

[47] N. Jalili and D. W. Knowles IV, structural vibration control using an active resonator absorber: modelling and control implementation, Smart Materials and Structures, 2004, 13: 998-1005

[48] S. M. Kim, S. Wang and M. J. Brennan, dynamic analysis and optimal design of a passive and an active piezo-electrical dynamic vibration absorber, Journal of Sound and Vibration, 2011, 330: 603-614

[49] M. H. Tso, J. Yuan and W. O. Wong, suppression of random vibration in flexible structures using a hybrid vibration absorber, Journal of Sound and Vibration, 2012, 331: 974-986

[50] H. Jo and H. Yabuno, amplitude reduction of primary resonance of nonlinear oscillator by a dynamic vibration absorber using nonlinear coupling, Nonlinear Dynamics, 2009, 55: 67-78

[51] J. C. Ji and N. Zhang, suppression of the primary resonance vibrations of a forced nonlinear system using a dynamic vibration absorber, Journal of Sound and Vibration, 2010, 239: 2044-2056

[52] S. Sgobba and G. C. Marano, optimum design of linear tuned mass dampers for structures with nonlinear behaviour, Mechanical Systems and Signal Processing, 2010, 24: 1739-1755

[53] T. Balendra, C. M. Wang and H. F. Cheong, effectiveness of tuned liquid column dampers for vibration control of towers, Engineering Structures, 1995, Vol. 17, No. 9: 668-675

[54] K. Fujii, Y. Tamura, T. Sato and T. Wakahara, wind-induced vibration of tower and practical applications of tuned sloshing damper, Journal of Wind Engineering and Industrial Aerodynamics, 1990, Vol. 33: 263-272

[55] A. K. Noor, S. L. Venneri, D. B. Paul and M. A. Hopkins, structures technology for future aerospace systems, Computers and Structures, 2000, 74: 507-519

[56] N. Jalili, piezoelectric-based vibration control: from macro to micro/nano scale system, 2010

[57] A. S. Phani and K. Venkatraman, vibration control of sandwich beams using electro-rheological fluids, Mechanical Systems and Signal Processing, 2003, 17 (5): 1083-1095

[58] K. R. Kumar and N. Ganesan, vibration and damping studies on a hollow sandwich box column with a viscoelastic/electrorheological/magnetorheological fluid core layer by the finite element method, International Journal of Structural Stability and Dynamics, 2008, Vol. 8, No. 4: 531-546

[59] K. Ramkumar and N. Ganesan, vibration and damping of composite sandwich box column with viscoelastic/electrorheological fluid core and performance comparison, Materials and Design, 2009, 30: 2981-2994

[60] V. Rajamohan, R. Sedaghati and S. Rakheja, optimal vibration control of beams with total and partial MR-fluid treatments, Smart Materials and Structures, 2011, 20, 115016

[61] S. R. Hong, S. B. Choi and M. S. Han, vibration control of a frame structure using electro-rheological fluid mounts, International Journal of Mechanical Sciences, 2002, 44: 2027-2045

[62] S. Lim, S. M. Park and K. I. Kim, AI vibration control of high-speed rotor systems using electrorheological fulid, Journal of Sound and Vibration, 2005, 284: 685-703

[63] Y. Sun and M. Thomas, control of torsional rotor vibrations using an electrorheological fluid dynamic absorber, Journal of Vibration and Control, 2011, 17: 1253-1264

[64] C. Y. Lai and W. H. Liao, vibration control of a suspension system via a magnetorheological fluid damper, Journal of Vibration and Control, 2002, 8: 527-547

[65] G. Z. Yao, F. F. Yap, G. Chen, W. H. Li and S. H. Yeo, MR damper and its application for semi-active control of vehicle suspension system, Mechatronics, 2002, 12: 963-973

[66] M. M. Rashid, M. J. E. Salami, M. Raisuddin K. and R. Mozasser, development of vibration suppression devices from smart fluids, Advanced Materials Research, 2011, Vol. 264-265: 548-553

[67] S. Choi, S. H. Ha and J. Jeon, vibration control of flexible structures using semi-active mount: experimental investigation, the 5th chapter of book “advances in vibration engineering and structural dynamics”.

[68] A. M. Sharabash and B. O. Andrawes, application of shape memory alloy dampers in the seismic control of cable-stayed bridges, Engineering Structures, 2009, 31: 607-616

[69] X. B. Zuo, A. Q. Li, W. Sun and X. H. Sun, optimal design of shape memory alloy damper for cable vibration control, Journal of Vibration and Control, 2009, 15: 897-921

[70] H. Qian, H. Li, D. Cui and H. Chen, case studies of seismic vibration control of civil structures using shape memory alloys, Advanced Materials Research, 2011, Vols. 243-249: 5427-5434

[71] Y. Suzuki and Y. Kagawa, active vibration control of a flexible cantilever beam using shape memory alloy actuators, Smart Materials and Structures, 2010, 19, 085014

[72] K. Dhanalakshmi, A. Avinash, M. Umapathy and M. Marimuthu, experimental study on vibration control of shape memory alloy actuated flexible beam, International Journal on Smart Sensing and Intelligent Systems, 2010, Vol. 3, No. 2: 156-175

[73] Y. Zhang, S. Zhao, L. Long and K. Li, numerical simulation of solar array with shape memory alloy in active vibration control, Applied Mechanics and Materials, 2010, Vols. 29-32, 589-595

[74] J. C. Hannen, J. H. Crews and G. D. Buckner, indirect intelligent sliding mode control of a shape memory alloy actuated flexible beam using hysteretic recurrent neural networks, Smart Materials and Structures, 2012, 21, 085015

[75] K. M. Majewska, A. J. Żak and W. M. Ostachowicz, vibration control of a rotor by magnetic shape memory actuators-an experimental work, Smart Materials and Structures, 2010, 19, 085004

[76] R. L. Forward, electronic damping of vibrations in optical structures, Applied Optics, 1979, Vol. 18, issue 5: 690-697

[77] G. A. Lesieutre, vibration damping and control using shunted piezoelectric materials, The Shock and Vibration Digest, 1998, Vol. 30, No. 3: 187-195

[78] S. O. R. Moheimani and A. J. Fleming, piezoelectric transducers for vibration control and damping, 2006

[79] Y. F. Duan and S. W. Or, self-sensing tunable vibration absorber incorporating piezoelectric ceramic-magnetostrictive composite sensoriactuator, Smart Materials and Structures, 2011, 20, 085007

[80] T. Zhang, B. T. Yang, H. G. Li and G. Meng, dynamic modeling and adaptive vibration control study for giant magnetostrictive actuators, Sensors and Actuators A, 2013, 190: 96-105

[81] F. Braghin, S. Cinquemani and F. Resta, a low frequency magnetostrictive inertial actuator for vibration control, Sensors and Actuators A, 2012, 180: 67-74

[82] G. Ausanio, V. Iannotti, E. Ricciardi, L. Lanotte, C. Hison and E. Hristoforou, potentiality of a novel elastomagnetic attenuator for vibration control, Sensors and Actuators A, 2010, 159: 219-226

[83] M. E. F. Kasarda, H. Mendoza, R. G. Kirk and A. Wicks, reduction of subsynchronous vibration in a single-disk rotor using an active magnetic damper, Mechanics Research Communications, 2004, 31: 689-695

[84] N. W. Hagood and A. V. Flotow, damping of structural vibrations with piezoelectric materials and passive electric networks, Journal of Sound and Vibration, 1991, 146 (2): 243-268

[85] A. J. Fleming, S. Behrens and S. O. R. Moheimani, reducing the inductance requirements of piezoelectric shunt damping system, Smart Materials and Structures, 2003, 12: 57-64

[86] J. J. Hollkamp, multimodal passive vibration suppression with piezoelectric materials and resonance shunts, Journal of Intelligent Material Systems and Structures, 1994, 5: 49-57

[87] S. Y. Wu, method for multiple mode piezoelectric shunting with single PZT transducer for vibration control, Journal of Intelligent Material Systems and Structures, 1998, 9: 991-998

[88] S. Behrens, S. O. R. Moheimani and A. J. Fleming, multiple mode current flowing passive piezoelectric shunt controller, Journal of Sound and Vibration, 2003, 266: 929-942

[89] S. O. R. Moheimani, A. J. Fleming and S. Behrens, on the feedback structure of wideband piezoelectric shunt damping systems, Smart Materials and Structures, 2003, 12: 49-56

[90] F. Dell'Isola, C. Maurini and M. Porfiri, passive damping of beam vibrations through distributed electric networks and piezoelectric transducers: prototype design and experimental validation, Smart Materials and Structures, 2004, 13: 299-308

[91] S. Alessandroni, U. Andreaus, F. Dell'Isola and M. Porfiri, a passive electric controller for multimodal vibrations of thin plates, Computers and Structures, 2005, 83: 1236-1250

[92] U. Andreaus, F. Dell'Isola and M. Porfiri, multimodal vibration control by using piezoelectric transducers and passive circuits', (2010)

[93] M. A. Trindade and C. E. B. Maio, multimodal passive vibration control of sandwich beams with shunted shear piezoelectric materials, Smart Materials and Structures, 2008, 17, 055015

[94] R. Alkhatib and M. F. Golnaraghi, active structural vibration control: a review, The Shock and Vibration Digest, 2003, Vol. 35, No. 5: 367-383

[95] D. J. Inman, vibration with control, 2006

[96] C. R. Fuller, S. J. Elliot and P. A. Nelson, active control of vibration, 1996, Academic press, London

[97] J. E. Hubbard Jr., method and apparatus using a piezoelectric film for active control of vibration, 1986, US Patent, 4565940

[98] H. C. Lester and S. Lefebvre, piezoelectric actuator models for active sound and vibration control of cylinders, Journal of Intelligent Material Systems and Structures, 1993, 4: 295-306

[99] N. W. Hagood, W. H. Chung and A. V. Flotow, modelling of piezoelectric actuator dynamics for active structural control, Journal of Intelligent Material Systems and Structures, 1990, 1: 327-354

[100] C. K. Lee, W. W. Chiang and T. C. O'Sullivan, piezoelectric modal sensor/actuator pairs for critical active damping vibration control, Acoustical Society of America, 1991, 90 (1): 374-384

[101] V. Balamurugan and S. Narayanan, shell finite element for smart piezoelectric composite plate/shell structures and its application to the study of active vibration control, Finite Elements in Analysis and Design, 2001, 37: 713-738

[102] J. M. S. Moita, I. F. P. Correia, C. M. M. Soares and C. A. M. Soares, active control of adaptive laminated structures with bonded piezoelectric sensors and actuators, Computers and Structures, 2004, 82: 1349-1358

[103] W. S. Hwang, H. C. Park and W. Hwang, vibration control of a laminated plate with piezoelectric sensor/actuator: finite element formulation and modal analysis, Journal of Intelligent Material Systems and Structures, 1993, 4: 317-329

[104] M. A. Trindade, A. Benjeddou and R. Ohayon, piezoelectric active vibration control of damped sandwich beams, Journal of Sound and Vibration, 2001, 246 (4): 653-677

[105] G. S. Agnes, development of a modal model for simultaneous active and passive piezoelectric vibration suppression, Journal of Intelligent Material Systems and Structures, 1995, 6: 482-487

[106] S. Leleu, H. Abou-Kandil and Y. Bonnassieux, piezoelectric actuators and sensors location for active control of flexible structures, IEEE Transactions on Instrumentation and Measurement, 2001, Vol. 50, No. 6: 1577-1582

[107] X. Q. He, T. Y. Ng, S. Sivashanker and K. M. Liew, active control of FGM plates with integrated piezoelectric sensors and actuators, International Journal of Solids and Structures, 2001, 38: 1641-1655

[108] C. M. A. Vasques and J. D. Rodrigues, active vibration control of smart piezoelectric beams: comparison of classical and optimal feedback control strategies, Computers and Structures, 2006, 84: 1402-1414

[109] K. R. Kumar and S. Narayanan, active vibration control of beams with optimal placement of piezoelectric sensor/actuator pairs, Smart Materials and Structures, 2008, 17, 055008

[110] S. O. R. Moheimani, a survey of recent innovations in vibration damping and control using shunted piezoelectric transducers, IEEE Transactions on Control Systems Technology, 2003, Vol. 11, No. 4: 482-494

[111] W. W. Clark, semi-active vibration control with piezoelectric materials as variable stiffness actuators, SPIE conference on passive damping and isolation, 1999, Vol. 3672: 123-130

[112] W. W. Clark, vibration control with state-switched piezoelectric materials, Journal of Intelligent Material Systems and Structures, 2000, Vol. 11: 263-271

[113] C. Richard, D. Guyomar, D. Audigier and G. Ching, semi-passive damping using continuous switching of a piezoelectric device, SPIE, 1999, Vol. 3672

[114] C. Richard, D. Guyomar, D. Audigier and H. Bassaler, enhanced semi passive damping using continuous switching of a piezoelectric device on an inductor, SPIE, 2000, Vol. 3989

[115] J. Ducarne, O. Thomas and J. -F. Deü, structural vibration reduction by switch shunting of piezoelectric elements: modeling and optimization, Journal of Intelligent Material Systems and Structures, 2010, 21: 797-816

[116] C. Richard, D. Guyomar and E. Lefeuvre, Self-Powered Electronic Breaker with Automatic Switching by Detecting Maxima or Minima of Potential Difference between its Power Electrodes, Patent # PCT/FR2005/003000, publication number: WO/2007/063194.

[117] M. Lallart, E. Lefeuvre, C. Richard and D. Guyomar, self-powered circuit for broadband, multimodal piezoelectric vibration control, Sensors and Actuators A, 2008, 143:377-382

[118] L. R. Corr and W. W. Clark, energy dissipation analysis of piezoceramic semi-active vibration control, Journal of Intelligent Material Systems and Structures, 2001, vol. 12: 729-736

[119] L. R. Corr and W. W. Clark, comparison of low-frequency piezoelectric switching shunt techniques for structural damping, Smart Materials and Structures, 2002, 11: 370-376

[120] L. R. Corr and W. W. Clark, a novel semi-active multi-modal vibration control law for a piezoceramic actuator, Transactions of the ASME, 2003, vol.125, 214-222

[121] K. Makihara, J. Onoda and M. Tsuchihashi, semi-active vibration suppression of beam structures based on energy-recycling method, the Japan Society for Aeronautical and Space Sciences, 2004, Vol. 47, No. 157: 167-174

[122] K. Makihara, J. Onoda and M. Tsuchihashi, investigation of performance in suppressing various vibrations with energy-recycling semi-active method, Acta Astronautica, 2006, 58: 506-514

[123] K. Makihara, J. Onoda and K. Minesugi, a self-sensing method for switching vibration suppression with a piezoelectric actuator, Smart Materials and Structures, 2007, 16:455-461

[124] L. Petit, E. Lefeuvre, C. Richard and D. Guyomar, a broadband semi-passive piezoelectric technique for structural damping, Proc. of SPIE Smart Structures and Materials: Damping and Isolation, 2004, Vol. 5386: 414-425

[125] E. Lefeuvre, A. Badel, L. Petit, C. Richard and D. Guyomar, semi-passive piezoelectric structural damping by synchronized switching on voltage sources, Journal of Intelligent Material Systems and Structures, 2006, Vol. 17: 653-660

[126] A. Badel, G. Sebald, D. Guyomar, M. Lallart, E. lefeuvre, C. Richard and J. Qiu, piezoelectric vibration control by synchronized switching on adaptive voltage sources: towards wideband semi-active damping, Acoustical Society of America, 2006, 119 (5): 2815-2825

[127] M. Lallart, A. Badel and D. Guyomar, nonlinear semi-active damping using constant or adaptive voltage sources: a stability analysis, Journal of Intelligent Material Systems and Structures, 2008, Vol. 19: 1131-1142

[128] H. Ji, J. Qiu, A. Badel and K. Zhu, semi-active vibration control of a composite beam using an adaptive SSDV approach, Journal of Intelligent Material Systems and Structures, 2008

[129] M. Lallart, C. Magnet, C. Richard, E. Lefeuvre, L. Petit, D. Guyomar and F. Bouillault, new synchronized switch damping methods using dual transformations, Sensors and Actuators A, 2008, 143: 302-314

[130] D. Guyomar, M. Lallart and T. Monnier, stiffness tuning using a low-cost semiactive nonlinear technique, IEEE/ASME Transactions on Mechatronics, 2008, Vol. 13, No. 5: 604-607

[131] M. Lallart, S. Harari, L. Petit, D. Guyomar, T. Richard, C. Richard and L. Gaudiller, blind switch damping (BSD): a self-adaptive semi-active damping technique, Journal of Sound and Vibration, 2009, 328: 29-41

[132] J. Tang and K. W. Wang, active-passive hybrid piezoelectric networks for vibration control: comparisons and improvement, Smart Materials and Structures, 2001, 10: 794-806

[133] S. Harari, C. Richard and L. Gaudiller, hybrid active/ semi-active modal control of smart structures", Proc. SPIE active and passive smart structures and integrated system, 2009, vol. 7288

[134] D. Guyomar and A. Badel, nonlinear semi-passive multimodal vibration damping: an efficient probabilistic approach, Journal of Sound and Vibration, 2006, 294: 249-268

[135] D. Guyomar, C. Richard and S. Mohammadi, semi-passive random vibration control based on statistics, Journal of Sound and Vibration, 2007, 307: 818-833

[136] H. Ji, J. Qiu, K. Zhu, Y. Chen and A. Badel, multi-modal vibration control using a synchronized switch based on a displacement switching threshold, Smart Materials and Structures, 2009, 18, 035016

[137] H. Ji, J. Qiu, K. Zhu and A. Badel, two-mode vibration control of a beam using nonlinear synchronized switching damping based on the maximization of converted energy, Journal of Sound and Vibration, 2010, 329: 2751-2767

[138] S. Harari, C. Richard and L. Gaudiller, new semi-active multi-modal vibration control using piezoceramic components, Journal of Intelligent Material Systems and Structures, 2009, Vol. 20 No. 13: 1603-1613

[139] C. Richard, S. Harari and L. Gaudiller, Enhanced piezoelectric voltage build-up for semi-active control of smart structures, Proc. SPIE active and passive smart structures and integrated system, 2009, Vol. 7288

[140] O. Wallner, W. R. Leeb and R. Flatscher, design of spatial and modal filters for nulling interferometers, Proc. SPIE, 2003, Vol. 4838: 668-679

[141] A. Preumont, A. François, P. De Man and V. Piefort, spatial filters in structural control, Journal of Sound and Vibration, 2003, 265: 61-79

[142] A. Deraemaeker and A. Preumont, vibration based damage detection using large array sensors and spatial filters, Mechanical Systems and Signal Processing, 2006, 20: 1615-1630

[143] Y. W. Kwon and H. C. Bang, the finite element method using MATLAB, 2000, 2nd edition.

[144] K. A. Bani-Hani, vibration control of wind-induced response of tall buildings with an active tuned mass damper using neural networks, structural control and health monitoring, 2007, 14: 83-108

[145] G. Cazzulani, F. Resta and F. Ripamonti, the active modal tuned mass damper (AMTMD) for vibration suppression in flexible structures, 2011, Proceedings of the World Congress on Engineering, London, Vol. 3

[146] K. A. Cunefare, state-switched absorber for vibration control of point-excited beams, Journal of Intelligent Material Systems and Structures, 2002, Vol. 13: 97-105

[147] M. H. Holdhusen and K. A. Cunefare, experimental vibration control of a single-degree of freedom system using a state-switched absorber, Journal of Intelligent Material Systems and Structures, 2008, Vol. 19: 1435-1442

[148] S. Nagarajaiah, Structural vibration damper with continuously variable stiffness, United States Patent No. 6,098,969 (2000).

[149] S. Nagarajaiah and E. Sonmez, structures with semiactive variable stiffness single/multiple tuned mass dampers, Journal of Structural Engineering, 2007, Vol. 133: 67-77

[150] R. P. Eason, C. Sun, A. J. Dick and S. Nagarajaiah, attenuation of a linear oscillator using a nonlinear and a semi-active tuned mass damper in series, Journal of Sound and Vibration, 2013, 332: 154-166

[151] G. Lin, C. Lin, L. Lu and Y. Ho, experimental verification of seismic vibration control using a semi-active friction tuned mass damper, earthquake engineering and structural dynamics, 2012, 41: 813-830

[152] F. Ricciardelli, A. Occhiuzzi and P. Clemente, semi-active tuned mass damper control strategy for wind-excited structures, Journal of wind engineering and industrial aerodynamics, 2000, 88: 57-74

[153] M. Chey, J. G. Chase, J. B. Mander and A. J. Carr, semi-active tuned mass damper building system: application, earthquake engineering and structural dynamics, 2010, 39: 69-89

[154] M. Lallart, dissertation

[155] A. Baz, active control of periodic structures, Transactions of the ASME, 2001, Vol.123: 472-479

[156] O. Thorp, M. Ruzzene and A. Baz, attenuation and localization of wave propagation in rods with periodic shunted piezoelectric patches, Smart Materials and Structures, 2001, 10: 979-989

[157] O. Thorp, M. Ruzzene and A. Baz, attenuation of wave propagation in fluid-loaded shells with periodic shunted piezoelectric rings, Smart Materials and Structures, 2005, 14: 594-604

[158] A. Spadoni, M. Ruzzene and K. Cunefare, vibration and wave propagation control of plates with periodic arrays of shunted piezoelectric patches, Journal of Intelligent Material Systems and Structures, 2009, 20: 979-990

[159] M. Collet, K. A. Cunefare and M. N. Ichchou, wave motion optimization in periodically distributed shunted piezocomposite beam structures, Journal of Intelligent Material Systems and Structures, 2009, 20: 787-808

[160] Y. Pang, Y. Wang, J. Liu and D. Fang, a study of the band structures of elastic wave propagating in piezoelectric/piezomagnetic layered periodic structures, Smart Materials and Structures, 2010, 19: 055012

[161] F. Casadei, M. Ruzzene, L. Dozio and K. A. Cunefare, broadband vibration control through periodic arrays of resonant shunts: experimental investigation on plates, Smart Materials and Structures, 2010, 19: 015002

[162] F. Casadei, B. S. Beck, K. A. Cunefare and M. Ruzzene, vibration control of plates through hybrid configurations of periodic piezoelectric shunts, Journal of Intellignent Material Systems and Structures, 2012, 23(10): 1169-1177

[163] G. Wang, S. Chen and J. Wen, low-frequency locally resonant band gaps induced by arrays of resonant shunts with Antoniou's circuit: experimental investigation on beams, Smart Material and Structures, 2011, 20: 015026

[164] G. Wang, J. Wang, S. Chen and J. Wen, vibration attenuations induced by periodic arrays of piezoelectric patches connected by enhanced resonant shunting circuits, Smart Materials and Structures, 2011, 20: 125019

[165] L. Airoldi and M. Ruzzene, Wave propagation control in beams through periodic multi-branch shunts, Journal of Intelligent Material Systems and Structures, 2011

[166] A. Y. Aköz and M. Aksoydan, Transfer and stiffness matrix for Timoshenko beams on Elastic Foundations, Bull. Istanbul Tech. Univ., 2004, 54 (3): 1-16

Publications

Journal papers

L. Yan, M. Lallart and D. Guyomar, *Multimodal nonlinear damping technique using spatial filtering*, Journal of Intelligent Material Systems and Structures (*in press*).

M. Lallart, **L. Yan**, Y. Wu and D. Guyomar, *Electromechanical semi-passive nonlinear tuned mass damper for efficient vibration damping*, Journal of Sound and Vibration, 2013, Vol. 332 (22): 5696-5709.

M. Lallart, Y. Wu, **L. Yan**, C. Richard and D. Guyomar, *The effect of seismic energy scavenging on host structure and harvesting performance*, Smart Materials and Structures, 2013, Vol. 22: 035009.

M. Lallart, **L. Yan**, C. Richard and D. Guyomar, damping of periodic bending structures featuring nonlinearly interfaced piezoelectric elements, Smart Materials and Structures (*submitted*).

Conference

L. Yan, M. Lallart and D. Guyomar, *Multimodal nonlinear damping technique using spatial filtering*, International Conference on Advanced Materials for Photonics, Sensing and Energy Conversion Applications, Dec. 5-7, 2012, El Jadida Morocco

Appendix: Finite element modelling of Euler-Bernoulli electro-mechanical beam

An electromechanical model based on finite element method is introduced in this section aiming at analyzing the dynamical behaviour of a bending beam with piezoelectric elements as depicted in Figure A.1. Mechanical equations as well as the electrical relationships are derived in detail. For simplicity, axes x_1, x_2 and x_3 are defined along the length, width and thickness of the beam, respectively and following assumptions are made:

1. The beam is governed by Euler-Bernoulli beam theory (i.e. $T_3 = 0$), so that transverse shear is not taken into account ;
2. Strain has only two dimensions (i.e. $S_2 = 0$) and no torsion is considered;
3. x_3 is assigned to the direction of the polarization of piezoelectric patches and the electric field intensity along the thickness is constant.
4. The piezoelectric material is viewed as a transversely isotropic material.

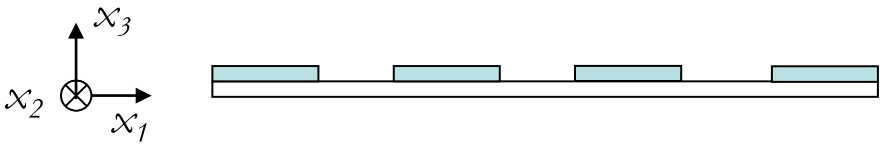

Figure A.1. Schematic of bending beam with distributed piezoelectric patches.

Stress of the Structure

Under the previous assumptions, the longitudinal stress of the rigid structure is given by:

$$T_{b1} = E_b S_1 \tag{A.1}$$

where E_b denotes elastic rigidity of the rigid beam in-plane strain whose value can be obtained by:

$$E_b = \frac{Y}{1-\upsilon^2} \tag{A.2}$$

with Y the Young's modulus and υ the Poisson's ratio.

For isotropic piezoelectric materials and under the considered assumptions, the constitutive equations can be reduced as:

$$\begin{bmatrix} S_1 \\ S_2 \\ D_3 \end{bmatrix} = \begin{bmatrix} s_{11}^E & s_{12}^E & \sigma d_{31} \\ s_{12}^E & s_{11}^E & \sigma d_{31} \\ \sigma d_{31} & \sigma d_{31} & \varepsilon_{33}^T \end{bmatrix} \begin{bmatrix} T_{p1} \\ T_{p2} \\ E_3 \end{bmatrix} \tag{A.3}$$

where s^E corresponds to the mechanical compliance tensor of the piezoelectric material under constant electric field and ε^T is the electrical permittivity under constant stress. d_{31} is piezoelectric charge constant. E_3 and D_3 are given as the electric field intensity and electrical displacement along x_3 direction, respectively. σ is the sign of the piezoelectric constant which depends on the polarization of the material.

Hence, the strain along the length and width can be rewritten as follows:

$$\begin{cases} S_1 = s_{11}^E T_{p1} + s_{13}^E T_{p3} + s_{12}^E T_{p2} + \sigma d_{31} E_3 \\ S_2 = s_{12}^E T_{p1} + s_{23}^E T_{p3} + s_{11}^E T_{p2} + \sigma d_{31} E_3 \end{cases} \tag{A.4}$$

Then, the longitudinal stress of the piezoelectric patch can be obtained from Eq. (A.4):

$$T_{p1} = \frac{s_{11}^E}{s_{11}^{E2} - s_{12}^{E2}} S_1 - \frac{\sigma d_{31}}{s_{11}^E + s_{12}^E} E_3 \tag{A.5}$$

When the piezoelectric patch experiences vibrations, electromechanical interaction occurs between mechanical and electrical states and the electric field can be expressed as a function of piezoelectric voltage V_p as:

$$E_3 = -\frac{V_p}{t_p} \tag{A.6}$$

where t_p denotes the thickness of the piezoelectric patch. Thus, the longitudinal stress of Eq. (A.5) can be further rewritten by:

$$T_{p1} = E_p S_1 + \frac{\sigma d_{31}}{t_p \left(s_{11}^E + s_{12}^E \right)} V_p \tag{A.7}$$

Bending Moment

The longitudinal strain is defined as the product of the distance from the neutral axis x_c and the second spatial derivative of the deflection u_3 on the basis of the Euler-Bernoulli beam theory and has the form:

$$S_1 = -\left(x_3 - x_c \right) \frac{\partial^2 u_3}{\partial x_1^2} \tag{A.8}$$

Assuming that $x_3=0$ is the lower surface of the beam, the neutral axes of the elements shown in Figure A.2 are given by:

$$\begin{cases} \text{Without piezoelectric material:} & x_c = \dfrac{t_b}{2} \\ \text{With piezoelectric material:} \begin{cases} \text{one surface covered:} & x_c = \dfrac{E_b t_b^{\,2} + E_p t_p^{\,2} + 2 t_b t_p E_p}{2(E_b t_b + E_p t_p)} \\ \text{both surfaces covered:} & x_c = \dfrac{t_b}{2} \end{cases} \end{cases} \tag{A.9}$$

where t_b is the thickness of the substrate structure.

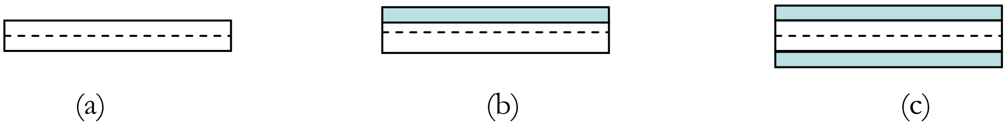

Figure A.2. Elements of electromechanical bending beam: (a) a beam element without piezoelectric material; (b) a beam element with piezoelectric material covered on one surface; (c) a beam element with piezoelectric material covered on both surfaces.

Moreover, the bending moment $M_{bending}$ is expressed by integrating the product of longitudinal stress and relative deflection over the cross area, which is given as

$$M_{bending} = w\int T_1\left(x_3 - x_c\right)dx_3 \tag{A.10}$$

with w the width of the bending beam.

Mechanical Equation

Based on the theory of finite element method [143], a structure can be divided into sections and each section can be regarded as an element. The equilibrium of force along the thickness of a Euler-Bernoulli beam element can be presented as:

$$m\frac{\partial^2 u}{\partial t^2} + \frac{\partial^2 M_{bending}}{\partial x_1^2} = q(x_1, t) \tag{A.11}$$

where $q(x_1, t)$ is the externally applied load and x_1, t indicate spatial and time axes. m is the mass per unit length of the bending beam. For an electromechanical beam, there are two kinds of elements: beam elements without piezoelectric material and beam elements with piezoelectric material which are shown in Figure A.2.

Thus, the dynamical equations of an element can be written in detail with Hermitian shape functions $H_{er}(x)$ as:

$$\begin{cases} \text{Without piezoelectric material:} \left[M^e\right]\left\{\ddot{d}^e\right\} + \left[K^e\right]\left\{d^e\right\} = \left\{F^e(t)\right\} \\ \text{With piezoelectric material:} \left[M^e\right]_p\left\{\ddot{d}^e\right\} + \left[K^e\right]_p\left\{d^e\right\} - \left[B_1^e\right]\left\{V^e{}_p\right\} = \left\{F^e(t)\right\} \end{cases} \tag{A.12}$$

where $\left\{d^e\right\} = \left\{u_i \quad \theta_i \quad u_{i+1} \quad \theta_{i+1}\right\}^T$, $i = 1,2,...,n-1$ are the variables of a beam element; $\theta = \frac{\partial u_3}{\partial x_1}$ denotes the slope of deflection; $M^e = \int_0^l m\left[H_{er}\right]^t \left[H_{er}\right] dx$ and $M^e{}_p$ denote mass matrix of element (without/with piezoelectric material respectively); $K^e = \int_0^l \left[H_{er}''\right]^T EI \left[H_{er}''\right] dx$ and $K^e{}_p$ denote stiffness matrix of the element (without/with piezoelectric material respectively); EI is the rigidity of the structure; $F^e\left(t\right) = \int_0^l q\left(x,t\right)\left[H_{er}\right]^T dx$ is the force vector for dynamic analysis; $B_1^e = b_1 \int_0^l \left[H_{er}''\right]^T dx$ is the force factor vector produced by piezoelectric material during the vibration, with $b_1 = \frac{\sigma d_{31} w}{t_p\left(s_{11}^E + s_{12}^E\right)} \int_{t_b}^{t_b+t_p} (u_3 - x_c) dx_3$.

Assembling all the elements [143], the dynamical equation of the whole structure can be obtained in terms of the nodal variables in matrix-vector notation as:

$$\left[M\right]\left\{\ddot{d}\right\} + \left[K\right]\left\{d\right\} - \left[B_1\right]\left\{V_p\right\} = \left\{F(t)\right\} \tag{A.13}$$

M, K denote mass matrix and stiffness matrix, respectively. B_1 is global force factor matrix. Introducing a damping matrix C, the global motion equation holds the form:

$$\left[M\right]\left\{\ddot{d}\right\} + \left[C\right]\left\{\dot{d}\right\} + \left[K\right]\left\{d\right\} - \left[B_1\right]\left\{V_p\right\} = \left\{F(t)\right\} \tag{A.14}$$

It should be noted here that generally the damping matrix is calculated from the experimental measured damping ratio or is considered as proportional to mass and stiffness. Moreover, it could also be defined from the complex stiffness matrix.

Electrical Equation

For the piezoelectric patch, the electrical displacement is expressed as follows:

$$D_3 = \frac{-\sigma d_{31} t_p}{\left(s_{11}^E + s_{12}^E\right)} \frac{\partial^2 u_3}{\partial x_1^2} - \frac{\varepsilon_{33}^T \left(s_{11}^E + s_{12}^E\right) - 2\left(\sigma d_{31}\right)^2}{\left(s_{11}^E + s_{12}^E\right)} \frac{V_p}{t_p} \tag{A.15}$$

Then, the electric charge quantity Q of one piezoelectric patch can be expressed by integrating the electrical displacement over the overall length of the piezoelectric patch:

$$Q = w \int D dx_1 \tag{A.16}$$

For simplicity, assuming that the piezoelectric patches are identical and the i^{th} piezoelectric element with the length L_{pi} is bonded at the position $x_{i0} \le x_1 \le x_{i0} + L_{pi}$ of the bending beam, the substitution of Eq. (A.15) into Eq. (A.16) yields:

$$Q_i = -\frac{wt_p\left(\sigma d_{31}\right)_i \theta\Big|_{x_{i0}}^{x_{i0}+L_{pi}}}{\left(s_{11}^E + s_{12}^E\right)} - \frac{wL_{pi}\left[\varepsilon_{33}^T\left(s_{11}^E + s_{12}^E\right) - 2d_{31}{}^2\right]}{t_p\left(s_{11}^E + s_{12}^E\right)} V_{pi} \qquad \text{(A.17)}$$

Then, the electrical equation can be given in matrix-vector notation:

$$\{Q\} = [B_2]\{d\} + [B_3]\{V_p\} \qquad \text{(A.18)}$$

With B_2 assembled by

$$B_2{}^e = -\frac{wt_p d_{31}}{s_{11}^E + s_{12}^E}[\sigma]\cdot\int_0^l \left[H_{er}{}''\right]dx \qquad \text{(A.19)}$$

and

$$B_3 = -\frac{w\left[\varepsilon_{33}^T\left(s_{11}^E + s_{12}^E\right) - 2d_{31}{}^2\right]}{t_p\left(s_{11}^E + s_{12}^E\right)}\left[L_p\right] \qquad \text{(A.20)}$$

where $[\sigma]$ and $\left[L_p\right]$ are diagonal matrices which respectively depend on the polarization and length of the bonded piezoelectric patches.

From the previous analysis, a finite element model of electromechanical bending beam is established, which is valid under any boundary condition. The electromechanical relationships are summarized as:

$$\begin{cases} [M]\{\ddot{d}\} + [C]\{\dot{d}\} + [K]\{d\} - [B_1]\{V_p\} = \{F(t)\} \\ \{Q\} = [B_2]\{d\} + [B_3]\{V_p\} \end{cases} \qquad \text{(A.21)}$$

Based on this model, the electromechanical behaviour of a smart bending beam under external excitation can be simulated and evaluated.

FOLIO ADMINISTRATIF

THESE SOUTENUE DEVANT L'INSTITUT NATIONAL DES SCIENCES APPLIQUEES DE LYON

NOM : YAN DATE de SOUTENANCE : 04 Octobre 2013
(avec précision du nom de jeune fille, le cas échéant)

Prénoms : Linjuan

TITRE : Contrôle de vibrations large bande à l'aide d'éléments piézoélectriques utilisant une technique non-linéaire

NATURE : Doctorat Numéro d'ordre : 2013-ISAL-0107

Ecole doctorale : Electronique, Electrotechnique et Automatique

Spécialité : Energie et Système

RESUME :

Afin de limiter les contraintes dans les matériaux pour accroître leur durée de vie et améliorer la sécurité des structures (par exemple dans les transports), ainsi que d'améliorer le confort des utilisateurs, le contrôle de vibrations mécaniques et leur amortissement a fait l'objet de nombreuses recherche scientifiques depuis de nombreuses décennies. De plus, la prolifération récente des matériaux dits « intelligents » couplant plusieurs disciplines de la physique telles que la mécanique et l'électricité a permis l'élaborations de techniques de contrôle de vibration fiables, robustes et performantes tout en étant très intégrables, permettant ainsi de disposer de méthodes totalement adaptées aux système embarqués ou aux structures où les contraintes d'encombrement sont relativement restrictives. Notamment, il a récemment été proposé l'utilisation de techniques non linéaires basées sur une commutation synchronisée d'éléments piézoélectriques sur une impédance afin d'amélioration la conversion d'énergie mécanique sous forme électrique et ainsi de disposer de systèmes de contrôle de vibrations très performants et intégrables.

Néanmoins, du fait du principe de cette commutation synchronisée avec la déformation, le contrôle de vibrations large bande, très présents dans les environnements réels, conduit à une dégradation des performances de ces techniques. L'objectif des travaux rapportés dans cette thèse consiste à proposer et à étudier théoriquement et expérimentalement des approches dérivées de ces techniques mais totalement adaptées au large bande.

Ainsi, après une introduction relatant l'état de l'art en termes de contrôle vibratoire, la première technique exposée dans cette thèse propose d'utiliser un filtrage spatial permettant de séparer les modes de vibrations pour ensuite connecter de manière appropriée des éléments piézoélectriques afin de pouvoir simultanément contrôler plusieurs modes de vibrations en flexion.

La deuxième méthode pour disposer de systèmes de contrôle de vibrations efficaces se base sur la combinaison d'amortisseurs à masse accordée avec l'approche non-linéaire afin d'améliorer le pouvoir d'amortissement par un contrôle supplémentaire des transferts énergétiques via le couplage électromécanique, conduisant à une méthode efficace, robuste et pouvant être installée facilement.

La troisième et dernière approche consiste à utiliser les propriétés remarquables des structures périodiques en les couplant avec l'approche non-linéaire, cette dernière permettant une augmentation de l'amortissement et un élargissement significatif des bandes fréquentielles réduisant significativement l'amplitude de l'onde.

Enfin, une conclusion générale exposera les principaux résultats obtenus et proposera des pistes d'évolution des concepts exposés.

MOTS-CLES : vibration, amortissement, piézoélectrique, non-linéaire

Laboratoire (s) de recherche : LGEF - Laboratoire de Génie Electrique et Ferroélectricité-INSA Lyon

Directeur de thèse: Pr. Daniel GUYOMAR
Co-directeur de thèse: Dr. Mickaël LALLART

Président de jury :

Composition du jury : Pr. Manuel COLLET Pr. Jean-François DEÜ
Pr. Mohamed ICHCHOU Pr. Joël POUGET
Pr. Daniel GUYOMAR Dr. Mickaël LALLART